

INFORMATION TO USERS

This manuscript has been reproduced from the microfilm master. UMI films the text directly from the original or copy submitted. Thus, some thesis and dissertation copies are in typewriter face, while others may be from any type of computer printer.

The quality of this reproduction is dependent upon the quality of the copy submitted. Broken or indistinct print, colored or poor quality illustrations and photographs, print bleedthrough, substandard margins, and improper alignment can adversely affect reproduction.

In the unlikely event that the author did not send UMI a complete manuscript and there are missing pages, these will be noted. Also, if unauthorized copyright material had to be removed, a note will indicate the deletion.

Oversize materials (e.g., maps, drawings, charts) are reproduced by sectioning the original, beginning at the upper left-hand corner and continuing from left to right in equal sections with small overlaps. Each original is also photographed in one exposure and is included in reduced form at the back of the book.

Photographs included in the original manuscript have been reproduced xerographically in this copy. Higher quality 6" x 9" black and white photographic prints are available for any photographs or illustrations appearing in this copy for an additional charge. Contact UMI directly to order.



University Microfilms International
A Bell & Howell Information Company
300 North Zeeb Road, Ann Arbor, MI 48106-1346 USA
313/761-4700 800/521-0600

Order Number 9414670

**The Gravity Probe B niobium bird experiment: Experimental
verification of a data reduction scheme with a prototypical dc
SQUID readout system**

Uematsu, Hirohiko, Ph.D.

Stanford University, 1994

Copyright ©1993 by Uematsu, Hirohiko. All rights reserved.

U·M·I

**300 N. Zeeb Rd.
Ann Arbor, MI 48106**

**THE GRAVITY PROBE B
NIOBIUM BIRD EXPERIMENT:
EXPERIMENTAL VERIFICATION OF
A DATA REDUCTION SCHEME WITH
A PROTOTYPICAL DC SQUID READOUT SYSTEM**

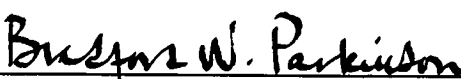
**A DISSERTATION SUBMITTED TO THE
DEPARTMENT OF AERONAUTICS AND ASTRONAUTICS
AND THE COMMITTEE ON GRADUATE STUDIES
OF STANFORD UNIVERSITY
IN PARTIAL FULFILLMENT OF THE REQUIREMENTS
FOR THE DEGREE OF
DOCTOR OF PHILOSOPHY**

**By
Hirohiko Uematsu**

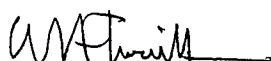
October 1993

© Copyright by Hirohiko Uematsu 1993
All Rights Reserved

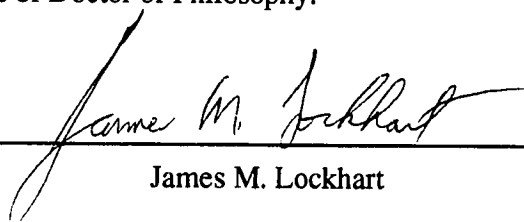
I certify that I have read this dissertation and that in my opinion it is fully adequate, in scope and quality, as a dissertation for the degree of Doctor of Philosophy.


Bradford W. Parkinson (Principal Advisor)

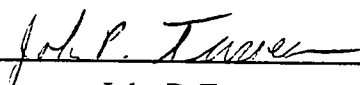
I certify that I have read this dissertation and that in my opinion it is fully adequate, in scope and quality, as a dissertation for the degree of Doctor of Philosophy.


C. W. Francis Everitt

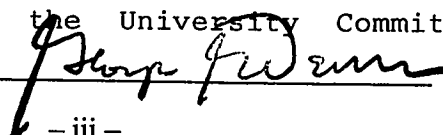
I certify that I have read this dissertation and that in my opinion it is fully adequate, in scope and quality, as a dissertation for the degree of Doctor of Philosophy.


James M. Lockhart

I certify that I have read this dissertation and that in my opinion it is fully adequate, in scope and quality, as a dissertation for the degree of Doctor of Philosophy.


John P. Turneure

Approved for the University Committee on Graduate Studies



ABSTRACT

This dissertation describes the concept and the latest results from the niobium bird experiment, which is an integrated, end-to-end test environment for the data reduction scheme and the readout system designed for the Gravity Probe B program (GP-B).

The Gravity Probe B program is a relativity gyroscope experiment begun at Stanford University in 1960 and supported by NASA since 1963. This experiment, for the first time, will check the relativistic precession of an Earth-orbiting gyroscope that was predicted by Einstein's General Theory of Relativity, to an accuracy of 1 milliarcsecond per year or better. A drag-free satellite will carry four gyroscopes in a polar orbit to observe their relativistic precession. The primary sensor for measuring the direction of the gyroscope spin axis is the SQUID (superconducting quantum interference device) magnetometer. The data reduction scheme designed for the GP-B program processes the signal from the SQUID magnetometer and estimates the relativistic precession rates. I reformulated the two-step Kalman filters, originally developed by J. V. Breakwell and X. Qin, and designed the niobium bird experiment to verify the performance of the data reduction scheme experimentally with SQUID readout hardware within the test loop.

The niobium bird experiment comprised three major components: a truth model, Kalman filters, and a SQUID readout system. The truth model simulated the science signal, which was injected into the SQUID readout system. The SQUID output was then fed into the two-step Kalman filters as a measurement, and the true values and the estimates by the filters were compared to evaluate the filter performance. I also evaluated the performance of the readout hardware in terms of the stability and the signal-to-noise ratio, including the SQUID magnetometer, the lowpass filter, and the A-to-D converter.

The latest results from the niobium bird experiment showed that the temperature-dependent bias drift in a commercially available dc SQUID was too large to achieve the required estimation accuracy. I used a commercially available dc SQUID manufactured by Quantum Design, Inc., which showed a strong correlation between the readout bias and the temperature of the SQUID controller with a cross-correlation coefficient of 0.968 or a temperature coefficient of about 1 arcsecond per Kelvin. This correlation, with a lack of temperature regulation, yielded a large bias drift in the SQUID magnetometer which was about twenty times larger than what I assumed in the simulation. For the GP-B science mission, the bias drift in the SQUID readout can be reduced to meet the requirement by implementing a temperature regulation system and designing a SQUID controller with a smaller temperature coefficient.

I also examined the effect of the gyroscope's polhode motion in the presence of the trapped flux, the effect of a faster roll period, and the effect of the telescope pointing error on the data reduction by simulations. I modeled the trapped flux signal by modulation of a SQUID scale factor. Even though the model I used may not represent the actual effects accurately, the simulation showed that the trapped flux signal can be spectrally separated by using a faster polhode period.

ACKNOWLEDGMENTS

I would like to thank my principal advisor, Professor Bradford W. Parkinson for his advice, support, and encouragement that he has provided for so many years. In addition to the fact that he has been an inspirational advisor who always provided a broader picture of the research, he has been a mentor. His leadership taught me something that I will benefit from throughout my life. An equally great debt of gratitude is due Professor James M. Lockhart. Without his dedication and enthusiasm, the niobium bird experiment would not have been possible. He not only provided an excellent apparatus including the SQUID magnetometer with which to begin my work, he has continuously given generously of his time to provide advice and assistance in all phases of this experiment. His dedication to this experiment was probably the driving force for me to finish my dissertation, and I am honored to acknowledge his support. He also made many useful comments on the manuscript of this thesis.

I would like to thank Dr. Barry Muhlfelder for his advice and support. He spent a considerable amount of time discussing the SQUID performance and made valuable comments on the manuscript of this thesis.

I would like to acknowledge the advice and important suggestions from Professor C. W. Francis Everitt and Professor John P. Turneaure not only in revising this dissertation but throughout my research. I became very confident of what I put into this dissertation after going through so many hours of discussions with them, and I would like to thank them for the time they spent to carefully go through the manuscript of this thesis.

During the course of this work, I have profited from many discussions with Dr. Jeremy Kasdin, Dr. Mac Keiser, Richard Van Patten, Todd Walter, and Dr. Yueming Xiao, and would like to thank them for inspirational suggestions. I also wish to thank Gregory Gutt and Gordon Haupt for providing vital calibration results for the experiment and thank Mike Condron for assisting to set up the experiment. It is a pleasure to

acknowledge the support provided by Ted Ale, who helped me set up the dewar and the support structure. It was such a pleasant experience to work with Ted, who is so experienced and knowledgeable in mechanical design.

Many people have contributed to the success of the niobium bird experiment. I wish to thank Jeff Wade for setting up the computers for the experiment, which were such vital parts of the experiment. I would like to thank Denise Freeman for her support and incredible skill to arrange an appointment with Brad when I needed to see him. I am grateful to both Monica Jarnot of GP-B and Loren Rusk of the Technical Communication Program of the Engineering School for proof-reading the entire manuscript. They have been patient with a lack of my writing skill and helped me convert engineer's jargon to more understandable words. My thanks go to all the members of the GP-B program for providing a cheerful support. I would like to thank Pete Cruz, Thorwald von Hooydonk, Carolyn Kaye, Tom Langenstein, Mae Sato, Jeri Stallard and all the others for making my days at GP-B more cheerful and less painful.

Gratitude is acknowledged to NASA for supporting this research under Contract No. NAS8-36125.

I am tremendously grateful to my parents, Dr. Kunihiko Uematsu and Dr. Setsuko Uematsu, for supporting us on all aspects. I have never felt it difficult to have two Doctors as parents. Nonetheless, I have learned how difficult it is to earn a doctorate. Understanding their struggles and appreciating their accomplishments are the best I can do to answer their unconditional love.

After many seasons have passed, my wife Ikuko and I don't even remember how we made those days through. One thing is sure that Ikuko has always been by my side, has supported me, and has gone through all the emotions, joy, sorrow, and anger, together. Without her support and understanding, this would not have been possible. She deserves as much credit on my degree as I, and with great pleasure and some relief, I dedicate this dissertation to her.

TABLE OF CONTENTS

List of Figures	xiii
List of Tables.....	xvii
Symbols	xix
Chapter 1. Introduction	1
1.1 Problem Statement	1
1.2 GP-B Program Overview	3
1.2.1 GP-B Program Objectives.....	6
1.2.2 GP-B Satellite Orbit	8
1.2.3 GP-B Satellite Pointing Control.....	9
1.2.4 GP-B Satellite Roll Control.....	10
1.2.5 GP-B Gyroscopes.....	10
1.2.6 GP-B Readout System.....	11
1.3 Overview of the Niobium Bird Project	13
1.4 Previous Results	17
1.4.1 Vassar's Work.....	17
1.4.2 Duhamel's Work.....	18
1.4.3 DiEsposti's Work.....	20
1.4.4 Qin's Work	22
1.5 Contributions.....	24
1.6 Thesis Outline	25

Chapter 2. Coordinate Frame Definition	27
2.1 Introduction	27
2.2 Primary Frames	29
2.2.1 Orientation of the A-0 Frame	30
2.2.2 Orientation of the B-0 Frame	31
2.2.3 Orientation of the C-0 Frame	33
2.2.4 Transformation Among Primary Frames	35
2.3 Secondary Frames	36
2.3.1 Secondary Frames in Category A.....	37
2.3.2 Secondary Frames in Category E.....	42
2.3.3 Secondary Frames in Category C.....	46
2.4 Frame Definition Summary.....	50
 Chapter 3. Random Sequence Generation.....	 52
3.1 Introduction	52
3.2 Uniformly Distributed Random Sequence (UDRS).....	53
3.2.1 Generation of a UDRS	56
3.2.2 Verification of Simulated UDRSs.....	58
3.3 Gaussian Random Sequence (GRS).....	63
3.3.1 Generation of a GRS	64
3.3.2 Verification of Simulated GRSs.....	65
3.4 Wiener Random Sequence (WRS).....	67
3.4.1 Generation of a WRS	69
3.4.2 Verification of Simulated WRSs.....	71
3.5 Band-Limited Wiener Random Sequence (BLWRS)	73
3.5.1 Generation of a BLWRS	74
3.5.2 Verification of Simulated BLWRSs.....	78
3.6 Summary of Random Sequence Simulation.....	80
 Chapter 4. Truth Modeling	 81
4.1 Introduction	81
4.2 Truth Models.....	82
4.2.1 Standard Units.....	83

4.2.2	Models of Celestial Motion.....	84
4.2.2.1	Earth Motion	85
4.2.2.2	Satellite Orbital Motion.....	87
4.2.2.3	Parallax of Rigel.....	91
4.2.2.4	Aberration.....	92
4.2.2.5	Deflection of Starlight.....	95
4.2.2.6	Proper Motion of Rigel	97
4.2.2.7	Summary of Observational Corrections.....	97
4.2.3	Structural Model of SQUID Readout System.....	98
4.2.3.1	Misalignment of Gyro Pickup Loop.....	98
4.2.3.2	Structural Creeping of the Gyro Pickup Loop	100
4.2.4	Models of the Satellite Dynamic.....	101
4.2.4.1	Pointing Control	101
4.2.4.2	Roll Phase Control	103
4.2.5	Model of Satellite Data Acquisition.....	104
4.2.5.1	SQUID Magnetometer	104
4.2.5.2	Analog-to-Digital Converter	110
4.2.5.3	Anti-Aliasing Lowpass Filter	112
4.2.6	Gyro Model	113
4.3.	Simulation of the Science Signal	114
4.3.1	Measurement Equation.....	114
4.3.1.1	Idealized Measurement Equation	116
4.3.1.2	Realistic Measurement Equation.....	121
4.3.2	Signal Availability.....	123
4.3.2.1	Occultation	124
4.3.2.2	Flux Jumps	125
4.3.2.3	Signal Interruption.....	127
Chapter 5.	Data Reduction Scheme Synthesis.....	128
5.1	Introduction	128
5.2	Filter Formulation	129
5.2.1	Formulation of Step 1 Filter	130
5.2.2	Formulation of Step 2 Filter	135
5.2.3	Results of Two-step Filter Simulation.....	137
5.2.3.1	Condition of Simulation.....	137

5.2.3.2	Results of Step 1 Filtering.....	140
5.2.3.3	Results of Step 2 Filtering.....	141
5.3	Recursive Algorithm	146
5.3.1	Formulation of Recursive Filters.....	146
5.3.2	Results of Recursive Filter Simulation.....	148
5.4	Polhode Modeling and Estimation	150
5.4.1	Modeling of Polhode Motion in Science Signal	150
5.4.2	Results of Two-step Filtering with Polhode Simulation	151
5.4.3	Effects on Gyroscope Dynamics and Requirements of Readout System	158
5.5	Effects of Pointing Error	163
5.6	Effects of Roll Period.....	167
5.7	Summary of Data Reduction Synthesis.....	170
Chapter 6.	Experimental Verification	171
6.1	Introduction	171
6.2	Experimental Configuration.....	172
6.2.1	Data Injection Instruments	174
6.2.2	Cryogenic Instruments	174
6.2.2.1	Supporting Structures.....	175
6.2.2.2	SQUID Readout System.....	175
6.2.2.3	Temperature Control System	179
6.2.3	Data Sampling Instruments.....	180
6.3	Calibration of Niobium Bird Experiment.....	181
6.3.1	Results of Temperature Regulation of Liquid Helium.....	181
6.3.2	Settings and Noise Performance of SQUID Magnetometer.....	182
6.3.3	Stability of Scale Factor and Bias in SQUID Readout.....	184
6.3.4	Scaling of Injection Current to Calibration Coil	190
6.3.5	Calibration of Data Injection Instruments.....	194
6.3.6	Calibration of Data Sampling Instruments.....	199
6.3	Experimental Results.....	201
6.3.1	Step 1 Filtering with Nominal Process Noise (Case I).....	203
6.3.2	Step 1 Filtering with Adjusted Process Noise (Case II).....	206
6.3.3	Summary of Experimental Results.....	208

Chapter 7. Conclusions	210
7.1 Conclusions	210
7.2 Limitations of This Study and Recommendations for Future Work.....	213
References	216
Appendices	223
Appendix A. Program Lists of Truth Model.....	223
A.1 Example of Conditional File COND.DAT.....	224
A.2 Program List of GLOBALS.H	224
Appendix B. Formulation of SQUID Noise Shaping Filter	227
B.1 Program List of GSQUID.M.....	227
B.2 Program List of CVRTQ.M	229

LIST OF FIGURES

<u>Figure Number</u>	<u>Title</u>	<u>Page Number</u>
1.1	Gravity Probe B program. A gyroscope in an Earth orbit will undergo two relativistic precessions according to general relativity.	4
1.2	GP-B satellite outside view. The main body of the GP-B satellite is a dewar that holds liquid helium for temperature control.	6
1.3	GP-B signal flow diagram. The direction of the gyroscope's spin axis is measured onboard and sent to the ground station. The Kalman filters process the data there.	7
1.4	London moment readout of a superconducting gyroscope and a SQUID magnetometer.	12
1.5	Simplified power spectral density of several SQUIDs (Ref. 14).	13
1.6	Conceptual diagram and three major tasks of niobium bird experiment.	16
2.1	Orientation of the A-0 and C-0 frames with respect to solar barycenter, vernal equinox, mean equator, and Rigel. A-0 is the I_0 reference frame, and C-0 is the barycentric celestial frame.	31
2.2	Orientations of body-fixed frames, B-0 and B-1. B-0 is the nominal control frame, and B-1 is the assembly frame.	34
2.3	Orientation of the A-i frames ($i=0,\dots,6$).	41
2.4	Orientations of the B-0 and B-2 frame with respect to the proof mass cavity. B-0 is the nominal control frame, and B-2 is the control frame.	44
2.5	Orientations of the C-1 and C-2 frames. C-1 is the geocentric celestial frame and C-2 is the orbital frame whose xz plane is parallel to the orbit.	48
2.6	Hierarchical diagram of standardized coordinate frames. Each arrow connecting two frames indicates the dependency. The frame that the arrow points to is defined with respect to the other frame.	51
3.1	Histogram of a simulated UDRS (16384 samples).	59
3.2	Data segmentation for a modified periodogram.	60
3.3	Predicted vs. estimated power spectral density of a UDRS.	61

3.4	Histogram of a GRS generated by two methods.	66
3.5	Predicted vs. estimated PSD of a GRS generated by two methods.....	67
3.6	Predicted vs. estimated PSD of a WRS ($\Delta t=10$ seconds, $\alpha_w=0.001$).	71
3.7	Time history of Wiener random sequences (10 samples).	72
3.8	Covariance coefficient function of a BLWRS.	75
3.9	Covariance coefficient function vs. T_c after one year ($\Delta t=10$ seconds).....	76
3.10	Crossover frequency vs. $1/T_c$ of a BLWRS with $\Delta t=10$ seconds, $\alpha_w=0.001$	77
3.11	Predicted vs. estimated PSD of a WRS and a BLWRS.	78
3.12	Time history of band-limited Wiener random sequence (10 samples). $T_c=100$ seconds, $\Delta t=10$ seconds, $\alpha_w=0.001$	79
4.1	Nominal GP-B satellite orbit.....	90
4.2	Parallax caused by the position of the Earth with respect to the Sun.....	91
4.3	Aberration caused by observer's velocity.....	93
4.4	Deflection of starlight caused by the Sun's gravity. The treatment of the light as a particle explains only a half of the effect. General relativity explains the other half.....	95
4.5	SQUID sensor noise simulation.	105
4.6	Power spectral density of ideal $1/f$ noise, four-pole shaping filter, and simulated $1/f$ noise with $f_s=0.1$ Hz.....	107
4.7	Definition of spin direction vectors s_i , readout vectors R_i , and readout angles θ_i ($i=1, 2, 3, 4$).....	115
4.8	Definition of occultation limit circle around the Earth. Shaded part of the orbit is called Rigel invalid.	124
5.1	Diagram of two-step Kalman filters.....	130
5.2	Frequency components of a science signal and demodulation by step 1 filters (f_r =roll frequency, f_o =orbital frequency).....	134
5.3	Results of step 1 filtering from a one-year simulation	140
5.4	Results of step 2 filtering from a one-year simulation	143
5.5	Results of step 2 filtering from a one-year simulation. Time history of the estimation error and 1σ envelope of the relativistic precession rates.	145
5.6	Diagram of recursive two-step Kalman filters.	147

5.7	Results of recursive two-step filtering from a one-year simulation. Time history of the estimation error and 1s envelope of the relativistic precession rates.....	149
5.8	Final estimation error of the relativistic precession rates after a one-year simulation with polhode modulation of the scale factor.	152
5.9	Frequency components of a science signal with polhode modulation of the scale factor (f_r =roll frequency, f_o =orbital frequency, f_p =polhode frequency).	154
5.10	Spectral decomposition of the science signal with various polhode periods.....	156
5.11	Spectral decomposition of the science signal with an optimal polhode period 0.2 hour. Spectral separation between the roll signal and the polhode signals is about 1.4 mHz.	157
5.12	Poinsot's inertia ellipsoid and an invariable plane.	159
5.13	Normalized polhode period vs. separation angle between the spin vector and the inertia principal axis of symmetry with $\omega_s=170$ Hz, $\epsilon_i=8.2 \times 10^{-6}$	161
5.14	Time history of the estimation error of the relativistic precession rates with various telescope pointing errors.	166
5.15	Time history of the estimation error of the relativistic precession rates with various satellite roll periods.....	169
6.1	Experimental configuration of the niobium bird experiment.	173
6.2	Quartz housing and gyroscope with niobium coating.	175
6.3	Simulated London moment and SQUID readout system for the niobium bird experiment.	176
6.4	Dimensions of the gyroscope, pickup loop, and calibration coil.	178
6.5	Temperature control system of liquid helium with vacuum pump, Ge resistance thermometer, heater, temperature bridge, and PID controller.	180
6.6	Temperature regulation error of liquid helium with a set point of 1.93 K.	182
6.7	Square-root power spectral density of Quantum Design dc SQUID noise (indicated by o's).	183
6.8	Calibration of scale factor and bias drift in the SQUID readout system.	186
6.9	Calibration results of the SQUID scale factor.	187

6.10	Correlation between the bias in the SQUID readout and the temperature of the SQUID controller.....	188
6.11	Inductive coupling of the SQUID readout system for the science mission.	190
6.12	Output noise and temperature of the waveform generator HP3245A.....	196
6.13	Power spectral density of the SQUID noise (Quantum Design Model 5000) and the output noise of the waveform generator (HP3245A).	197
6.14	Output noise and temperature of the voltage divider.	198
6.15	Power spectral density of the SQUID noise (Quantum Design Model 5000) and the output noise of the voltage divider.	199
6.16	Comparison of noise performance among signal generator (HP3245A), sensor (Quantum Design SQUID), and signal sampler (K196).	200
6.17	Sampled science signal in the niobium bird experiment.....	202
6.18	Estimation errors of NS_s and ES_s terms by three step 1 filters with nominal process noise (Case I) and SQUID measurements from the niobium bird experiment.	205
6.19	Estimation residual of three step 1 filters with nominal process noise (Case I) and SQUID measurements from the niobium bird experiment.	206
6.20	Estimation errors of NS_s and ES_s terms by three step 1 filters with adjusted process noise (Case II) and SQUID measurements from the niobium bird experiment.	207
6.21	Estimation residual of three step 1 filters with adjusted process noise (Case II) and SQUID measurements from the niobium bird experiment.	208

LIST OF TABLES

<u>Table Number</u>	<u>Title</u>	<u>Page Number</u>
2.1	Definition of Primary Frames	29
2.2	Orientation of the A-0 Frame	30
2.3	Orientation of the B-0 Frame	32
2.4	Orientation of C-0 Frame	35
2.5	Rotational Matrices Among Primary Frames.....	36
2.6	Definition of Observer and Observational corrections for Frames A-1 to A-5.....	38
2.7	Secondary Frame Definitions for Category A.....	40
2.8	Category B Secondary Frame Definitions	42
2.9	Secondary Frame Definitions for Category C.....	47
3.1	PSD Estimation by Modified Periodogram.....	62
3.2	Advantages and Disadvantages of the Three Random Sequences.....	80
4.1	Standard SI Units for the Niobium Bird Truth Models.....	83
4.2	Conversion Factors Among Units	84
4.3	Model of Earth's Position with Respect to the Sun	86
4.4	Model of Earth's Velocity with Respect to the Sun	87
4.5	Nominal Orbital Elements for the GP-B Satellite.....	88
4.6	Nominal Satellite Position and Velocity	89
4.7	Equation for the Parallax Model	92
4.8	Equation for the Aberration Model	94
4.9	Equation for the Deflection of Starlight Model	96
4.10	Summary of Observational Corrections.....	98
4.11	Models for the Structural Misalignment and Creeping of Gyro Readout.....	100
4.12	Model of Satellite Pointing Error	102
4.13	Model of the Satellite Roll Phase Error	103
4.14	Pseudo-1/f-Noise Model for a 5-Hour SQUID Magnetometer.....	108
4.15	Bias Drift Model for Science SQUID Magnetometer.....	109
4.16	Nominal Parameters for the Science Signal A-to-D Converter.....	111
4.17	Assumptions and Their Effects for Idealized Measurement Equation	117

5.1	Statistical Conditions of Truth Model.....	138
5.2	Initial Conditions and Noise Parameters to Step 1 Filters	138
5.3	Initial Conditions and Noise Parameters to Step 2 Filter	139
5.4	Final Estimates and Estimation Accuracy of Step 2 Filter.....	142
5.5	Final estimation accuracy of original filters and recursive filters.....	148
5.6	Final estimation accuracy of two-step filters with various roll periods	170
6.1	Stability of SQUID Scale Factor and Bias -- Comparison Between Simulation and Experiment.....	186
6.2	Initial Conditions for Step 1 Filters in the Niobium Bird Experiment	203
6.3	Nominal (Case I) and Adjusted Process Noises (Case II) for Step 1 Filters in the Niobium Bird Experiment.....	203
6.4	Final Estimation Accuracy of Step 1 Filter – Simulation vs. Experiment (Case II)	208

SYMBOLS

α	parallax coefficient
α_S	right ascension of the Sun (degrees)
a_{i1}	(3,1) element of the A-i frame ($i=1,\dots,5$)
a_{i2}	(3,2) element of the A-i frame ($i=1,\dots,5$)
${}^jA^i$	rotation matrix from the A-i frame to the A-j frame ($i, j=0,\dots,6$)
a_L	lowpass filter coefficient for the band-limited Wiener random sequence
α_w	covariance coefficient of the Wiener random sequence
β_e	ecliptic latitude of the Sun (degrees)
B_{ad}	number of bits in A-to-D converter
${}^jB^i$	rotation matrix from the B-i frame to the B-j frame ($i, j=0,\dots,3$)
B_L	magnitude of London field (T)
b_{sq}	SQUID readout bias (arcseconds)
c	speed of light in vacuum (meters/second)
C_G	scale factor of SQUID readout
\hat{C}_G	<i>a posteriori</i> estimate of SQUID scale factor from a step 1 filter
${}^jC^i$	rotation matrix from the C-i frame to the C-j frame ($i, j=0,\dots,3$)
δ	declination of the Sun (degrees)
$\delta(t)$	impulse function
δe_{ve}	perturbation of the eccentricity of the GP-B satellite
$\delta\phi_R, \delta\theta_R, \delta\psi_R$	structural misalignment angles of a pickup loop about the x_{B0} , y_{B0} , and z_{B0} axes, respectively (radians)
δ_{ij}	Kronecker delta function
δi_{ve}	perturbation of the inclination of the GP-B satellite (radians)

$\delta\theta_a$	aberration correction term from special relativity (radians)
δ_R	declination of Rigel at t_0 (radians)
$\delta\Omega_{ve}$	perturbation of the right ascension of the GP-B satellite (radians)
$\delta\psi_r$	roll phase control error (radians)
$\delta\hat{\psi}_r$	<i>a posteriori</i> estimate of roll phase bias from a step 1 filter (radians)
Δf_1	step 1 frequency bin size (Hz)
Δt	sampling period (seconds)
ϵ	obliquity of ecliptic (degrees)
$\vec{\epsilon}_a^{es}$	telescope observational correction vector caused by the annual aberration (radians)
$\vec{\epsilon}_a^{ve}$	telescope observational correction vector caused by the orbital aberration (radians)
$\vec{\epsilon}_d$	telescope observational correction vector caused by the deflection of starlight from Rigel because of the mass of the Sun (radians)
$\vec{\epsilon}_f$	telescope observational correction vector caused by the refraction of starlight through the Earth's atmosphere (radians)
ϵ_i	moment of inertia unbalance
$\vec{\epsilon}_l$	telescope observational correction vector observed by s_i ($i=1,\dots,5$) (radians)
ϵ_p	amplitude of polhode modulation of the scale factor
$\vec{\epsilon}_r$	telescope observational correction vector caused by the proper motion of Rigel (radians)
$\vec{\epsilon}_p^{es}$	telescope observational correction vector caused by the annual parallax (radians)
$\vec{\epsilon}_p^{ve}$	telescope observational correction vector caused by the orbital parallax (radians)
\bar{e}_{ve}	nominal eccentricity of the GP-B satellite

EW_0	East-West component of initial misalignment of gyroscope spin axis (arcseconds)
EW_S	East-West static term of step 1 filter states (arcseconds)
$EW_S^{\hat{}}$	<i>a posteriori</i> estimate of East-West static term from a step 1 filter (arcseconds)
Φ_1, Γ_1	transition matrices of the process model for the step 1 filters
Φ_2, Γ_2	transition matrices of the process model for the step 2 filter
ϕ_a, θ_a, ψ_a	1-2-3 Euler angles from the A-0 frame to the B-0 frame: absolute yaw control error, absolute pitch control error, and absolute roll phase, respectively (radians)
$\phi_{\text{mass}}, \theta_{\text{mass}}, \psi_{\text{mass}}$	1-2-3 Euler angles from the B-0 frame to the B-3 frame: mass property trimming angles about X_{B0} , Y_{B0} , and Z_{B0} , respectively (radians)
f_N	Nyquist frequency: $f_N = \frac{f_s}{2}$
$\phi_{\text{null}}, \theta_{\text{null}}$	1-2 Euler angles from the B-0 frame to the B-2 frame: telescope null trimming angles about X_{B0} and Y_{B0} , respectively (radians)
Φ_p	magnetic flux in the pickup loop (Wb)
f_p	polhode frequency (Hz)
ϕ_{p0}	initial phase of the polhode motion (radians)
f_r	roll frequency (Hz)
ϕ_r, θ_r, ψ_r	1-2-3 Euler angles from the A-5 frame to the B-2 frame: relative yaw control error, relative pitch control error, and relative roll phase, respectively (radians)
Φ_S	magnetic flux in the SQUID loop (Wb)
f_s	gyroscope spin frequency (Hz)
f_s	sampling frequency (Hz): $f_s = \frac{1}{\Delta t}$
$\Phi_{sq}, \Gamma_{sq}, D_{sq}$	discrete state matrices of the SQUID noise shaping filter
F_{sq}, G_{sq}, H_{sq}	continuous state matrices of the SQUID noise shaping filter

$f_w(a_L, k)$	covariance coefficient function of the band-limited Wiener random sequence
f_x	cross-over frequency (Hz)
g	mean anomaly of the Sun (degrees)
$H(z)$	z-transform of the transfer function from n_i to w_i
H_l	measurement matrix of linearized measurement of the step 1 filters
$H_{sq}(s)$	continuous transfer function of the SQUID noise shaping filter
i, j, k	random sequence index
I_p	induced current in the pickup loop (A)
i_{ve}	GP-B satellite orbital inclination
\bar{i}_{ve}	nominal inclination of the GP-B satellite (degrees)
\underline{j}	square root of -1 : $\underline{j} = \sqrt{-1}$
κ	deflection of starlight coefficient
L_s	mean longitude of the Sun (degrees)
L	number of segments for the modified periodogram calculation
λ	ecliptic longitude of the Sun (degrees)
λ_1, λ_2	aberration terms in North-South and East-West directions, respectively (arcseconds)
$L(z)$	z-transform of the transfer function from w_i to v_i
L_i	self inductance of the input coil (H)
L_p	self inductance of the pickup loop (H)
λ_R	right ascension of Rigel at t_0 (radians)
M	number of samples in a data segment for the modified periodogram calculation
M_c	mutual inductance of the input coil to the SQUID loop (Φ_0/A)
μ_\oplus	gravitational constant of the Earth (meter ³ /second ²)

m_s	gravitational radius of the Sun (meters)
N	number of turns in the pickup loop
n	number of days from J2000.0 (days)
\tilde{N}	unit vector pointing from barycenter to celestial north
$N(z)$	z-transform of n_i
N^*	effective number of turns in the pickup loop
\tilde{n}_1	unit vector normal to the calibration surfaces of gyros #1 and #2
\tilde{n}_2	unit vector normal to the calibration surfaces of gyros #3 and #4
\tilde{n}_3	unit vector normal to the telescope interface surface
n_i	Gaussian random sequence with zero mean and unity standard deviation ($i=0,1,\dots$)
NS_0	North-South component of initial misalignment of gyroscope spin axis (arcseconds)
n_{sq}	SQUID readout noise (arcseconds)
NS_S	North-South static term of step 1 filter states (arcseconds)
\hat{NS}_S	<i>a posteriori</i> estimate of North-South static term from a step 1 filter (arcseconds)
n_{ve}	nominal orbital rate of the GP-B satellite (radians/second)
q_{ad}	A-to-D converter quantization bin size (arcseconds)
θ_i	angle between the gyroscope spin axis and the pickup loop (arcseconds)
θ_L	angle between the London moment and the pickup loop (arcseconds)
Q_{sq}	power spectral density of the SQUID noise at the roll frequency (arcsecond ² /Hz)
R	distance from the Sun to Rigel (meters)
r_0	mean radius of pickup loop (meters)

ρ_i	measurement vector of the step 2 filter
R_{ad}	A-to-D converter range (arcseconds)
r_{es}	distance from the Sun to the Earth (meters)
\vec{r}_{es}	position vector of the Earth with respect to the Sun (meters)
\hat{R}_i	a unit vector perpendicular to the i-th pickup loop
R_{\oplus}	mean radius of the Earth (meters)
ρ_{oc}	radius of the occultation limit circle (meters)
r_{ve}	distance from the Earth center to the satellite (meters)
\vec{r}_{ve}	position vector of the GP-B satellite with respect to the Earth (meters)
$\bar{\rho}_{ve}$	nominal altitude of the GP-B satellite (meters)
σ_{ad}	quantization error (rms) in A-to-D converter (arcseconds)
s_i	observer who determines the optical direction of Rigel for the A-i frame ($i=1,\dots,5$)
\hat{s}_i	a unit vector aligned to the i-th gyroscope spin axis
t_0	science mission initiation time (seconds)
A^0T^{C0}	rotation matrix from the C-0 frame to the A-0 frame
B^0T^{A0}	rotation matrix from the A-0 frame to the B-0 frame
B^2T^{A5}	rotation matrix from the A-5 frame to the B-2 frame
T_c	lowpass filter time constant for the band-limited Wiener random sequence (seconds)
u_i	uniformly distributed random sequence between [0,1] ($i=0,1,\dots$)
$V(z)$	z-transform of v_i
\vec{v}_{es}	velocity vector of the Earth with respect to the Sun (meters/second)
v_i	band-limited Wiener random sequence ($i=0,1,\dots$)

V_{in}	input voltage at the voltage divider (volts)
V_{out}	output voltage at the SQUID controller (volts)
\vec{v}_{ve}	velocity vector of the GP-B satellite with respect to the Earth (meters/second)
$W(z)$	z-transform of w_i
W_1	step 1 window size (seconds)
w_1	process noise sequence of the step 1 filters
w_2	process noise sequence of the step 2 filter
w_i	Wiener random sequence ($i=0,1,\dots$)
ω_p	angular velocity of the polhode motion (radians/second)
ω_s	spin angular velocity of the gyroscope (radians/second)
Ω_{ve}	GP-B satellite orbital right ascension (degrees)
ω_{ve}	nominal orbital initial phase of the GP-B satellite (radians)
$\overline{\Omega}_{ve}$	nominal right ascension of the GP-B satellite (degrees)
x, y, z	equatorial rectangular coordinates of the Earth in the C-0 frame (AUs)
x_1	state vector of the step 1 filter
\bar{x}_1	<i>a priori</i> estimate of the step 1 filter states
\hat{x}_1	<i>a posteriori</i> estimate of the step 1 filter states
x_2	state vector of the step 2 filter
\bar{x}_2	<i>a priori</i> estimate of the step 2 filter states
\hat{x}_2	<i>a posteriori</i> estimate of the step 2 filter states
X_{Ai}, Y_{Ai}, Z_{Ai}	x, y, z axes of the A-i frame
X_{Bi}, Y_{Bi}, Z_{Bi}	x, y, z axes of the B-i frame
X_{Ci}, Y_{Ci}, Z_{Ci}	x, y, z axes of the C-i frame
ξ_{sq}	SQUID pseudo 1/f noise (arcseconds)

y	nonlinear measurement of the step 1 filters (arcseconds)
y_{Gi}	science signal from the i-th gyroscope (arcseconds)
ψ_{rc}	command roll angle for satellite roll control (radians)
z	linearized measurement of the step 1 filters (arcseconds)

OPERATORS

$U(a,b)$	uniform random distribution between [a,b]
$N(0,1)$	Gaussian random distribution with zero mean and unity standard deviation
$E()$	expected value
$f_U()$	probability distribution function of the uniform distribution
$R_U()$	autocorrelation function of the uniform distribution
$S_U()$	two-sided power spectrum density function of the uniform distribution
$f_N()$	probability distribution function of the Gaussian distribution
$R_N()$	autocorrelation function of the Gaussian distribution
$S_N()$	two-sided power spectrum density function of the Gaussian distribution
$f_W()$	probability distribution function of the Wiener distribution
$R_W()$	autocorrelation function of the Wiener distribution
$S_W()$	two-sided power spectrum density function of the Wiener distribution
$S_V()$	two-sided power spectrum density function of the band-limited Wiener distribution

ABBREVIATIONS

BLWRS	band-limited Wiener random sequence
--------------	-------------------------------------

FFT	fast Fourier transform
GP-B	Gravity Probe B
GRS	Gaussian random sequence
J2000.0	Julian year 2000.0
PDF	probability distribution function
PSD	power spectral density
RMS	root mean square
SQUID	superconducting quantum interference device
UDRS	uniformly distributed random sequence
WGS 84	Department of Defense World Geodetic System 1984
WRS	Wiener random sequence
WSS	wide-sense stationary

CHAPTER 1. INTRODUCTION

1.1 Problem Statement

In June 1990, when the scientists at the Space Science Institute received the first image from the Hubble Space Telescope (HST), they were convinced that there was a major focusing error in the telescope and/or instrument package. An investigatory panel later concluded that erroneous positioning of the refractive field lens during assembly caused a blurred focus of the telescope. R. R. Shannon (Ref. 1), a member of the investigatory panel, pointed out two factors that prevented the assembly error from being detected: (1) lack of communication among the scientists regarding the test results and (2) management pressure to avoid any additional testing because of cost concerns. He also pointed out that all the optical components were “assembled into a structure with final alignment determined by the test data on the components. No overall system test then would be carried out, primarily to save a significant amount of money.” Shannon's

observations suggest that the assembly error could have been detected if an overall system test had been performed prior to the system's implementation.

The kinds of management that sacrificed accuracy to cost containment setting the stage for the HST problem, may also threaten other current space programs. In particular, in NASA's Great Observatories (Ref. 2, 3), which include the Advanced X-ray Astrophysics Facility (AXAF), the Space Infrared Telescope Facility (SIRTF) and the Gamma-Ray Observatory (GRO) as well as the HST, hardware requirements on the Earth-orbiting satellites have become more and more challenging, especially for angular resolution. As a result, unexpected system error is more likely to occur. Although the satellite components are tested and calibrated individually prior to integration, overall system testing is sometimes neglected. In order to avoid unexpected system error during integration, one needs to establish an overall end-to-end test environment that includes core satellite software and hardware, as well as ground support software and hardware, at a reasonable cost.

I applied this concept of the integrated test environment to the Gravity Probe B program (GP-B) at Stanford University and actualized it as the niobium bird experiment. The critical hardware for the GP-B program, analogous to the telescope of the HST program, includes the SQUID (superconducting quantum interference device) magnetometer, the primary sensor for collecting scientific data. The data collected by the SQUID magnetometer are corrupted by various noises associated with the hardware instrumentation and have to be processed by a data reduction scheme to extract useful information. As explained in following sections, the accuracy requirements for the data reduction scheme are very tight given the state of the art of the SQUID magnetometer; it is not overstated to say that the optimization of the data reduction scheme and the

development of a low-noise SQUID readout system¹ are key to the success of the GP-B program. The two tasks are closely related. The noise profile of the SQUID readout system provides the optimization parameters for the data reduction scheme, and, inversely, the performance of the data reduction scheme determines the tolerance margins for the SQUID readout system errors. The niobium bird experiment was designed primarily to test the data reduction scheme in a closed loop environment with a prototypical SQUID readout system in the same loop. This integration of the data reduction scheme and the sensor hardware within a single test loop establishes a vital link between the two tasks that, essentially, cannot be completed independently. Thus, the niobium bird experiment leaves very little space for unexpected integration error to creep into the readout system. This thesis describes the development of the niobium bird experiment as my doctoral research. This chapter comprises an overview of the Gravity Probe-B program and the niobium bird experiment, followed by descriptions of previous related work and an outline of the rest of the thesis.

1.2 GP-B Program Overview

Albert Einstein's General Theory of Relativity ushered in a new era of physics. His most famous work, it is also, however, his most argued because, 77 years after the theory was unveiled, it is still short of sturdy experimental evidence. L. I. Schiff was aware of the weak experimental foundation of the theory in 1959, when he wrote (Ref. 4):

¹ The SQUID readout system denotes a package of sensor instruments including the SQUID magnetometer, a pickup loop, a lowpass filter, an analog-to-digital converter, a temperature controller, and magnetic shielding.

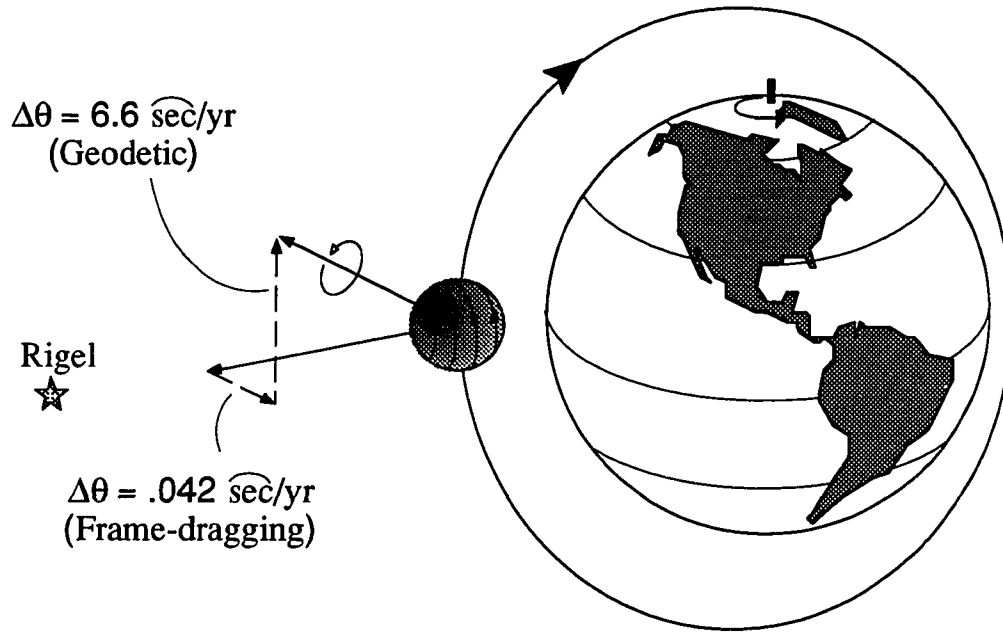


Figure 1.1 Gravity Probe B program. A gyroscope in an Earth orbit will undergo two relativistic precessions according to general relativity.

Since the first two of the three “crucial tests” can be derived from the equivalence principle and special relativity without reference to the geodesic equation or the field equations of general relativity, it follows that only the orbit precession really provides a test of general relativity.² (p. 343)

Later the same year, Schiff conceived the idea of testing general relativity by means of Earth-orbiting gyroscopes (Ref. 5). According to the General Theory of Relativity, it was predicted that an Earth-orbiting gyroscope would undergo two types of non-Newtonian precession given by the following equation:

$$\vec{\Omega} = \vec{\Omega}_G + \vec{\Omega}_F \quad (1.1)$$

² The “three crucial tests” of general relativity are the gravitational red shift, the deflection of starlight, and the planetary orbit precession, as indicated by Einstein.

where

$$\vec{\Omega}_G = \frac{3\mu_\oplus}{2c^2 r_{ve}^3} (\vec{r}_{ve} \times \vec{v}_{ve})$$

$$\vec{\Omega}_F = \frac{GI_\oplus}{c^2 r_{ve}^3} \left[\frac{3\vec{r}_{ve}}{r_{ve}^2} (\vec{\omega}_\oplus \cdot \vec{r}_{ve}) - \vec{\omega}_\oplus \right]$$

$\vec{\Omega}$: total precession rate vector of gyroscope's spin axis caused by general relativity

$\vec{\Omega}_G$: geodetic precession rate vector of gyroscope's spin axis

$\vec{\Omega}_F$: frame-dragging precession rate vector of gyroscope's spin axis

μ_\oplus : Earth's gravitational constant

c : speed of light in vacuum

\vec{r}_{ve} : satellite's position vector with respect to Earth's center, $r_{ve} \equiv |\vec{r}_{ve}|$

\vec{v}_{ve} : satellite's velocity vector with respect to Earth's center

I_\oplus : Earth's moment of inertia about its spin axis

$\vec{\omega}_\oplus$: Earth's spin vector

The first term is known as geodetic precession and the second term as frame-dragging precession. Schiff's idea was to obtain measurements of these relativistic precession rates for a "torque-free gyroscope," which would provide possible evidence for the validity of general relativity, and he suggested that "experiments of this type might be more easily performed in a satellite than in an Earth-bound laboratory." Together with W. M. Fairbank, Schiff first contacted NASA in 1961, and a NASA grant for his experiment to test general relativity by observing the precession of an Earth-orbiting gyroscope started in November 1963. This NASA-funded experiment was later designated Gravity Probe B and is currently conducted by engineers and scientists at the W. W. Hansen Experimental Physics Laboratory, the Aeronautics and Astronautics Department, and the Physics Department of Stanford University, with Lockheed Space and Missile Company as the payload subcontractor. The objectives and engineering considerations of the GP-B program are explained in the following sections.

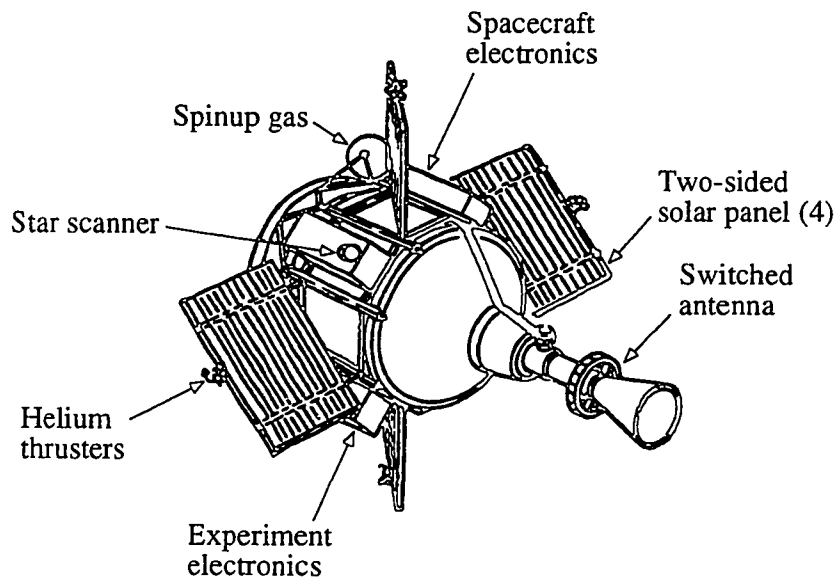


Figure 1.2 GP-B satellite outside view. The main body of the GP-B satellite is a dewar that holds liquid helium for temperature control.

1.2.1 GP-B Program Objectives

The primary objective of the GP-B program is to measure the relativistic precession of Earth-orbiting gyroscopes to an accuracy of 1 milli-arcsecond per year or better. As shown in Figure 1.1, according to general relativity, a gyroscope in a polar orbit at the altitude of 650 kilometers undergoes geodetic precession of 6.6 arcseconds per year in the North-South direction and frame-dragging precession of 0.042 arcsecond per year in the East-West direction. In the actual science mission, four gyroscopes are carried on a drag-free satellite for redundancy. Figure 1.2 shows the outside view of the GP-B satellite. The satellite also carries an optical telescope whose axis is aligned with the satellite's axis of symmetry. The satellite's attitude is regulated by the control system so that the telescope is always pointing at a guide star—Rigel, the brightest star of the constellation Orion. The telescope axis regulated to the optical direction of Rigel

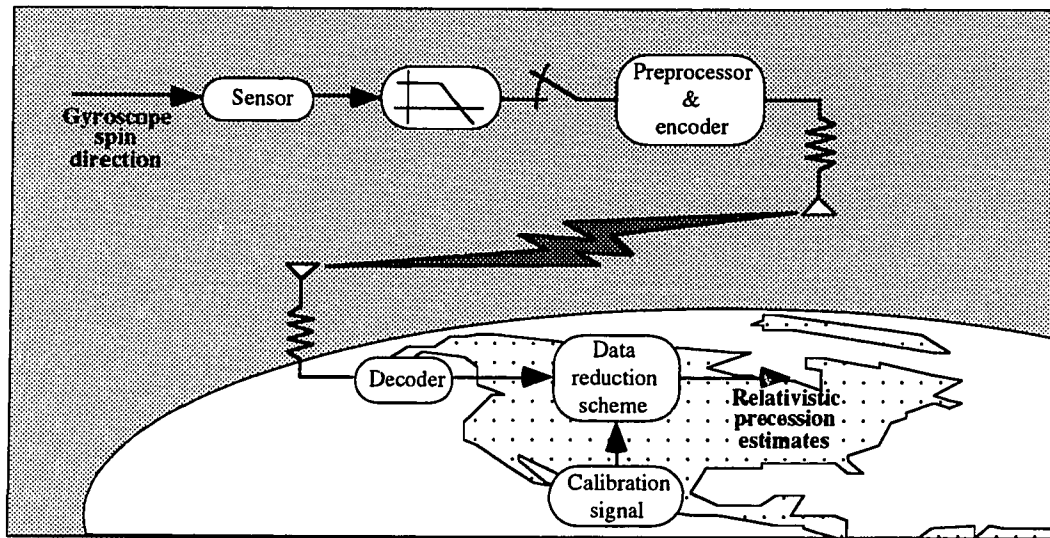


Figure 1.3 GP-B signal flow diagram. The direction of the gyroscope's spin axis is measured onboard and sent to the ground station. The Kalman filters process the data there.

provides a distant inertial reference from which gyroscope's precession, including relativistic precession, is measured.

The signal processing of the GP-B program can be divided into two parts: satellite on-board process and ground station process. Figure 1.3 is a simplified flow diagram of the GP-B science signal.³ Within the satellite, the direction of each gyroscope spin axis is measured by the primary sensor (explained in Section 1.2.6), and the measurement signal goes through the lowpass filter for anti-aliasing. The output of the lowpass filter is then quantized by an analog-to-digital converter, and the preprocessor encodes the digitized signal into an appropriate form for transmission to the ground station. At the ground station, the received signal is decoded and sent to the data reduction scheme. The data reduction scheme then works on the decoded science signal and estimates the

³ Hereafter, *science signal* denotes a series of measurements of the gyroscope spin axis direction with respect to the telescope axis in a form available at the ground station.

relativistic precession terms given a calibration signal. The following sections describe engineering challenges involved in the instrumentation of this signal flow.

1.2.2 GP-B Satellite Orbit

The nominal orbit for the GP-B satellite is a polar orbit at the altitude of 650 kilometers. One of the major reasons for choosing a polar orbit instead of an inclined orbit was the simplicity of data reduction formulation. The first term of Equation 1.1, the geodetic precession rate vector, is parallel to the orbital angular momentum vector $\vec{h}_{ve} \equiv \vec{r}_{ve} \times \vec{v}_{ve}$, and the second term, the frame-dragging precession rate vector, is a function of the satellite position vector and the Earth's spin vector. If the orbit is polar, the following conditions hold:

$$\vec{h}_{ve} \cdot \vec{\omega}_{\oplus} = 0 \quad (1.2a)$$

$$\vec{h}_{ve} \cdot \vec{r}_{ve} = 0 \quad (1.2b)$$

$$\text{then,} \quad \vec{\Omega}_G \cdot \vec{\Omega}_F = 0 \quad (1.3)$$

where

\vec{h}_{ve} : orbital angular momentum vector of the GP-B satellite

$\vec{\omega}_{\oplus}$: spin vector of the Earth

\vec{r}_{ve} : position vector of the GP-B satellite with respect to the Earth's center

$\vec{\Omega}_G$: geodetic precession rate vector

$\vec{\Omega}_F$: frame-dragging precession rate vector

Thus, in the case of a polar orbit, the two precession terms become orthogonal with the geodetic precession rate vector perpendicular to the orbital plane and the frame-dragging precession rate vector parallel to the orbital plane. The measurement equation for the science signal developed in Chapter 4 shows that the geodetic precession rate term and

the frame-dragging precession rate term are out of phase by 90 degrees, which simplifies the formulation of the Kalman filters presented in Chapter 5.

A detailed discussion of the orbit selection can be found in the work by J. V. Breakwell, et al. (Ref. 6) and R. Vassar (Ref. 7). Even though they found that the final estimation accuracy of the frame-dragging precession rate improved with a slightly inclined orbit compared with a perfect polar orbit, I selected the polar orbit as the nominal orbit for the GP-B satellite because of the simplicity of the filter formulation. C. W. F. Everitt discussed this trade-off (Ref. 8) and concluded that

In conclusion, I remark that intriguing as nonpolar orbits are, it is wise, in the first instance anyway, to stick with the near polar orbit. Doing so minimizes the burden of data reduction and hence the possibility of error in the reduction process. Particularly important is the fact that in a near polar orbit gravity gradient torques have no influence on the determination of the motional precession of the gyroscope.⁴ (p. 623)

P. Axelrad investigated the orbital perturbation for the GP-B satellite in the polar orbit and simulated the long-term perturbation over the one-year mission by MATLAB (Ref. 9).

1.2.3 GP-B Satellite Pointing Control

Since the precession of the gyroscope spin axis is measured from the telescope axis, it is crucial to align the telescope axis to some inertial reference direction that is not affected by the local Earth gravity. Rigel, the brightest star of the constellation Orion, was chosen as a distant inertial direction, and N. J. Kasdin (Ref. 26) designed the satellite pointing control system, which can regulate the telescope axis within 20 milliarcseconds (RMS) of the optical direction of Rigel. I constructed a simulation model for the satellite pointing error, which is presented in Chapter 4.

⁴ The “motional precession” means the frame-dragging precession of the gyroscope.

1.2.4 GP-B Satellite Roll Control

The GP-B satellite is rotated about its axis of symmetry at a roll period of 10 minutes⁵ in order to average the disturbance torque on the gyroscope and to increase the signal-to-noise ratio of the science signal because the readout sensor has a $1/f$ noise profile. Since our goal is to measure the relativistic precession of a gyroscope, the other type of precession—Newtonian precession hinders that goal. In order to reduce the amount of Newtonian precession, we use a drag-free satellite with roll, which has an averaging effect on the transverse torque so that the net disturbance torque is minimized. Another reason for rolling the satellite is to modulate the science signal. Since the readout sensor (explained in Section 1.2.6) has a $1/f$ noise profile, it is better to have the science signal at a higher frequency than dc. The science signal received at the ground station is modulated at the roll frequency and is demodulated using the roll phase measurement from the roll phase controller designed by B. W. Parkinson and J. R. Crierie (Ref. 11). Crierie demonstrated that the roll phase could be controlled within 25 arcseconds (RMS) and measured within 10 arcseconds (RMS) of accuracy. The simulation model for the satellite roll phase error that I constructed is described in Chapter 4.

1.2.5 GP-B Gyroscopes

The objective of the GP-B program, to measure the relativistic precession rates to an accuracy of 1 milliarcsecond per year or better, requires that the Newtonian precession be regulated within 1 milliarcsecond per year. The drift rate of the gyroscope spin axis caused by Newtonian precession must be less than 10^{-18} radian per second in order not to corrupt the measurement of the relativistic precession. Three major types of torque

⁵ During a recent conversation with me, B. W. Parkinson suggested that we speed up the roll to as much as a one-minute period (Ref. 10). Doing so increases the effective signal-to-noise ratio of the science signal because of the $1/f$ noise profile of the readout sensor.

contribute to the Newtonian precession of the GP-B gyroscope: gravity gradient torque, suspension torque, and electric torque, from which, respectively, are derived the following three requirements on the construction of the gyroscope: (1) homogeneity better than 3×10^{-7} , (2) sphericity better than 5×10^{-7} , and (3) electric dipole moment smaller than 1×10^{-10} e.s.u. (Ref. 12).

In order to satisfy all three requirements, the GP-B gyroscope is 1.5 inches in diameter and made of quartz with a thin-film niobium coating. Niobium is a metal that becomes superconducting when cooled below 9 K. The gyroscope is cooled to 1.8 K for the science mission. Then the gyroscope is electrically levitated inside the drag-free satellite and spun up to about 170 Hz. According to the physicist Fritz London (Ref. 13), a spinning superconducting object generates a magnetic dipole moment called the *London moment*. The gyroscope spun up to 170 Hz generates a London field of about 1.2×10^{-4} gauss (Ref. 14). Importantly, the London moment is always aligned with the instantaneous spin axis of the gyroscope. Thus, the London moment works as a tag on the gyroscope that indicates the direction of the spin axis. The next section explains the technique used to measure the direction of the London moment.

1.2.6 GP-B Readout System

In order to measure the direction of the gyroscope's spin axis, the GP-B program uses a magnetometer called a SQUID (superconducting quantum interference device), which operates according to the flux quantization principle of a superconducting loop. As shown in Figure 1.4, an inductive coil called a *pickup loop* is placed around the gyroscope and inductively coupled to the London field created by the spinning gyroscope. The SQUID magnetometer is a flux-to-voltage converter, and the output is a voltage proportional to the magnetic flux within the SQUID loop. The magnetic flux of the London field is inductively coupled to the SQUID loop within the SQUID probe.

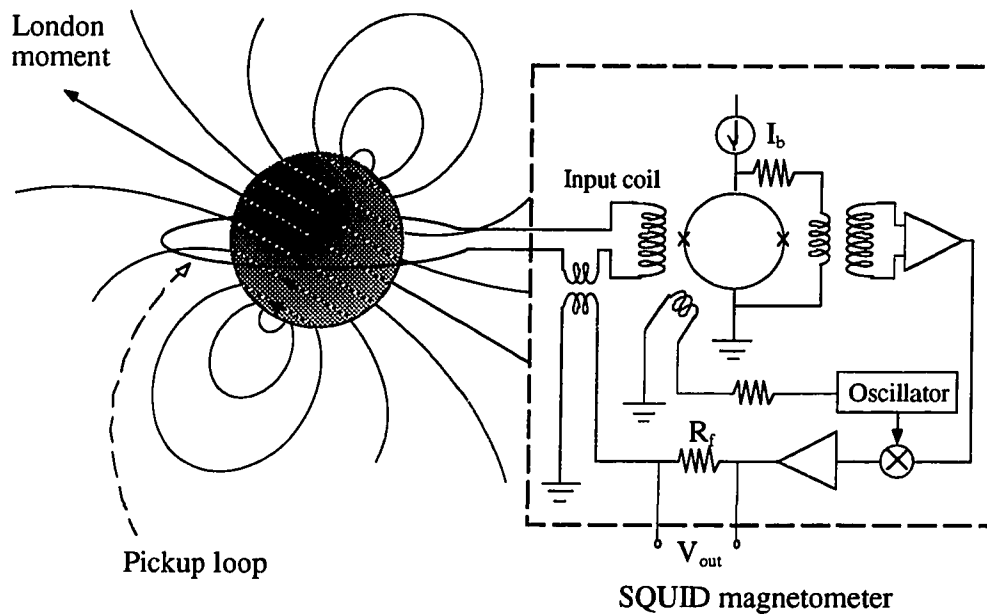


Figure 1.4 London moment readout of a superconducting gyroscope and a SQUID magnetometer.

Any change in the direction of the London moment, that is, any change in the direction of the spin axis perpendicular to the loop, induces current in the pickup loop. The induced current is then sent to the input coil coupled to the SQUID loop. The total flux within the SQUID loop is kept constant by the control effort through the feedback coil that is coupled to the SQUID loop. The output of the SQUID controller is a voltage proportional to the amount of the flux coupled from the input coil, which is, in turn, proportional to the amount of flux within the pickup loop (Ref. 15). T. V. Duzer, et al. (Ref. 16) and S. T. Ruggiero, et al. (Ref. 17) explain the operational principles of the superconducting devices including the dc SQUID.

The sensor noise of the SQUID magnetometer has $1/f$ power spectral density. Figure 1.5 shows the noise power spectral density of several SQUIDs (Ref. 14). For the

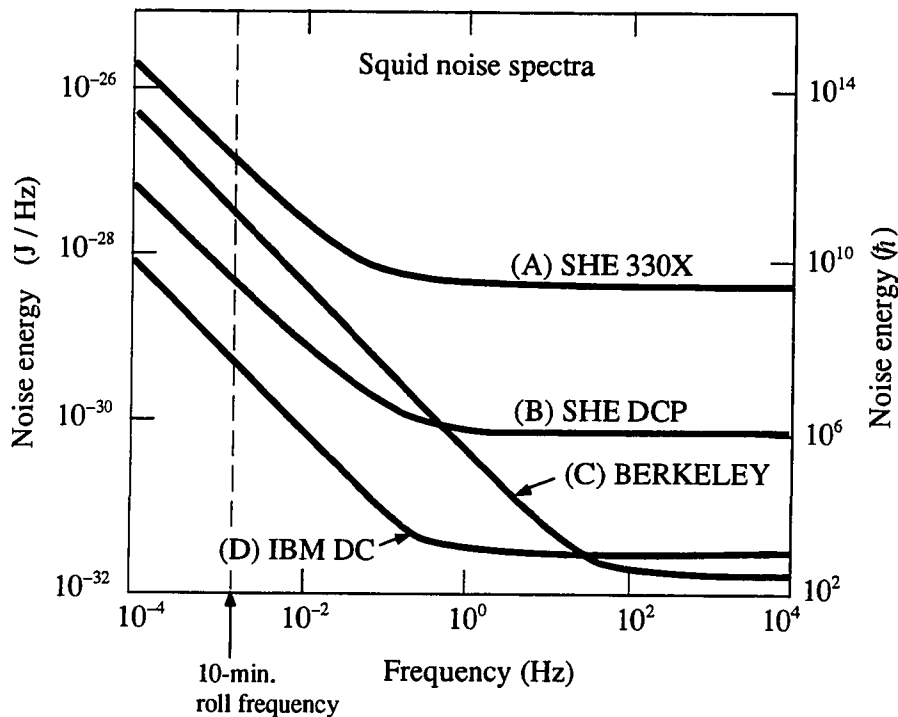


Figure 1.5 Simplified power spectral density of several SQUIDs (Ref. 14).

lower frequencies, the power spectral density is inversely proportional to the frequency⁶ and is flat above the corner frequency, which is typically 0.1 Hz to 1 Hz. Since the noise power spectral density of SQUID has a 1/f profile, it cannot be modeled as white noise going through a linear lowpass filter, which makes simulating the SQUID noise very difficult. The modeling of the SQUID noise is discussed in Chapter 5.

1.3 Overview of the Niobium Bird Project

The niobium bird experiment⁷ (NbBird) was conceived by B. W. Parkinson in 1987; Parkinson and I performed the initial investigation of the experiment in the fall of

⁶ A noise with power spectrum density that is inversely proportional to the frequency is called a 1/f noise.

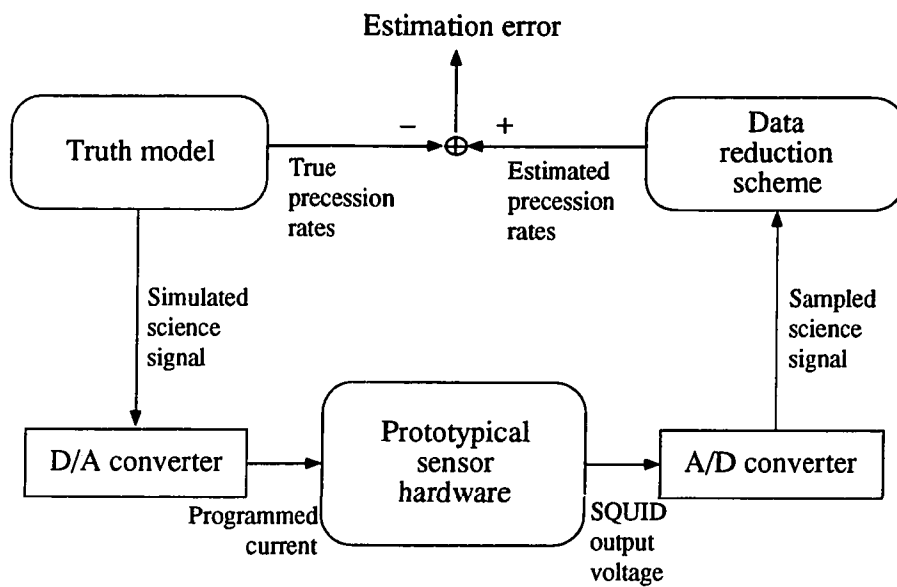
⁷ Analogous to the “Iron birds” of aircraft ground testing, this experiment was named by Parkinson referring to the extensive use of superconductive niobium in the test setup and in the science mission payloads.

that year. During the science mission, the output of the SQUID magnetometer will be sent down to the ground station (see Figure 1.3). At the ground station, the data reduction scheme will estimate the relativistic precession rates from the received signal, and the requirement on the estimation accuracy is better than 1 milliarcsecond per year. Therefore, the optimization of the data reduction scheme and the construction of a low-noise SQUID readout system are fundamental for the success of the GP-B program. The primary objective of the niobium bird experiment is to verify the data reduction scheme in a closed-loop environment where the actual readout hardware is installed. Figure 1.6 (a) is a conceptual diagram of the niobium bird experiment. Figure 1.6 (b) shows the three major tasks of the niobium bird experiment: truth model construction, data reduction synthesis and experimental verification.

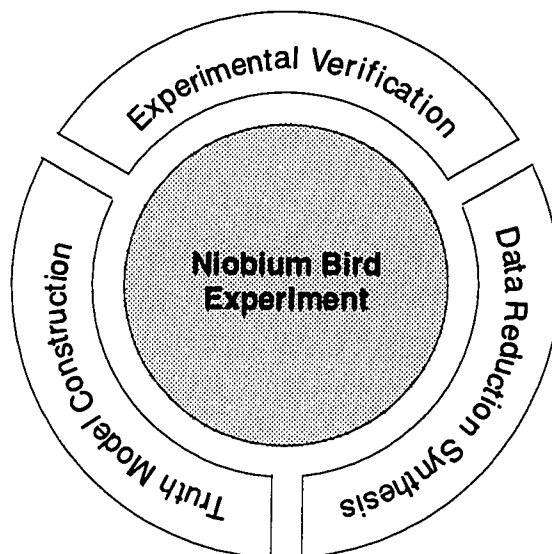
To accomplish these tasks, the niobium bird experiment consists of three major parts: the truth model, the SQUID readout system, and the data reduction scheme. The truth model and the data reduction scheme are C programs stored in a computer, and the SQUID readout system consists of a D-to-A converter, a gyroscope, a SQUID probe, a SQUID controller, a lowpass filter, and an A-to-D converter. Figure 1.6 (a) describes how these elements are connected, and the niobium bird experiment comprises five steps:

- (1) The truth model generates a simulated science signal in a digital format, and the digital signal is converted to an analog voltage by the D-to-A converter;
- (2) The analog voltage is then injected into the SQUID readout system, which includes the pickup loop, the SQUID magnetometer and so on;
- (3) The A-to-D converter samples the output of the SQUID readout system, and the quantized readout signal is sent back to the computer for data reduction;
- (4) The data reduction scheme processes the readout signal as if it were from the science mission and estimates the relativistic precession rates;
- (5) The estimated values are compared with the true values stored in the truth model, and the difference becomes the estimation error.

After these five steps, the estimation error is evaluated to verify the performance of the data reduction scheme and refine the hardware requirements embedded in the truth model. If the resulting estimation error is too large, the error tolerances in the truth model are reduced to improve the accuracy. In addition, the niobium bird experiment serves as a platform to develop a prototypical SQUID readout system. The prototype is calibrated in terms of the signal-to-noise ratio, the stability, and the repeatability and ultimately tested by the data reduction scheme. The experimental setup and results are presented in Chapter 6.



(a) Conceptual diagram of niobium bird experiment. Niobium bird experiment consists of truth model, prototypical readout system, and data reduction scheme.



(b) Three major tasks of niobium bird experiment.

Figure 1.6 Conceptual diagram and three major tasks of niobium bird experiment.

1.4 Previous Results

The data reduction scheme has been synthesized and analyzed by R. Vassar (Ref. 7), T. G. Duhamel (Ref. 18), R. S. DiEsposti (Ref. 19), and X. Qin (Ref. 20). Vassar established the measurement equation for the covariance analysis and initiated an end-to-end error analysis. Following Vassar, Duhamel analyzed the error sources that Vassar did not treat. He also converted Vassar's Kalman filter from a covariance form to a square root information filter. DiEsposti further elaborated the error models by adding the satellite dither model, the SQUID noise shaping filter, and the lowpass filter model. He verified the data reduction scheme with the simulated science signal generated by his truth model. Qin's work is the most recent; he synthesized and analyzed the two-step data reduction scheme. The following sections summarize the work of each of these researchers.

1.4.1 Vassar's Work

Vassar initiated a systematic end-to-end error analysis by integrating previous work by C. W. F. Everitt (Ref. 21, 22) and others who investigated various error sources individually. Vassar used covariance analysis to optimize various science mission parameters, such as the orbital inclination and the launch date. His contributions to the GP-B program were as follows (Ref. 7):

- Deriving the measurement equation of the science signal for covariance analysis;
- Optimizing the orbital inclination and the launch date according to the covariance analysis;
- Determining the dominant error sources;
- Analyzing the sensitivity of the estimation error to the SQUID noise, roll phase error and the scale factor drift;
- Analyzing the disturbance torque on the gyroscope.

Vassar derived the measurement equation and synthesized the Kalman filter in a covariance form. His Kalman filter estimated the two relativistic precession terms, geodetic precession and frame-dragging precession, according to his measurement model. The estimation error was then evaluated to optimize the orbital inclination and the launch date. Although he found that the optimal inclination was slightly less than 90 degrees, 90-degree inclination is the current nominal value for the GP-B program as discussed in Section 1.2.2. He also found that the optimal launch date of the GP-B satellite was September for a polar orbit. During the optimization process, Vassar determined the dominant error sources to be the SQUID sensor noise and the proper motion of Rigel.

The validity of Vassar's covariance analysis was limited by the unmodeled error sources such as the gyroscope trapped flux, the bending of starlight by the Sun's gravity, the ambient magnetic field leakage, the temperature-dependent bias drift⁸, and so on. He also assumed that there would be two orthogonal pickup loops per gyroscope whereas the current configuration is a single pickup loop per gyroscope. Thus, his covariance analysis was better than the actual case by a factor of $\sqrt{2}$.

1.4.2 Duhamel's Work

Duhamel amended Vassar's error model by incorporating the bending of starlight and the polhode motion of the gyroscope. His major contributions to the GP-B program were as follows (Ref. 18):

- Modeling the bending of starlight caused by the Sun's gravity;
- Analyzing the dynamics of the gyroscope, taking into account the effect of elasticity;
- Analyzing the effect of data interruption during the science mission;
- Analyzing the effect of trapped flux and its use of scale factor calibration;

⁸ Interestingly, the temperature-dependent bias drift has turned out to be one of the most dominant error sources in the niobium bird experiment.

- Pointing out the special relativity correction of the aberration of starlight;
- Converting Vassar's Kalman filter to a square root information filter.

Duhamel modeled the bending of starlight by the Sun claiming that the data reduction scheme could estimate the bending of starlight to an accuracy of 1.4 %, which can be measured by a separate method, very long base interferometry (VLBI), to an accuracy of 0.9 % (Ref. 23, 24, 25). Another notable contribution was the analysis of the effect of trapped flux. He claimed that the trapped flux signal at the spin frequency had a better signal-to-noise ratio than the science signal at the roll frequency and could be used to calibrate the scale factor. The scale factor calibration in turn improved the estimate of relativistic precession by a factor of 2, but Duhamel did not show how much improvement was observed in the scale factor estimate. I have elaborated his work on scale factor calibration; Chapter 5 shows that the scale factor can be estimated to three parts in 10^5 accuracy using only the science signal at the roll frequency if I assume a constant trapped flux.

Duhamel's other important contribution was the introduction of the square root information filter (SRIF). Even though the SRIF is mathematically equivalent to the Kalman filter in a covariance form, it is more stable and accurate when implemented in a digital computer and often suitable when the accuracy of estimation is more important than the speed of estimation.

The limitations of Duhamel's work are similar to those of Vassar's, since Duhamel inherited Vassar's signal model. Even though Duhamel amended Vassar's model to a certain extent, he did not resolve many of the issues raised by Vassar's research, including ambient magnetic field leakage, temperature-dependent bias drift, and the miscentering torque on the gyroscope.

1.4.3 DiEsposti's Work

DiEsposti's most significant contribution was the establishment of the “truth model.” DiEsposti defined the truth model as a simulation model that *simulates* the science signal. The simulated science signal then becomes the input to the data reduction scheme as if it were from the actual science mission (Ref. 19). Even though Vassar and Duhamel created their own measurement models in conjunction with the error analysis, the measurement models mainly served as tools to develop their Kalman filters. The truth model was not distinguished clearly from the process model of the Kalman filter. DiEsposti, on the other hand, constructed the truth model and the Kalman filter process model separately, stating that “simulated gyro and telescope measurement data is generated by the ‘Truth Model’ approach. ... Sampled data is processed by Kalman Filter algorithms. The Kalman Filter extracts optimal estimates of the relativistic precessions from the measurement data.” His statement implicitly suggests the concept of the niobium bird experiment; moreover, he envisioned such an experiment in his conclusion: “After a final Kalman Filter design has been chosen, hardware elements, which include the data instrumentation system, should be inserted into the simulation” (Ref. 19).

His other contributions include the following:

- Modeling of 1/f SQUID noise by a third-order shaping filter in the truth model and a first-order shaping filter in the Kalman filter process model;
- Installing a matching scheme for the gyroscope readout gain and the telescope readout gain using the satellite dithering;
- Installing a first-order lowpass filter in the truth model and an equivalent digital first-order lowpass filter in the Kalman filter process model.

The SQUID readout noise has a power spectral density that is inversely proportional to the frequency in the low-frequency region. Since the 1/f power spectral density cannot be accurately modeled by the white noise going through a linear filter, DiEsposti

approximated the $1/f$ power spectral density as the white noise going through a three-pole lowpass filter. I later took the same approach by approximating the SQUID readout noise with a four-pole lowpass filter (explained in Chapter 4). DiEsposti also installed the scale factor matching scheme using the dithering of the satellite and showed that the gyroscope readout gain and the telescope readout gain could be matched to 1% or better. The scale factor matching scheme was designed to subtract the telescope pointing error from the gyroscope science signal. However, N. J. Kasdin later demonstrated that the satellite pointing controller could regulate the pointing error within 20 milliarcseconds (RMS) (Ref. 26). Given this pointing accuracy and assuming that the pointing error has a zero mean⁹, Chapter 5 shows that the subtraction of the telescope signal from the science signal does not affect the estimation accuracy and, therefore, that it is not necessary to install the matching scheme. DiEsposti's other major contribution was installing an anti-aliasing lowpass filter in the truth model and an equivalent digital filter model in the Kalman filter.

In terms of the design specification, DiEsposti's assumption was closer to the current design of the GP-B hardware than Vassar's or Duhamel's. DiEsposti assumed a 5-hour integration SQUID instead of the 70-hour integration SQUID assumed by Vassar and Duhamel. He also assumed a single pickup loop per gyroscope, which is the current design, whereas Vassar and Duhamel assumed two pickup loops per gyroscope.

An important limitation of DiEsposti's work was that the anti-aliasing lowpass filter in his truth model was still an equivalent digital filter and did not represent the analog filter correctly. The niobium bird experiment overcomes this limitation by having an actual readout system within the test loop.

⁹ J. P. Turneure pointed out that the assumption of a zero-mean pointing error may limit the validity of my conclusion. I agree that the effect of a pointing error with a non-zero mean has to be analyzed to verify my claim.

The other limitation of DiEsposti's research is that he did not compare the Kalman filter's performance with and without the additional models in the Kalman process model. Although he added the SQUID shaping filter model and the lowpass filter model to the Kalman process model, he did not state how much improvement those additions achieved. Thus, the foundation of the need for those models was weak. In fact, Chapter 6 shows that the data reduction scheme converges without the addition of those two models.

1.4.4 Qin's Work

Qin's major contribution to the GP-B program was the development of a two-step data reduction scheme (Ref. 20) that gave much clearer insight into the state variables than the single-step data reduction schemes developed by Vassar, Duhamel, and DiEsposti. Qin divided the estimation state vector components into two parts: slow variables at the annual frequency and fast variables at the orbital frequency. Even though the idea of dividing the state vector was not completely original as Vassar et al. (Ref. 6) implied, Qin formulated the two-step data reduction scheme and analyzed it thoroughly. The two-step data reduction scheme is reformulated in Chapter 5.

Qin's other contributions were as follows:

- Installing a covariance reset technique;
- Analyzing the estimation sensitivity to the roll phase error;
- Analyzing the estimation sensitivity to the initial gyroscope spin axis misalignment;
- Investigating the application of a Σ - Δ A-to-D converter.

Covariance resetting is a useful technique when the measurement equation is a nonlinear function of the states. It prevents the data reduction scheme from converging to incorrect solutions. In the case of a linear optimization problem, there is only one

optimal solution that minimizes the quadratic cost function. On the other hand, in case of a nonlinear optimization problem, the Kalman filter has to linearize the measurement equation about the estimated states and is called the *extended Kalman filter*. With an extended Kalman filter, there can be multiple solutions that locally minimize the quadratic cost function. If one gives an incorrect initial condition to the extended Kalman filter, the steady-state estimate can converge to an incorrect solution in a stable manner. Such a false convergence was discussed by H. W. Sorenson (Ref. 27) and K. W. Iliff and R. E. Main (Ref. 28). The covariance resetting technique prevents the extended Kalman filter from sleeping on the measurement and forces it to use the measurement to update the estimate. Qin's two-step data reduction scheme is in an ideal form for applying this technique because it consists of a series of short term, nonlinear, first-step filters and a long term, linear, second-step filter. The initial estimate and covariance of each first-step filter are reset so that each filter is independent of the others and the linearization process is divided into short-term steps. The first-step filters estimate the linear combination of the final states, including the relativistic precession terms, and the second-step filter takes the results from the first-step filters as measurements that are linear in the state variables. Qin's other main contributions were the sensitivity analysis of the roll phase error and the initial gyroscope spin axis misalignment.

The limitations of Qin's work are similar to those of Vassar's, Duhamel's, and DiEsposti's. Qin left many of the issues raised by Vassar unresolved, including temperature-dependent bias drift and ambient magnetic field leakage. All four researchers mentioned those issues as unresolved problems or future research topics but they have never been analyzed thoroughly because to do so would be extremely difficult without experimentation. All the previous work heavily relied on the modeling of error sources, which resulted in similar limitations. The niobium bird experiment provides

important experimental data for the modeling of temperature-dependent bias drift and magnetic field leakage.

1.5 Contributions

The three major contributions of this thesis are:

- (1) Systematization of the GP-B truth model;
- (2) Improvement of the two-step Kalman filters and further analysis of the data reduction;
- (3) Establishment of the niobium bird experiment.

The truth model of the GP-B science mission was systematically established by the following steps:

- Defining a standardized set of coordinate frames for the GP-B simulation and hardware assembly;
- Developing and verifying random sequence generators for the GP-B simulation;
- Modeling individual components of the truth model with unambiguous documentation;
- Integrating individual models into the truth model.

The truth model provided the simulated science signal to test the data reduction scheme.

After completing the truth model, I developed the data reduction scheme in accord with Qin's synthesis of the data reduction scheme. My contributions to the data reduction synthesis are:

- Implementing a recursive algorithm to the two-step Kalman filters;
- Analyzing the effects of trapped flux signal on the data reduction;
- Analyzing the effects of pointing error on the data reduction;
- Analyzing the effects of roll period on the data reduction.

After I verified the Kalman filters by simulation, I tested the filters with the experimental data, which was the primary objective of the niobium bird experiment. My last contribution, establishment of the niobium bird experiment, includes:

- Assembling an end-to-end apparatus to verify total system behavior;
- Calibrating the dc SQUID magnetometer manufactured by Quantum Design, Inc.
- Testing the temperature-dependent bias in the readout instruments, such as the A-to-D converter and the SQUID controller;
- Testing and tuning the Kalman filters with experimental data.

The subsequent chapters explain these contributions in detail following the outline presented in the next section.

1.6 Thesis Outline

The subsequent chapters comprise three main topics and a conclusion. Chapters 2, 3, and 4 detail the construction of the truth model; Chapter 5 explains the data reduction scheme synthesis ;and Chapter 6 describes the experimental verification of the data reduction scheme, that is, the niobium bird experiment. The last chapter, Chapter 7 summarizes the findings and implications of the thesis.

In regard to the construction of the truth model, Chapter 2 defines the standardized set of coordinate frames that are the basis for developing the truth model. Chapter 3 develops and verifies three random sequence generators that are used in the

truth model to simulate random events such as sensor noise and control error. Chapter 4 develops the individual components of the truth model, which are based on the coordinate frames defined in Chapter 2 and the random sequence generator derived in Chapter 3. The individual components include the Earth motion model, the satellite motion model, observational error models, and so on. The realistic and idealized measurement equations are also derived in Chapter 4.

Chapter 5 reformulates the data reduction scheme that Qin proposed. A recursive algorithm is introduced into the data reduction, and the filtering problem is converted to a smoothing problem. Chapter 5 also investigates other factors such as the trapped flux signal, the pointing error, and the roll period, and tests the Kalman filters by simulation.

Chapter 6 describes the niobium bird experiment in detail and presents the latest results of the experiment. It then evaluates the results, specifying which hardware requirements have yet to be met or need to be re-evaluated.

Chapter 7 summarizes the results of my thesis, stating conclusions, limitations of the research, and recommendations for future work.

CHAPTER 2. COORDINATE FRAME DEFINITION

2.1 Introduction

In late 1989, because the size of the GP-B group had grown, the need for a standardized set of coordinate frames arose. Because of the larger number of engineers working on various tasks such as computer simulation, experimental verification and hardware assembly, miscommunication among the engineers regarding the coordinate frames used in their simulation programs or assembly diagrams became inevitable. I proposed a standardized set of fifteen coordinate frames on the basis of my previous work. The reasons for constructing the standardized frame set were (1) to minimize the possibility of miscommunication among engineers caused by inconsistent reference frame definition, (2) to allow transformation among inertial frames and satellite body fixed frames without ambiguity, and (3) to allow integration of simulation programs written by different engineers without the burden of frame conversion. This chapter presents the

standardized set of coordinate frames that is the updated version of the original set that I proposed (Ref. 29). Subsequent chapters describe how the standardized set was used to construct the truth models that simulate the science gyroscope signal.

The standardized set of frames comprises three categories labeled A, B, and C. Category A consists of inertial coordinate frames whose orientations are determined by the optical direction of Rigel¹. Category B consists of satellite body-fixed frames determined by the structure of the satellite. Category C consists of conventional celestial frames such as the barycentric celestial frame, geocentric celestial frame, satellite orbital frame, and WGS 84 frame.

Each category has one reference frame, called the *primary frame*; all others are called *secondary frames*. The secondary frames are defined with respect to the primary frame through rotational matrices. By having only one primary frame in each category, conflict and redundancy among frame definitions can be avoided. The three primary frames of Categories A, B, and C are defined first in the next section; the secondary frames are defined with respect to the primary frames in the sections that follow.

Each frame is defined by four elements: (1) I.D. number, (2) name, (3) origin, and (4) orientation. An I.D. number is used to specify each frame without ambiguity during the truth model construction. A name is then used to identify the characteristics of that frame. The last two elements, origin and orientation, determine the origin of the frame and the orientation of its three axes. The three axes of each frame follow the right-handed rule of Cartesian coordinate frames; therefore, the direction of two axes determines the direction of the third axis without ambiguity.

¹ The optical direction of Rigel is defined as the direction of a vector which is drawn from an observer to the apparent location of Rigel observed by an optical device such as a telescope. Since an optical device is used to determine the apparent location of Rigel, it depends on the position and velocity of the observer with respect to Rigel.

2.2 Primary Frames

There are three primary frames, each of which is assigned to one of the three categories. They are labeled by I.D. number as A-0, B-0, and C-0. The letter indicates the category and the number indicates the level of definition. Zero means that the frame is at the most primary level in the frame definition hierarchy. The origins of A-0 (the I_0 reference frame) and C-0 (the barycentric celestial frame) are located at the solar barycenter, while the origin of B-0 (the nominal control frame) is fixed to the geometric center of the satellite proof mass cavity. The A-0 and C-0 frames are inertial frames and the B-0 frame is a satellite body-fixed frame. Table 2.1 lists the definitions of the three primary frames in terms of the four elements. The orientations of the three frames are shown in Figures 2.1 and 2.2, and are explained in detail in Sections 2.2.1, 2.2.2, and 2.2.3.

Table 2.1 Definition of Primary Frames

	Category A	Category B	Category C
I.D. Number	A-0	B-0	C-0
Name	I_0 reference frame	Nominal control frame	Barycentric celestial frame
Origin	Solar barycenter	Geometric center of proof mass cavity	Solar barycenter
Orientation	Defined in §2.2.1 (Figure 2.1)	Defined in §2.2.2 (Figure 2.2)	Defined in §2.2.3 (Figure 2.1)

2.2.1 Orientation of the A-0 Frame

The orientation of the A-0 frame is determined by the optical direction of Rigel from the solar barycenter at time t_0 at which the science mission will start. Let \bar{x} , \bar{y} , and \bar{z} be the unit vectors along the three axes of the A-0 frame². The y and z axes are determined first in terms of the solar barycenter, the apparent direction of Rigel at time t_0 , and the mean equatorial plane at the Julian year 2000 (J2000.0). The remaining axis, the x axis, forms a right-handed Cartesian coordinate frame. Table 2.2 gives detailed definitions of \bar{x} , \bar{y} , and \bar{z} . The orientation of the A-0 frame is also shown in Figure 2.1.

The purpose of the A-0 frame is to provide a reference frame from which the precession angle of the gyroscope spin axis is defined. The z axis of the A-0 frame is fixed to the optical direction of Rigel at t_0 , and is fixed to the distant galaxy regardless of the proper motion of Rigel for $t > t_0$. Thus, it serves as a distant, inertial reference direction from which the gyroscope's precession angle is defined. Any deviation of gyroscope spin axis from z_{A0} is owing to the Newtonian precession, the relativistic precession, and the initial misalignment of the gyroscope's spin axis. These three terms

Table 2.2 Orientation of the A-0 Frame

- \bar{z} is parallel to the line which is drawn from the solar barycenter at time t_0 to the optical direction of Rigel at t_0 as observed by an observer at the solar barycenter
- \bar{y} is perpendicular to \bar{z} and parallel to the mean equatorial plane of J2000.0 and points toward the vernal equinox
- \bar{x} forms a right-handed Cartesian coordinate frame with \bar{y} and \bar{z} , which satisfies $\bar{x} \cdot \bar{N} > 0$, where \bar{N} is a unit vector pointing to the celestial north

² The direction of \bar{x} , \bar{y} , and \bar{z} together with the position of origin completely determines the coordinate frame without ambiguity.

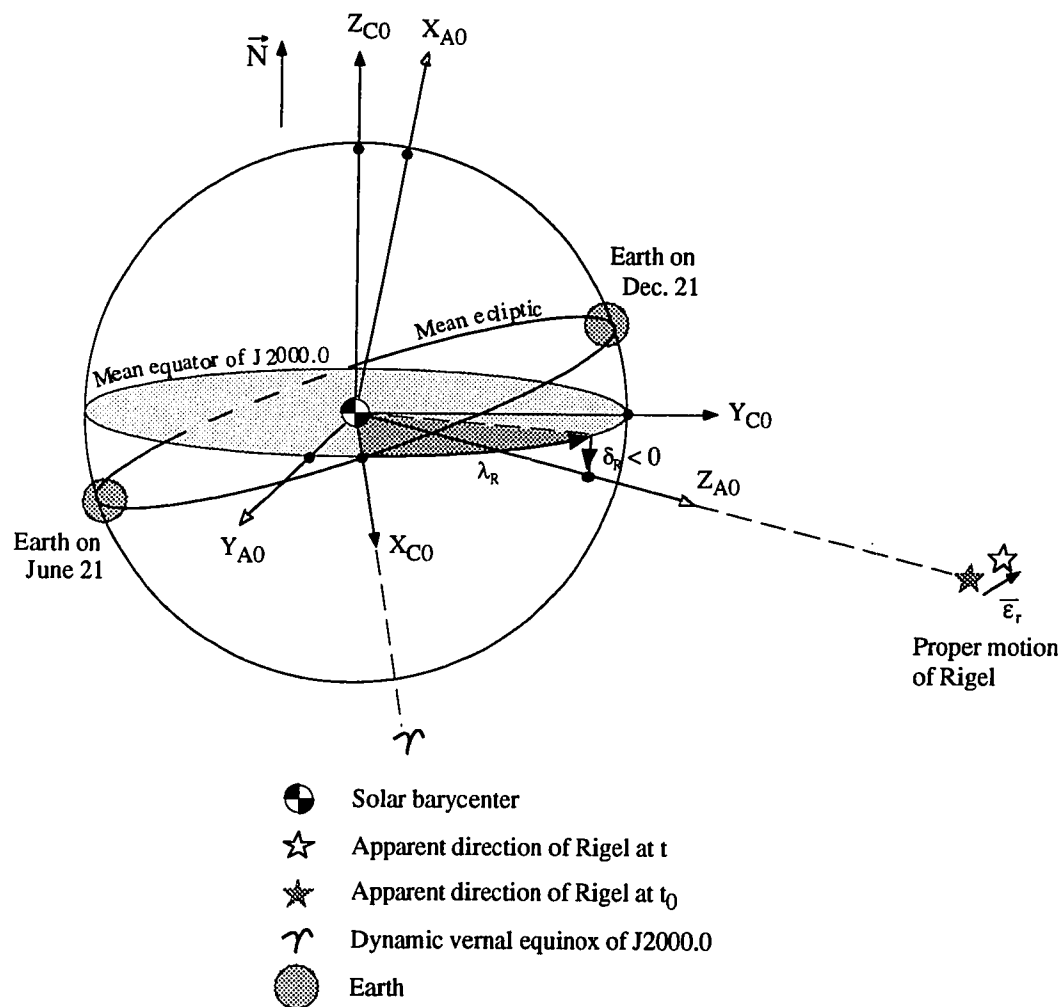


Figure 2.1 Orientation of the A-0 and C-0 frames with respect to solar barycenter, vernal equinox, mean equator, and Rigel. A-0 is the I_0 reference frame, and C-0 is the barycentric celestial frame.

are modeled in the A-0 frame and then estimated by the Kalman filters, as explained in Chapters 4 and 5.

2.2.2 Orientation of the B-0 Frame

The orientation of the B-0 frame is determined by the structural configuration of the quartz housing that contains four science gyroscopes and one proof mass. Let us

define three unit vectors, \bar{n}_1 , \bar{n}_2 , and \bar{n}_3 , each of which is perpendicular to one of the calibrated surfaces of the quartz block [see Figure 2.2 (a)]. Vector \bar{n}_1 is perpendicular to the calibrated surface of gyro #1 and #2 sockets and points outward from the geometrical center of the quartz block cavity. Similarly, \bar{n}_2 is perpendicular to the calibrated surface of gyro #3 and #4 sockets and points outward from the geometrical center of the quartz block cavity. Vector \bar{n}_3 is perpendicular to the telescope mounting surface at the geometric center and points from the proof mass cavity toward the telescope interface surface. After \bar{n}_1 , \bar{n}_2 , and \bar{n}_3 are determined by the geometric property of the quartz block, the unit vectors \bar{x} , \bar{y} , and \bar{z} along the three axes of B-0 can be determined as shown in Table 2.3. The orientation of B-0 seen from the outside of the satellite is also shown in Figure 2.2 (b).

Table 2.3 Orientation of the B-0 Frame

- \vec{z} is determined by the normal vector of telescope interface surface as follows:

$$\vec{z} = \vec{n}_3$$

- \vec{y} is determined by the normal vector of the calibration surfaces of gyros #3 and #4 as follows:

$$\vec{y} = \frac{\vec{z} \times \vec{n}_1}{|\vec{z} \times \vec{n}_1|}$$

- \vec{x} forms a right-handed Cartesian coordinate frame with \vec{y} and \vec{z} as follows:

$$\vec{x} = \vec{y} \times \vec{z}$$

The purpose of the B-0 frame is to determine the orientation of the SQUID pickup loops with respect to the calibrated surfaces of the quartz housing. The SQUID pickup loops are located around the science gyroscope and are inductively coupled to the magnetic flux created by the London moment of the spinning gyroscope. The change in the direction of the spin axis is reflected in the change of the magnetic flux inside the

pickup loop and measured by the SQUID magnetometer. Since the requirement for the estimation accuracy of the precession angle is better than 1 milliarcsecond, the orientation of the pickup loop has to be modeled to a submilliarcsecond precision in the simulation to provide a realistic science signal to the Kalman filter. The B-0 frame serves as a reference frame to determine the orientation of the pickup loops, and the misalignment and creeping of the pickup loops are determined with respect to the B-0 frame.

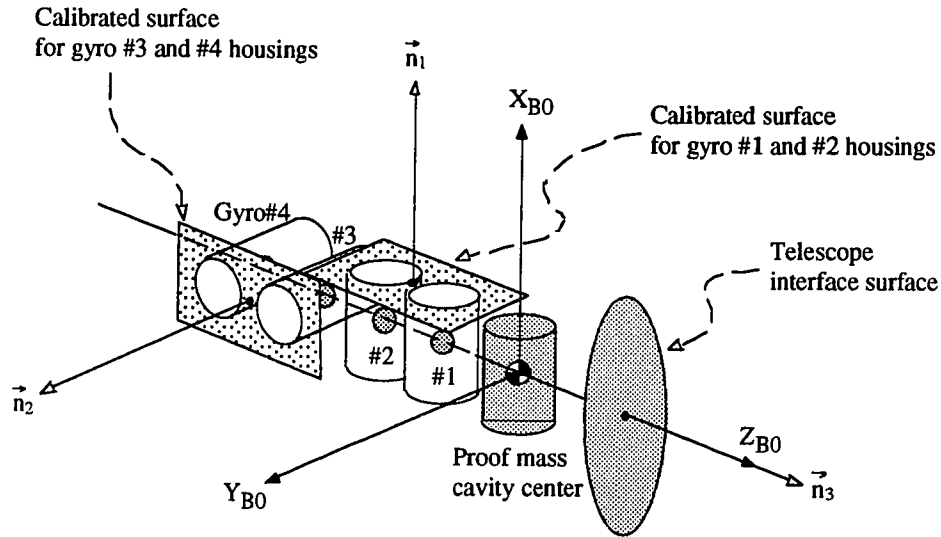
2.2.3 Orientation of the C-0 Frame

The C-0 frame is the *barycentric celestial frame*, which is a very common frame in astronomy along with the *geocentric celestial frame*. The barycentric and geocentric celestial frames are used to determine the position of stars and galaxies as well as the solar system planets with respect to the barycenter and the geocenter, respectively. These two frames are often interchangeable through linear translation between the two origins, the geocenter and the barycenter. The orientation of the C-0 frame is shown in Figure 2.1 together with the A-0 frame, and the unit vectors \vec{x} , \vec{y} , and \vec{z} along the three axes are defined in Table 2.4.

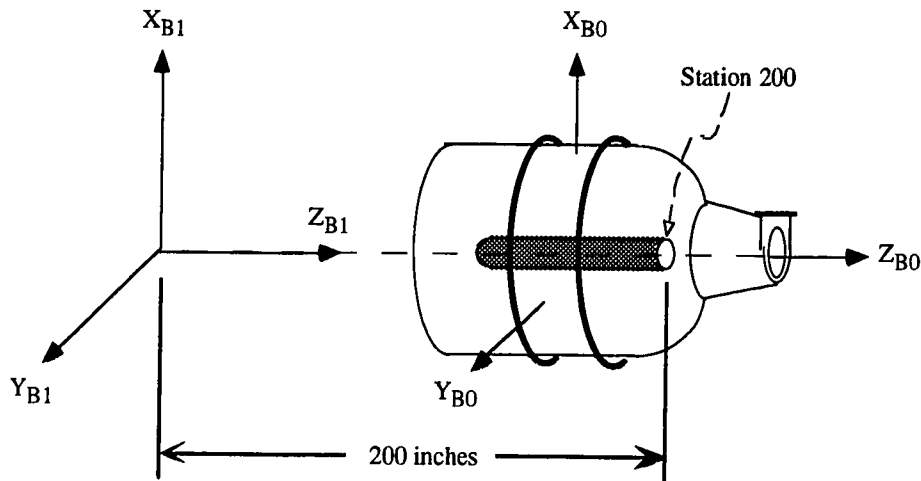
The C-0 frame serves as a reference frame for the following purposes:

- To define the optical direction of Rigel observed from the solar barycenter;
- To define the motion of the Earth with respect to the Sun.

The optical direction of Rigel observed from the barycenter is determined by the right ascension and the declination in the star catalogs. The star catalogs use the barycentric frame (C-0) as the reference frame. The C-0 frame is also useful when the motion of the Earth has to be defined, since the Earth travels about the Sun in a near-circular orbit [see Figure 2.1].



(a) Orientation of the B-0 frame and definitions of calibration vectors, \vec{n}_1 , \vec{n}_2 , and \vec{n}_3 .



(b) Orientation of the B-0 and B-1 frames viewed from outside.

Figure 2.2 Orientations of body-fixed frames, B-0 and B-1. B-0 is the nominal control frame, and B-1 is the assembly frame.

Table 2.4 Orientation of C-0 Frame

- \vec{x} points from the solar barycenter to the dynamic equinox of J2000.0
- \vec{y} is in a plane that goes through the solar barycenter and is parallel to the mean equator of J2000.0
- $\vec{z} = \vec{x} \times \vec{y}$, which satisfies $\vec{z} \cdot \vec{N} > 0$, where \vec{N} is a unit vector pointing from the barycenter to the celestial north.

2.2.4 Transformation Among Primary Frames

The three independent primary frames, A-0, B-0 and C-0, defined in Section 2.2, can be related to each other by defining the rotational matrices among them. The rotational matrices from C-0 to A-0 and from A-0 to B-0 are shown in Table 2.5³. An arbitrary vector \vec{r} can be expressed either in A-0, B-0, or C-0 by translating the coordinate frame as follows:

$$\vec{r}_{A0} = {}^{A0}T^{C0} \vec{r}_{C0} \quad (2.1)$$

$$\vec{r}_{B0} = {}^{B0}T^{A0} \vec{r}_{A0} \quad (2.2)$$

³ Note that, to complete the transformation of two frames, the origin of the starting frame has to be linearly translated to that of the destination frame in addition to the frame rotation.

Table 2.5 Rotational Matrices Among Primary Frames

Rotational matrix from C-0 to A-0:

$${}^{A0}T^{C0} = \begin{bmatrix} -\sin \delta_R \cos \lambda_R & -\sin \delta_R \sin \lambda_R & \cos \delta_R \\ \sin \lambda_R & -\cos \lambda_R & 0 \\ \cos \delta_R \sin \lambda_R & \cos \delta_R \cos \lambda_R & \sin \delta_R \end{bmatrix} \quad (2.3)$$

where

δ_R : declination of Rigel at time t_0

λ_R : right ascension of Rigel at time t_0

Rotational matrix from A-0 to B-0:

$${}^{B0}T^{A0} = \begin{bmatrix} \cos \psi_a & \sin \psi_a & -\theta_a \cos \psi_a + \phi_a \sin \psi_a \\ -\sin \psi_a & \cos \psi_a & \theta_a \sin \psi_a + \phi_a \cos \psi_a \\ \theta_a & -\phi_a & 1 \end{bmatrix} \quad (2.4)$$

where

ϕ_a, θ_a, ψ_a : 1-2-3 Euler angles from A-0 to B-0, respectively

ϕ_a : yaw angle with respect to A-0

θ_a : pitch angle with respect to A-0

ψ_a : roll angle with respect to A-0

2.3 Secondary Frames

The secondary frames are defined with respect to the primary frames through the rotational matrices. The purpose of secondary frames is to provide reference frames in which various truth models can be constructed. Category A has six secondary frames, labeled A-1 to A-6. Category B has three secondary frames, labeled B-1 to B-3, and Category C also has three secondary frames, labeled C-1 to C-3. The next three subsections define the secondary frames in Categories A, B, and C, respectively. As with the primary frames, the secondary frames are also defined by four elements: (1) I.D. number, (2) name, (3) origin, and (4) orientation with respect to the primary frame.

2.3.1 Secondary Frames in Category A

Six secondary frames A-i ($i=1,\dots,6$) are defined with respect to the primary frame A-0 through linear translation of the origin and axis rotation through the rotational matrices. The transformation from A-0 to A-i ($i=1,\dots,5$) is completed by two infinitesimal rotations about the x_{A0} and y_{A0} axes so that z_{Ai} ($i=1,\dots,5$) points in the optical direction of Rigel from the observer s_i ($i=1,\dots,5$). The rotational matrices from A-0 to A-i ($i=1,\dots,5$) are given by the following equations:

$${}^iA^0 = \begin{bmatrix} 1 & 0 & -a_{i1} \\ 0 & 1 & -a_{i2} \\ a_{i1} & a_{i2} & 1 \end{bmatrix} \quad (i=1,\dots,5) \quad (2.5)$$

where

$$\begin{aligned} a_{i1} &= \bar{x}_{A0} \cdot \vec{\epsilon}_i & |a_{i1}| &\ll 1 \\ a_{i2} &= \bar{y}_{A0} \cdot \vec{\epsilon}_i & |a_{i2}| &\ll 1 \end{aligned}$$

Vector $\vec{\epsilon}_i$ ($i=1,\dots,5$) is a vector-sum of various observational corrections in the optical direction of Rigel from observer s_i ($i=1,\dots,5$). The definition of observer s_i ($i=1,\dots,5$) determines which observational corrections should be included in the error vector $\vec{\epsilon}_i$ ($i=1,\dots,5$). Table 2.6 lists the definition of observer s_i ($i=1,\dots,5$) and corresponding correction vector $\vec{\epsilon}_i$ ($i=1,\dots,5$). The other nomenclatures used in Table 2.6 are as follows:

- $\vec{\epsilon}_r$: Observational correction vector caused by the proper motion of Rigel
- $\vec{\epsilon}_d$: Observational correction vector caused by the deflection of starlight from Rigel because of the mass of Sun
- $\vec{\epsilon}_p^{cs}$: Observational correction vector caused by the annual parallax
- $\vec{\epsilon}_p^{ve}$: Observational correction vector caused by the orbital parallax
- $\vec{\epsilon}_a^{cs}$: Observational correction vector caused by the annual aberration
- $\vec{\epsilon}_a^{ve}$: Observational correction vector caused by the orbital aberration

$\vec{\epsilon}_f$: Observational correction vector caused by the refraction of starlight through the Earth's atmosphere

Table 2.6 Definition of Observer and Observational corrections for Frames A-1 to A-5

i	ID#	Observer s_i	Observational correction vector $\vec{\epsilon}_i$
1	A-1	Observer at the solar barycenter traveling with respect to the distant galaxy	$\vec{\epsilon}_1 = \vec{\epsilon}_r$
2	A-2	Observer at the geocenter who is stationary with respect to the solar barycenter at the time of observation	$\vec{\epsilon}_2 = \vec{\epsilon}_r + \vec{\epsilon}_d + \vec{\epsilon}_p^{es}$
3	A-3	Observer at the geocenter who is traveling with the geocenter at the time of observation	$\vec{\epsilon}_3 = \vec{\epsilon}_r + \vec{\epsilon}_d + \vec{\epsilon}_p^{es} + \vec{\epsilon}_a^{es}$
4	A-4	Observer at the satellite proof mass cavity who is stationary with respect to the geocenter at the time of observation	$\vec{\epsilon}_4 = \vec{\epsilon}_r + \vec{\epsilon}_d + \vec{\epsilon}_p^{es} + \vec{\epsilon}_a^{es} + \vec{\epsilon}_p^{ve} + \vec{\epsilon}_f$
5	A-5	Observer at the satellite proof mass cavity who is traveling with the satellite at the time of observation	$\vec{\epsilon}_5 = \vec{\epsilon}_r + \vec{\epsilon}_d + \vec{\epsilon}_p^{es} + \vec{\epsilon}_a^{es} + \vec{\epsilon}_p^{ve} + \vec{\epsilon}_f + \vec{\epsilon}_a^{ve}$

The last secondary frame, A-6, can be obtained by rotating the A-5 frame about its z_{A5} axis by command roll angle ψ_{rc} , which is measured counterclockwise from the x_{A5} axis. The rotational matrix from A-0 to A-6 is given by the following equation:

$$\begin{aligned}
{}^6A^0 &= \begin{bmatrix} \cos \psi_{rc} & \sin \psi_{rc} & 0 \\ -\sin \psi_{rc} & \cos \psi_{rc} & 0 \\ 0 & 0 & 1 \end{bmatrix} {}^5A^0 \\
&= \begin{bmatrix} \cos \psi_{rc} & \sin \psi_{rc} & -a_{51} \cos \psi_{rc} - a_{52} \sin \psi_{rc} \\ -\sin \psi_{rc} & \cos \psi_{rc} & a_{51} \sin \psi_{rc} - a_{52} \cos \psi_{rc} \\ a_{51} & a_{52} & 1 \end{bmatrix}
\end{aligned} \tag{2.6}$$

where

ψ_{rc} : command roll phase with respect to the A-5 frame

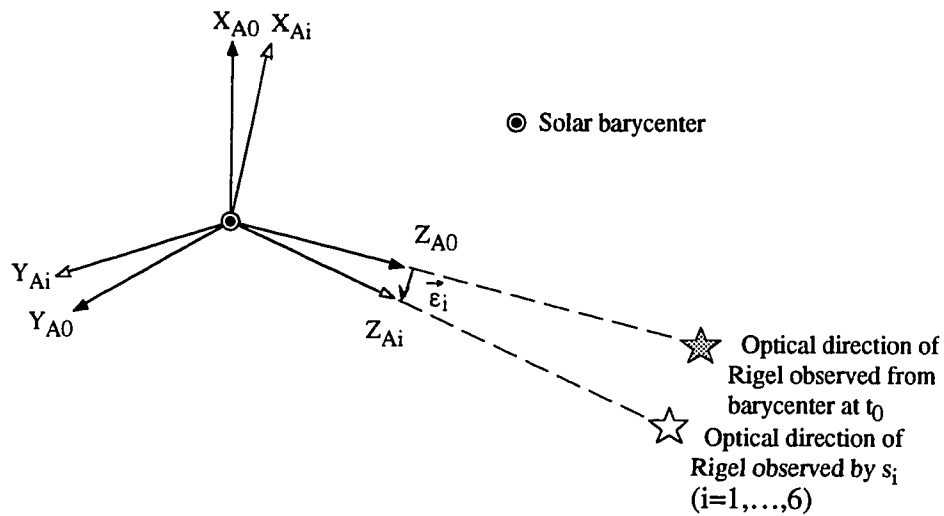
$$a_{51} = \vec{x}_{A0} \cdot \vec{e}_5$$

$$a_{52} = \vec{y}_{A0} \cdot \vec{e}_5$$

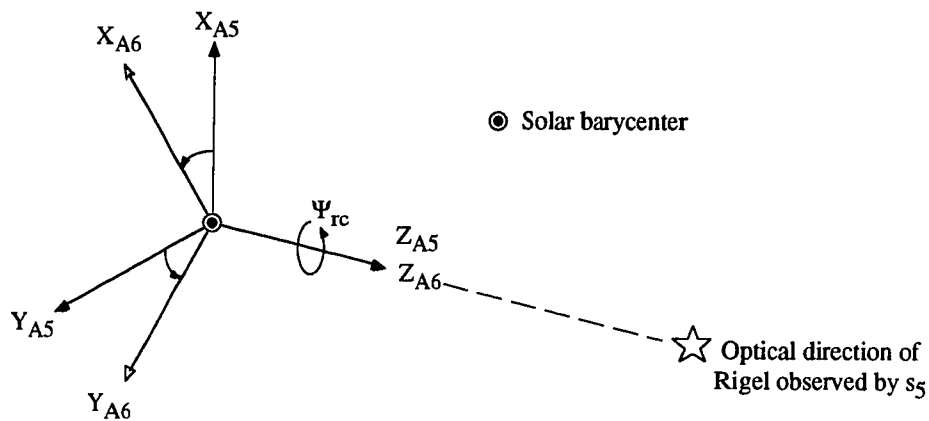
The A-6 frame serves as a reference frame for satellite pointing and roll control because the orientation of the B-0 and A-6 frames should coincide if there have been no control errors. Each secondary frame is defined in Table 2.7 in terms of its I.D. number, name, origin, and orientation. The italicized components in the orientation column are the additional effects of the preceding frame. In the case of the A-1 frame, the additional effects are based on the A-0 frame. The orientations of A-i (i=1,...,6) are also shown in Figure 2.3.

Table 2.7 Secondary Frame Definitions for Category A

ID#	Name	Origin	Orientation
A-1	I ₀ dynamic	Barycenter	\vec{z}_{A1} points in the optical direction of Rigel, including the <i>proper motion of Rigel after t_0</i>
A-2	Earth static	Geocenter	\vec{z}_{A2} points in the optical direction of Rigel, including the proper motion after t_0 , <i>deflection of starlight, and annual parallax</i>
A-3	Earth dynamic	Geocenter	\vec{z}_{A3} points in the optical direction of Rigel, including the proper motion after t_0 , <i>deflection of starlight, annual parallax, and annual aberration</i>
A-4	Satellite static	Satellite center of mass	\vec{z}_{A4} points in the optical direction of Rigel, including the proper motion after t_0 , <i>deflection of starlight, annual parallax, annual aberration, orbital parallax, and refraction of starlight through the atmosphere</i>
A-5	Satellite dynamic	Satellite center of mass	\vec{z}_{A5} points in the optical direction of Rigel, including the proper motion after t_0 , <i>deflection of starlight, annual parallax, annual aberration, orbital parallax, refraction of starlight through the atmosphere, and orbital aberration</i>
A-6	Satellite roll	Satellite center of mass	\vec{z}_{A6} coincides with \vec{z}_{A5} , and the axes of x_{A6} and y_{A6} undergo <i>rotation about z_{A5} by the command roll angle ψ_{rc}</i>



(a) Orientation of the A-i frames ($i=1, \dots, 6$) with respect to the A-0 frame.



(b) Orientation of the A-5 and A-6 frames.

Figure 2.3 Orientation of the A-i frames ($i=0, \dots, 6$).

2.3.2 Secondary Frames in Category B

The three secondary frames B-i (i=1,...,3) are defined with respect to the primary frame B-0 through linear translation of the origin and axis rotation through the rotational matrices. Each secondary frame, B-i (i=1,...,3), is fixed to the satellite body but has a different origin and/or orientation. The following table shows the I.D. number, name, origin, and orientation of each frame.

Table 2.8 Category B Secondary Frame Definitions

ID#	Name	Origin	Orientation
B-1	Assembly frame	200 inches behind Station 200 along the z_{B0} axis	Same as B-0 frame
B-2	Control frame	Proof mass position sensor null	\vec{z}_{B2} points from the proof mass toward the telescope parallel to the telescope readout null line $\vec{y}_{B2} = \frac{\vec{z}_{B2} \times \vec{n}_1}{ \vec{z}_{B2} \times \vec{n}_1 }$ $\vec{x}_{B2} = \vec{y}_{B2} \times \vec{z}_{B2}$
B-3	Mass property frame	Satellite center of mass	\vec{z}_{B3} points from the proof mass toward the telescope parallel to the principal axis of satellite inertia that is closest to the axis of satellite symmetry \vec{x}_{B3} is along the minor axis of inertia $\vec{y}_{B3} = \vec{z}_{B3} \times \vec{x}_{B3}$

The B-1 frame has the same orientation as the B-0 frame, but the origin is moved along the z_{B0} axis to be consistent with the hardware assembly environment. The origin of B-1 is placed 200 inches behind Station 200, which is the geometrical center of the axial locking ring [see Figure 2.2(b)]. The B-1 and B-0 frames were initially proposed by G. Ross of Lockheed in a FAXed letter to B. W. Parkinson on February 19, 1990, in an effort to develop new assembly coordinate frames.

The B-2 frame is named the *control frame* because its origin is placed on the sensor null point and the z axis is along the telescope readout null axis. The proof mass is used as a gravity sensor in drag-free control, and the proof mass position sensor null point does not necessarily coincide with the geometric center of the proof mass cavity that is the origin of B-0. The drag-free control effort is performed about the origin of B-2 because the origin of B-2 is placed at the proof mass position sensor null. Similarly, the telescope is used as a direction sensor in pointing control, and the telescope readout null axis does not necessarily coincide with the z_{B0} axis. The pointing control effort is performed about the z_{B2} axis, because the z_{B2} axis is placed parallel to the telescope readout null axis. The misalignment of the telescope readout null axis from the z_{B0} axis can be specified by the null trimming angles ϕ_{null} and θ_{null} about the x_{B0} and y_{B0} axes, respectively. Figure 2.4 shows the relation between the B-0 and B-2 frames. The transformation from B-0 to B-2 is completed by a linear translation of the origin and axis rotations about the x_{B0} and y_{B0} axes by ϕ_{null} and θ_{null} , respectively.

The B-3 frame is named the *mass property frame* because its origin is placed at the center of mass of the satellite and its three axes are aligned with the principal axes of inertia. The purpose of the B-3 frame is to provide a body-fixed frame for dynamic analysis of the satellite.

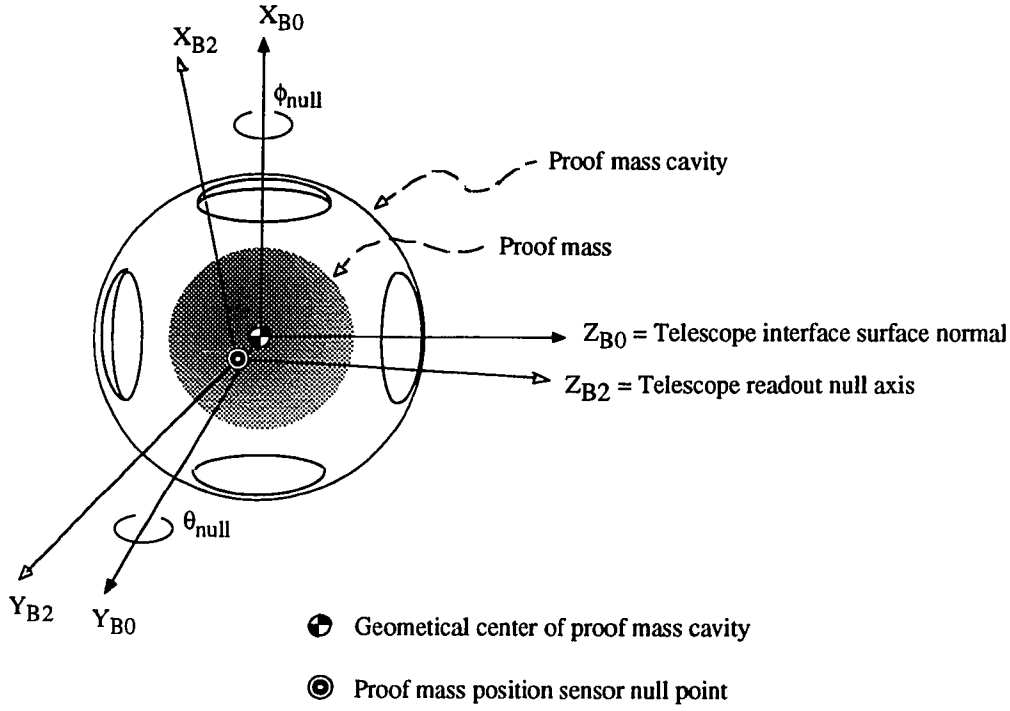


Figure 2.4 Orientations of the B-0 and B-2 frame with respect to the proof mass cavity. B-0 is the nominal control frame, and B-2 is the control frame.

The rotational matrices from B-0 to B-i ($i=1,\dots,3$) are defined by the following equations:

$${}^1B^0 = \begin{bmatrix} 1 & 0 & 0 \\ 0 & 1 & 0 \\ 0 & 0 & 1 \end{bmatrix} \quad (2.7)$$

$${}^2B^0 = \begin{bmatrix} 1 & 0 & -\theta_{null} \\ 0 & 1 & \phi_{null} \\ \theta_{null} & -\phi_{null} & 1 \end{bmatrix} \quad (2.8)$$

$${}^3B^0 = \begin{bmatrix} \cos \psi_{mass} & \sin \psi_{mass} & -\theta_{mass} \cos \psi_{mass} + \phi_{mass} \sin \psi_{mass} \\ -\sin \psi_{mass} & \cos \psi_{mass} & \theta_{mass} \sin \psi_{mass} + \phi_{mass} \cos \psi_{mass} \\ \theta_{mass} & -\phi_{mass} & 1 \end{bmatrix} \quad (2.9)$$

where

$\phi_{null}, \theta_{null}$: 1-2 Euler angles from B-0 to B-2: telescope null trimming angles about x_{B0} and y_{B0} , respectively

$\phi_{mass}, \theta_{mass}, \psi_{mass}$: 1-2-3 Euler angles from B-0 to B-3: mass property trimming angles about x_{B0} , y_{B0} , and z_{B0} , respectively

The orientations of the B-0 and B-1 frames are the same, and the rotational matrix is an identity matrix. The rotational matrix from B-0 to B-2 is determined by the telescope null alignment, and the telescope null has to be calibrated by preflight testing and on-board calibration. The rotational matrix from B-0 to B-3 is determined by the satellite mass distribution and should be estimated from the final configuration of satellite hardware. Because the z_{B3} axis is defined along the principal axis of inertia closest to the satellite axis of symmetry, rotations about the x_{A0} and y_{A0} axes are assumed to be infinitesimal.

Besides defining the sensor nulls, the B-2 frame plays an important part in relating Categories A and B. In Section 2.2.4, the rotational matrix ${}^{B0}T^{A0}$ (Equation 2.4) was defined to relate the A-0 and B-0 frames. The matrix ${}^{B0}T^{A0}$ is determined by three angles: two *absolute pointing error angles* (ϕ_a, θ_a) and the *absolute roll angle* (ψ_a), which are the 1-2-3 Euler angles from A-0 to B-0. Since ϕ_a, θ_a and ψ_a are defined with respect to the A-0 frame, these angles cannot be calculated directly. Instead, the actual pointing error is defined with respect to the optical direction of Rigel from the satellite, that is, the direction of the z_{A5} axis. The relative attitude of the B-2 frame with respect to the A-5 frame is determined by the *relative pointing error angles* (ϕ_r, θ_r) and the *relative roll*

angle (ψ_r), which are the 1-2-3 Euler angles from A-5 to B-2. The rotational matrix from A-5 to B-2 is determined by the following equation:

$$\begin{aligned}
 {}^{B2}T^{A5} &= \begin{bmatrix} \cos \psi_r & \sin \psi_r & 0 \\ -\sin \psi_r & \cos \psi_r & 0 \\ 0 & 0 & 1 \end{bmatrix} \begin{bmatrix} 1 & 0 & -\theta_r \\ 0 & 1 & \phi_r \\ \theta_r & -\phi_r & 1 \end{bmatrix} \\
 &= \begin{bmatrix} \cos \psi_r & \sin \psi_r & -\theta_r \cos \psi_r + \phi_r \sin \psi_r \\ -\sin \psi_r & \cos \psi_r & \theta_r \sin \psi_r + \phi_r \cos \psi_r \\ \theta_r & -\phi_r & 1 \end{bmatrix}
 \end{aligned} \tag{2.10}$$

where

ϕ_r, θ_r, ψ_r : 1-2-3 Euler angles from A-5 to B-2: relative yaw angle, relative pitch angle, and relative roll phase, respectively

The relative pointing error angles ϕ_r and θ_r are determined by the pointing controller performance, and the relative roll phase ψ_r is determined by the roll phase controller performance. The performance of both controllers is discussed in Chapter 4, which describes the truth models.

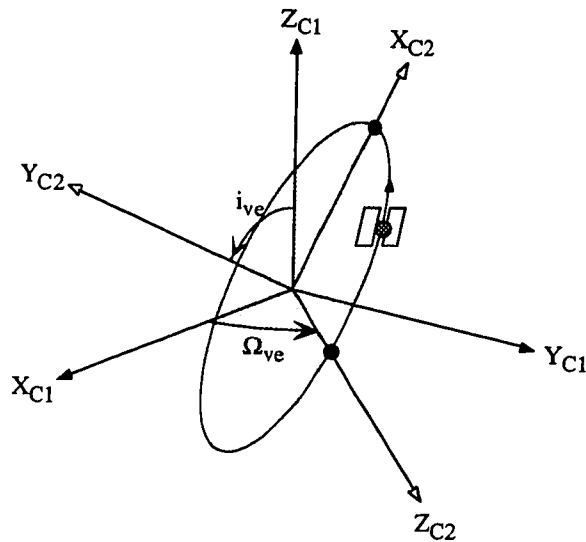
2.3.3 Secondary Frames in Category C

The three secondary frames C-i ($i=1,\dots,3$) are defined with respect to the primary frame C-0 through linear translation of the origin and axis rotation through rotational matrices. The C-i ($i=1,\dots,3$) frames are conventional or predefined frames and include the geocentric celestial frame, the satellite orbital frame, and the WGS 84 frame. Table 2.9 shows the I.D. number, name, origin, and orientation of each frame.

Table 2.9 Secondary Frame Definitions for Category C

ID#	Name	Origin	Orientation
C-1	Geocentric celestial frame	Geocenter	Same as for the C-0 frame
C-2	Orbital frame	Geocenter	\bar{y}_{C2} points in the instantaneous direction of orbital angular momentum \bar{z}_{C2} points in the instantaneous ascending node of the satellite orbit \bar{x}_{C2} forms a right-handed Cartesian coordinate frame
C-3	WGS 84	Geocenter	\bar{z}_{C3} is parallel to the direction of the conventional terrestrial pole (CTP) for polar motion \bar{x}_{C3} points at the intersection of the WGS 84 reference meridian plane and the plane of the CTP's Equator \bar{y}_{C3} forms a right-handed Cartesian coordinate frame

The geocentric celestial frame C-1 is interchangeable with the barycentric celestial frame C-0 through linear translation of the origin. The star coordinates, such as right ascension and declination, are given in the barycentric celestial frame and are called *catalog* coordinates. In other words, the locations of stars are defined with respect to the solar barycenter. On the other hand, the satellite orbits are defined with respect to the geocenter, and the catalog coordinates of Rigel have to be converted into the C-1 frame to obtain the apparent coordinates of Rigel from the geocenter.



i_{ve} = inclination of GP-B orbit
 Ω_{ve} = right ascension of GP-B orbit

Figure 2.5 Orientations of the C-1 and C-2 frames. C-1 is the geocentric celestial frame and C-2 is the orbital frame whose xz plane is parallel to the orbit.

The C-2 frame is called the *orbital frame* because the instantaneous satellite orbit determines its orientation. The instantaneous satellite orbit is determined by the orbital perturbation about the nominal orbit caused by the Earth's oblateness, the gravity fields of the Sun and the Moon, the precession of equinoxes, and the satellite residual drag. The origin of C-2 is placed at the geocenter and the y_{C2} axis points in the direction of the instantaneous orbital angular momentum. The z_{C2} axis points in the direction of the instantaneous ascending node. The rotational matrix from C-1 to C-2 is, therefore, determined by two orbital elements: inclination i_{ve} and right ascension Ω_{ve} of the ascending node. Figure 2.5 shows the relation between the C-1 and C-2 frames.

The C-3 frame is called the *Department of Defense World Geodetic System 1984* or WGS 84 for short. WGS 84 was defined by the Defense Mapping Agency (Ref. 30) in

an effort to provide a frame of reference for the global navigation of ships, airplanes, automobiles, and satellites. WGS 84 is fixed to the Earth and rotates about the z_{C3} axis. Even though WGS 84 is designed for military use, it is available for commercial use to a certain extent; the most recent application of WGS 84 is the global positioning system (GPS). P. Axelrad (Ref. 9) analyzed the GP-B satellite orbit, using the GPS for the satellite navigation. Because the output of the GPS system is usually in WGS 84 coordinates, the WGS 84 has been included in the standardized set for the satellite navigation analysis.

The rotational matrices from C-0 to C-1 and from C-1 to C-2 are defined by the following equations:

$${}^1C^0 = \begin{bmatrix} 1 & 0 & 0 \\ 0 & 1 & 0 \\ 0 & 0 & 1 \end{bmatrix} \quad (2.11)$$

$${}^2C^1 = \begin{bmatrix} -\cos i_{ve} \sin \Omega_{ve} & \cos i_{ve} \cos \Omega_{ve} & \sin i_{ve} \\ \sin i_{ve} \sin \Omega_{ve} & -\sin i_{ve} \cos \Omega_{ve} & \cos i_{ve} \\ \cos \Omega_{ve} & \sin \Omega_{ve} & 0 \end{bmatrix} \quad (2.12)$$

where

i_{ve} : instantaneous inclination of GP-B satellite's orbit

Ω_{ve} : instantaneous right ascension of GP-B satellite's orbit

The rotational matrix from C-0 to C-1 is an identity matrix since the frames have the same orientation but different origins. The C-3 frame (WGS 84) is fixed to the Earth, and the transformation from C-1 to C-3 is completed by the rotation about the Earth spin axis at the Earth's spin rate ω_{\oplus} . The exact rotational matrix from C-1 to C-3 (WGS 84) can be found in the DMA Technical Report DMA TR 8350.2 (Ref. 30).

2.4 Frame Definition Summary

The preceding sections defined a total of fifteen frames, including three primary frames and twelve secondary frames. The frames are divided into three categories, Categories A, B, and C. Each category is assigned one primary frame, which serves as a reference frame for its secondary frames. The conversions among the frames are defined by linear translation of the origin and axis rotation through rotational matrices. Figure 2.6 summarizes the relations among the frames. Each coordinate frame is indicated by a name and an I.D. number in parentheses. The arrows connecting the frames indicate the relations among the frames. Two frames connected by an arrow are related by linear translation of the origin and axis rotation through a rotational matrix. The rotational matrices are defined in the direction of the arrows. The elements of the rotational matrices are indicated beside the arrows.

The coordinate frames defined in this chapter serve as the reference frames upon which the truth models are developed. The clearly defined rotational matrices among the coordinate frames eliminate the error during the derivation of measurement equations in Chapter 4.

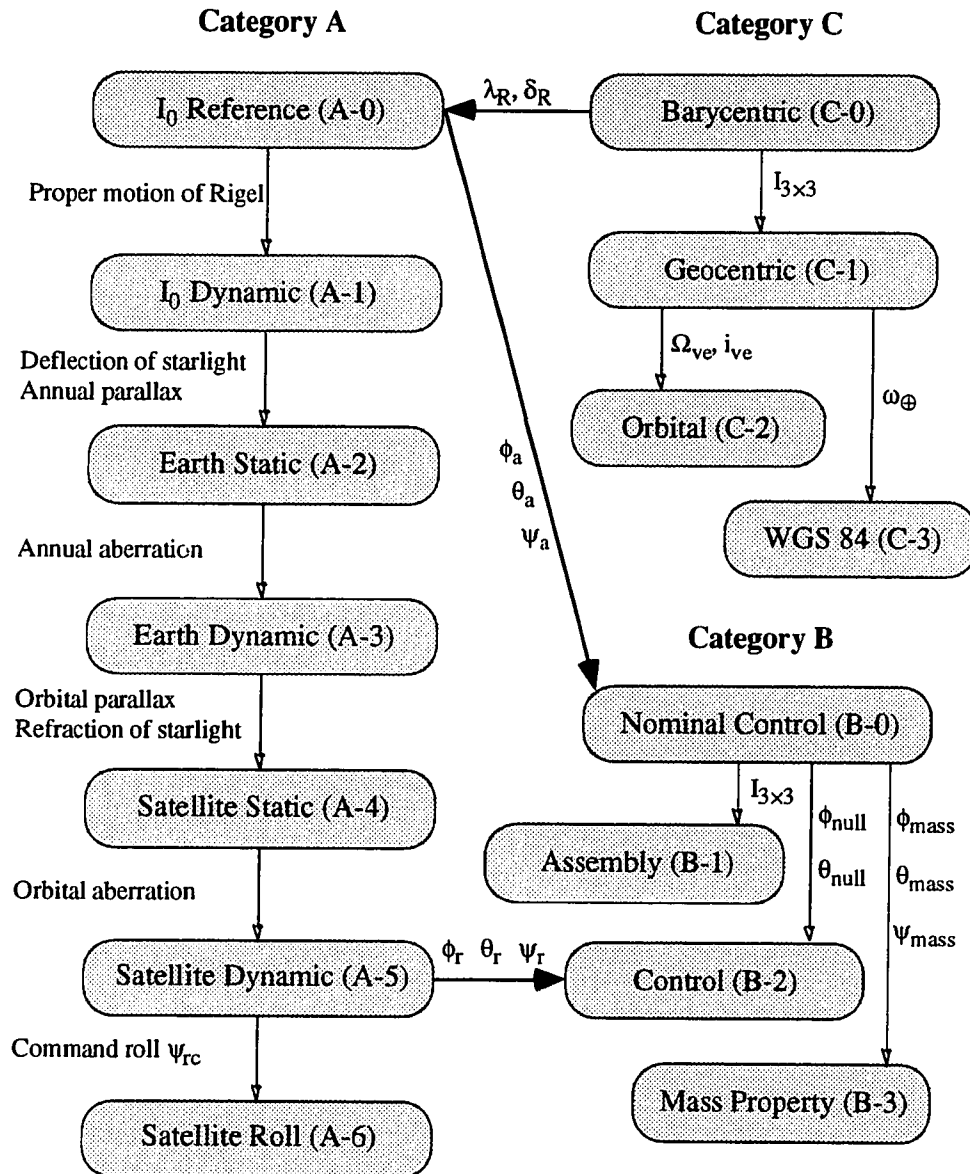


Figure 2.6 Hierarchical diagram of standardized coordinate frames. Each arrow connecting two frames indicates the dependency. The frame that the arrow points to is defined with respect to the other frame.

CHAPTER 3. RANDOM SEQUENCE GENERATION

3.1 Introduction

The science signal from the SQUID magnetometer or the telescope signal from the pointing controller includes deterministic and random signals. Deterministic signals include telescope observational errors such as parallax, aberration, and deflection of starlight. They can be modeled by an explicit function of time and/or space. Random signals, on the other hand, cannot be modeled by an explicit function but only specified by an expected value such as a root mean square (RMS) value. Such signals include satellite pointing error, satellite roll phase error, SQUID readout noise, scale factor drift, structural creeping, and so on. In order to simulate the science signal for the niobium bird experiment, random signals had to be generated by the computer programs. I wrote several C programs to simulate the three basic random sequences. This chapter describes

these random sequence generators and verifies them both in the time domain and in the frequency domain.

Three kinds of random signals are generated from a uniformly distributed random sequence between zero and one that is readily available in any computer language. First, a Gaussian random sequence is generated from the uniformly distributed random sequence. Second, a Wiener random sequence, based on the Gaussian random sequence, is generated. And last, a band-limited Wiener random sequence, based on the Wiener random sequence, is generated.

Regarding the notation, *random process* denotes a continuous random variable as a function of time, and *random sequence* denotes a group of samples from a continuous random process. The sampling period is assumed to be Δt , and the random sequence is indexed from zero according to the time of sampling.

3.2 Uniformly Distributed Random Sequence (UDRS)

Let us define the uniformly distributed random sequence first. It is the most basic random sequence in the computer environment and a UDRS generator is usually available as a built-in function in most of the high-level language compilers. The validity of the computer-generated UDRS depends on the algorithm of the built-in function and varies from one compiler to another. Verification of the simulated UDRS is especially important because the other random distributions such as the Gaussian and Wiener distributions are generated on the basis of the UDRS, . In this section, the UDRS generator provided by the Sun Sparcstation 330 C compiler is described, and verified in terms of time and frequency domain properties such as the probability density function and power spectral density function.

The conventional notation for a uniformly distributed random sequence between zero and one is

$$u_i = U(0,1) \quad (i=0,1,\dots) \quad (3.1)$$

This equation denotes the fact that u_i ($i=0,1,\dots$) has a probability density function (PDF) given by the following equation:

$$f_u(u) = \begin{cases} 1 & 0 \leq u \leq 1 \\ 0 & \text{otherwise} \end{cases} \quad (3.2)$$

The mean value m_i and variance σ_i of u_i ($i=0,1,\dots$) are given as

$$m_i \equiv E(u_i) = \frac{1}{2} \quad (i=0,1,\dots) \quad (3.3)$$

$$\sigma_i^2 \equiv E(u_i^2) - [E(u_i)]^2 = \frac{1}{12} \quad (i=0,1,\dots) \quad (3.4)$$

where

m_i : mean value of a UDRS

σ_i : standard deviation of a UDRS

Other useful properties of u_i ($i=0,1,\dots$) can be expressed in terms of the autocorrelation function, or equivalently, the power spectral density function. In order to derive the autocorrelation function of the UDRS, u_i ($i=0,1,\dots$) has to be divided into a deterministic bias m_i and a random offset δu_i as follows:

$$u_i = m_i + \delta u_i \quad (i=0,1,\dots) \quad (3.5)$$

where

δu_i : zero mean random offset

then

$$\delta u_i = U\left(-\frac{1}{2}, \frac{1}{2}\right) \quad (i=0,1,\dots) \quad (3.6)$$

$$E(\delta u_i) = 0 \quad (i=0,1,\dots) \quad (3.7)$$

If we assume that the random sequence δu_i ($i=0,1,\dots$) is serially independent, the autocorrelation function of δu_i is given as

$$E(\delta u_i \delta u_j) = \frac{1}{12} \delta_{ij} \quad (i,j=0,1,\dots) \quad (3.8)$$

By using this independent property of δu_i ($i=0,1,\dots$), we can calculate the autocorrelation function of u_i ($i=0,1,\dots$) as follows:

$$\begin{aligned} R_U(i, j) &\equiv E(u_i u_j) = E[(m_i + \delta u_i)(m_j + \delta u_j)] \\ &= m_i m_j + m_j E(\delta u_i) + m_i E(\delta u_j) + E(\delta u_i \delta u_j) \\ &= \frac{1}{4} + \frac{1}{12} \delta_{ij} \equiv R_U(k) \quad (k = j - i \text{ and } i, j = 0, 1, \dots) \end{aligned} \quad (3.9)$$

The constant term indicates the complete correlation of u_i ($i=0,1,\dots$) through the bias m_i , and the impulse term indicates the whiteness, or independence, of random offset δu_i around the bias. Since the autocorrelation function $R_U(i,j)$ is expressed as a function of $k = j - i$, the uniformly distributed random sequence u_i ($i=0,1,\dots$) is wide-sense stationary (WSS).

Let us now derive the power spectral density function of u_i ($i=0,1,\dots$) from the autocorrelation function $R_U(k)$ ($k=0,\pm 1,\dots$), assuming that the random sequence u_i ($i=0,1,\dots,\infty$) consists of samples from a uniformly distributed random process $u(t)$ at a sampling period of Δt . Then the power spectral density function of the original random process $u(t)$ can be obtained as a discrete Fourier transform of the autocorrelation function $R_U(k)$ ($k=0,\pm 1,\dots,\pm\infty$) as follows:

$$\begin{aligned}
S_U(f) &= \sum_{k=-\infty}^{\infty} R_U(k) \exp(-j2\pi kf) \\
&= \frac{1}{4} \delta(f) + \frac{1}{12}
\end{aligned}
\quad (-f_N < f < f_N) \quad (3.10)$$

where

$$j = \sqrt{-1}$$

$\delta(f)$: impulse function

f_N : Nyquist frequency

The valid frequency range of $S_U(f)$ is determined by the Nyquist frequency f_N of sampling. If we compare Equation 3.10 to Equation 3.9, the correlated term is now expressed as an impulse function and the independent term as a constant term in the frequency domain. This power spectral density function $S_U(f)$ is used to check the validity of the computer-generated UDRS presented in the next section.

3.2.1 Generation of a UDRS

The uniformly distributed random sequence analyzed above was generated by a built-in function provided by the SunOS (Version 4.1) C compiler on a Sparcstation 330. This section briefly describes this built-in function.

Although Equation 3.8 assumes that the random offset δu_i around the bias m_i is independent, this assumption is not always true when the random variables u_i ($i=0,1,\dots$) are generated by a computer. The randomization algorithm often employs a feedback random number generator and has a period as a result. I used the C language random number generator *random()* that is provided by the C compiler on Sun Sparcstation 330 with SunOS Version 4.1. *Random()* uses a nonlinear additive feedback random number generator and returns a uniformly distributed random number between zero and $(2^{31} - 1)$. Thus, the uniformly distributed random sequence u_i ($i=0,1,\dots$) between zero and one can be obtained as follows:

$$u_i = \frac{1}{2^{31}-1} \text{random}() \quad (i=0,1,\dots) \quad (3.11)$$

The C compiler manual claims that this generator has a period of $16(2^{31} - 1)$, which is adequately long for the GP-B simulation because the number of measurements is about 2^{22} to 2^{23} for the two-year mission, but the periodicity of this random sequence generator has to be tested to verify the claim.

Another feature of the randomization utility provided by the SunOS C compiler is its ability to accept a user-defined seed¹. In addition to *random()*, another built-in function, *srandom(i_{seed})*, is available from the C compiler. It takes an integer seed as an argument for the randomization process performed by *random()*. After *srandom(i_{seed})* sets the seed, a series of successive calls of *random()* generates a random sequence. Since the seed determines the starting value of a random sequence, identical random sequences will be generated if the same seed is used every time the sequence is restarted. Thus, the seed itself has to be chosen randomly if we want a different random sequence to be generated every time the program is restarted. The following is the algorithm I used to generate a random seed for *random()*:

$$\begin{aligned} t_{ep} &= \text{elapsed time in second from 00:00 GMT, January 1, 1970} \\ &= t_{\text{sec}} + 10^{-6} t_{\mu\text{sec}} \end{aligned} \quad (3.12)$$

where

$$\begin{aligned} t_{\text{sec}} &= \text{integer second of } t_{ep} \\ t_{\mu\text{sec}} &= \text{integer microsecond fraction of } t_{ep} \end{aligned}$$

then

$$i_{\text{seed}} = t_{\text{sec}} \% t_{\mu\text{sec}} \quad (3.13)$$

¹ A seed is an integer value that is used as a starting value for the random sequence generated by *random()*. If a seed is not specified by a user, the compiler assumes the default seed, i.e., one.

Two integer values, t_{sec} and $t_{\mu\text{sec}}$, are available from the UNIX system call *gettimeofday()*. For example, if the random sequence is initiated at 21:51:23 PST on September 1992, the seed is determined as follows:

From *gettimeofday()*,

$$\begin{aligned} t_{\text{sec}} &= 716183482 \text{ (second)} \\ t_{\mu\text{sec}} &= 530000 \text{ (microsecond)} \end{aligned}$$

thus

$$\begin{aligned} i_{\text{seed}} &= 716183482 \% 530000 \\ &= 153482 \end{aligned}$$

According to this method, the seed is determined by the time of the program execution, which is arbitrary. The actual program list of this generator is given in the appendix and the validity of this method is verified in the next section.

3.2.2 Verification of Simulated UDRSs

The validity of a simulated random sequence can be checked in two ways. The first method uses a histogram and the second uses power spectral density estimation. The histogram method is useful when the probability distribution function (PDF) of a simulated random sequence has to be tested. The percentage of occurrence in a specific histogram bin should follow the integral of the PDF over the bin. If we assume that u_i ($i=0,1,\dots,N-1$) has a PDF $f_U(u)$, then the occurrence in a specific bin $[a,b]$ should follow the integral of the PDF in the following way:

$$\frac{(\text{Number of occurrence of } u_i \text{ in bin } [a,b])}{N} = \int_a^b f_U(u) du \quad (3.14)$$

where

N: number of samples

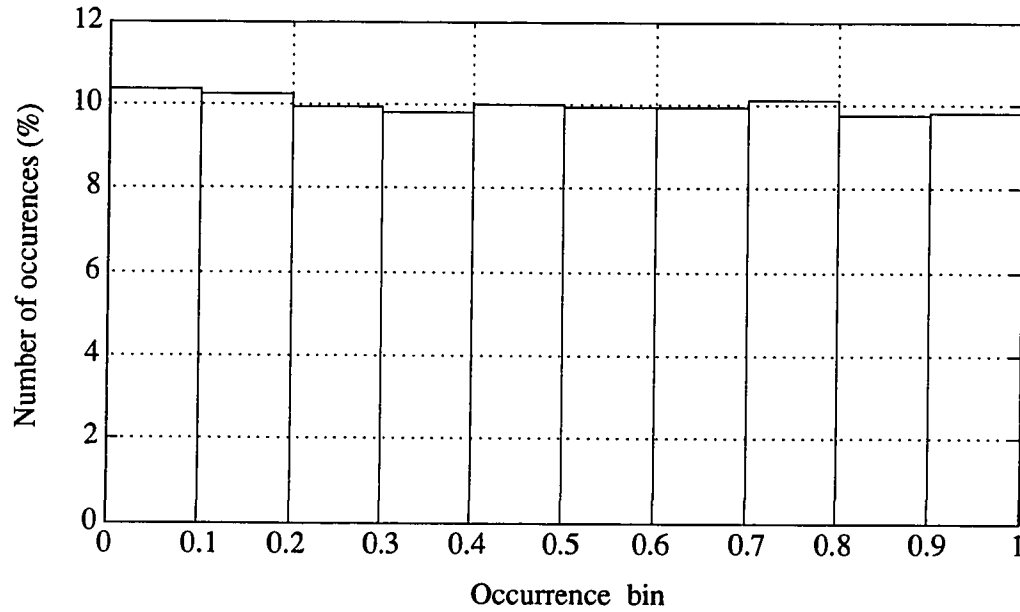


Figure 3.1 Histogram of a simulated UDRS (16384 samples).

Figure 3.1 shows a histogram of 16,384 samples created by the generator presented in the preceding section. The histogram indicates that the simulated UDRS is uniformly distributed between zero and one and has a valid PDF.

The second method uses the power spectral density (PSD) estimation called the *periodogram*. This method is useful when frequency domain properties such as whiteness and power distribution have to be tested. Let us assume that the random process $u(t)$ is sampled at time interval Δt to create the random sequence u_i ($i=0,1,\dots,N-1$). The sampled random sequence u_i ($i=0,1,\dots,N-1$) is then divided into L segments without an overlap, and each segment has M data points where $N=LM$ [see Figure 3.2]. The power spectral density function $S_U(f)$ of the original random process $u(t)$ can be estimated from the L segments of sampled data using a modified periodogram (Ref. 31). This algorithm is summarized in Table 3.1. The mean and variance of the averaged periodogram $\hat{S}_U(f)$ were thoroughly investigated by Oppenheim & Schaffer (Ref. 32) and

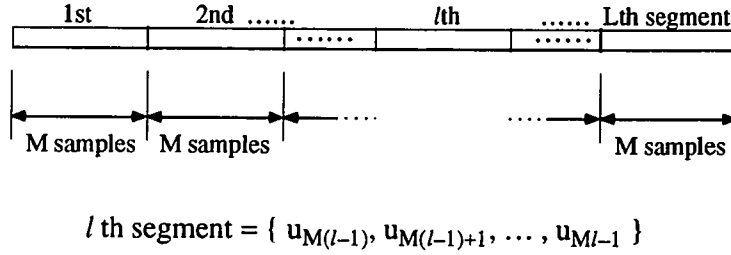


Figure 3.2 Data segmentation for a modified periodogram.

Shanmugan & Breipohl (Ref. 33). The estimation bias and the variance approach zero as the number of samples $N \rightarrow \infty$. Thus, $\hat{S}_U(f)$ is an asymptotically unbiased and consistent estimator of $S_U(f)$.

During the data segmentation (Equation 3.15), the dc component, that is, the bias of the segment was subtracted from the data in order to avoid deformation of the PSD estimate caused by spectral leakage. Spectral leakage is characterized as smeared edges of a true PSD. Assume that a periodogram of a constant signal is calculated from the N points of sampled data. If N is infinite, the periodogram shows an impulse function at the origin. If N is finite as in realistic cases, the periodogram shows a blurred peak around the origin that often conceals the true PSD at the higher frequencies. When a simulated random sequence is to be verified by the PSD over a wide range of frequency, the dc component often deforms the higher frequency estimate and should be subtracted. Also, the dc component can be tested separately by taking an average value of the random sequence.

The modified periodogram (Equation 3.20) is provided by MATLAB as the *spectrum* function. This function requires M to be a power of two in order to use the FFT algorithm and has a scaling error by a factor of the sampling period Δt . To correct the error, the solution by *spectrum* has to be multiplied by Δt . *Spectrum* also does not correct for the noise power leakage caused by the side lobes of the Hanning window. To correct

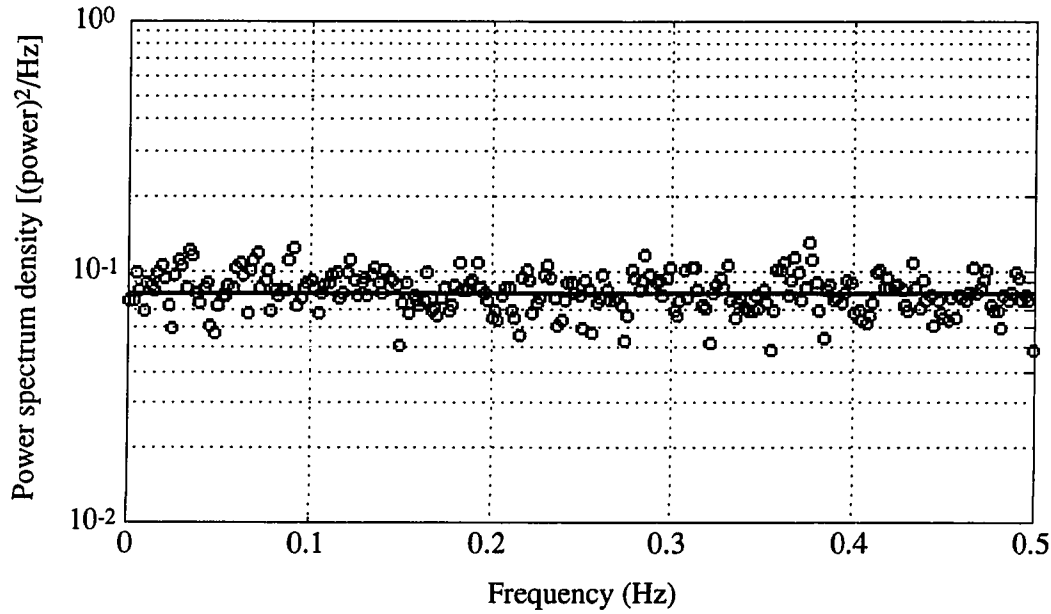


Figure 3.3 Predicted vs. estimated power spectral density of a UDRS. Solid line: predicted PSD, circles: estimated PSD of UDRS.

for the leakage, the solution by *spectrum* has to be divided by 1.5 [see Table 3.1]. Figure 3.3 shows the predicted PSD function of $u(t)$ (Equation 3.10) and the estimated PSD by *spectrum* based on u_i ($i=0, \dots, 16383$) with $M=512$. Again, the dc component of u_i was subtracted from the estimate to avoid deformation caused by the spectral leakage. The flatness of the estimated PSD indicates that the random offset δu_i around the bias is independent, or white.

From the two tests given in this section, the uniformly distributed random number generator (Equation 3.11) was verified to have a uniform distribution between $[0,1]$ and an independent offset around the bias. The other random distributions, such as the Gaussian, Wiener and band-limited Wiener random sequences, are generated based on u_i ($i=0,1,\dots$) in Sections 3.3, 3.4 and 3.5.

Table 3.1 PSD Estimation by Modified Periodogram

Data segment:

$$u_l(k) = u_j - \frac{1}{M} \sum_{k=0}^{M-1} u_j \quad \begin{pmatrix} j \equiv M(l-1) + k \\ k = 0, \dots, M-1 \\ l = 1, \dots, L \end{pmatrix} \quad (3.15)$$

Hanning window:

$$h_w(k) = \begin{cases} 0.5 - 0.5 \cos \frac{2\pi k}{M-1} & k = 0, \dots, M-1 \\ 0 & \text{otherwise} \end{cases} \quad (3.16)$$

Weighted samples in the l -th segment:

$$x_l(k) = h_w(k) u_l(k) \quad (k=0, \dots, M-1) \quad (3.17)$$

Discrete Fourier transform of $x_l(k)$:

$$U_l(f) = \sum_{k=0}^{M-1} x_l(k) \exp(-j2\pi kf) \quad (l=1, \dots, L) \quad (3.18)$$

where $f = 0, \frac{f_s}{M}, \frac{2f_s}{M}, \dots, \frac{(M-1)f_s}{M}$

Modified periodogram² (two-sided) of the l -th segment:

$$\hat{S}_U(f, l) = \frac{\Delta t}{1.5 \left[\sum_{k=0}^{M-1} h_w^2(k) \right]} |U_l(f)|^2 \quad (3.19a)$$

or one-sided periodogram:

$$\hat{G}_U(f, l) = \frac{2\Delta t}{1.5 \left[\sum_{k=0}^{M-1} h_w^2(k) \right]} |U_l(f)|^2 \quad (3.19b)$$

Averaged periodogram³ (two-sided) over L segments:

$$\hat{S}_U(f) = \frac{1}{L} \sum_{l=1}^L \hat{S}_U(f, l) \quad (3.20a)$$

or one-sided averaged periodogram:

$$\hat{G}_U(f) = \frac{1}{L} \sum_{l=1}^L \hat{G}_U(f, l) \quad (3.20b)$$

² The factor of $1/1.5$ corrects the noise power leakage caused by the side lobes of the Hanning window. This correction is necessary in the case of analyzing broad-band noise power (Ref. 59, 60).

³ This modified periodogram is a real, even, and non-negative function that satisfies the conditions of a real signal PSD function.

3.3 Gaussian Random Sequence (GRS)

The Gaussian random sequence is the most versatile random sequence in engineering applications because of the central limit theorem⁴. This section describes the generation of an independent Gaussian random sequence based on the uniformly distributed random sequence developed in Section 3.2. The conventional notation for the Gaussian random sequence with a zero mean and a unity standard deviation is as follows:

$$n_i = N(0,1) \quad (i=0,1,\dots) \quad (3.21)$$

This equation is equivalent to the fact that n_i ($i=0,1,\dots$) has a PDF given by the equation

$$f_N(n) = \frac{1}{\sqrt{2\pi}} \exp\left(-\frac{n^2}{2}\right) \quad (3.22)$$

If we assume the independence or whiteness⁵ of the Gaussian random sequence n_i ($i=0,1,\dots$), then the autocorrelation function is given as follows:

$$R_N(k) \equiv E(n_i n_j) = \delta_{ij} \quad (k=j-i \text{ and } i,j=0,1,\dots) \quad (3.23)$$

where

δ_{ij} : Kronecker delta function

Let us assume that n_i ($i=0,1,\dots,\infty$) are samples from a continuous random process $n(t)$; then the PSD function of $n(t)$ can be obtained as a discrete Fourier transform of the autocorrelation function as follows:

⁴ The central limit theorem is defined as follows. Let X_1, X_2, \dots be a sequence of independent and identically distributed random variables each having mean μ and variance σ^2 . Then the distribution of

$$\frac{X_1 + \dots + X_n - n\mu}{\sigma\sqrt{n}}$$

tends to the standard normal (Gaussian) as $n \rightarrow \infty$ (Ref. 34).

⁵ Gaussian distribution does not necessarily indicate that the Gaussian random sequence is independent. The Gaussian random sequence is independent, or white, if the covariance matrix of joint Gaussian distribution function is diagonal.

$$S_N(f) = \sum_{k=-\infty}^{\infty} R_N(k) \exp(-j2\pi kf) \quad (-f_N < f < f_N) \quad (3.24)$$

$$= 1$$

This PSD function is used to test the spectral composition of the simulated Gaussian random sequence presented in the next section.

3.3.1 Generation of a GRS

Two methods of generating a GRS from a uniformly distributed random sequence u_i ($i=0,1,\dots$) between zero and one are presented in this section. The first method uses the central limit theorem, which states that the sum of any independent, identically distributed random sequence approaches the Gaussian distribution as the number of samples increases. The following equation generates an approximated GRS by adding twelve uniformly distributed random numbers.

$$n_i = \sum_{j=0}^{11} u_j - 6 \quad (i=0,1,\dots) \quad (3.25)$$

where

u_i : uniformly distributed random sequence between zero and one

n_i : Gaussian random sequence with zero mean and unity variance

The mean value of this model is zero and the standard deviation is one if the random variables u_j ($j=0,\dots,11$) are independent, that is, if $E(u_i u_j)=0$ for $i \neq j$. The advantage of this method is its simplicity and the disadvantage is its inability to provide any number greater than 6 or less than -6.

The second method uses the transformation of random variables. Assume that two random variables x_1 and x_2 have a joint distribution function $f_{x_1, x_2}(x_1, x_2)$. Then the transformation, $y_1 = g_1(x_1, x_2)$ and $y_2 = g_2(x_1, x_2)$, creates two random variables y_1 and

y_2 with a joint distribution function $f_{Y_1, Y_2}(y_1, y_2)$. This distribution function is related to the original distribution function in the following way:

$$f_{Y_1, Y_2}(y_1, y_2) = f_{X_1, X_2}(x_1, x_2) \left| \begin{array}{cc} \frac{\partial g_1}{\partial x_1} & \frac{\partial g_1}{\partial x_2} \\ \frac{\partial g_2}{\partial x_1} & \frac{\partial g_2}{\partial x_2} \end{array} \right|^{-1} \quad (3.26)$$

The second algorithm uses this transformation property and generates two jointly Gaussian random variables n_1 and n_2 from two uniformly distributed random variables u_1 and u_2 by the following transformation:

$$\begin{aligned} n_1 &= \sqrt{-2 \log u_1} \cos 2\pi u_2 \\ n_2 &= \sqrt{-2 \log u_1} \sin 2\pi u_2 \end{aligned} \quad (3.27)$$

where

$$u_1 = U(0,1)$$

$$u_2 = U(0,1)$$

The proof of this algorithm can be found in Ross (Ref. 34). In contrast to the first method, this method can provide two Gaussian random variables that range from $-\infty$ to ∞ based on only two uniformly distributed random variables. A disadvantage is that this method is more prone to a correlated random number generator because the central limit theorem cannot be applied. Both methods presented above are tested in the next section.

3.3.2 Verification of Simulated GRSs

The Gaussian random sequences generated by the two methods presented in the preceding section can be tested in terms of the histogram and the power spectral density. Figure 3.4 (a) and (b) show the histogram of 16,384 samples created by both methods. The histogram distribution of the simulated GRS follows the ideal Gaussian distribution for both methods. Even though both histograms match the ideal PDF very well, the range

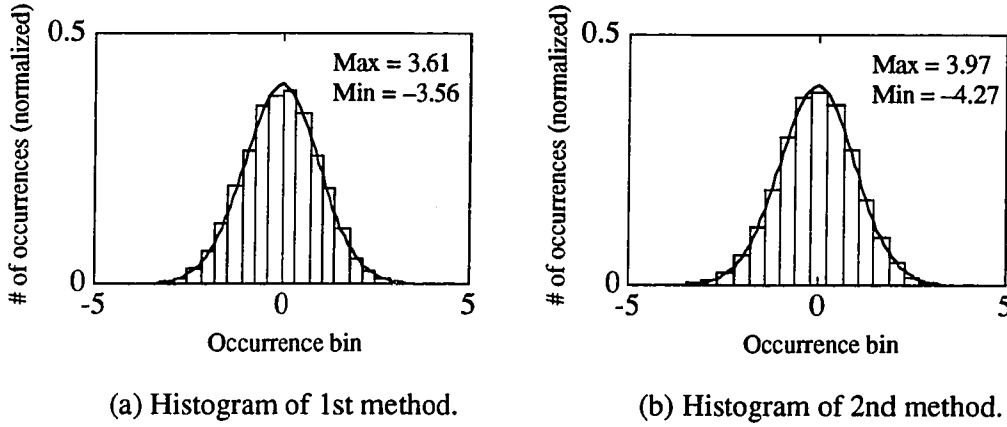
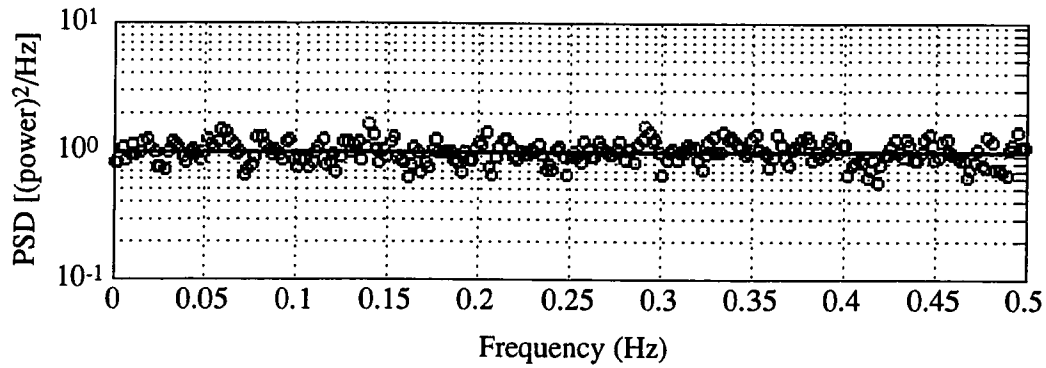


Figure 3.4 Histogram of a GRS generated by two methods.

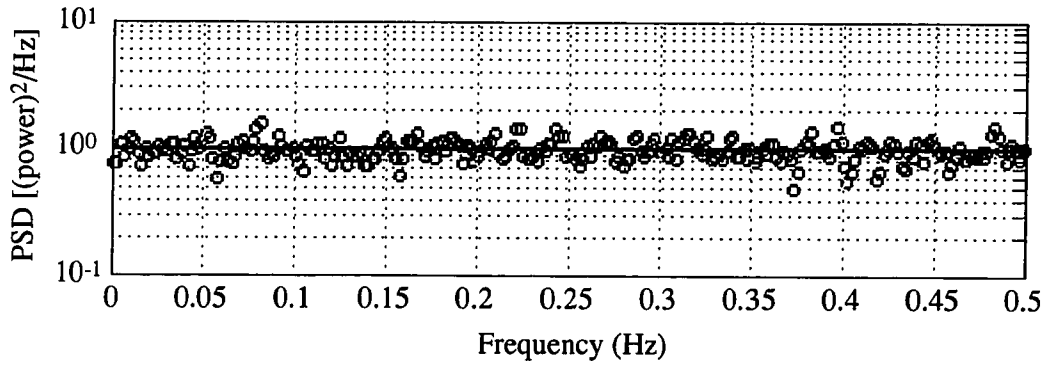
of the GRS generated by the first method is only about 87% of that of the second method, which reflects the inability of the first method to provide any number greater than 6 or less than -6.

Let us now test the simulated GRS in terms of the PSD function. Assume that a Gaussian random process $n(t)$ is sampled at $\Delta t=1$ to create a Gaussian random sequence n_i ($i=0,1,\dots$). The PSD function $S_N(f)$ of $n(t)$ is then given by Equation 3.24. Alternatively, $S_N(f)$ can be estimated from the sampled sequence n_i ($i=0,\dots,N-1$) by the modified periodogram. Figure 3.5 compares the predicted PSD and the estimated PSD based on the simulated GRS with $N=16384$ and $M=512$. The estimated PSD matches the predicted PSD and verifies the whiteness of the simulated random sequence n_i ($i=0,1,\dots,16383$) for both methods.

With these two tests, I verified that the Gaussian random sequences generated by Equations 3.25 and 3.27 have a valid PDF and a valid PSD of the GRS. The second method (Equation 3.27) was used in the simulation program *gpb.c* because it provides a wider random number range than the first method (Equation 3.25). Section 3.4 explains



(a) PSD of a GRS generated by method 1.



(b) PSD of a GRS generated by method 2.

Figure 3.5 Predicted vs. estimated PSD of a GRS generated by two methods. Solid line: predicted PSD, circles: estimated PSD.

the generation of a Wiener random sequence based on the GRS generated by the second method.

3.4 Wiener Random Sequence (WRS)

A Wiener random sequence is often called *random walk* in analogy to the path of a drunk person trying to walk a straight line: the direction and length of his next step cannot be predicted from his current position. This analogy is useful for modeling a

random signal that drifts away from an original value. This section describes a method used to generate a Wiener random sequence and verifies that method in the time and frequency domains.

In order to describe the Wiener random sequence in detail, it is necessary to first define the Wiener random process. It is a continuous random process with an independent increment that has a Gaussian distribution with a zero mean and a covariance proportional to time t . The definition is given by the conventional notation as

$$\begin{aligned} w(0) &= 0 \\ w(t) &= N(0, \alpha_w t) \end{aligned} \tag{3.28}$$

where

α_w : covariance coefficient of a WRS

The amount of increment $w(t)-w(t')$ also has a Gaussian distribution with a zero mean and a covariance proportional to $(t-t')$ that can be expressed as

$$w(t) - w(t') = N(0, \alpha_w (t - t')) \quad \text{for } t > t' \geq 0 \tag{3.29}$$

These properties indicate that the Wiener process is both a nonstationary Markov and a Martingale process. Since the Wiener process is nonstationary, the autocorrelation function cannot be expressed as a function of $\tau=t-t'$, but rather as a function of t and t' , as follows:

$$R_w(t, t') = \alpha_w \min(t, t') \quad \text{for } t, t' \geq 0 \tag{3.30}$$

The continuous Wiener random process is discretized by the sampling period Δt ; the next section presents a computer algorithm for generating the Wiener random sequence.

3.4.1 Generation of a WRS

If a Wiener random process is sampled at an interval Δt , it becomes a Wiener random sequence, or a random walk. A difference equation for the Wiener random sequence can be derived using the second property of the Wiener process (Equation 3.29). Assuming that the sampling period is Δt , the difference equation is given as

$$\begin{aligned} w_0 &= 0 \\ w_k &= w_{k-1} + \sqrt{\alpha_w \Delta t} n_k \end{aligned} \quad (k=1,2,\dots) \quad (3.31)$$

where

$$n_k = N(0,1) \quad (k=1,2,\dots)$$

This difference equation⁶ can be solved explicitly, and w_k can be expressed as a function of n_l ($l=1,\dots,k$) as follows:

$$w_k = \sqrt{\alpha_w \Delta t} \sum_{l=1}^k n_l \quad (k=1,2,\dots) \quad (3.32)$$

This equation indicates that w_k is a Gaussian random variable because it is expressed as a linear combination of jointly Gaussian random variables n_l ($l=1,\dots,k$). The mean value and the covariance of w_k can be calculated from Equation 3.32 under the assumption of Equation 3.23 and are given in the conventional expression

$$\begin{aligned} w_0 &= 0 \\ w_k &= N(0, \alpha_w (k\Delta t)) \end{aligned} \quad (k=1,2,\dots) \quad (3.33)$$

⁶ The index of an input Gaussian random variable is equal to that of the output Wiener random variable. This difference equation is not in a conventional discrete form but is acceptable for this case because the input Gaussian sequence is independent and the index is irrelevant.

This equation is consistent with the continuous Wiener process (Equation 3.28) evaluated at $t=k\Delta t$.

In addition to the time domain properties given above, the frequency domain property, that is, the power spectral density, becomes important when a simulated random sequence has to be verified. The PSD of w_i ($i=1,\dots$) can be predicted from that of n_i ($i=1,\dots$) and the transfer function $H(z)$, which can be obtained from the z-transform of the difference equation (Equation 3.31) as follows:

$$\frac{W(z)}{N(z)} = H(z) \quad (3.34)$$

where

$$H(z) = \frac{\sqrt{\alpha_w \Delta t}}{1 - z^{-1}}$$

$$W(z) \equiv Z[w_k]$$

$$N(z) \equiv Z[n_k]$$

Given the PSD of n_i ($i=1,\dots$) (Equation 3.24) and the transfer function $H(z)$, the PSD of w_i ($i=1,\dots$) is predicted thus

$$S_w(f) = |H(z)|_{z=\exp(j2\pi f\Delta t)}^2 S_n(f)$$

$$= \frac{\alpha_w \Delta t}{2(1 - \cos 2\pi f\Delta t)} \quad (0 < f < f_N) \quad (3.35)$$

This PSD indicates that the crossover frequency f_x is determined by α_w and Δt as follows:

$$f_x = \frac{f_s}{2\pi} \cos^{-1} \left(1 - \frac{\alpha_w \Delta t}{2} \right) \quad (3.36)$$

where

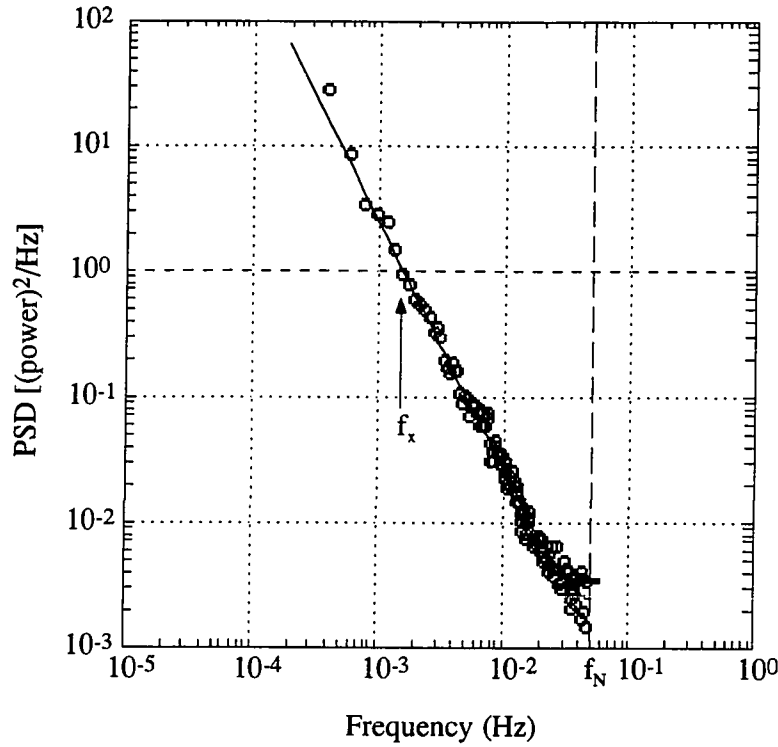


Figure 3.6 Predicted vs. estimated PSD of a WRS ($\Delta t=10$ seconds, $\alpha_w=0.001$). Solid line: predicted PSD, circles: estimated PSD, f_x =crossover frequency, f_N =Nyquist frequency.

$$S_w(f) \Big|_{f=f_x} = 1$$

For $\Delta t=10$ seconds and $\alpha_w=0.001$, the cross-over frequency is $1.6e-3$ Hz.

A WRS was generated by a C program using the difference equation (Equation 3.31) based on the GRS simulated in the previous section. The predicted covariance and the PSD of w_i ($i=1, \dots$) (Equations 3.33 and 3.35, respectively) were used to check the validity of the simulated WRS; the results are presented in the next section.

3.4.2 Verification of Simulated WRSs

I tested the WRS generated by the difference equation (Equation 3.31) based on the simulated GRS in terms of the power spectral density. Figure 3.6 compares the

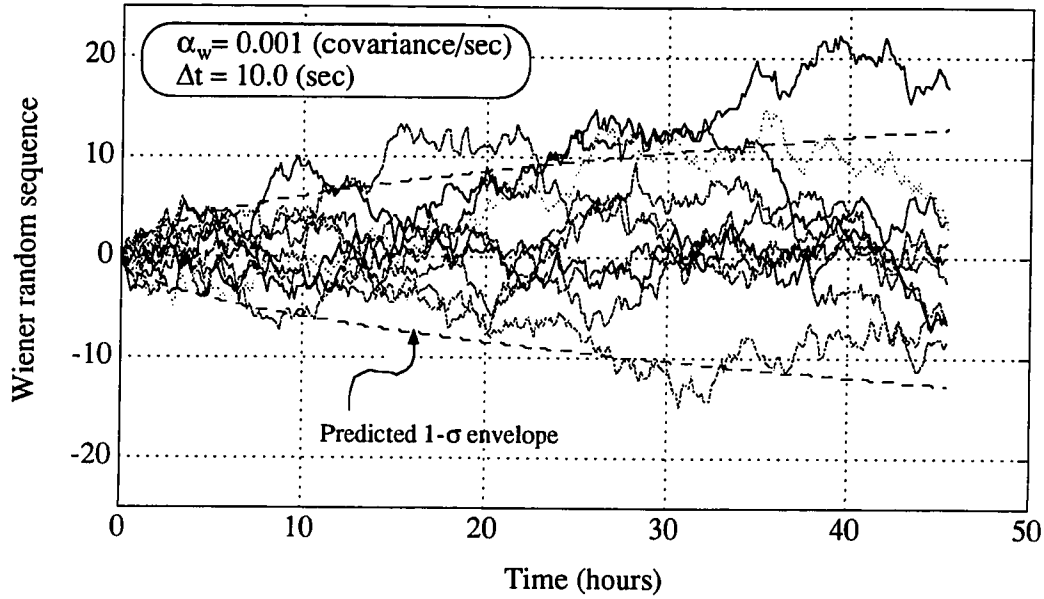


Figure 3.7 Time history of Wiener random sequences (10 samples).

predicted PSD (Equation 3.35) with the PSD estimated by the periodogram based on 16,384 points of the simulated WRS for $\Delta t=10$ seconds and $\alpha_w=0.001$. The predicted PSD and the estimated PSD match very closely; thus, the simulated Wiener sequence has a valid frequency composition.

I also tested the simulated WRS in the time domain. Figure 3.7 shows the time history of 10 different simulated WRSs with predicted one-sigma envelopes given by $\pm\sqrt{\alpha_w t}$. About 90% of the random sequences stay inside of the predicted envelopes, which verifies that the simulated WRS has a valid covariance.

These two tests prove that the random sequence simulated by the difference equation (Equation 3.31) has valid WRS time and frequency properties. Another class of random sequence, a band-limited Wiener random sequence, constructed on the basis of the WRS developed above, is introduced in the next section.

3.5 Band-Limited Wiener Random Sequence (BLWRS)

The time-varying covariance of the Wiener random sequence is useful when a plant with a random drift has to be simulated. In fact, Wiener derived the Wiener process to model the Brownian motion of a small particle in 1923. Another famous application of the Wiener process is the thermal noise analysis in electrical circuits. As for the GP-B program, random drifts can be found in the proper motion of Rigel, sensor scale factor drifting, sensor bias drifting, structural creeping, and so on. These drift terms are usually band-limited to very slow components with time constants of hours to months. Unfortunately, the Wiener process itself has undesirable high-frequency components. As shown in Figure 3.6, the crossover frequency of the WRS with $\Delta t=10$ seconds and $\alpha_w=0.001$ is 1.6 mHz, which is equivalent to a time constant of about 10 minutes. This means that any frequency components slower than 1.6 mHz have gain of more than one. Also, the attenuation ratio of the higher frequencies is only -40 dB/decade. This weak attenuation of the higher frequency components becomes a problem when a slowly varying term such as the structural creeping of the satellite body has to be modeled. The other problem with the WRS is that it does not allow one to choose the crossover frequency. As shown in Equation 3.36, the crossover frequency f_x is determined by the sampling frequency and the covariance coefficient α_w of the WRS. Thus, f_x is not an independent variable. I therefore constructed a band-limited Wiener random sequence in order to overcome the limitation of the WRS. The following sections describe the band-limited Wiener random sequence, which provides a better attenuation of the higher frequency components and the flexibility of allowing one to choose the crossover frequency.

3.5.1 Generation of a BLWRS

The band-limited Wiener random sequence can be generated by running the Wiener random sequence through a first-order digital filter $L(z)$ given as follows:

$$\frac{V(z)}{W(z)} = L(z) \quad (3.37)$$

where

$$a_L \equiv \exp\left(-\frac{\Delta t}{T_c}\right)$$

$$L(z) = \frac{1 - a_L}{1 - a_L z^{-1}}$$

The difference equation corresponding to this transfer function is given as follows:

$$v_0 = 0$$

$$v_k = a_L v_{k-1} + (1 - a_L) w_k \quad (k=1, 2, \dots) \quad (3.38)$$

This difference equation can be solved explicitly in terms of w_k as follows:

$$v_k = (1 - a_L) \sum_{m=0}^k a_L^{k-m} w_m \quad (k=0, 1, \dots) \quad (3.39)$$

If we substitute the explicit expression for w_k (Equation 3.32), v_k can be expressed in terms of the Gaussian random sequence u_l ($l=1, \dots$) as follows:

$$v_k = \sqrt{\alpha_w \Delta t} \sum_{l=1}^k (1 - a_L^{k-l+1}) u_l \quad (k=1, 2, \dots) \quad (3.40)$$

Again, under the assumption of Equation 3.23, the mean and the covariance of v_k ($k=1, \dots$) can be calculated thus:

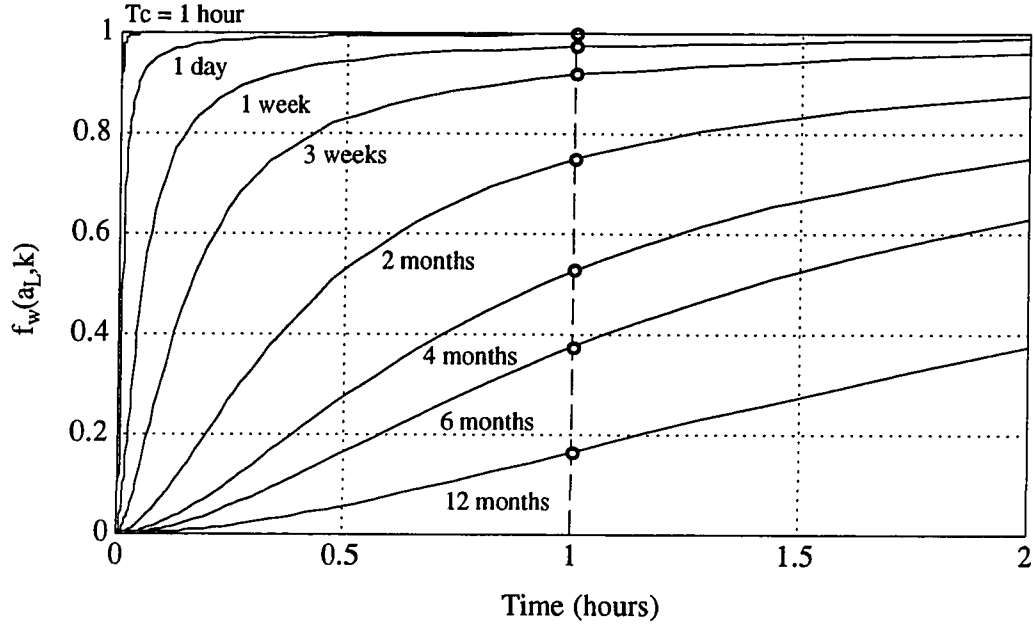


Figure 3.8 Covariance coefficient function of a BLWRS.

$$\begin{aligned}
 E(v_k) &= 0 \\
 E(v_k^2) &= \alpha_w \Delta t k f_w(a_L, k) \quad (k=1,2,\dots) \quad (3.41)
 \end{aligned}$$

where

$$f_w(a_L, k) \equiv 1 - \frac{a_L(1-a_L^k)}{(1-a_L^2)k} (2 + a_L - a_L^{k+1})$$

As shown by Equation 3.41, the covariance of the BLWRS is not equal to that of the WRS but is modulated by the covariance coefficient function $f_w(a_L, k)$. Figure 3.8 shows $f_w(a_L, k)$ plotted as a function of time for various time constants T_c where $t=k\Delta t$ and $\Delta t=10$ seconds. For $T_c=2$ months, the predicted covariance of the BLWRS reaches 75% of that of the WRS after one year. Figure 3.9 shows $f_w(a_L, k)$ as a function of the time constant T_c after a one-year simulation with $\Delta t=10$ seconds. As the time constant T_c increases, the covariance coefficient function after one year decreases from one toward

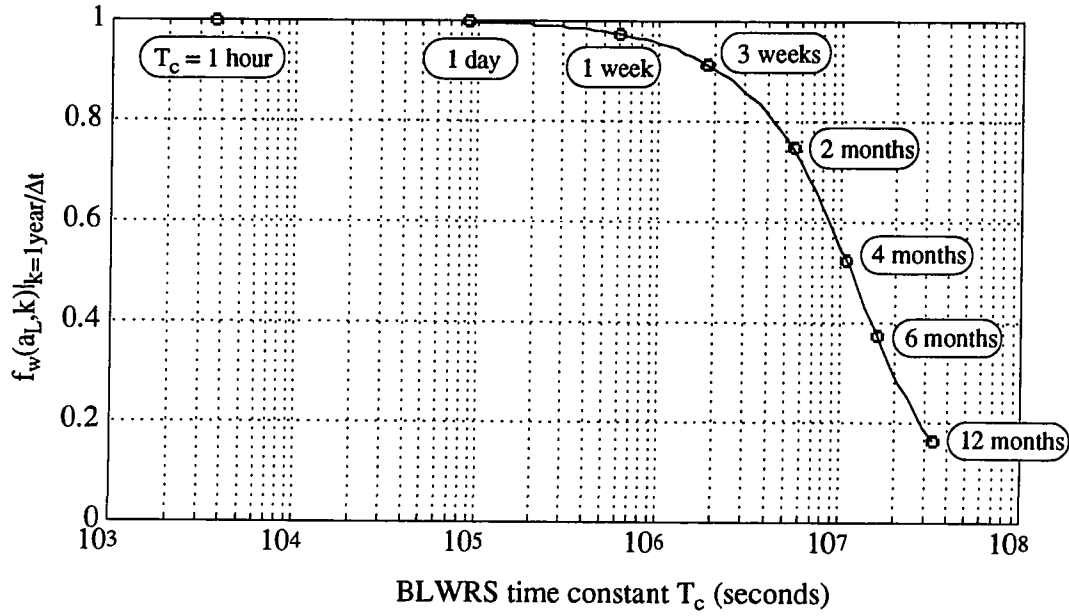


Figure 3.9 Covariance coefficient function vs. T_c after one year ($\Delta t=10$ seconds).

zero. This predicted covariance (Equation 3.41) is used to verify the simulated BLWRS in Section 3.5.2.

Another approach to analyzing the random sequence uses the power spectral density. The PSD function of the BLWRS can be predicted by the transfer functions $L(z)$ and $H(z)$. If we substitute Equation 3.34 into Equation 3.37, we obtain the transfer function from $N(z)$ to $V(z)$ as follows:

$$\frac{V(z)}{N(z)} = L(z)H(z) \quad (3.42)$$

Thus, the PSD function of v_k ($k=1, \dots$) can be derived as follows:

$$\begin{aligned} S_V(f) &= |L(z)H(z)|_{z=\exp(j2\pi f\Delta t)}^2 S_N(f) \\ &= \frac{\alpha_w \Delta t (1 - a_L)^2}{2(1 - \cos 2\pi f \Delta t)(1 + a_L^2 - 2a_L \cos 2\pi f \Delta t)} \end{aligned} \quad (3.43)$$

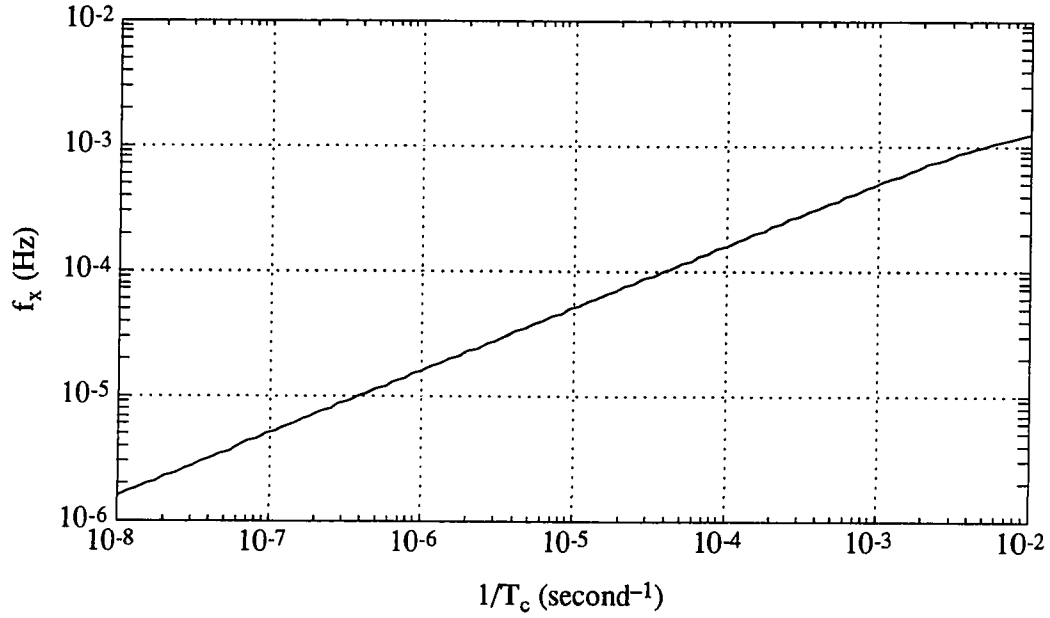


Figure 3.10 Crossover frequency vs. $1/T_c$ of a BLWRS with $\Delta t=10$ seconds, $\alpha_w=0.001$.

The slope of the PSD curve is -80 dB/decade for frequencies higher than the cut-off frequency, and the BLWRS has better attenuation of the undesirable high frequencies than the WRS. The crossover frequency of the BLWRS can be calculated from the predicted PSD as follows:

$$f_x = \frac{f_s}{2\pi} \cos^{-1} \left\{ \frac{1}{4a_L} \left[(1+a_L)^2 - (1-a_L) \sqrt{(1-a_L)^2 + 4\alpha_w \Delta t a_L} \right] \right\} \quad (3.44)$$

where

$$S_v(f) \Big|_{f=f_x} = 1$$

Figure 3.10 shows f_x as a function of $1/T_c$ with $\Delta t=10$ seconds and $\alpha_w=0.001$. In contrast to the crossover frequency of the WRS (Equation 3.36), that of the BLWRS can be chosen arbitrarily by choosing the time constant T_c , even if the other parameters Δt and α_w are unchanged. This additional degree of freedom with the BLWRS is useful when

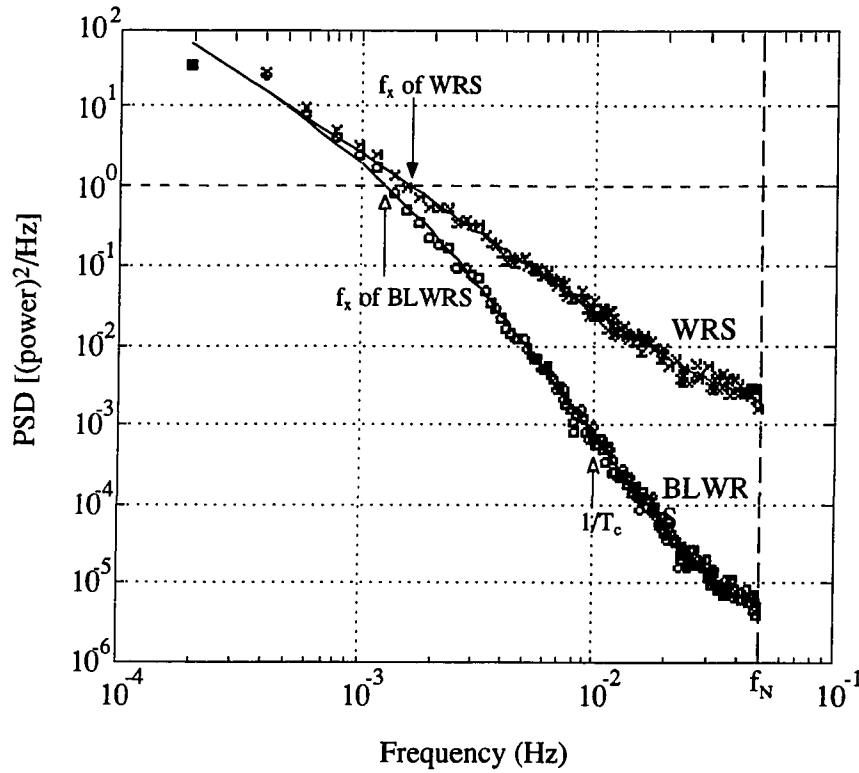


Figure 3.11 Predicted vs. estimated PSD of a WRS and a BLWRS. Solid lines: predicted PSD, x line: estimated PSD of a WRS, o line: estimated PSD of a BLWRS ($T_c=100$ seconds), f_x =crossover frequency, T_c =cutoff time constant.

simulating a Wiener process with a slower crossover frequency. The predicted PSD (Equation 3.43) is used in the next section to verify the simulated BLWRS.

3.5.2 Verification of Simulated BLWRSs

The band-limited Wiener random sequence simulated in the preceding section is verified in terms of the power spectral density and the time history. Figure 3.11 compares the predicted PSD with the estimated PSD from w_k ($k=0, \dots, 16383$) and v_k ($k=0, \dots, 16383$) using the periodogram. The predicted and the estimated PSD curves match very closely, showing that the simulated BLWRS has a valid frequency composition. Figure 3.11 also shows that the BLWRS has a better attenuation of the

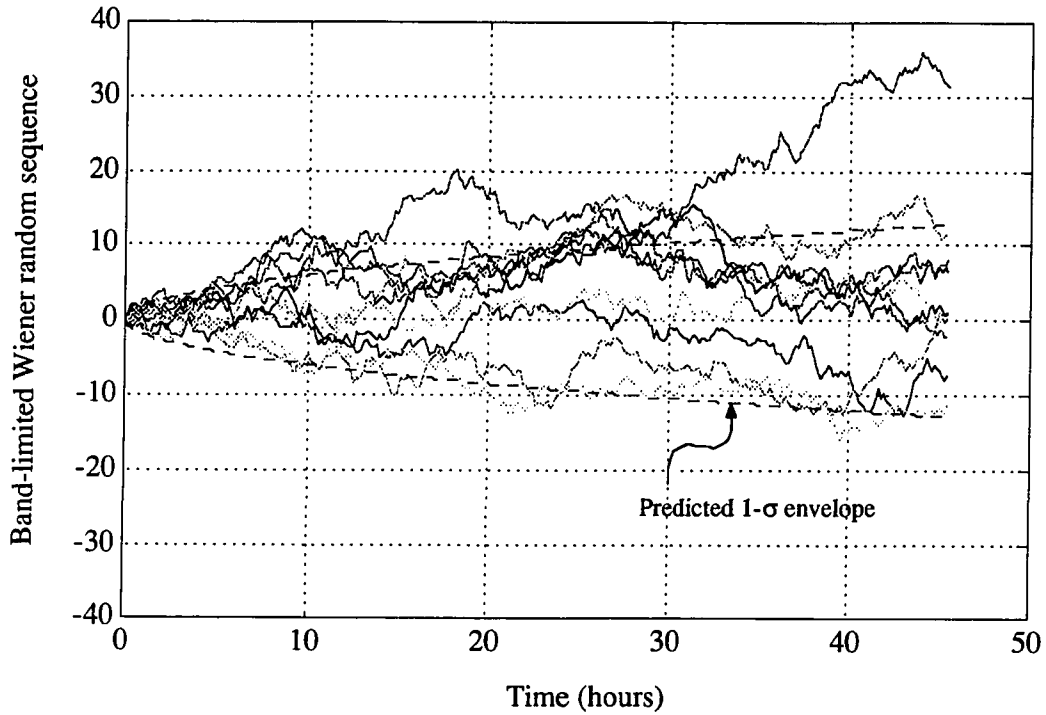


Figure 3.12 Time history of band-limited Wiener random sequence (10 samples).
 $T_c=100$ seconds, $\Delta t=10$ seconds, $\alpha_w=0.001$.

higher frequency components than the WRS and that the crossover frequency of the BLWRS is slower than that of the WRS.

Figure 3.12 shows the time history of ten different samples of v_k ($k=0, \dots, 16383$) with $\Delta t=10$ seconds, $\alpha_w=0.001$, and $T_c=100$ seconds. About 90% of the simulated sequence stays inside of the predicted one-sigma envelopes given by $\pm \sqrt{\alpha_w t f_w(a_L, k)}$. Thus, Figure 3.12 indicates that the simulated BLWRS has a valid covariance.

These two tests verify that the BLWRS generated by Equation 3.38 has the following properties:

- The BLWRS has a zero mean and a covariance that is proportional to time t and is modulated by the covariance coefficient function;

- The frequency components higher than $1/T_c$ are attenuated at -80 dB/decade;
- The crossover frequency f_x is determined by three parameters, that is, the sampling period Δt , covariance coefficient α_w and time constant T_c , which provides a greater degree of freedom in comparison to the WRS.

3.6 Summary of Random Sequence Simulation

Three different classes of random sequence based on the uniformly distributed random sequence were developed: the Gaussian random sequence, Wiener random sequence, and band-limited Wiener random sequence. A computer algorithm for each random sequence was derived and verified in both the time and frequency domains. The properties of each random sequence are summarized in Table 3.2. These random sequences are used in the truth model to simulate random signals such as satellite pointing error, satellite roll phase error, structural creeping, sensor noise, and the proper motion of Rigel. Chapter 4 constructs the truth model that simulates the GP-B science signal including deterministic signals such as the aberration of starlight as well as random signals based on the random number generator developed in this chapter.

Table 3.2 Advantages and Disadvantages of the Three Random Sequences

Class	Notation	Advantages	Disadvantages
Gaussian	$N(0, \sigma)$ (Equation 3.21)	Universally applicable because of the central limit theorem	Unsuitable for band-limited random signals
Wiener	$N(0, \alpha_w k \Delta t)$ (Equation 3.33)	Suitable for time-variant random drift	Weak attenuation of high-frequency components
Band-limited Wiener	$N(0, \alpha_w k \Delta t f_w(a_L, k))$ (Equation 3.41)	Strong attenuation of high-frequency components and flexibility for choosing crossover frequency	Modulated covariance as a function of crossover frequency

CHAPTER 4. TRUTH MODELING

4.1 Introduction

The niobium bird experiment (NbBird) consists of three vital parts: (1) truth modeling, (2) filter synthesis, and (3) experimental verification. The construction of the truth model was a crucial part of the niobium bird experiment in the sense that it would provide a standard for the filter verification process. The purpose of the truth model is to simulate the science gyroscope signal and the telescope signal, which in turn become the inputs to the data reduction scheme. The data reduction scheme processes the simulated gyroscope signal as if it were from the science mission. The results of the data reduction scheme, the estimates of the gyroscope precession rates, are then compared with the true values stored in the truth model to verify the estimation accuracy of data reduction scheme.

Various components of the science signal such as parallax, aberration, and deflection of starlight were analyzed and modeled by R. Vassar (Ref. 7), T. G. Duhamel (Ref. 18), R. S. DiEsposti (Ref. 19), and X. Qin (Ref. 20) in conjunction with the data reduction scheme development, but the niobium bird experiment was the first attempt to integrate those models into one computer program to generate accurate gyro¹ and telescope signals. I wrote the truth model *gpb.c* in C language on the Sun Sparcstation 330. Although I first wrote the program in Pascal on the IBM-PC XT, I converted it into C on the Sparcstation to attain the following benefits:

- Greater speed with the Sun Sparcstation 330 and SunOS C compiler;
- Better optimization with the SunOS C compiler;
- The flexibility of C because of such aspects as the structure and the pointer;
- The prospect of converting to C++.

Once *gpb.c* is compiled into an executable file named *gpb*, one can run the program under SunOS (Version 4.0) which is the UNIX-type operating system provided on Sun Sparcstations. Appendix A explains how to use *gpb* and includes a partial list of programs.

This chapter describes in detail the models used in *gpb.c*, which are based on the standardized coordinate frames developed in Chapter 2 and the random number generators developed in Chapter 3.

4.2 Truth Models

This section defines and explains a model for each gyro signal component. The modeling of each component is based on one of the coordinate frames defined in Chapter 2. After all the models are defined, the science signal equation is derived for the

¹ Hereafter, the terms, *gyro* and *gyroscope*, are used interchangeably.

A-0 frame. All the models listed here are consistent with the truth model program *gpb.c*, which is available on request.

4.2.1 Standard Units

In addition to defining a standardized set of coordinate frames, I defined standard units for the niobium bird truth models in order to avoid combining different models that are expressed in different units. For example, the position of the Earth with respect to the Sun is best described in terms of astronomical units (AUs), while the position of the satellite with respect to the Earth is best described in terms of kilometers. Regarding units of time, relativistic precession rates are best described in terms of arcseconds per year, the roll phase drift in terms of arcseconds per second. Even though each model uses the units best suited to it, the output from each model is converted into standard SI units for consistency. Table 4.1 shows the standard units for the niobium bird truth models. Note that angles are measured in radians instead of arcseconds. Although many error analyses have been conducted using arcseconds, for the niobium bird truth models, the standard unit for measuring angles is the radian because the truth modeling involves an intensive use of trigonometric functions. Table 4.2 shows the conversion factors among different units that are used in *gpb.c*.

Table 4.1 Standard SI Units for the Niobium Bird Truth Models

Parameter	Unit
Time	Seconds
Length	Meters
Angle	Radians
Velocity	Meters per second

Table 4.2 Conversion Factors Among Units

Conversion from	To	Factor
Days	Seconds	24×3600
Years	Seconds	$365.25 \times 24 \times 3600$
AUs	Meters	$1.49597870e11$
Arcseconds	Radians	$\frac{\pi}{180 \times 3600}$

4.2.2 Models of Celestial Motion

Since the pointing control of the GP-B satellite employs the telescope as a primary sensor, and the SQUID pickup loop is body-fixed to the telescope axis, the direction of the gyro spin axis is measured with respect to the telescope axis. As a result, the gyro signal includes observational corrections that are inherent in optical observations of the celestial bodies, such as parallax, aberration, deflection of starlight, and proper motion of the guide star. Except for the proper motion, these observational corrections are each a function of the position and velocity of the observer with respect to the reference point, which, in this case, is the Sun.

In order to model the observational corrections, I had to first model the motion of the observer, that is, the GP-B satellite, with respect to the Sun. The observer's motion was divided into annual and orbital motion. Annual motion is the motion of the Earth with respect to the Sun; orbital motion is the motion of the satellite with respect to the Earth. The models for these two types of motion are presented in the next two sections.

4.2.2.1 *Earth Motion*

The motion of the Earth with respect to the Sun was modeled according to the equations given in *Astronomical Almanac* (Ref. 35). The set of equations given in Table 4.3 yields the apparent coordinates of the Earth with respect to the Sun between 1950 and 2050 to a precision of 0.01° .

Precautions have to be taken when this set is used in computer programs. First, the coordinate frame used for the last set of equations (Equation 4.10), the C-0 frame, has to be converted to the A-0 frame using the rotational matrices given in Chapter 2 because the measurement equation for the filter development is to be developed in the A-0 frame. Second, angles are measured in degrees, which have to be converted to radians. Last, position is measured in AUs, which have to be converted to meters.

The velocity of the Earth with respect to the Sun is obtained by differentiating the last set of equations (Equation 4.10) in Table 4.3. The velocity components of the Earth with respect to the Sun in the C-0 frame, in AUs per day, are shown in Table 4.4. Precautions have to be taken for the velocity terms as well. First, the velocity terms expressed in the C-0 frame (Equation 4.16) have to be converted into the A-0 frame through the rotational matrix ${}^{A_0}T^{C_0}$. Second, the time derivatives of angles are expressed in radians per day instead of degrees per day in order to use the derivatives of trigonometric functions. Last, the velocity terms are expressed in AUs per day, which have to be converted to meters per second.

Table 4.3 Model of Earth's Position with Respect to the Sun

Number of days from J2000.0 (days):

$$n = -4749.5 + \text{day of year} + \text{fraction of day from } 0^h \text{ UT} \quad (4.1)$$

Mean longitude of the Sun, corrected for aberration (degrees):

$$L_s = 280.460^\circ + 0.9856474^\circ n \quad (4.2)$$

Mean anomaly (degrees):

$$g = 357.528^\circ + 0.9856003^\circ n \quad (4.3)$$

Ecliptic longitude (degrees):

$$\lambda = L_s + 1.915^\circ \sin g + 0.020^\circ \sin 2g \quad (4.4)$$

Ecliptic latitude (degrees): $\beta_e = 0^\circ$

$$(4.5)$$

Obliquity of the ecliptic (degrees):

$$\varepsilon = 23.439^\circ - 0.0000004^\circ n \quad (4.6)$$

Right ascension in the same quadrant as λ (degrees):

$$\alpha_s = \tan^{-1}(\cos \varepsilon \tan \lambda) \quad (4.7)$$

Declination (degrees): $\delta = \sin^{-1}(\sin \varepsilon \sin \lambda)$

$$(4.8)$$

Distance of the Earth from the Sun (AUs):

$$r_{es} = 1.00014 - 0.01671 \cos g - 0.00014 \cos 2g \quad (4.9)$$

Equatorial rectangular coordinates of the Earth² in the C-0 frame (AUs):

$$\begin{aligned} x &= -r_{es} \cos \lambda \\ y &= -r_{es} \cos \varepsilon \sin \lambda \\ z &= -r_{es} \sin \varepsilon \sin \lambda \end{aligned} \quad (4.10)$$

² Equation 4.10 shows the position of the Earth with respect to the Sun, while the Astronomical Almanac (Ref. 35) gives the position of the Sun with respect to the Earth. Thus, in Equation 4.10, the signs are positive.

Table 4.4 Model of Earth's Velocity with Respect to the Sun

Time derivative of the mean longitude of the Sun (radians/day):

$$\dot{L}_s = 0.0172027923 \quad (4.11)$$

Time derivative of the mean anomaly (radians/day):

$$\dot{g} = 0.0172019703 \quad (4.12)$$

Time derivative of the ecliptic longitude (radians/day):

$$\dot{\lambda} = \dot{L}_s + 0.03342306\dot{g}\cos g + 0.00069813\dot{g}\cos 2g \quad (4.13)$$

Time derivative of the obliquity of the ecliptic (radians/day):

$$\dot{\epsilon} = 6.9813170\text{e-}9 \quad (4.14)$$

Time derivative of the distance from the Sun to the Earth (AUs/day):

$$\dot{r}_{es} = 0.01671\dot{g}\sin g + 0.00028\dot{g}\sin 2g \quad (4.15)$$

Velocity components of Earth with respect to the Sun in the C-0 frame (AUs/day):

$$\begin{aligned} \dot{x} &= -\dot{r}_{es}\cos\lambda + r_{es}\dot{\lambda}\sin\lambda \\ \dot{y} &= -\dot{r}_{es}\cos\epsilon\sin\lambda + r_{es}\dot{\epsilon}\sin\epsilon\sin\lambda - r_{es}\dot{\lambda}\cos\epsilon\cos\lambda \\ \dot{z} &= -\dot{r}_{es}\sin\epsilon\sin\lambda - r_{es}\dot{\epsilon}\cos\epsilon\sin\lambda - r_{es}\dot{\lambda}\sin\epsilon\cos\lambda \end{aligned} \quad (4.16)$$

4.2.2.2 Satellite Orbital Motion

As described in Section 1.2.2, the nominal orbit for the GP-B program was determined to be a polar orbit. Table 4.5 lists the nominal orbital elements: altitude, inclination, eccentricity, and right ascension of the GP-B satellite.

Table 4.5 Nominal Orbital Elements for the GP-B Satellite

Nominal altitude:	$\bar{\rho}_{ve} = 650km$	(4.17)
Nominal inclination:	$\bar{i}_{ve} = 90^\circ$	(4.18)
Nominal eccentricity:	$\bar{e}_{ve} = 0$	(4.19)
Nominal right ascension:	$\bar{\Omega}_{ve} = \lambda_R$	(4.20)

The nominal values for the orbital altitude and eccentricity were chosen by considering the trade-off between a larger precession rate and a smaller atmospheric drag on the satellite. As indicated by Equation 1.1, a lower altitude results in a larger relativistic precession rate, and thus a larger signal-to-noise ratio. But it also results in a larger atmospheric drag, which in turn requires larger thrust to overcome the drag and reduces the dewar lifetime. The nominal altitude of 650 kilometers was chosen for the GP-B satellite to balance the larger signal-to-noise ratio and the smaller atmospheric drag. Similarly, the nominal orbit was designated as circular, because a circular orbit yields the minimum net atmospheric drag with a constant mean altitude.

Given these nominal orbital elements, the idealized satellite position and velocity were simulated in the orbital frame C-2 as described in Table 4.6. The orbital initial phase was chosen so that Rigel will be occulted by the Earth when the experiment is started. Figure 4.1 shows the nominal orbit, along with the A-0 frame³.

³ Note that the origin of A-0 is the barycenter and that of C-2 is the geocenter even though they are shown together.

Table 4.6 Nominal Satellite Position and Velocity

Nominal orbital radius (meters):

$$r_{ve} = R_{\oplus} + \bar{\rho}_{ve} = 7021000.7900 \quad (4.21)$$

where

R_{\oplus} : mean radius of the Earth

Nominal orbital rate (radians/second):

$$n_{ve} = \sqrt{\frac{\mu_{\oplus}}{r_{ve}^3}} = 1.07317460376 \times 10^{-3} \quad (4.22)$$

where

μ_{\oplus} : gravitational constant of the Earth

Initial phase of the nominal orbit (radians):

$$\omega_{ve}(t_0) = \pi \quad (4.23)$$

where

t_0 : time of mission initialization

Nominal satellite position in the C-2 frame (meters):

$$\frac{\vec{r}_{ve}}{C2} = \begin{bmatrix} r_{ve} \sin[n_{ve}(t - t_0) + \omega_{ve}(t_0)] \\ 0 \\ r_{ve} \cos[n_{ve}(t - t_0) + \omega_{ve}(t_0)] \end{bmatrix}_{C-2} \quad (4.24)$$

Nominal satellite velocity in the C-2 frame (meters/second):

$$\frac{\vec{v}_{ve}}{C2} = \begin{bmatrix} n_{ve} r_{ve} \cos[n_{ve}(t - t_0) + \omega_{ve}(t_0)] \\ 0 \\ n_{ve} r_{ve} \sin[n_{ve}(t - t_0) + \omega_{ve}(t_0)] \end{bmatrix}_{C-2} \quad (4.25)$$

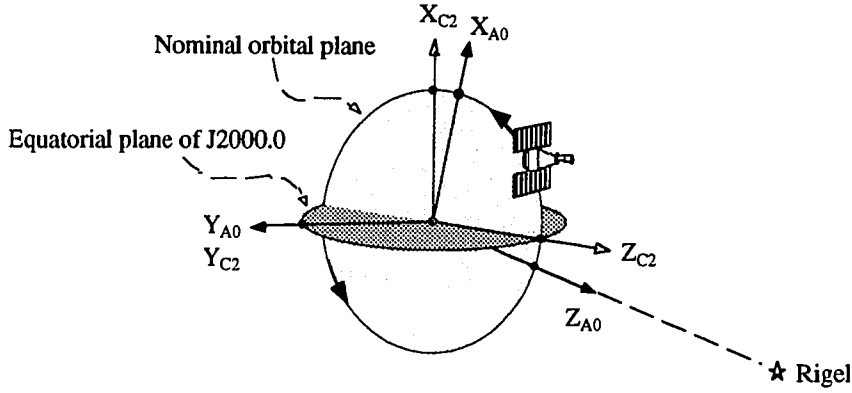


Figure 4.1 Nominal GP-B satellite orbit.

The satellite orbital elements presented in Table 4.5 provide the nominal values about which the orbital perturbation is calculated. P. Axelrad (Ref. 9) investigated the orbital perturbation caused by the Earth's noncentral gravitational field, the gravitational fields of the Sun and the Moon, the precession of the equinoxes, and the residual drag of the spacecraft. Axelrad calculated the orbital perturbation of eccentricity, δe_{ve} , inclination, δi_{ve} , and right ascension, $\delta \Omega_{ve}$, both for the short term and the long term. Axelrad also provided the MATLAB file *outsim.m*, which calculates δi_{ve} and $\delta \Omega_{ve}$. The actual inclination and right ascension corrected for the long-term perturbations are as follows:

$$i_{ve} = \bar{i}_{ve} + \delta i_{ve} \quad (4.26)$$

$$\Omega_{ve} = \bar{\Omega}_{ve} + \delta \Omega_{ve} \quad (4.27)$$

where δi_{ve} and $\delta \Omega_{ve}$ are calculated by *outsim.m*. The actual inclination and right ascension were then substituted into the rotational matrix ${}^2C^1$ (Equation 2.12).

Since I did not consider the perturbation of the eccentricity, the eccentricity stays at the nominal value throughout the simulation. Therefore, the orbit is always circular,

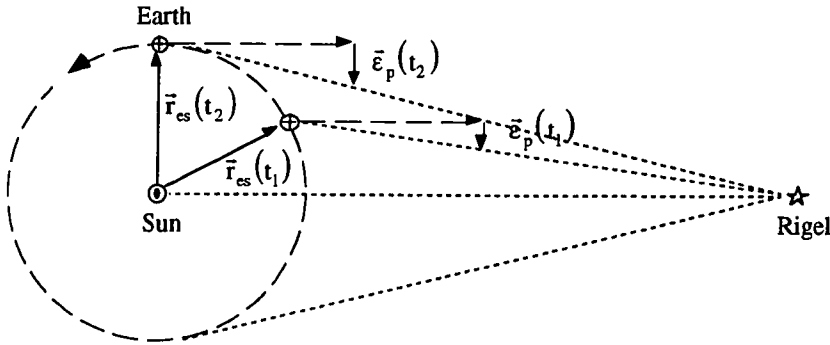


Figure 4.2 Parallax caused by the position of the Earth with respect to the Sun.

and the nominal position and velocity equations (Equations 4.24 and 4.25) still hold in the C-2 frame, which is corrected for δi_{ve} and $\delta \Omega_{ve}$. Similar to the Earth's motion, the satellite motion has to be expressed in the A-0 frame because the measurement equation is to be developed in that frame. The rotation is completed through the two rotational matrices ${}^2C^1$ and ${}^{A0}T^{C0}$.

4.2.2.3 Parallax of Rigel

The parallax is caused by the position of the observer relative to the Sun (Ref. 36). As the observer moves away from the line drawn from the Sun to Rigel (the line of sight to Rigel observed from the Sun), the parallax angle increases as shown in Figure 4.2. The observational correction caused by the parallax is included in the rotational matrices ${}^iA^0$ ($i=2,\dots,6$) and is represented by the parallax vector \bar{e}_p as described in Section 2.3.1 [see Table 2.6]. Table 4.7 defines the parallax vector in radians.

The position of the observer is approximated by the position of the Earth, since the contribution from the position of the observer with respect to the Earth is less than 10^{-2} milliarcsecond for the GP-B orbit at the altitude of 650 kilometers [see Table 4.10]. Note that the equation (Equation 4.28) is expressed in the form of a vector and has to be

coordinated in the A-0 frame. Thus, the position vector of the Earth has to be expressed in the A-0 frame.

Table 4.7 Equation for the Parallax Model

Parallax observational correction (radians):

$$\begin{aligned}
 \vec{\varepsilon}_p &= -\frac{\vec{r}}{R} \\
 &= -\alpha \frac{\vec{r}}{R_{es}} \\
 &= -\alpha \left(\frac{\vec{r}_{es}}{R_{es}} + \frac{\vec{r}_{ve}}{R_{es}} \right) \\
 &\approx -\alpha \frac{\vec{r}_{es}}{R_{es}}
 \end{aligned} \tag{4.28}$$

where

$$\alpha \equiv \frac{R_{es}}{R}$$

α : parallax coefficient

R: distance from the Sun to Rigel

R_{es} : astronomical unit (1 AU)

\vec{r}_{es} : position vector of the Earth with respect to the Sun

\vec{r}_{ve} : position vector of the GP-B satellite with respect to the Earth

4.2.2.4 Aberration

In contrast to the parallax, the aberration is caused by the velocity of the observer perpendicular to the line of sight to the guide star—Rigel (Ref. 36). The light from the guide star travels at a speed of light, while the observer itself moves with respect to the guide star with a finite velocity. Because of this observer motion, an observational correction called *aberration* is created in the optical direction of the guide star [see

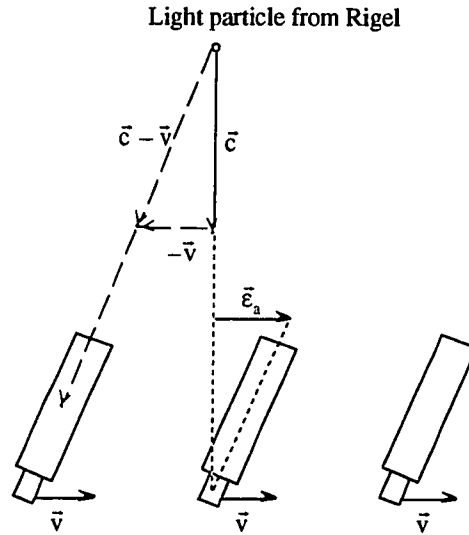


Figure 4.3 Aberration caused by observer's velocity.

Figure 4.3]. The observational correction caused by the aberration is included in the rotational matrices ${}^iA^0$ ($i=3,\dots,6$) and is represented by the aberration vector \bar{e}_a as described in Section 2.3.1 [see Table 2.6]. Table 4.8 defines the aberration vector in radians.

The first term is a sinusoidal component at the annual frequency called *annual aberration*. Similarly, the second term is a sinusoidal component at the orbital frequency and called *orbital aberration*. The first term has a magnitude of about 20 arcseconds, the second term about 5 arcseconds for the GP-B orbit [see Table 4.10]. As does the parallax vector, the aberration vector has to be expressed in the A-0 frame, which implies that the velocity vectors of the Earth and the satellite have to be expressed in that frame as well.

Duhamel pointed out that the higher order terms of the aberration of starlight in v/c could be calculated from special relativity and that the second-order term could not be neglected for this experiment (Ref. 18). Duhamel presented the formula for the aberration calculated from special relativity as follows:

Table 4.8 Equation for the Aberration Model

Aberration observational correction (radians):

$$\begin{aligned}\bar{\epsilon}_a &= \frac{\bar{v}}{c} \\ &= \frac{\bar{v}_{es}}{c} + \frac{\bar{v}_{ve}}{c}\end{aligned}\quad (4.29)$$

where

- c : speed of light in vacuum
- \bar{v}_{es} : velocity vector of the Earth with respect to the Sun
- \bar{v}_{ve} : velocity vector of the GP-B satellite with respect to the Earth

$$\Delta\theta_a = \beta \sin \theta - \frac{\beta^2}{4} \sin 2\theta - \frac{\beta^3}{6} \sin \theta (1 + 2 \cos^2 \theta) \quad (4.30)$$

where

$$\begin{aligned}\beta &\equiv \frac{v}{c} \\ \theta &\equiv \cos^{-1} \left(-\frac{\bar{c} \cdot \bar{v}}{cv} \right)\end{aligned}$$

Duhamel showed that the second term of Equation 4.30 was 0.5 milliarcsecond for the annual aberration and 0.03 milliarcsecond for the orbital aberration. The second order term of the annual aberration is larger than the required estimation accuracy and, thus, cannot be neglected. For the niobium bird experiment, to simplify the equation, this second-order term was not included in the truth model, but the term has to be corrected for the actual science mission. Duhamel also suggested that the Earth's velocity could be obtained by the JPL ephemeris DE96 to a precision of 10 cm per second which corresponds to an error in aberration of 0.07 milliarcsecond. The model of the Earth's

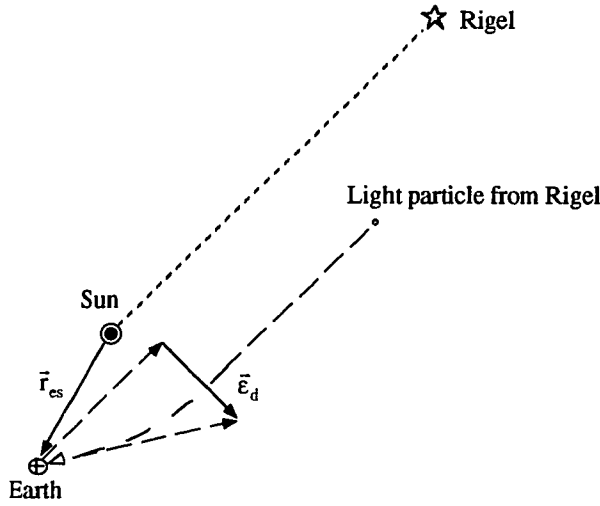


Figure 4.4 Deflection of starlight caused by the Sun's gravity. The treatment of the light as a particle explains only a half of the effect. General relativity explains the other half.

motion of the niobium bird experiment does not use this precise ephemeris but uses an approximated model as shown in Section 4.2.2.1. Using the approximate model does not hinder the main objective of the niobium bird experiment, because the data reduction scheme can still be verified as long as the truth model provides a realistic reference against which the estimation results are compared.

4.2.2.5 Deflection of Starlight

The third observational correction, the deflection of starlight, is predicted by the General Theory of Relativity, as were the geodetic and frame-dragging precessions of spinning gyros. If we consider the light from the guide star as a traveling particle, we can say that it undergoes gravitational forces as a point mass [see Figure 4.4]. If the observer is measuring the optical direction of the guide star from an Earth-orbiting satellite as in the GP-B program, the observer receives the light after the large masses in the solar system, such as the Sun, Jupiter, and Saturn, have deflected the trajectory of the light

particle. This explains only half of the deflection of starlight. General relativity⁴ explains the other half of the deflection of starlight, which is related to the space curvature around the Sun. V. A. Brumberg (Ref. 37) predicted the amount of deflection caused by the solar mass; the equation Brumberg derived is shown in Table 4.9. The deflection of starlight vector is divided into components of the A-0 frame. Note that the z component is constant and does not have any effect on the telescope pointing, even though it is shown along with the x and y components.

Table 4.9 Equation for the Deflection of Starlight Model

Deflection of starlight observational correction (radians):

$$\begin{aligned}\bar{\epsilon}_d &= \kappa \frac{R_{es}}{r_{es}} \left[\bar{z}_{A0} + \frac{\bar{z}_{A0} \times (\bar{r}_{es} \times \bar{z}_{A0})}{r_{es} - (\bar{z}_{A0} \cdot \bar{r}_{es})} \right] \\ &= \left[\begin{array}{c} \kappa \frac{R_{es}}{r_{es}} \frac{\bar{r}_{es} \cdot \bar{x}_{A0}}{r_{es} - (\bar{z}_{A0} \cdot \bar{r}_{es})} \\ \kappa \frac{R_{es}}{r_{es}} \frac{\bar{r}_{es} \cdot \bar{y}_{A0}}{r_{es} - (\bar{z}_{A0} \cdot \bar{r}_{es})} \\ \kappa \frac{R_{es}}{r_{es}} \end{array} \right]_{A-0}\end{aligned}\quad (4.31)$$

where

$$\kappa \equiv \frac{2m_s}{R_{es}}$$

κ : coefficient of deflection of starlight

m_s : gravitational radius of the Sun

R_{es} : astronomical unit (1 AU)

r_{es} : distance from the Sun to the Earth

\bar{r}_{es} : position vector of the Earth with respect to the Sun

$\bar{x}_{A0}, \bar{y}_{A0}, \bar{z}_{A0}$: unit vectors of the A-0 frame

⁴ L. I. Schiff argued that the deflection of starlight can be explained by special relativity and thus did not provide proof for general relativity (Ref. 8).

4.2.2.6 Proper Motion of Rigel

The last effect, the proper motion of the guide star, is caused by the motion of the guide star itself with respect to distant galaxies. The proper motion of Rigel was investigated by J. T. Anderson and C. W. F. Everitt (Ref. 38), and the result was presented in R. Vassar (Ref. 7). The best estimate they obtained had an uncertainty of 1.7 milliarcseconds per year in the east-west direction and 0.9 milliarcsecond per year in the north-south direction in rms (1σ). The proper motion of Rigel over two years can also be expanded in a Taylor series as follows:

$$\bar{\epsilon}_r(t) = \bar{\epsilon}_r(t_0) + \left. \frac{d\bar{\epsilon}_r}{dt} \right|_{t_0} (t - t_0) + \left. \frac{d^2\bar{\epsilon}_r}{dt^2} \right|_{t_0} (t - t_0)^2 + \dots$$

for $0 \leq t \leq 2$ years (4.32)

The first-order term in $(t-t_0)$, unfortunately, cannot be distinguished from the relativistic precession terms by the Kalman filter because the relativistic precession terms are also linear in time. Thus, the first-order term of Rigel's proper motion has to be calibrated by a separate measurement or experiment. Since the main focus of the niobium bird experiment is on the experimental verification of the Kalman filters, the proper motion of Rigel was not modeled in the simulation program *gpb.c*.

4.2.2.7 Summary of Observational Corrections

The four observational corrections discussed in the previous section, parallax, aberration, deflection of starlight, and the proper motion of Rigel, are summarized in Table 4.10 (Ref. 39), which shows approximate magnitude of each error except the proper motion.

Table 4.10 Summary of Observational Corrections

Observational Corrections	Magnitude
Annual parallax	0.003 arcsecond
Orbital parallax	0.002 milliarcsecond
Annual aberration	20.7 arcseconds
Orbital aberration	5.4 arcseconds
Deflection of starlight caused by the Sun	0.014 arcsecond
Deflection of starlight caused by Jupiter ⁵	0.004 milliarcsecond

4.2.3 Structural Model of SQUID Readout System

The structural models of the readout apparatus such as the quartz housings, the quartz block, and the SQUID readout loops, are developed in this section. Since the accuracy requirement on the precession estimate is on the order of 0.1 milliarcsecond per year, structural misalignment and creeping play important parts in the error budget. The following sections describe the models for a stationary misalignment and a time-variant misalignment of the gyro pickup loops.

4.2.3.1 Misalignment of Gyro Pickup Loop

The nominal alignment of the SQUID pickup loops is defined with respect to the nominal control frame B-0. For gyros #1 and #2, the nominal pickup loop plane is parallel to the yz plane of the B-0 frame. Similarly, for gyros #3 and #4, the nominal pickup loop plane is parallel to the xz plane of the B-0 frame. Any orientation error of

⁵ The deflection of starlight caused by Jupiter's gravity was estimated by R. Vassar (Ref. 7).

the pickup loop with respect to the nominal alignment is defined as a misalignment of the pickup loop and is modeled in this section.

Pickup loop misalignment can be categorized as longitudinal and lateral misalignment. Longitudinal misalignment is defined as a rotational misalignment of the pickup loop plane about the z_{B0} axis. It has the same effect on the Kalman filtering as roll phase bias does. In other words, the Kalman filter cannot distinguish longitudinal misalignment from roll phase bias. Lateral misalignment, on the other hand, is defined as a rotational misalignment of the pickup loop plane about the y_{B0} axis for the gyros #1 and #2, and about the x_{B0} axis for the gyros #3 and #4, respectively. Lateral misalignment has the same effect on the Kalman filtering as the gyro readout bias does. In other words, the Kalman filter cannot distinguish lateral misalignment from the gyro readout bias.

The GP-B Twelve Science Requirements (Ref. 40) suggests the following requirements on the accuracy of the pickup loop alignment:

- Pickup loops for gyros #1 and #2 should be parallel to each other to within 10 arcseconds and measured within 3 arcseconds; the same should be true for gyros #3 and #4;
- Pickup loops #1 and #2 should each be perpendicular to pickup loops #3 and #4 to within 10 arcseconds and measured to within 5 arcseconds.

In terms of estimating the relativistic precessions, the longitudinal and lateral misalignments are not corruptive errors since they are included in the estimates of the roll phase bias and the gyro readout bias, respectively. Thus, the requirements on the pickup loop alignments could be looser as long as the misalignments were calibrated to 3 arcseconds. This claim is verified in Section 4.3.1, where the measurement equation is constructed.

4.2.3.2 Structural Creeping of the Gyro Pickup Loop

Structural creeping is structural deformation of the readout apparatus as a function of time. Even though quartz is a very stable material in terms of temperature and aging, modeling of structural creeping is important because of the required accuracy of the estimation. I modeled the structural creeping of the gyro readout structure using the band-limited Wiener random sequence with a time constant of a few months. Similar to the pickup loop misalignment, structural creeping can be categorized into longitudinal and lateral creeping. Longitudinal creeping is sensed as a roll phase drifting by the Kalman filter and can be estimated by adding a process noise to the phase offset state. Lateral creeping has the same effect as the bias drift to the Kalman filter and can be estimated by adding a process noise to the bias state. This claim is also verified in Section 4.3.1, where the measurement equation is constructed. The simulation model for

Table 4.11 Models for the Structural Misalignment and Creeping of Gyro Readout

Lateral misalignment and creeping for gyro #1 or #2:

$$\delta\theta_R = \delta\theta_{R0} + \delta\theta_R(t) \quad (4.33)$$

Lateral misalignment and creeping for gyro #3 or #4:

$$\delta\phi_R = \delta\phi_{R0} + \delta\phi_R(t) \quad (4.34)$$

Longitudinal misalignment and creeping:

$$\delta\psi_R = \delta\psi_{R0} + \delta\psi_R(t) \quad (4.35)$$

where

$\delta\phi_{R0}, \delta\theta_{R0}, \delta\psi_{R0}$ initial misalignment terms
 $\delta\phi_R(t), \delta\theta_R(t), \delta\psi_R(t)$ band-limited Wiener random sequences
with following parameters:
 $\alpha_w = 1 \times 10^{-3}$ (arcsecond / $\sqrt{\text{year}}$)
 $\Delta t = 10$ (second)
 $T_c = 1$ (month)

the structural misalignment and creeping is given in Table 4.11. The constant terms represent the initial misalignment, and the time-variant terms represent the creeping. Even though longitudinal and lateral creeping have different stability, I used the same parameters to simulate them for this thesis. Longitudinal creeping may have much worse stability than lateral creeping because it is referenced by the star blipper, which is mounted on the outside of the dewar and subject to heat expansion of the structure. Hence, longitudinal creeping must be analyzed and modeled more carefully for further investigations.

4.2.4 Models of the Satellite Dynamic

The dynamic behavior of the GP-B satellite has been investigated by N. J. Kasdin (Ref. 26) and J. R. Crier (Ref. 11). Kasdin designed the pointing controller, and Crier designed the roll phase controller for the GP-B satellite. Because the numerical integration of equations of motion requires extensive computational time, the truth model does not include the dynamic models of the satellite but only the stochastic models of the pointing and roll phase control errors. The next two sections describe the stochastic models for the pointing and roll phase control of the GP-B satellite.

4.2.4.1 Pointing Control

The GP-B Twelve Science Requirements (Ref. 40) suggests that the satellite pointing accuracy should be within 20 milliarcseconds rms about the optical direction of Rigel during Rigel valid (explained in Section 4.3.2.1) and within 2 arcseconds rms during Rigel invalid. N. J. Kasdin (Ref. 26) demonstrated that the required pointing accuracy during Rigel valid can be achieved by using a pointing controller with the telescope as a sensor and a controller band-width of about 0.2 Hz.

Telescope pointing error was modeled by a band-limited white noise with zero mean, 20 milliarcseconds rms, and a time constant of 2 seconds. The pointing errors in the x_{A0} direction and y_{A0} direction were assumed to be uncorrelated and were updated every 0.5 second in the truth model by the difference equations given in Table 4.12.

Table 4.12 Model of Satellite Pointing Error

Initial conditions:

$$\begin{aligned}\phi_r(0) &= 0 \\ \theta_r(0) &= 0\end{aligned}\tag{4.39}$$

Differential equations:

$$\begin{aligned}\phi_r(k+1) &= a_p \phi_r(k) + c_p (1 - a_p) n_1(k) \\ \theta_r(k+1) &= a_p \theta_r(k) + c_p (1 - a_p) n_2(k)\end{aligned}\quad (k=0, \dots)\tag{4.40}$$

where

$\phi_r(k)$: k -th sample of the telescope pointing error in the x_{A0} direction ($k=0, \dots$);

$\theta_r(k)$: k -th sample of the telescope pointing error in the y_{A0} direction ($k=0, \dots$);

$n_1 = N(0,1)$ independent GRS;

$n_2 = N(0,1)$ independent GRS;

$$a_p \equiv \exp\left(-\frac{\Delta t_p}{T_{cp}}\right)$$

$$c_p \equiv \sqrt{\frac{1+a_p}{1-a_p}} \sigma_p$$

$\Delta t_p = 0.5$ pointing model update period (seconds);

$T_{cp} = 2.0$ pointing model time constant (seconds);

$\sigma_p = 0.020$ expected rms error (arcseconds)

4.2.4.2 Roll Phase Control

The GP-B Twelve Science Requirements (Ref. 40) suggests that the satellite roll phase control accuracy should be within 10 arcseconds (rms) and that the roll frequency should be accurate to one part in 10^4 . J. R. Cerie (Ref. 11) designed the roll phase controller and demonstrated that the roll phase could be controlled within 10 arcseconds. I assumed zero mean, 10 arcseconds (rms) error in the roll phase with a time constant of 10 seconds.

I modeled the roll phase error using a band-limited white noise with zero mean, 10 arcseconds rms, and a time constant of 10 seconds. I updated the model every second in the truth model using the difference equation given in Table 4.13.

Table 4.13 Model of the Satellite Roll Phase Error

Initial condition:	$\delta\psi_r(0) = 0$	(4.41)
Difference equation:	$\delta\psi_r(k+1) = a_r\delta\psi_r(k) + c_r(1-a_r)n_3(k) \quad (k=0,\dots)$	(4.42)
where		
$\delta\psi_r(k)$:	k-th sample of the roll phase control error (k=0,...);	
$n_3 = N(0,1)$	independent GRS;	
$a_r \equiv \exp\left(-\frac{\Delta t_r}{T_{cr}}\right)$		
$c_r \equiv \sqrt{\frac{1+a_r}{1-a_r}}\sigma_r$		
$\Delta t_r = 1.0$	roll model update period (seconds);	
$T_{cr} = 10.0$	roll model time constant (seconds);	
$\sigma_r = 10.0$	expected rms error (arcseconds)	

4.2.5 Model of Satellite Data Acquisition

I modeled the noise characteristics of the satellite data acquisition hardware, including the SQUID magnetometer and the A-to-D converter, to develop the data reduction scheme. Since the main objective of the niobium bird experiment is to verify the data reduction scheme with actual readout hardware, the models for the SQUID sensor and the A-to-D converter were constructed strictly for the debugging of data reduction programs. Before the data reduction programs were applied to the actual niobium bird data, they were tested with a simulated SQUID noise and a model of an A-to-D converter. The next two sections describe the SQUID noise model and the A-to-D converter model used in the simulation.

4.2.5.1 SQUID Magnetometer

I modeled the sensor noise of the SQUID magnetometer to evaluate the data reduction scheme before I applied the scheme to the actual experimental data. Accurate modeling of the SQUID sensor noise was critical in evaluation because R. Vassar (Ref. 7) determined that the SQUID noise was the dominant error for the data reduction. This section describes the modeling procedure that I employed to simulate the SQUID noise.

The SQUID noise generally has a $1/f$ power spectral density for the lower frequencies and a flat power spectral density for the higher frequencies; typical noise power spectral densities of several SQUIDs are shown in Figure 1.5. The corner frequency typically ranges from 0.1 Hz to 1 Hz. DiEsposti modeled the SQUID noise with a three-pole linear filter (Ref. 19), and Qin used DiEsposti's model for his error analysis. N. J. Kasdin (Ref. 26) developed a more precise model of the $1/f$ noise. I simulated the SQUID noise with a combination of a four-pole $1/f$ shaping filter and a band-limited Wiener random sequence [see Figure 4.5], as given by the following equation:

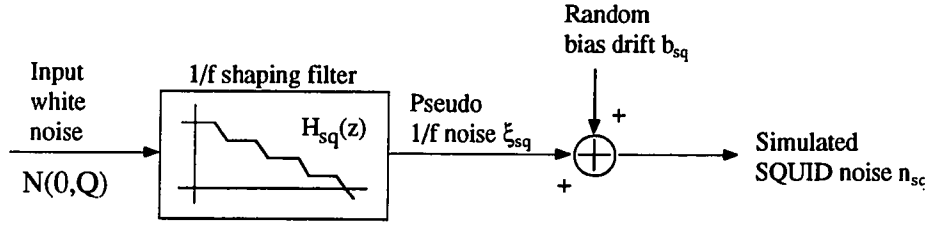


Figure 4.5 SQUID sensor noise simulation.

$$n_{sq} = \xi_{sq} + b_{sq} \quad (4.43)$$

where

ξ_{sq} : pseudo $1/f$ noise term

b_{sq} : bias drift term

The background white noise over the corner frequency was not simulated in the niobium bird experiment because the Nyquist frequency⁶ was below the corner frequency. The band-limited Wiener random sequence was added to simulate the dc drift because the $1/f$ shaping filter has a finite dc gain. The next two sections describe the $1/f$ shaping filter and the dc drift term.

1/f Shaping Digital Filter

I first designed an analog $1/f$ shaping filter, matching the gain at the roll frequency to 0 dB, and then converted it to a digital filter by Van Loan's algorithm (Ref. 41, 42). Continuous $1/f$ noise $\xi_{sq}(t)$ was simulated by white noise $n_a(t)$ and a shaping filter $H_{sq}(s)$ as follows:

⁶ The nominal sampling rate for the niobium bird experiment is 0.1 Hz, and, therefore, the Nyquist frequency is 0.05 Hz, which is lower than the typical corner frequency of SQUID noise. Thus, the background white noise is attenuated by the anti-alias lowpass filter and does not affect the data reduction scheme.

$$\frac{\Xi_{sq}(s)}{N_a(s)} = H_{sq}(s) \quad (4.44)$$

where

$$\begin{aligned} \Xi_{sq}(s) &\equiv L[\xi_{sq}(t)] \\ N_a(s) &\equiv L[n_a(t)] \end{aligned}$$

$$H_{sq}(s) = \frac{k_{sq}(s - z_1)(s - z_2)(s - z_3)}{(s - p_1)(s - p_2)(s - p_3)(s - p_4)}$$

$$k_{sq} = 5.19126$$

$$z_1 = 6\pi \times 10^{-4}, z_2 = 6\pi \times 10^{-3}, z_3 = 6\pi \times 10^{-2}$$

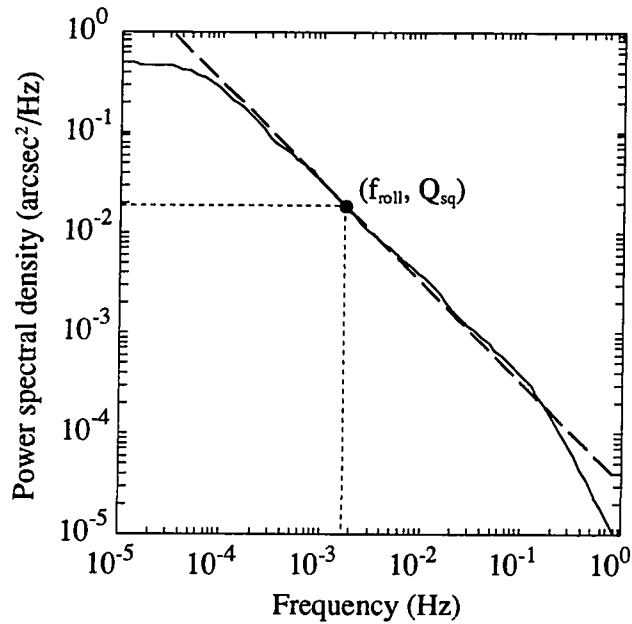
$$p_1 = 2\pi \times 10^{-4}, p_2 = 2\pi \times 10^{-3}, p_3 = 2\pi \times 10^{-2}, p_4 = 2\pi \times 10^{-1}$$

Figure 4.6 (a) shows the power response $|H_{sq}(s)|_{s=j\omega}^2$, which approximates the 1/f power spectral density. The locations of poles and zeros were determined by trial and error to satisfactorily fit the power spectral density to the 1/f power. The coefficient k_{sq} was chosen so that the gain at the roll frequency would be unity. Thus, $\xi_{sq}(t)$, the output of $H_{sq}(s)$ is a pseudo 1/f noise given an input white noise $n_a(t)$. I assumed a 5-hour SQUID noise to determine the power spectral density of the input white noise. The SQUID magnetometer with a 5-hour integration time gives a 1-milliarcsecond resolution at the roll frequency after 5 hours of averaging (Ref. 43). Thus, the power spectral density of the input white noise is given by the following equation:

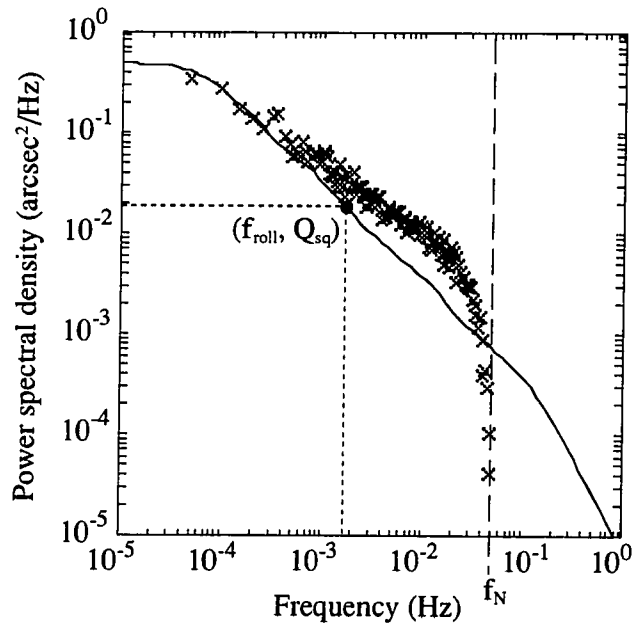
where

$$n_a(t) = N(0, Q_{sq}) \quad (4.45)$$

$$\begin{aligned} Q_{sq} &= (1 \times 10^{-3} \text{ (arcsecond)})^2 \times (5 \times 3600 \text{ (second)}) \\ &= 0.018 \text{ arcsecond}^2 / \text{Hz} \end{aligned}$$



(a) Power spectral density of output process of continuous shaping filter (solid line) vs. ideal $1/f$ noise (dashed line).



(b) Predicted power spectral density (solid line) vs. power spectral density of simulated $1/f$ noise (x's). The Nyquist frequency was 0.05 Hz because the sampling period was 10 seconds.

Figure 4.6 Power spectral density of ideal $1/f$ noise, four-pole shaping filter, and simulated $1/f$ noise with $f_s=0.1$ Hz.

The analog shaping filter (Equation 4.44) was then expressed in a state-space format as follows:

$$\begin{aligned}\dot{x}_{sq}(t) &= F_{sq}x_{sq}(t) + G_{sq}n_a(t) \\ \xi_{sq}(t) &= H_{sq}x_{sq}(t)\end{aligned}\quad (4.46)$$

where

$$F_{sq} = \begin{bmatrix} -6.9806 \times 10^{-1} & 1.0 & 0 & 0 \\ -4.4259 \times 10^{-2} & 0 & 1.0 & 0 \\ -2.7558 \times 10^{-4} & 0 & 0 & 1.0 \\ -1.5585 \times 10^{-7} & 0 & 0 & 0 \end{bmatrix}, \quad G_{sq} = \begin{bmatrix} 1.2081 \times 10^{-1} \\ 2.5276 \times 10^{-2} \\ 4.7645 \times 10^{-4} \\ 8.0908 \times 10^{-7} \end{bmatrix}, \quad H_{sq} = \begin{bmatrix} 1.0 \\ 0 \\ 0 \\ 0 \end{bmatrix}^T$$

Table 4.14 Pseudo-1/f-Noise Model for a 5-Hour SQUID Magnetometer

$$\text{Initial condition:} \quad x_{sq}(0) = \begin{bmatrix} 0 \\ 0 \\ 0 \\ 0 \end{bmatrix} \quad (4.47)$$

Difference equation:

$$\begin{aligned}x_{sq}(k+1) &= \Phi_{sq}x_{sq}(k) + \Gamma_{sq}n_4(k) \\ \xi_{sq}(k) &= H_{sq}x_{sq}(k) + D_{sq}n_4(k)\end{aligned} \quad (k=0, \dots) \quad (4.48)$$

where

$$n_4(k) = N(0, 1 \text{ (arcsecond}^2))$$

$$E[n_d(j)n_d(k)] = \delta_{jk}$$

$$\Phi_{sq} = \begin{bmatrix} -6.3260 \times 10^{-2} & 8.7088 \times 10^{-1} & 9.9898 \times 10^0 & 4.7779 \times 10^1 \\ -4.1305 \times 10^{-2} & 5.4467 \times 10^{-1} & 7.8444 \times 10^0 & 4.3343 \times 10^1 \\ -2.4156 \times 10^{-4} & -2.7605 \times 10^{-3} & 9.8681 \times 10^{-1} & 9.9591 \times 10^0 \\ -1.3573 \times 10^{-7} & -1.5570 \times 10^{-6} & -7.4466 \times 10^{-6} & 9.9998 \times 10^{-1} \end{bmatrix}$$

$$\Gamma_{sq} = \begin{bmatrix} 1.9065 \times 10^{-2} \\ 7.0900 \times 10^{-3} \\ 1.7505 \times 10^{-4} \\ 3.2689 \times 10^{-7} \end{bmatrix}, \quad H_{sq} = \begin{bmatrix} 1.0 \\ 0 \\ 0 \\ 0 \end{bmatrix}^T, \quad D_{sq} = 1.5153 \times 10^{-2}$$

The analog pseudo 1/f noise $\xi_{sq}(t)$ was discretized by the Van Loan's algorithm, and the discrete pseudo 1/f noise $\xi_{sq}(k)$ was simulated by the difference equation given in Table 4.14. Figure 4.6 (b) shows the power spectral density of the 1/f noise simulated by Equation 4.45 and the predicted spectral density. Even though distortion of the power spectral density by the Nyquist frequency was apparent at the higher frequencies, the spectral density of the simulated noise matched with the predicted density at the lower frequencies where the science signal is located. I listed the MATLAB program *gsquid.m*, which I used to design the discrete shaping filter, in Appendix B.

SQUID Bias Drift

The SQUID bias drift had to be simulated separately from the pseudo 1/f noise because the 1/f shaping filter has a finite dc gain and does not model the dc drift of the

Table 4.15 Bias Drift Model for Science SQUID Magnetometer

Initial condition: $b_{sq}(0) = 0$ (4.49)

Difference equation:

$$b_{sq}(k+1) = a_{sq}b_{sq}(k) + (1 - a_{sq})w_1(k) \quad (4.50)$$

where

$b_{sq}(k)$: k-th sample of the readout bias in the SQUID magnetometer;

$w_1(k) = N(0, \alpha_{sq}k\Delta t)$ WRS with parameter α_{sq} ;

$$a_{sq} \equiv \exp\left(-\frac{\Delta t_{sq}}{T_{sq}}\right)$$

$\Delta t_{sq} = 10.0$ SQUID bias drift update rate (seconds);

$T_{sq} = 10.0$ SQUID bias drift time constant (hours)

$\alpha_{sq} = 1.0$ WRS expected covariance (arcsecond²/year);

SQUID magnetometer readout. The bias drift is a very important part of the science signal because it is estimated by the Kalman filter and has a significant effect on the final estimation accuracy of the relativistic precession rates. The SQUID bias drift was simulated by an additional band-limited Wiener random sequence using the difference equation given in Table 4.15.

Equation 4.43 simulates the total SQUID readout noise by combining the pseudo 1/f noise and the bias drift. The data reduction scheme analysis in Chapter 5 is based on this simulated SQUID noise.

4.2.5.2 *Analog-to-Digital Converter*

Similarly to the SQUID readout noise, the A-to-D converter was modeled in the truth model to verify the data reduction scheme before the scheme was applied to the actual experimental data. The nominal values for the A-to-D converter are shown in Table 4.16.

The nominal converter range was determined to allow the full range of the science signal, which is about ± 25 arcseconds, and the additional margin of about 300% of the science signal. The additional margin gives the converter a conservative operational range in case of flux jumps of the SQUID magnetometer⁷ (explained in Section 4.3.2.2) or large pointing error caused by failure of the pointing controller.

The nominal resolution was determined according to the results obtained by Qin⁸ (Ref. 20). Qin showed that the quantization error introduced by the 14-bit A-to-D converter has little effect on the final estimation accuracy compared with the effect of the

⁷ The SQUID output will be saturated in the case of flux jumps and can be reset by the SQUID controller. Thus, the A-to-D converter for the science mission can have an input range of less than 200 arcseconds (Ref. 44).

⁸ Qin did not consider other errors in the A-to-D converter such as nonlinearity, scale error, and differential nonlinearity (Ref. 45, 46).

5-hour SQUID noise, and that quantization error did not become a dominant error with 14-bit or better resolution. Thus I chose 16-bit resolution in case a better SQUID sensor with a lower integration time was constructed or a wider-range A-to-D converter was required. The quantization level of the 16-bit converter is given as follows:

$$q_{ad} = \frac{R_{ad}}{2^{B_{ad}}} \quad (4.51)$$

$$= 3.1 \text{ (milliarcsecond)}$$

where

R_{ad} : range of A-to-D converter

B_{ad} : number of bits in A-to-D converter

q_{ad} : quantization bin size in A-to-D converter

Thus, the rms value of the quantization error is given by the following equation (Ref. 47):

$$\sigma_{ad} = \frac{q_{ad}}{\sqrt{12}} \quad (4.52)$$

$$= 0.9 \text{ (milliarcsecond)}$$

where

Table 4.16 Nominal Parameters for the Science Signal A-to-D Converter

Nominal range:	<i>200 arcseconds (± 100 arcseconds)</i>
Nominal resolution:	<i>16 bits</i>
Nominal bias:	<i>0 arcsecond</i>
Nominal scale factor:	<i>1 volt/arcsecond</i>

σ_{ad} : *standard deviation of quantization error in A-to-D converter*

This quantization error is much smaller than the 5-hour SQUID noise and does not become a dominant error. The only problem with the 16-bit A-to-D converter is the lack of space applications because it became available as a space-qualified unit only a few years ago (Ref. 48). A case study has to be conducted to determine actual space applications of the 16-bit A-to-D converter.

4.2.5.3 Anti-Aliasing Lowpass Filter

A lowpass filter has to be applied to an analog signal prior to discretization to avoid aliasing of higher frequency components. This is a common practice for digital controller/estimator application; the niobium bird experiment is no exception. Because the sampling rate for the niobium bird experiment is 0.1 Hz, the Nyquist frequency is 0.05 Hz, and the cutoff frequency of the lowpass filter must be equal to or lower than the Nyquist frequency. The lowpass filter installed for the niobium bird experiment was not modeled in the truth model for following reasons:

- The lowpass filter would introduce gain change and a time delay to the science signal that would not change the formulation of the data reduction scheme;
- It is generally difficult to construct a digital filter that represents an analog filter correctly;
- The science signal is modulated at the roll frequency, which is only about 3% of the Nyquist frequency, and the lowpass filter has little effect on the science signal.

The actual analog filter installed for the niobium bird experiment is described in Chapter 6.

4.2.6 Gyro Model

Because the London moment is aligned to the instantaneous spin axis of the gyroscope, the science signal includes not only a relativistic precession but also a torque-free motion of the spin axis with respect to the angular momentum vector. In order to analyze the effects of the torque-free motion on the data reduction, the simulated science signal must include that model. The torque-free motion of the spin axis can be divided into two components, the herpolhode and the polhode (Ref. 49, 50). The herpolhode is represented by the motion of the spin axis in inertial space with respect to the angular momentum and has a frequency close to the spin speed. The polhode is represented by the motion of the spin axis in the body-fixed frame and has a very slow frequency ranging from several minutes to several days. The London moment aligned to the instantaneous spin axis follows the herpolhode trace in inertial space around the angular momentum vector. Thus, the science signal is modulated by the herpolhode frequency. However, because the separation angle between the London moment and the angular momentum vector is small ($\approx 10^{-5}$ radian), and the high-frequency components are attenuated by the anti-alias lowpass filter, I did not simulate the herpolhode motion in the truth model.

In addition to the London moment, there exists another kind of magnetic field in the gyroscope, which is that of the trapped flux. The trapped flux is flux literally trapped on the surface of the superconducting gyroscope and is fixed to the body frame of the gyroscope. Thus, the science signal includes reading not only from the London moment but also from the trapped flux. Because the trapped flux is fixed to the body frame, the trapped flux signal is modulated at the polhode frequency⁹, which is too slow to be

⁹ Even though the trapped flux signal is also modulated at the spin frequency of the gyroscope, I assumed that the spin frequency components were attenuated by the lowpass filter.

attenuated by the anti-alias lowpass filter. Chapter 5 analyzes the effect of this trapped flux on the science signal and the data reduction scheme.

4.3. Simulation of the Science Signal

The individual models developed in the previous sections are integrated to simulate the science signal for the niobium bird experiment. First, the measurement equations for the science signal are derived according to the standardized coordinate frames developed in Chapter 2. Then, the availability of the science signal to the data reduction scheme is discussed in terms of the occultation of the guide star and the hardware characteristics.

4.3.1 Measurement Equation

I developed two measurement equations for the science signal, each of which was intended for a different purpose. The first is an idealized measurement equation; the second is a realistic measurement equation. The idealized equation was developed to formulate the data reduction scheme and, therefore, to simplify the equation, some of the error models are not included. The realistic measurement equation was developed to analyze the effects of various error sources and thus includes all the error models described earlier in this chapter.

The measurement equation for the science signal was initially developed by Vassar, and his equation was modified by Duhamel, DiEsposti, and Qin. There seemed to be some confusion about the signs and the phase of the science signal, because each researcher used a different coordinate frame definition. The equations I formulated, which were based on the standard coordinate frames presented in Chapter 2, remove the ambiguity regarding the sign and phase of the measurement equation.

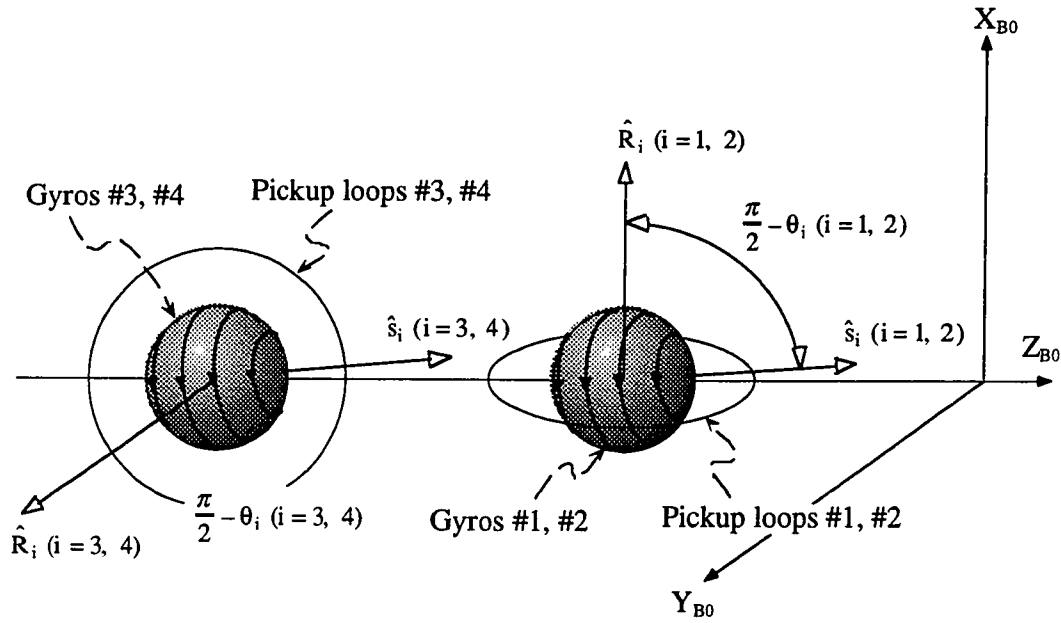


Figure 4.7 Definition of spin direction vectors \hat{s}_i , readout vectors \hat{R}_i , and readout angles θ_i ($i=1, 2, 3, 4$).

In order to derive the measurement equations, eight unit vectors are defined. Four unit vectors \hat{s}_i ($i=1, \dots, 4$) are defined, each of which is aligned to the i -th science gyroscope spin direction. The other four unit vectors \hat{R}_i ($i=1, \dots, 4$) are defined so that each is perpendicular to the pickup loop plane of the i -th gyroscope. Figure 4.7 shows the orientation of \hat{s}_i and \hat{R}_i ($i=1, \dots, 4$) with respect to the B-0 frame, whose definition is shown in Figure 2.2. Each of \hat{R}_i ($i=1, \dots, 4$) points from the center of the quartz housing toward the calibrated surface [see Figure 2.2]. Thus, if there is no structural misalignment, \hat{R}_1 and \hat{R}_2 are aligned to the x_{B0} axis and \hat{R}_3 and \hat{R}_4 are aligned to the y_{B0} axis. The angle between the gyroscope spin axis and the pickup loop is given by the following equation:

$$\theta_i \equiv \hat{s}_i \cdot \hat{R}_i \quad (i=1, \dots, 4) \quad (4.53)$$

where

$$|\theta_i| \ll 1$$

θ_i : angle between the London moment and the SQUID pickup loop for the i -th science gyroscope

\hat{s}_i : a unit vector aligned to the spin direction of the i -th science gyroscope

\hat{R}_i : a unit vector perpendicular to the pickup loop plane of the i -th science gyroscope

Thus the output of the SQUID magnetometer is proportional to θ_i and the science signal for the i -th gyroscope is given as follows:

$$y_{Gi} = f_R(\theta_i) \quad (i=1,\dots,4)$$

where

y_{Gi} : science signal from the i -th gyroscope

The function $f_R(\theta_i)$ includes the scale factor, bias, noise, and nonlinearity of the readout system. This science signal is elaborated in two different forms in the following sections by expressing \hat{s}_i and \hat{R}_i in the B-0 frame.

4.3.1.1 Idealized Measurement Equation

The idealized measurement equation for the science signal was developed to formulate the data reduction scheme. The assumptions listed in Table 4.17 were made in formulating the idealized equation.

Table 4.17 Assumptions and Their Effects for Idealized Measurement Equation

Assumptions	Effects
No misalignment of the null axis of the telescope readout with respect to the z_{B0} axis	${}^2B^0 = \begin{bmatrix} 1 & 0 & 0 \\ 0 & 1 & 0 \\ 0 & 0 & 1 \end{bmatrix} \quad (4.54)$
No misalignment or creeping of the telescope structure with respect to the B-0 frame	${}^4B^0 = \begin{bmatrix} 1 & 0 & 0 \\ 0 & 1 & 0 \\ 0 & 0 & 1 \end{bmatrix} \quad (4.55)$
No misalignment or creeping of the gyro readout structure with respect to the B-0 frame	$\begin{aligned} \hat{R}_{1,2} &= \bar{x}_{B0} \\ \hat{R}_{3,4} &= \bar{y}_{B0} \end{aligned} \quad (4.56)$
A linear science signal readout	$y_{Gi} = C_{Gi}\theta_i + b_i + n_{sq} \quad (4.57)$ <p>where</p> <p>C_{Gi}: i-th gyro scale factor</p> <p>b_i: i-th gyro readout bias</p> <p>n_{sq}: SQUID readout noise</p>
No satellite pointing error	${}^{B2}T^{A5} = \begin{bmatrix} \cos \psi_r & \sin \psi_r & 0 \\ -\sin \psi_r & \cos \psi_r & 0 \\ 0 & 0 & 1 \end{bmatrix} \quad (4.58)$ <p>where</p> <p>$\psi_r = \psi_{rc} + \delta\psi_r$</p> <p>$\psi_r$: actual roll phase</p> <p>ψ_{rc}: commanded roll phase</p> <p>$\delta\psi_r$: control error of roll phase</p>
No refraction of starlight through the atmosphere	$\bar{\epsilon}_f = 0 \quad (4.59)$
No mass unbalance, no electrical moment, and no external torque acting on the gyroscope	The gyroscope has no Newtonian precession. The London moment is aligned with the angular momentum vector.

The idealized measurement equation was derived by expressing the gyroscope spin vector in the B-0 frame using the rotational matrices defined in Chapter 2. From Equation 4.56, the readout normal vectors \hat{R}_i ($i=1,\dots,4$) can be expressed in the B-0 frame as follows:

$$\frac{\hat{R}_{1,2}}{B^0} = \begin{bmatrix} 1 \\ 0 \\ 0 \end{bmatrix}_{B-0} \quad (4.60a)$$

$$\frac{\hat{R}_{3,4}}{B^0} = \begin{bmatrix} 0 \\ 1 \\ 0 \end{bmatrix}_{B-0} \quad (4.60b)$$

The spin vectors \hat{s}_i ($i=1,\dots,4$) can be expressed in the A-0 frame through the relativistic precession angles and initial misalignment angles as follows:

$$\frac{\hat{s}_i}{A^0} = \begin{bmatrix} \zeta_1 \\ \zeta_2 \\ 1 \end{bmatrix}_{A-0} \quad (i=1,\dots,4) \quad (4.61)$$

where

$$\zeta_1 \equiv NS_0 + \Omega_G t$$

$$\zeta_2 \equiv EW_0 + \Omega_F t \cos \delta_R$$

NS_0 : initial misalignment of gyroscope's spin axis in North-South direction

EW_0 : initial misalignment of gyroscope's spin axis in East-West direction

Ω_G : geodetic precession rate

Ω_F : frame-dragging precession rate

t : elapsed time from the mission initialization

δ_R : declination of Rigel

Note that the spin vectors do not include the Newtonian precession angles. The spin vectors \hat{s}_i ($i=1,\dots,4$) coordinated in the A-0 frame (Equation 4.61) can be expressed in the B-0 frame through the rotational matrices ${}^5A^0$, ${}^{B^2}T^{A^5}$, and ${}^2B^0$ as follows:

$$\begin{aligned}
\frac{\hat{s}_i}{B0} &= \left({}^2B^0 \right)^T {}^{B2}T^{A5} {}^5A^0 \frac{\hat{s}_i}{A0} \\
&= \begin{bmatrix} 1 & 0 & 0 \\ 0 & 1 & 0 \\ 0 & 0 & 1 \end{bmatrix} \begin{bmatrix} \cos \psi_r & \sin \psi_r & 0 \\ -\sin \psi_r & \cos \psi_r & 0 \\ 0 & 0 & 1 \end{bmatrix} \begin{bmatrix} 1 & 0 & -a_{51} \\ 0 & 1 & -a_{52} \\ a_{51} & a_{52} & 1 \end{bmatrix} \begin{bmatrix} \zeta_1 \\ \zeta_2 \\ 1 \end{bmatrix}_{A-0} \\
&= \begin{bmatrix} -(a_{51} - \zeta_1) \cos \psi_r - (a_{52} - \zeta_2) \sin \psi_r \\ (a_{51} - \zeta_1) \sin \psi_r - (a_{52} - \zeta_2) \cos \psi_r \\ 1 \end{bmatrix}_{B-0}
\end{aligned} \tag{4.62}$$

where

$$\begin{aligned}
\psi_r &= \psi_{rc} + \delta \psi_r \\
a_{51} &= \bar{x}_{A0} \cdot \bar{e}_5 \\
a_{52} &= \bar{y}_{A0} \cdot \bar{e}_5
\end{aligned}$$

Assuming no refraction of starlight through the atmosphere (Equation 4.59), the observational correction vector \bar{e}_5 for the A-5 frame can be expressed by the following equation:

$$\bar{e}_5 = \bar{e}_r + \bar{e}_d + \bar{e}_p + \bar{e}_a^{es} + \bar{e}_a^{ve} \tag{4.63}$$

By substituting Equations 4.28 and 4.31 into \bar{e}_p and \bar{e}_d , respectively, the two terms a_{51} and a_{52} can be calculated as follows:

$$\begin{aligned}
a_{51} &= \varepsilon_{r1} + \lambda_1 - \alpha \frac{r_x}{R_{es}} + \kappa \frac{R_{es}}{r_{es}} \frac{r_x}{r_{es} - r_z} \\
a_{52} &= \varepsilon_{r2} + \lambda_2 - \alpha \frac{r_y}{R_{es}} + \kappa \frac{R_{es}}{r_{es}} \frac{r_y}{r_{es} - r_z}
\end{aligned} \tag{4.64}$$

where

$$\begin{aligned}
\varepsilon_{r1} &\equiv \bar{x}_{A0} \cdot \bar{e}_r, \quad \varepsilon_{r2} \equiv \bar{y}_{A0} \cdot \bar{e}_r \\
\lambda_1 &\equiv \bar{x}_{A0} \cdot (\bar{e}_a^{es} + \bar{e}_a^{ve}), \quad \lambda_2 \equiv \bar{y}_{A0} \cdot (\bar{e}_a^{es} + \bar{e}_a^{ve}) \\
r_x &\equiv \bar{x}_{A0} \cdot \bar{r}_{es}, \quad r_y \equiv \bar{y}_{A0} \cdot \bar{r}_{es}, \quad r_z \equiv \bar{z}_{A0} \cdot \bar{r}_{es} \\
r_{es} &\equiv \sqrt{r_x^2 + r_y^2 + r_z^2}
\end{aligned}$$

α : *parallax coefficient [see Table 4.7].*

κ : *deflection of starlight coefficient [see Table 4.9].*

By substituting Equations 4.60 and 4.62 into Equation 4.53, we obtain the angle between the London moment and the gyro pickup loop thus:

$$\theta_i = -(a_{s1} - \zeta_1) \cos \psi_r - (a_{s2} - \zeta_2) \sin \psi_r \quad \text{for } i=1,2 \quad (4.65)$$

$$\theta_i = (a_{s1} - \zeta_1) \sin \psi_r - (a_{s2} - \zeta_2) \cos \psi_r \quad \text{for } i=3,4 \quad (4.66)$$

Finally, the idealized measurement equation for the i -th gyroscope can be obtained by substituting Equation 4.65 or 4.66 into Equation 4.57 as follows:

$$y_{Gi} = C_{Gi} \left[-(NS_s + \lambda_1) \cos(\psi_{rc} + \delta\psi_r) - (EW_s + \lambda_2) \sin(\psi_{rc} + \delta\psi_r) \right] + b_i + n_{sq} \quad (4.67)$$

for $i=1,2$

$$y_{Gi} = C_{Gi} \left[(NS_s + \lambda_1) \sin(\psi_{rc} + \delta\psi_r) - (EW_s + \lambda_2) \cos(\psi_{rc} + \delta\psi_r) \right] + b_i + n_{sq} \quad (4.68)$$

for $i=3,4$

where

$$NS_s = -(NS_0 + \Omega_G t) + \varepsilon_{r1} - \alpha \frac{r_x}{R_{es}} + \kappa \frac{R_{es}}{r_{es}} \frac{r_x}{r_{es} - r_z}$$

$$EW_s = -(EW_0 + \Omega_F t \cos \delta_R) + \varepsilon_{r2} - \alpha \frac{r_y}{R_{es}} + \kappa \frac{R_{es}}{r_{es}} \frac{r_y}{r_{es} - r_z}$$

Note that the measurement equations for gyros #1 and #2 are 90 degrees out of phase from the measurement equations for gyros #3 and #4. Two aberration terms, λ_1 and λ_2 , are not included in the common terms NS_s and EW_s ,¹⁰ respectively, because these

¹⁰ I call NS_s and EW_s *north south static* and *east west static*, respectively. The term *static* is used to emphasize that these two terms do not include the aberration effects, which are caused by the motion of observer.

aberration terms are known to 0.07 milliarcsecond or better in uncertainty (Ref. 19). The data reduction scheme uses the aberration terms to calibrate the gyro scale factor C_{Gi} for each gyroscope. The data reduction scheme is developed in Chapter 5 on the basis of the idealized measurement equations (Equations 4.67 and 4.68).

4.3.1.2 Realistic Measurement Equation

I developed the realistic measurement equation for the science signal to analyze the effects of various error models neglected in the idealized equations. Thus, the assumptions made for the ideal equation were discarded in formulating the realistic equation. I derived the realistic measurement equation by expressing the spin vectors \hat{s}_i ($i=1,\dots,4$) and the readout normal vectors \hat{R}_i ($i=1,\dots,4$) in the B-0 frame. The readout normal vectors are expressed in the B-0 frame as follows:

$$\frac{\hat{R}_i}{B0} = \begin{bmatrix} 1 \\ \delta\psi_{Ri} \\ -\delta\theta_{Ri} \end{bmatrix}_{B-0} \quad \text{for } i=1,2 \quad (4.69a)$$

$$\frac{\hat{R}_i}{B0} = \begin{bmatrix} -\delta\psi_{Ri} \\ 1 \\ \delta\phi_{Ri} \end{bmatrix}_{B-0} \quad \text{for } i=3,4 \quad (4.69b)$$

where the structural misalignment and creeping terms, $\delta\phi_{Ri}$, $\delta\theta_{Ri}$, and $\delta\psi_{Ri}$, are given by Equations 4.32, 4.33, and 4.34. Now, the spin vectors can be expressed in the A-0 frame as follows:

$$\hat{s}_i = \begin{bmatrix} \zeta_1 \\ \zeta_2 \\ 1 \end{bmatrix}_{A-0} \quad (4.70)$$

where

$$\begin{aligned}
\zeta_1 &= NS_0 + \rho_1 + \Omega_G t \\
\zeta_2 &= EW_0 + \rho_2 + \Omega_F f_\Omega(t) \\
f_\Omega(t) &\equiv t \cos \delta_R - \frac{3}{2n_{ve}} \sin 2(n_{ve}t + \omega_{ve}(t_0)) \cos \delta_R + \frac{1}{2n_{ve}} \cos 2(n_{ve}t + \omega_{ve}(t_0)) \sin \delta_R
\end{aligned}$$

The frame-dragging precession term in ζ_2 assumes the nominal satellite orbit given in Table 4.6. The spin vectors can now be expressed in the B-0 frame through the rotational matrices, ${}^5A^0$, ${}^{B2}T^{A5}$, and ${}^2B^0$, which include the error sources ignored in the idealized measurement equation such as pointing error and structural misalignment. The spin vectors expressed in the B-0 frame are then given by the following equation:

$$\begin{aligned}
\hat{s}_i &= \left({}^2B^0 \right)^T {}^{B2}T^{A5} {}^5A^0 \hat{s}_i \\
&= \begin{bmatrix} 1 & 0 & \theta_{null} \\ 0 & 1 & -\phi_{null} \\ -\theta_{null} & \phi_{null} & 1 \end{bmatrix} \begin{bmatrix} \cos \psi_r & \sin \psi_r & -\theta_r \cos \psi_r + \phi_r \sin \psi_r \\ -\sin \psi_r & \cos \psi_r & \theta_r \sin \psi_r + \phi_r \cos \psi_r \\ \theta_r & -\phi_r & 1 \end{bmatrix} \begin{bmatrix} 1 & 0 & -a_{51} \\ 0 & 1 & -a_{52} \\ a_{51} & a_{52} & 1 \end{bmatrix} \begin{bmatrix} \zeta_1 \\ \zeta_2 \\ 1 \end{bmatrix}_{A=0} \quad (4.71) \\
&= \begin{bmatrix} -(a_{51} - \zeta_1 + \theta_r) \cos \psi_r - (a_{52} - \zeta_2 - \phi_r) \sin \psi_r + \theta_{null} \\ (a_{51} - \zeta_1 + \theta_r) \sin \psi_r - (a_{52} - \zeta_2 - \phi_r) \cos \psi_r - \phi_{null} \\ 1 \end{bmatrix}_{B=0}
\end{aligned}$$

Thus, the angles between the London moment and the gyro pickup loop can be obtained by substituting Equations 4.69 and 4.71 into Equation 4.53 as follows:

$$\theta_i = -(a_{51} - \zeta_1 + \theta_r) \cos \psi_r - (a_{52} - \zeta_2 - \phi_r) \sin \psi_r + \theta_{null} - \delta \theta_{Ri} \quad (4.72a)$$

for i=1,2

$$\theta_i = (a_{51} - \zeta_1 + \theta_r) \sin \psi_r - (a_{52} - \zeta_2 - \phi_r) \cos \psi_r - \phi_{null} + \delta \phi_R \quad (4.72b)$$

for i=3,4

The second-order terms are neglected in Equations 4.71 and 4.72. Finally, the realistic measurement equations are given by the following equations employing the same notation as the idealized measurement equation:

$$y_i = C_{Gi} \left[- (NS_s + \lambda_1 + \theta_r) \cos \psi_r - (EW_s + \lambda_2 - \phi_r) \sin \psi_r + \theta_{null} - \delta\theta_R \right] + b_i + n_{sq}$$

for i=1,2 (4.73a)

$$y_i = C_{Gi} \left[(NS_s + \lambda_1 + \theta_r) \sin \psi_r - (EW_s + \lambda_2 - \phi_r) \cos \psi_r - \phi_{null} + \delta\phi_R \right] + b_i + n_{sq}$$

for i=3,4 (4.73b)

where

$$NS_s = - (NS_0 + \rho_1 + \Omega_G t) + \varepsilon_{r1} + \varepsilon_{f1} - \alpha \frac{r_x}{R_{es}} + \kappa \frac{R_{es}}{r_{es}} \frac{r_x}{r_{es} - r_z}$$

$$EW_s = - (EW_0 + \rho_2 + \Omega_F f_\Omega(t)) + \varepsilon_{r2} + \varepsilon_{f2} - \alpha \frac{r_y}{R_{es}} + \kappa \frac{R_{es}}{r_{es}} \frac{r_y}{r_{es} - r_z}$$

$$\varepsilon_{f1} \equiv \vec{x}_{A0} \cdot \vec{\varepsilon}_f$$

$$\varepsilon_{f2} \equiv \vec{y}_{A0} \cdot \vec{\varepsilon}_f$$

The realistic measurement equation (Equation 4.73) includes the error sources that are not included in the idealized measurement equation. The data reduction scheme is developed in Chapter 5 on the basis of the idealized measurement equation but processes the data simulated by the realistic measurement equation (Equation 4.73).

4.3.2 Signal Availability

The usefulness of the science signal for the estimation is defined as *signal availability* in this section. During the science mission, the science signal is not always available to the ground station, or it may be invalid as a measurement even though it is available. In either case, if the data reduction scheme cannot use the science signal to estimate the relativistic precessions, we refer to the condition as *signal unavailable*. The science signal becomes unavailable when the following conditions occur:

- Rigel is occulted by the Earth and the telescope cannot be used as a sensor;

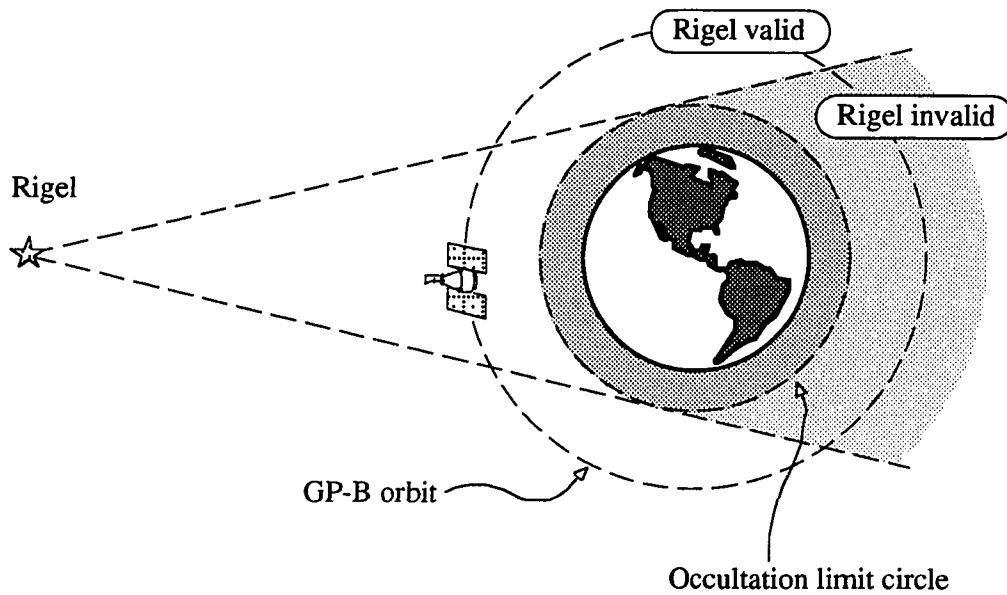


Figure 4.8 Definition of occultation limit circle around the Earth. Shaded part of the orbit is called *Rigel invalid*.

- Flux jumps cause a loss of the lock of the SQUID magnetometer or the saturation of readout hardware components;
- Transmission to the ground station is interrupted by hardware failure or signal interference.

Each case is discussed in the following sections, which describes the final steps of the truth modeling.

4.3.2.1 Occultation

Occultation of the guide star–Rigel occurs when the GP-B satellite is behind the Earth and the view of Rigel is blocked by the Earth itself or the atmospheric layer. During the occultation, the telescope loses the lock to Rigel and cannot be used as the pointing control sensor. This period is called *Rigel invalid*. On the other hand, when Rigel is visible from the satellite and the telescope can be used as the pointing control sensor, the period is called *Rigel valid*. N. J. Kasdin (Ref. 26) proposed the use of the

science gyroscopes as the pointing control sensor during Rigel invalid, but even with the gyroscopes, the pointing accuracy is much worse than during Rigel valid. In fact, the current hardware requirement on the pointing accuracy during Rigel invalid is 2 arcseconds rms (Ref. 26). Thus, the gyroscope signal during Rigel invalid is corrupted by the lack of a pointing reference and is not useful for the relativistic precession estimate.

The condition of Rigel invalid is determined by the position of the satellite relative to the Earth and the apparent direction of Rigel. A circle I call the *occultation limit circle* is defined around the Earth, as shown in Figure 4.8. The portion of the satellite orbit within the shaded area is the region of Rigel invalid. The validity of Rigel is checked by the following conditions:

If

$$(\vec{r}_{ve} \cdot \vec{x}_{A3})^2 + (\vec{r}_{ve} \cdot \vec{y}_{A3})^2 \leq \rho_{oc}^2 \quad (4.74)$$

and

$$\vec{r}_{ve} \cdot \vec{z}_{A3} \leq 0 \quad (4.75)$$

then Rigel is invalid.

where

\vec{r}_{ve} : position vector of the GP-B satellite with respect to the Earth

ρ_{oc} : radius of the occultation limit circle [see Figure 4.8]

$\vec{x}_{A3}, \vec{y}_{A3}, \vec{z}_{A3}$: unit vectors parallel to the xyz axes of the A-3 frame

The validity of Rigel is checked every time the truth model simulates the science signal.

If Rigel is invalid, the truth model returns no measurements.

4.3.2.2 Flux Jumps

Flux jumps within the SQUID magnetometer, which can cause an interruption of the measurement, may occur during the science mission. The SQUID magnetometer is a

flux-to-voltage converter that uses a superconductive loop with one or two Josephson junctions¹¹ (Ref. 15, 16, 17). The voltage across the SQUID loop is a nonlinear, periodic function of the total flux within the SQUID loop, and the period is the flux quantum Φ_0 . Because the transfer function from flux to voltage is periodic, there exist multiple flux states separated by Φ_0 that yield the same output voltage. In order to avoid this ambiguity and to linearize the transfer function, the total flux within the SQUID loop is regulated to a constant value by the SQUID electronics. As shown in Figure 1.4, the total flux within the SQUID loop is the sum of the input flux from the pickup loop and the control flux from the feedback loop¹². Because the total flux within the loop is regulated to be constant, the voltage across the loop is constant, and the feedback current is thus proportional to the input flux. Instead of measuring this feedback current, the SQUID magnetometer measures a proportional voltage across the feedback resistor R_f .

As long as the total flux within the loop is constant, the feedback voltage is a continuous, linear function of the input flux and we say that the SQUID is flux-locked. This lock can be lost in the case of sudden changes in the input flux (i.e., the external magnetic field), or of fluctuation of the electric ground. This phenomenon is analogous to that of the attitude controller of a model aircraft becoming unstable because of gusting wind. The loss of lock is usually temporary and the lock can be recovered quickly. But after the lock is recovered, the total flux has shifted by $n\Phi_0$ ($n=\pm 1, 2, \dots$). Because all of this happens almost instantaneously, the phenomenon is called a flux jump. Flux jumps cause spikes and/or steps in the measurement and affect the data reduction scheme by introducing extra noise or a data interruption.

¹¹ A superconductive device that uses one Josephson junction is called rf SQUID; one that uses two Josephson junctions is called a dc SQUID. For the GP-B science mission and the Niobium bird experiment, a dc SQUID magnetometer is used as the primary sensor.

¹² The SQUID feedback loop is called a flux-lock loop because it tries to keep the total flux within the superconductive loop constant.

The flux jump was not modeled in the truth model because it is difficult to model and can be observed in the SQUID magnetometer used in the niobium bird experiment. Flux jumps can be suppressed by providing adequate magnetic shielding and a stable electrical ground and by reducing the band-width of the flux-locked loop¹³.

4.3.2.3 Signal Interruption

In addition to the occultation of the guide star and the flux jumps, signal interruption can also be caused by other factors such as:

- Telemetry failure
- Abnormal pointing error
- Abnormal roll phase error
- SQUID hardware failure

In these cases, the science signal is either not available at the ground station or is corrupted by an unexpectedly large error, and the data reduction scheme cannot process the science data successfully. These cases are not discussed in this thesis, but the effects of such signal interruptions were analyzed by T. G. Duhamel (Ref. 18).

¹³ J. M. Lockhart suggested that the size of jump is likely to be a fraction of a quantum, and reducing the controller band-width may not be effective depending on the cause of jumps.

CHAPTER 5. DATA REDUCTION SCHEME SYNTHESIS

5.1 Introduction

In this section, I develop the data reduction scheme designed for the Gravity Probe B program with modifications to X. Qin's work (Ref. 20). The data reduction scheme is one of the three important components of the niobium bird experiment in the sense that it estimates the relativistic precession rates and determines the final estimation accuracy. It has been investigated by many people including C. W. F. Everitt et al. (Ref. 51) who started the error analysis as a part of the preliminary investigation of the relativity gyroscope experiment. J. V. Breakwell and R. Vassar (Ref. 7) developed a measurement equation for the science signal and conducted a covariance analysis, which showed that the SQUID noise was the dominant error source. T. G. Duhamel (Ref. 18) extended Vassar's analysis and developed a square root information filter, followed by R. S. DiEsposti (Ref. 19) who created a truth model for

simulation and developed a single-step Kalman filter. X. Qin (Ref. 20) then developed the two-step Kalman filter that gave better insights to the filter states and faster processing speed than DiEsposti's single step filter. I took Qin's approach to develop the two-step Kalman filters with slightly different filter states. The following sections describe the formulation of the two-step Kalman filters based on the idealized measurement equation (Equation 4.68) developed in Chapter 4.

5.2 Filter Formulation

I reformulated the two-step Kalman filters based on Qin's work. I used the SRIF (square root information filter) algorithm to implement the Kalman filters. The SRIF algorithm (Ref. 52) is numerically more stable than the conventional algorithm that propagates a covariance matrix. It is also less sensitive to the round-off errors within a computer and improves estimation accuracy. Qin chose the SRIF algorithm to implement the filters for the GP-B program because of these two advantages. Even though the SRIF algorithm requires intensive calculation involving matrix inversion, computational speed is not a limiting factor for the GP-B application because the GP-B program does not require real-time estimation during the mission. Qin formulated the step 1 and step 2 filters based on his own measurement equation. I reformulated the step 1 and step 2 filters based on the idealized measurement equation for gyros #3 and #4 (Equation 4.68). I did not derive the filters for gyros #1 and #2 because the measurement equations for these gyroscopes (Equation 4.67) are similar, and the filter can be converted through simple phase shifting by 90 degrees. The following sections describe the estimator states and develop the process models for the step 1 and step 2 filters.

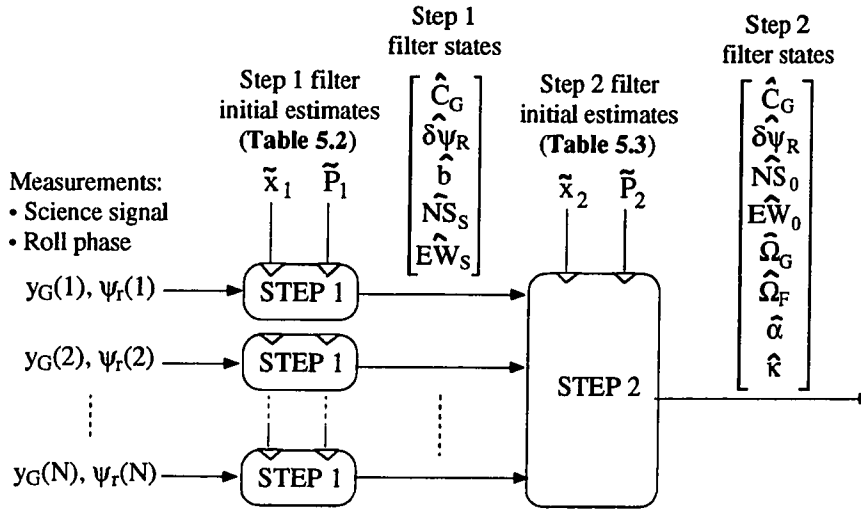


Figure 5.1 Diagram of two-step Kalman filters.

5.2.1 Formulation of Step 1 Filter

The step 1 filters receive the science signal from the SQUID magnetometer and estimate slowly varying terms by assuming them to be constant over one orbital period.

The estimator state vector for the step 1 filtering is given by

$$x_1 = [C_G \quad \delta\psi_r \quad b \quad NS_S \quad EW_S]^T \quad (5.1)$$

where

- C_G : scale factor of SQUID magnetometer (volts per arcsecond)
- $\delta\psi_r$: phase error of satellite roll (radians)
- b : readout bias in SQUID magnetometer (volts)
- NS_S : North-South static term defined in Equation 4.68 (arcseconds)
- EW_S : East-West static term defined in Equation 4.68 (arcseconds)

Each variable is slowly varying and assumed to be constant over one orbital period. During the one-year mission, the GP-B satellite orbits around the Earth about 5400 times, and there are as many step 1 filters as orbits. Each step 1 filter processes the science

signal sampled during one orbit and estimates the five parameters [see Figure 5.1]. The input to the step 1 filter comprises the roll phase measurement from the star blipper and the science signal from the SQUID magnetometer. The output comprises the estimates of the five states and the covariance matrix of the estimated states. The process model for the step 1 filter is given by the following equation:

$$x_1(k+1) = \Phi_1 x_1(k) + \Gamma_1 w_1(k) \quad (5.2)$$

where

$$\Phi_1 = I_{5 \times 5}, \quad \Gamma_1 = \begin{bmatrix} I_{3 \times 3} \\ \mathbf{0}_{2 \times 3} \end{bmatrix}$$

$$w_1(k) = \begin{bmatrix} w_{cl}(k) \\ w_{rl}(k) \\ w_b(k) \end{bmatrix}$$

- $w_{cl}(k)$: discrete equivalent of process noise on scale factor over sampling period Δt of step 1 filter, which is modeled by a Gaussian noise $N(0, \sigma_{cl}^2)$
- $w_{rl}(k)$: discrete equivalent of process noise on roll phase over sampling period Δt of step 1 filter, which is modeled by a Gaussian noise $N(0, \sigma_{rl}^2)$
- $w_b(k)$: discrete equivalent of process noise on SQUID bias over sampling period Δt of step 1 filter, which is modeled by a Gaussian noise $N(0, \sigma_b^2)$

The first three states are assumed to be slowly varying driven by white noise terms, and the other two states are constant without process noise. The standard deviations of three driving white noise terms are determined so that the final estimation accuracy of the relativistic precession rates is better than 1 milliarcsecond per year.

The input to the step 1 filters is the science signal given by Equation 4.68, which is a nonlinear function of step 1 filter states. Let us define the measurement function as follows:

$$y(k) = h(x_1(k)) + n_{sq}(k) \quad (5.3)$$

where

n_{sq} : sensor noise in SQUID magnetometer (volts)

$$h(x_1) \equiv C_G \left[(NS_s + \lambda_1) \sin(\psi_{rc} + \delta\psi_r) - (EW_s + \lambda_2) \cos(\psi_{rc} + \delta\psi_r) \right] + b$$

Qin formulated each step 1 filter as an extended Kalman filter linearizing the measurement equation around an *a priori* estimate. I took the same approach to linearize the measurement equation as follows:

$$\begin{aligned} z(k) &= H_1(k)x_1(k) + n_{sq}(k) \\ &= y(k) - h(\bar{x}_1(k)) + H_1(k)\bar{x}_1(k) + n_{sq}(k) \end{aligned} \quad (5.4)$$

where

$$H_1(k) \equiv \left. \frac{dh(x)}{dx} \right|_{x=\bar{x}_1(k)}$$

With the measurement equation given in a linear form (Equation 5.4) and the linear process model (Equation 5.2), I used the SRIF algorithm to implement the step 1 filters.

The function of the step 1 filters is characterized by demodulation of the science signal. If I expand the idealized measurement equation (Equation 4.68) neglecting the measurement noise, the science signal can be represented by three terms according to the frequency modulation as follows:

$$\begin{aligned} y_G &= C_G (NS_s \sin \psi_r - EW_s \cos \psi_r) \\ &+ C_G (\lambda_1 \sin \psi_r - \lambda_2 \cos \psi_r) \\ &+ b_{sq} \end{aligned} \quad (5.5)$$

The first term is spectrally located at the roll frequency f_r of the GP-B satellite, which is about $1.7\text{e-}2$ Hz to $1.7\text{e-}3$ Hz, and includes the relativistic precession terms. I call this term *roll signal* to distinguish from the other terms. Since the aberration terms, λ_1 and λ_2 , include the orbital aberration, the second term is spectrally separated from the roll signal by the orbital frequency f_o , which is about $1.7\text{e-}4$ Hz. I call this term the *calibration signal* because the aberration terms are known to an accuracy of 0.07 milliarcsecond or better (Ref. 18) and are used to calibrate the scale factor by the step 1 filters. The last term is a bias located at dc. This term is spectrally independent of the first two terms and is the only term that is linear in step 1 filter states. Figure 5.2 shows the spectral locations of the first two terms. Note that the amplitude of the peaks is not to scale. The calibration signals appear as the sidelobes to the center frequency. The step 1 filters use these sidelobes to calibrate the scale factor C_G and the roll phase bias $\delta\psi_r$. Therefore, it is important that these sidelobes are spectrally separated from the center frequency over the integration time of each step 1 filter. With current design specifications, the integration time of each step 1 filter is one orbital period, that is, each step 1 filter processes the science signal sampled during one orbital period. I call the time span of each step 1 filter *step 1 window* and have defined the size of each step 1 window W_1 as the time duration during which each step 1 filter processes the science signal. Considering the occultation of Rigel during each orbit, the nominal value of W_1 is given by

$$\begin{aligned} W_1 &= 61 \text{ minutes} \\ &= 3660 \text{ seconds} \end{aligned}$$

Thus, the frequency resolution of each step 1 filter is determined by the frequency bin size Δf_1 , which is given by:

$$\Delta f_1 = \frac{1}{W_1} \tag{5.6}$$

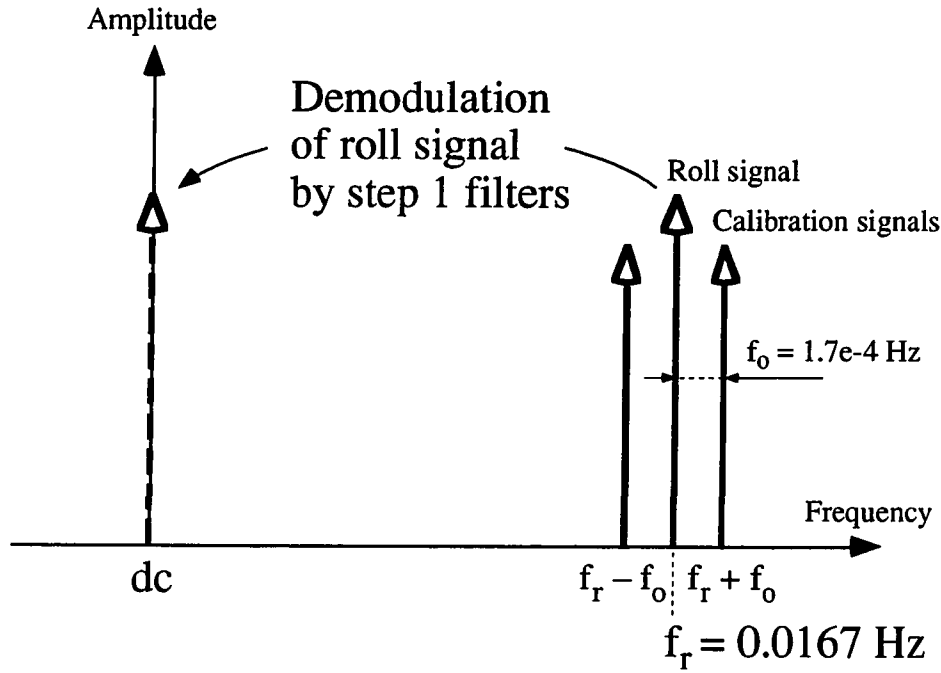


Figure 5.2 Frequency components of a science signal and demodulation by step 1 filters (f_r =roll frequency, f_o =orbital frequency).

The nominal bin size is then

$$\Delta f_l = 2.73e-4 \text{ Hz}$$

This nominal value barely gives the frequency resolution needed to separate the roll and calibration signals, which are separated only by the orbital frequency $f_o=1.7e-4$ Hz. In this scenario, it seems that a longer step 1 window gives finer frequency resolution, and that each step 1 filter can distinguish the roll and calibration signals with less frequency leakage from each other. Even though this claim is true, a longer step 1 window violates the assumption that the static terms, NS_s and EW_s , are constant over the window because they are modulated at the annual frequency. There is, hence, a trade-off between the higher frequency resolution and the assumption of constant parameters. The effects of longer step 1 window are discussed in Section 5.3.2.

After the scale factor and the roll phase bias are estimated from the calibration signal, the static terms, NS_s and EW_s , are estimated from the roll signal. The step 1 filters effectively demodulate the science signal from the roll frequency to dc, which is now processed by the step 2 filter. The output from the step 1 filter is now a dc signal and is linear in the step 2 filter states as explained in the next section.

5.2.2 Formulation of Step 2 Filter

The step 2 filter processes the output from the step 1 filters and estimates final parameters including the relativistic precession rates. The estimator state vector for the step 2 filter is given by

$$x_2 = [C_G \quad \delta\psi_r \quad NS_0 \quad EW_0 \quad \Omega_G \quad \Omega_F \quad \alpha \quad \kappa]^T \quad (5.7)$$

where

- C_G : scale factor of SQUID magnetometer (volts per arcsecond)
- $\delta\psi_r$: phase error of satellite roll (radians)
- NS_0 : North-South initial misalignment of gyroscope's spin axis (arcseconds)
- EW_0 : East-West initial misalignment of gyroscope's spin axis (arcseconds)
- Ω_G : geodetic precession rate (arcseconds per year)
- Ω_F : frame-dragging precession rate (arcseconds per year)
- α : parallax coefficient
- κ : deflection of starlight coefficient

$$\alpha \equiv \frac{R_{es}}{R}, \quad \kappa \equiv \frac{2m_s}{R_{es}}, \quad m_s \equiv \frac{\mu_s}{c^2}$$

- m_s : gravitational radius of the Sun
- R : distance from the Sun to Rigel
- R_{es} : astronomical unit (1 AU)
- μ_s : gravitational constant of the Sun
- c : speed of light in vacuum

As shown in Figure 5.1, the input to the step 2 filter comprises the estimates of step 1 filter states. The input vector to the step 2 filter is given by

$$\rho_1(k) = [\hat{C}_G(k) \quad \delta\hat{\psi}_r(k) \quad N\hat{S}_s(k) \quad E\hat{W}_s(k)]^T \quad (5.8)$$

where

- $\hat{C}_G(k)$: *a posteriori* estimate of SQUID scale factor from k-th step 1 filter
- $\delta\hat{\psi}_r(k)$: *a posteriori* estimate of roll phase bias from k-th step 1 filter
- $N\hat{S}_s(k)$: *a posteriori* estimate of North-South static term from k-th step 1 filter
- $E\hat{W}_s(k)$: *a posteriori* estimate of East-West static term from k-th step 1 filter

Note that the bias term from the step 1 filters is not included in the input to the step 2 filter because the bias term has little effect on the estimation accuracy of the relativistic precession rates as long as the step 1 filters successfully separate the bias from the roll signal¹. Each element is a linear combination of the estimator states of the step 2 filter. Thus, the step 2 filter is a linear Kalman filter and does not involve linearization of the measurement equation as was required for the step 1 filtering. Similar to the step 1 filter states, the estimator states for the step 2 filter are assumed to be constant²; the process model for the step 2 filter is given by the following equation:

$$x_2(k+1) = \Phi_2 x_2(k) + \Gamma_2 w_2(k) \quad (5.9)$$

where

$$\Phi_2 = I_{8 \times 8}, \quad \Gamma_2 = \begin{bmatrix} I_{2 \times 2} \\ \emptyset_{6 \times 2} \end{bmatrix}$$

$$w_2(k) = \begin{bmatrix} w_{c2}(k) \\ w_{r2}(k) \end{bmatrix}$$

¹ I initially included the bias term in the measurement of the step 2 filter, but excluded it later because the estimation accuracy of the relativistic precession term did not degrade without it as long as the step 1 filters successfully separate the bias term from the roll signal. In the case of a large bias drift, with which the step 1 filters may not be able to separate the bias term, it should be included in the step 2 filter [see Section 6.3.3].

- $w_{e2}(k)$: discrete equivalent of process noise on scale factor over integration time of step 1 filter, which is modeled by a Gaussian noise $N(0, \sigma_{e2}^2)$
- $w_{r2}(k)$: discrete equivalent of process noise on roll phase over integration time of step 1 filter, which is modeled by a Gaussian noise $N(0, \sigma_{r2}^2)$

Given the measurement equation (Equation 5.8) and the process model (Equation 5.9), I used the SRIF algorithm to reformulate the step 2 filter. Again, the step 2 filter is a linear filter and does not involve linearization of the measurement equation.

5.2.3 Results of Two-step Filter Simulation

Before testing the two-step filters with experimental data in the niobium bird experiment, I tested them with a science signal simulated by the realistic measurement equation (Equation 4.73) that I developed in Chapter 4. I conducted more than twenty Monte Carlo simulations and evaluated the final estimation error and the time history of estimation. I found that the filters yielded final estimation accuracy of better than 1 milliarcsecond per year at the end of one-year simulation, which satisfied the mission requirement on the estimation accuracy. This section presents the results of one of the Monte Carlo simulations.

5.2.3.1 Condition of Simulation

I conducted the Monte Carlo simulations with a ten-minute roll period under the statistical conditions given in Table 5.1. I used the error models that I developed in Chapter 4 to simulate various noises. The initial conditions and noise parameters given to the step 1 filters are summarized in Table 5.2, and those to the step 2 filter are summarized in Table 5.3.

Table 5.1 Statistical Conditions of Truth Model

Noise source	Noise model	Parameters
SQUID magnetometer	Approximated 1/f noise + BLWRS	5-hour integration time, 0.1 Hz corner frequency
Roll phase drift	Band-limited white noise	$\sigma = 10.0$ arcseconds $T_c = 10.0$ seconds
Roll phase measurement noise	White noise	$\sigma = 10.0$ arcseconds
Telescope pointing error	Band-limited white noise	$\sigma = 20.0$ milliarcseconds $T_c = 2.0$ seconds

Table 5.2 Initial Conditions and Noise Parameters to Step 1 Filters

Step 1 filter states	Initial estimates	Initial estimation accuracy (1σ)
Scale factor, C_G (volts/arcsecond)	1.0	0.01
Roll phase bias, $\delta\psi_r$ (radians)	0.0	0.0005
Readout bias, b_{sq} (arcseconds)	0.0	100.0
North-South static, NS_s (arcseconds)	0.0	100.0
East-West static, EW_s (arcseconds)	0.0	100.0
Process model states of step 1 filter	Process noise level ³ (1σ)	
Process noise on scale factor, w_{c1} (volts/arcsecond)	1e-10	
Process noise on roll phase bias, w_{r1} (radians)	1e-9	
Process noise on readout bias, w_b (arcseconds)	1e-20	

³ Process noise level for the step 1 filter is indicated by the noise standard deviation of the continuous process noise integrated over the sampling period of step 1 filter, which is 10 seconds. All of the process noise within the filter is assumed to be Gaussian.

Table 5.3 Initial Conditions and Noise Parameters to Step 2 Filter

Step 2 filter states	Initial estimates	Initial estimation accuracy (1σ)
Scale factor, C_G (volts/arcsecond)	1.0	0.01
Roll phase bias, $\delta\psi_r$ (radians)	0.0	0.0005
North-South initial misalignment, NS_0 (arcseconds)	0.0	50.0
East-West initial misalignment, EW_0 (arcseconds)	0.0	50.0
Geodetic precession rate, Ω_G (arcseconds/year)	0.0	30.0
Frame-dragging precession rate, Ω_F (arcseconds/year)	0.0	30.0
Parallax coefficient, α	3e-3	1e-3
Deflection-of-starlight coefficient, κ	4.1e-3	5e-4
Process model states of step 1 filter	Process noise level (1σ) ⁴	
Process noise on scale factor, w_{c2} (volts/arcsecond)	1e-3	
Process noise on roll phase bias, w_{r2} (radians)	5e-5	

⁴ Process noise level for the step 2 filter is indicated by the noise standard deviation of the continuous process noise integrated over the sampling period of step 2 filter, which is one orbital period. All of the process noise within the filter is assumed to be Gaussian.

5.2.3.2 Results of Step 1 Filtering

Figure 5.3 shows the results of step 1 filters. The estimates of the North-South static term NS_s and the East-West static term EW_s are plotted in the xy plane of the A-0 frame. The origin is located at the observer, the GP-B satellite. A unit vector that is aligned with the gyroscope's spin axis is projected on the plane. The solid line indicates the trajectory of the gyroscope precession observed with respect to the telescope axis over the one-year mission. The hollow circle represents the two components at the beginning of the mission, and the filled circle represents them at the end of the mission. The x's scattered around the solid line show the estimates from the step 1 filters. Each point represents the estimates of NS_s and EW_s from a step 1 filter. The dotted lines show the envelopes of the expected estimation error (1σ rms error). The expected estimation error

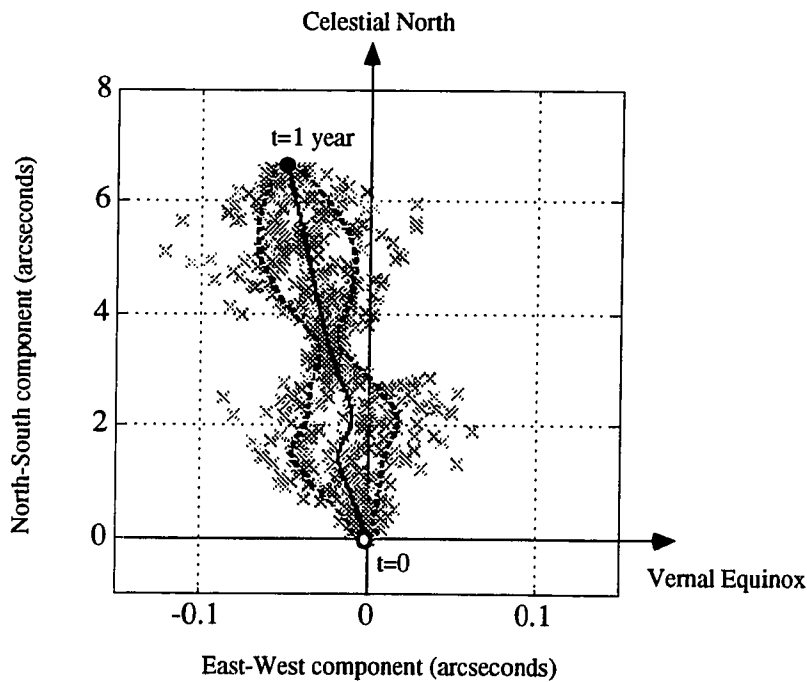


Figure 5.3 Results of step 1 filtering from a one-year simulation: true values of NS_s and EW_s (solid line) vs. estimated values (x's). Dashed lines indicate one-sigma envelope of the estimation accuracy.

is minimized at the beginning, in the middle, and at the end of the one-year mission because the annual aberration, which the step 1 filters use as a calibration signal, is modulated at the annual frequency and has maxima at these points. The maximal estimation error is about 80 milliarcseconds and is modulated at the annual frequency. The North-South and East-West components, NS_s and EW_s , comprise the slowly varying terms such as parallax, deflection of starlight, and relativistic precessions, which are now estimated by the step 2 filter.

5.2.3.3 Results of Step 2 Filtering

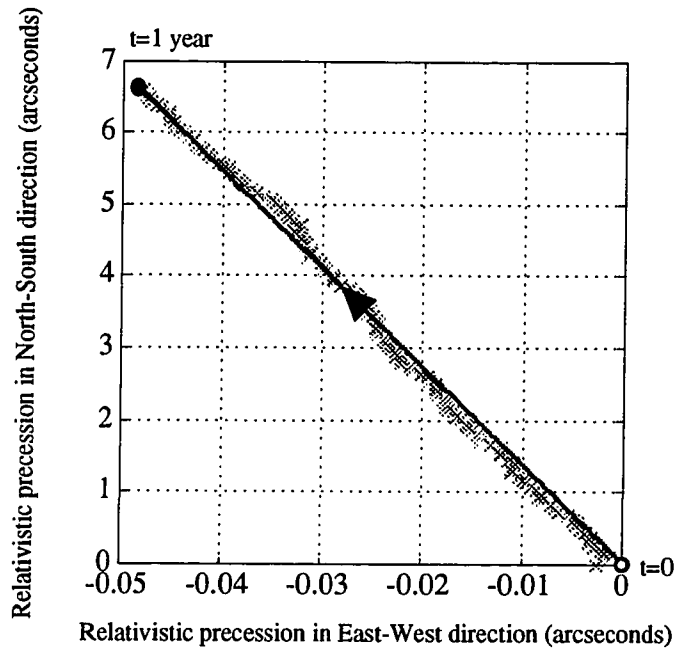
The step 2 filter processed the estimates from the step 1 filters by treating them as new measurements and estimated the final parameters given in Equation 5.7. Figures 5.4 (a), (b), and (c) show the estimates of the relativistic precession, the parallax, and the deflection of starlight, respectively. Again, the estimated values were plotted in the xy plane of the A-0 frame. The solid lines indicate the true values and the x's indicate the estimated values. The hollow circles represent the values at the beginning of the mission, and the filled circles represent them at the end of the mission. The North-South component of the relativistic precession is geodetic, and the East-West component is frame-dragging. The other two elements, parallax and deflection of starlight, are modulated at the annual frequency and are as small as the frame-dragging precession term. The final estimation errors and the expected rms errors calculated by the step 2 filter in a Monte Carlo simulation are listed in Table 5.4. For this Monte Carlo simulation, even though the final estimation error of the parallax was larger than the expected estimation error (1σ), those of the relativistic precession rates and the deflection of starlight were smaller than or equal to the expected error. I ran at least 20 Monte Carlo simulations and obtained the final estimation accuracy of Ω_G and Ω_F better than 0.5 milliarcsecond per year from each run. Figures 5.5 (a) and (b) show the time histories of Ω_G and Ω_F estimation, respectively. The dotted lines indicate the one-sigma envelope

of the expected estimation error, and the solid lines indicate the actual estimation errors. For both relativistic precession rates, the estimation error stayed within the one-sigma envelope about 60% of the one-year simulation, which indicated proper tuning of the Kalman filters. Thus, I verified that the two-step filters developed in Sections 5.2.1 and 5.2.2 yielded satisfactory final estimation errors with simulation.

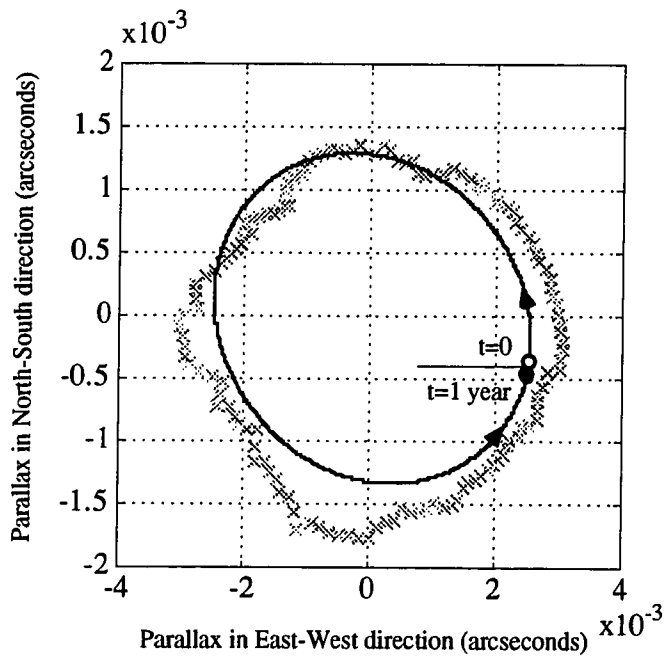
Although I used a science signal from only one gyroscope for the simulation, there will be four gyroscopes each with an independent SQUID readout system on-board for the science mission. It may be, hence, possible to improve the final estimation accuracy by a factor of two by combining the measurements from four readout systems assuming each measurement is independent.

Table 5.4 Final Estimates and Estimation Accuracy of Step 2 Filter

Step 2 filter states	Final estimation error	Final estimation accuracy (1σ)
North-South initial misalignment NS_0	-0.04 milliarcsecond	0.35 milliarcsecond
East-West initial misalignment EW_0	0.06 milliarcsecond	0.22 milliarcsecond
Geodetic precession rate Ω_G	0.17 milliarcsecond per year	0.53 milliarcsecond per year
Frame-dragging precession rate Ω_F	0.14 milliarcsecond per year	0.42 milliarcsecond per year
Parallax coefficient α	0.29 milliarcsecond	0.18 milliarcsecond
Deflection-of-starlight coefficient κ	0.12 milliarcsecond	0.12 milliarcsecond

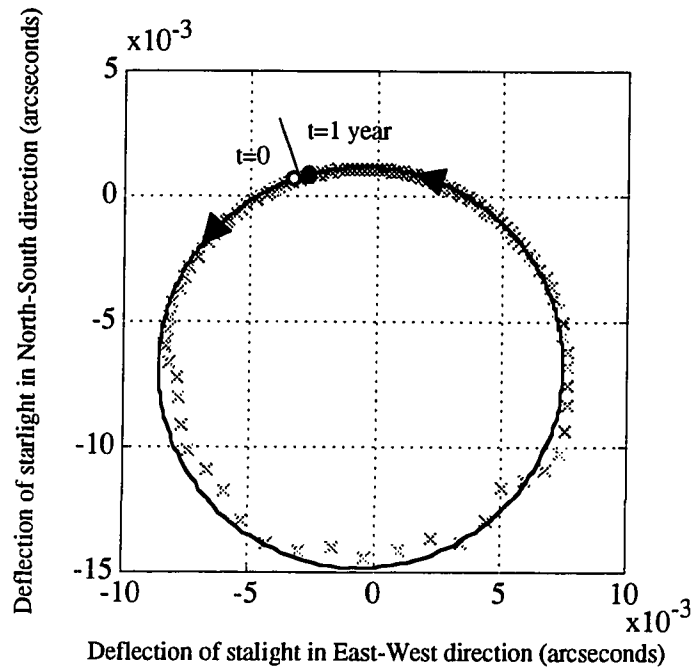


(a) Trajectory of relativistic precession - true values (solid line) vs. estimated values (x's).



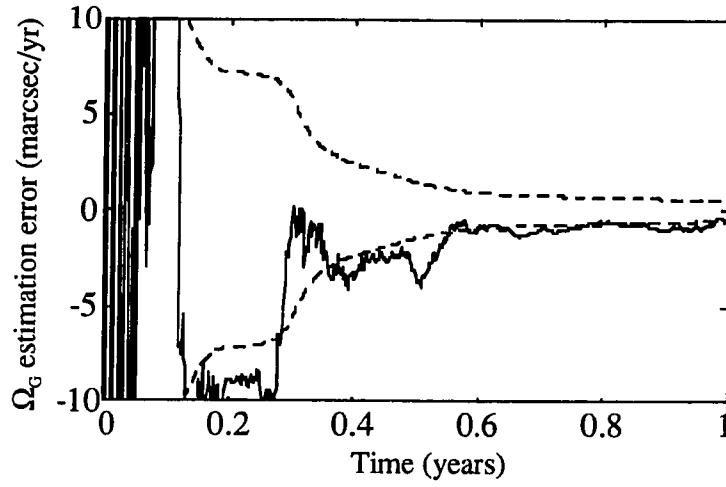
(b) Trajectory of parallax - true values (solid line) vs. estimated values (x's).

Figure 5.4 Results of step 2 filtering from a one-year simulation: true values (solid lines) vs. estimated values (x's) of relativistic precession, parallax, and deflection of starlight (continued on next page).

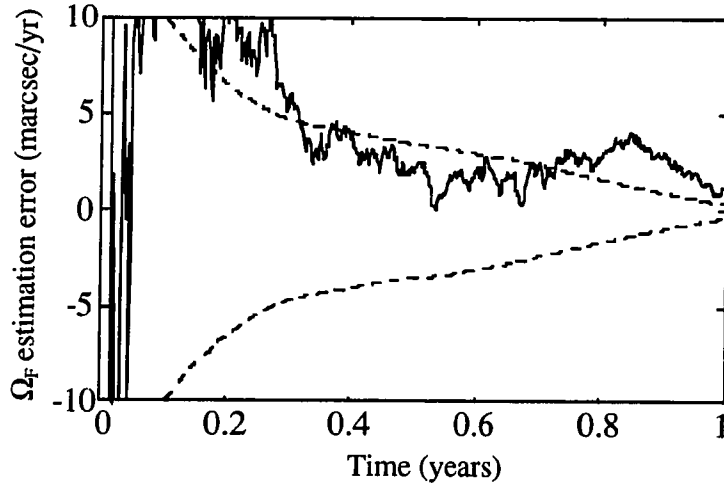


(c) True values (solid line) vs. estimated values (x's) of deflection of starlight.

Figure 5.4 Results of step 2 filtering from a one-year simulation: true values (solid lines) vs. estimated values (x's) of relativistic precession, parallax, and deflection of starlight (continued from previous page).



(a) Time history of estimation error (solid line) and 1σ envelope (dashed lines) of geodetic precession rate Ω_G . Final estimation accuracy = 0.53 (milliarcsecond per year).



(b) Time history of estimation error (solid line) and 1σ envelope (dashed lines) of frame-dragging precession rate Ω_F . Final estimation accuracy = 0.42 (milliarcsecond per year).

Figure 5.5 Results of step 2 filtering from a one-year simulation. Time history of the estimation error and 1σ envelope of the relativistic precession rates.

5.3 Recursive Algorithm

I developed a recursive algorithm for the data reduction, which further optimizes the estimation by providing better initial estimates to the step 1 and step 2 filters. The final estimation accuracy of two-step Kalman filters is mainly determined by three conditions: noise level of SQUID sensor, stability of SQUID readout parameters such as scale factor and bias, and accuracy of initial estimates. The effect of the last condition, the accuracy of initial estimates, is significant for the step 1 filters, which are extended Kalman filters. Extended Kalman filters linearize the measurement around *a priori* estimates, and the error associated with the linearization is proportional to the quadratic function of the estimation error. Thus, if the initial estimation error is too large, the linearization error becomes dominant compared with the measurement noise, and the solution of extended Kalman filter may converge to a false solution or the final estimation error may not be satisfactory. By giving better initial estimates to the extended Kalman filters, one can avoid such false convergence or unsatisfactory final estimation error.

5.3.1 Formulation of Recursive Filters

I modified the two-step filters to give them better initial estimates by feeding the output of step 2 filter back to restart the step 1 and step 2 filters. Figure 5.1 shows the diagrams of original two-step Kalman filters, and Figure 5.6 shows the modified filters. With the original filters, the initial conditions for the step 1 and step 2 filters are given by an operator and are summarized in Tables 5.2 and 5.3. The accuracy of the initial estimation depends on how well the operator knows the filter states prior to the estimation. Once the two-step filtering is completed using the initial conditions given by the operator, one obtains estimates of filter states with better accuracy and can use the estimated values to restart the step 1 and step 2 filters. Since the estimated states after

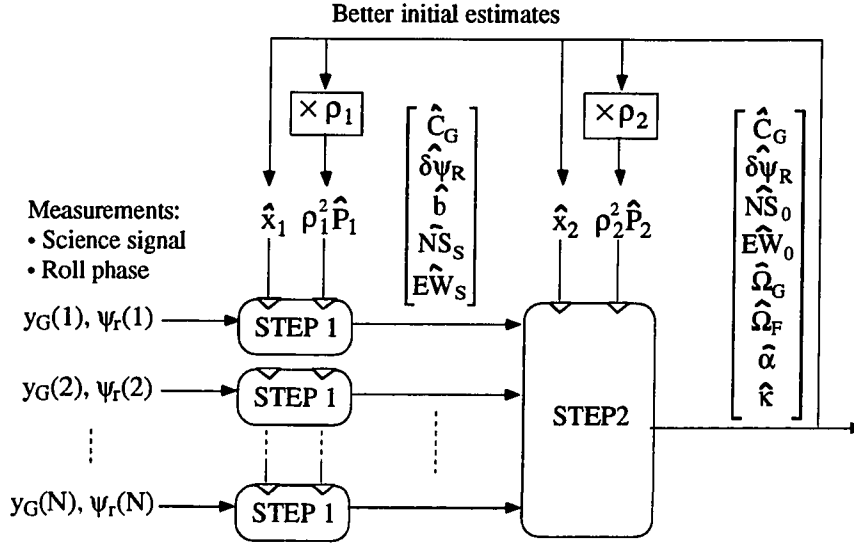


Figure 5.6 Diagram of recursive two-step Kalman filters.

one-year mission have much better accuracy than the initial estimates given by the operator, the linearization error of the second iteration (Figure 5.6) is decreased so that it does not become the dominant error compared with the SQUID sensor noise. Note that the final estimation accuracy terms, $\sqrt{\hat{P}_1(i,i)}$ ($i=1,\dots,5$) and $\sqrt{\hat{P}_2(i,i)}$ ($i=1,\dots,8$), are multiplied by the relaxation factors, ρ_1 and ρ_2 , respectively, when fed back to restart the step 1 and step 2 filters. The relaxation factors range from 15 to 40 and prevent the two-step filters from closing on the measurements. If the relaxation factors are set to one, the filters do not use the measurements to improve the estimation because the initial estimation error becomes smaller than the SQUID noise.

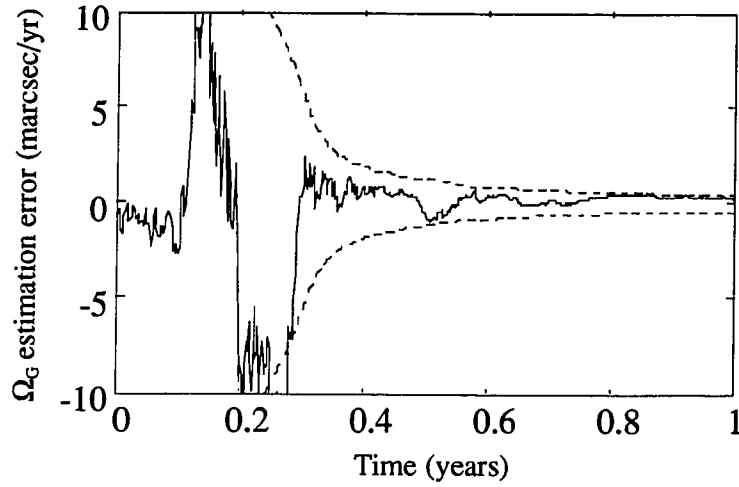
This iterative approach is possible because the GP-B program does not require real-time estimation of relativistic precession, and the data reduction can employ not only filtering but also smoothing. The following section presents the simulation results of this recursive algorithm.

5.3.2 Results of Recursive Filter Simulation

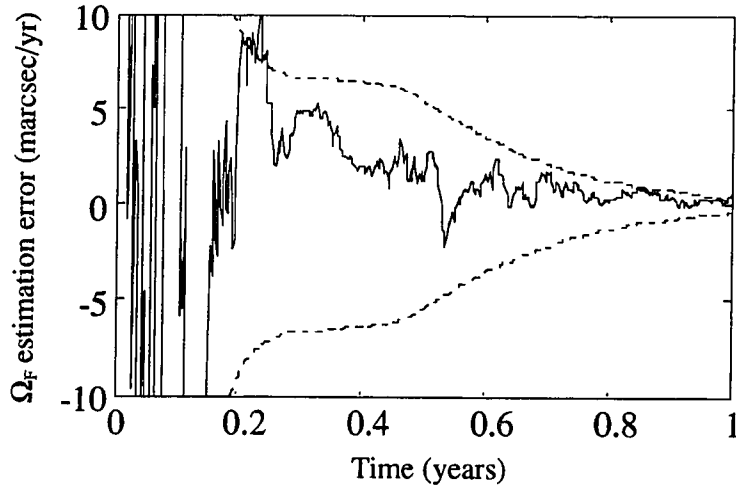
The recursive filters were tested with five Monte Carlo simulations, and this section presents the results of one of those simulations. The recursive filters consistently showed 18% better accuracy for the estimate of geodetic precession rate and 15% better accuracy for the estimate of frame-dragging precession rate. Figure 5.7 shows the time histories of Ω_G estimation error and Ω_F estimation error. The one-sigma envelopes were narrower and showed faster convergence than those of the original filters. Table 5.5 compares the final estimation accuracy of the original filters and the modified filters. Even though the first recursion showed consistent improvement over the original filtering, the second recursion and later did not show any further improvement because the linearization error was already smaller than the SQUID noise with the first recursion.

Table 5.5 Final estimation accuracy of original filters and recursive filters

Filter states	Final estimation accuracy of original filters (milliarcseconds per year)	Final estimation accuracy of recursive filters (milliarcseconds per year)
Geodetic precession rate Ω_G	0.53	0.43
Frame-dragging precession rate Ω_F	0.42	0.35



(a) Time history of estimation error (solid line) and 1σ envelope (dashed lines) of geodetic precession rate Ω_G . Final estimation accuracy = 0.43 (milliarcsecond per year).



(b) Time history of estimation error (solid line) and 1σ envelope (dashed lines) of frame-dragging precession rate Ω_F . Final estimation accuracy = 0.35 (milliarcsecond per year).

Figure 5.7 Results of recursive two-step filtering from a one-year simulation. Time history of the estimation error and 1σ envelope of the relativistic precession rates.

5.4 Polhode Modeling and Estimation

I investigated the effects of the polhode motion of the gyroscope on the final estimation accuracy of relativistic precession rates. As I pointed out in Section 1.2.5, the polhode motion of the gyroscope affects the science signal through the trapped flux. In this analysis, I modeled the effects of the polhode motion on the science signal by the scale factor variation of SQUID readout (Ref. 53). I tested the two-step Kalman filters with the scale factor variation and also modified the filters to estimate the variation terms. Even though the model I used was over-simplified⁵, it provided a good first-cut analysis and helped understand the data reduction from the frequency-separation point of view.

5.4.1 Modeling of Polhode Motion in Science Signal

I assumed a symmetrical rotor, for which the polhode motion is a sinusoidal motion of the spin axis in the gyro-body fixed frame. Therefore, a new measurement equation for the science signal is given by the following equation:

$$y_G = C_G \left[1 + \varepsilon_p \cos(\omega_p t + \phi_{p0}) \right] \left[(EW_s + \lambda_1) \sin \psi_r - (NS_s + \lambda_2) \cos \psi_r \right] + b_{sq} + n_{sq} \quad (5.10)$$

where ε_p : amplitude of polhode modulation
 ω_p : angular velocity of polhode motion (radians/second)
 ϕ_{p0} : initial phase of polhode motion (radians)

As an initial investigation, I assumed these three parameters to be constant throughout the mission, which may not be true for the actual experiment. I simulated the science signal according to Equation 5.10 and tested the original two-step filters developed in Section 5.1. In addition, I modified the two-step filters to accommodate the new

⁵ J. P. Turneaure pointed out that “over-simplified” might not describe the limitation of this study accurately because the actual trapped flux signal includes many harmonics in ω_p with comparable signal strength. I agree that the model I used may not lead to the heart of the problem because we don't know whether it has the same effect on data reduction as the actual trapped flux signal. This study is significant in the sense that it demonstrated the need for serious investigation.

unknown parameters such as ε_p and ϕ_{p0} . The modified two-step filters have extra states to estimate the polhode terms. The new state vectors for the step 1 and step 2 filters are given by the following equations, respectively:

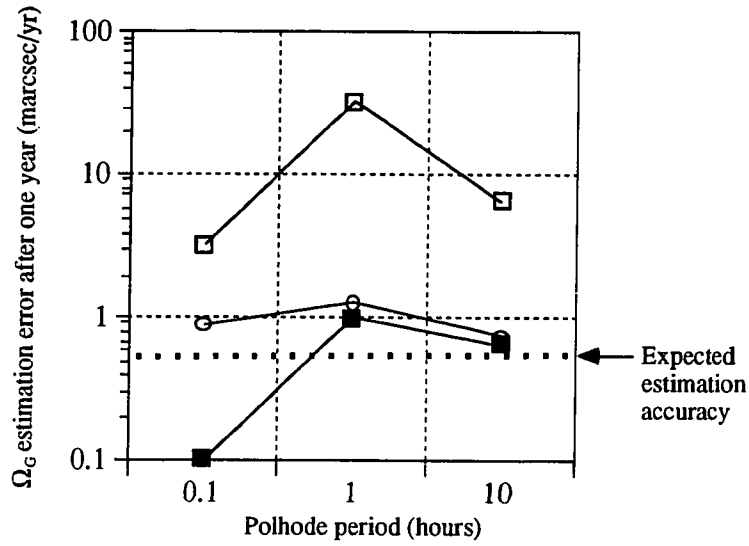
$$x_1 = [C_G \quad \delta\phi_r \quad b \quad NS_s \quad EW_s \quad \varepsilon_p \quad \phi_{p0}]^T \quad (5.11)$$

$$x_2 = [C_G \quad \delta\phi_r \quad NS_0 \quad EW_0 \quad \Omega_G \quad \Omega_F \quad \alpha \quad \kappa \quad \varepsilon_p \quad \phi_{p0}]^T \quad (5.12)$$

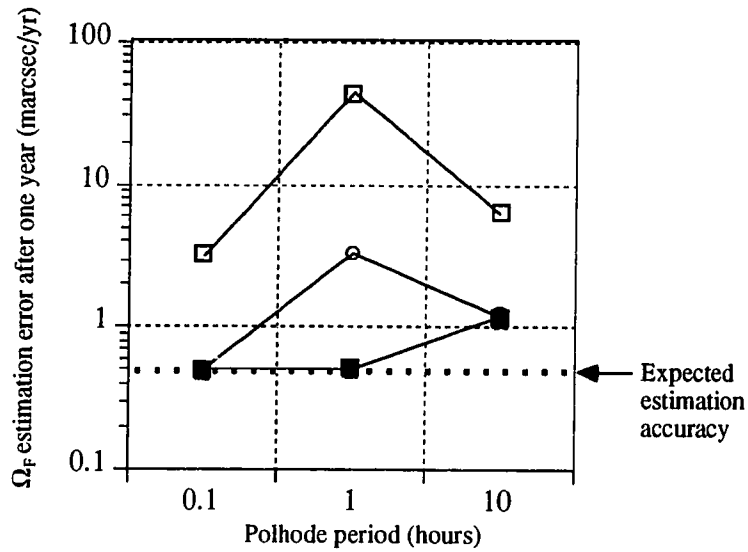
Thus, I tested two sets of two-step filters; one with original state vectors (Equations 5.1 and 5.7) and the other with modified state vectors with polhode states (Equations 5.11 and 5.12). I also investigated the effect of longer step 1 window on the estimation of polhode terms. The following section summarizes the results of two-step filtering with polhode simulation.

5.4.2 Results of Two-step Filtering with Polhode Simulation

I tested three polhode periods, 0.1 hour, 1 hour, and 10 hours with 1% modulation amplitude, i.e., $\varepsilon_p=0.01$. The results showed that the one-hour polhode period yielded the worst estimation accuracy at the end of a one-year simulation. The modified two-step filter consistently showed better accuracy than the original filters. Figures 5.8 (a) and (b) shows the final estimation error of relativistic precession rates with three different filter schemes: (1) original two-step filters with one-orbit step 1 window, (2) original two-step filters with fifteen-orbit step 1 window, and (3) modified two-step filters with fifteen-orbit step 1 window. The first scheme, the original filters with one-orbit window, became unstable with all polhode periods. The second scheme, longer window with fifteen orbits, stabilized the filters, but the final estimation accuracy was still worse than the expected accuracy, which is indicated by the dashed lines in Figure 5.8. The last filtering scheme, the modified two-step filters with a fifteen-orbit window, was stable for all the cases and yielded the best results.



(a) Final estimation error of geodetic precession rate Ω_G .



(b) Final estimation error of frame-dragging precession rate Ω_F .

- one-orbit step 1 window
- fifteen-orbit step 1 window
- fifteen-orbit step 1 window with polhode estimation

Figure 5.8 Final estimation error of the relativistic precession rates after a one-year simulation with polhode modulation of the scale factor.

The longer step 1 window clearly helped the filters by stabilizing them. I analyzed the frequency components of the modulated science signal to assess the effect of the window size and the polhode period. If I expand the science signal with polhode terms (Equation 5.10) according to the frequency modulation, the science signal is now represented by five terms as follows:

$$\begin{aligned}
y_G = & C_G (NS_s \sin \psi_r - EW_s \cos \psi_r) \\
& + C_G (\lambda_1 \sin \psi_r - \lambda_2 \cos \psi_r) \\
& + b_{sq} \\
& + \varepsilon_p C_G \cos(\omega_p t + \phi_{p0}) (NS_s \sin \psi_r - EW_s \cos \psi_r) \\
& + \varepsilon_p C_G \cos(\omega_p t + \phi_{p0}) (\lambda_1 \sin \psi_r - \lambda_2 \cos \psi_r)
\end{aligned} \tag{5.13}$$

The first three terms are the same as the original science signal (Equation 5.5), but the last two terms represent the modulation of the scale factor induced by the polhode motion of the gyroscope. Similarly to Equation 5.5, the first term is the roll signal located at the roll frequency f_r , the second term is the calibration signal located at $f_r \pm f_o$, where f_o is the orbital frequency, and the third term is bias at dc. I call the last two terms *polhode signals*, and they are spectrally located at $f_r \pm f_p$ and at $f_r \pm f_o \pm f_p$, respectively, where f_p is the polhode frequency. Figure 5.9 shows the frequency peaks of the modulated signal. Each peak corresponds to one of the five terms in Equation 5.12 and is labeled by the number of the corresponding term, i.e., the roll signal corresponds to the first term in Equation 5.13 and is labeled by No.1, and so on. Again the amplitude is not to scale. The peaks of polhode signals exist around the roll signal separated by the polhode frequency. As the polhode period increases, the polhode signals move closer to the roll signal and start to interfere with it. In order to predict the amount of interference, I defined a spectral *vicinity* around the roll and calibration signals, whose width is determined by the frequency bin size Δf_1 of step 1 filters. Figure 5.9 shows the spectral

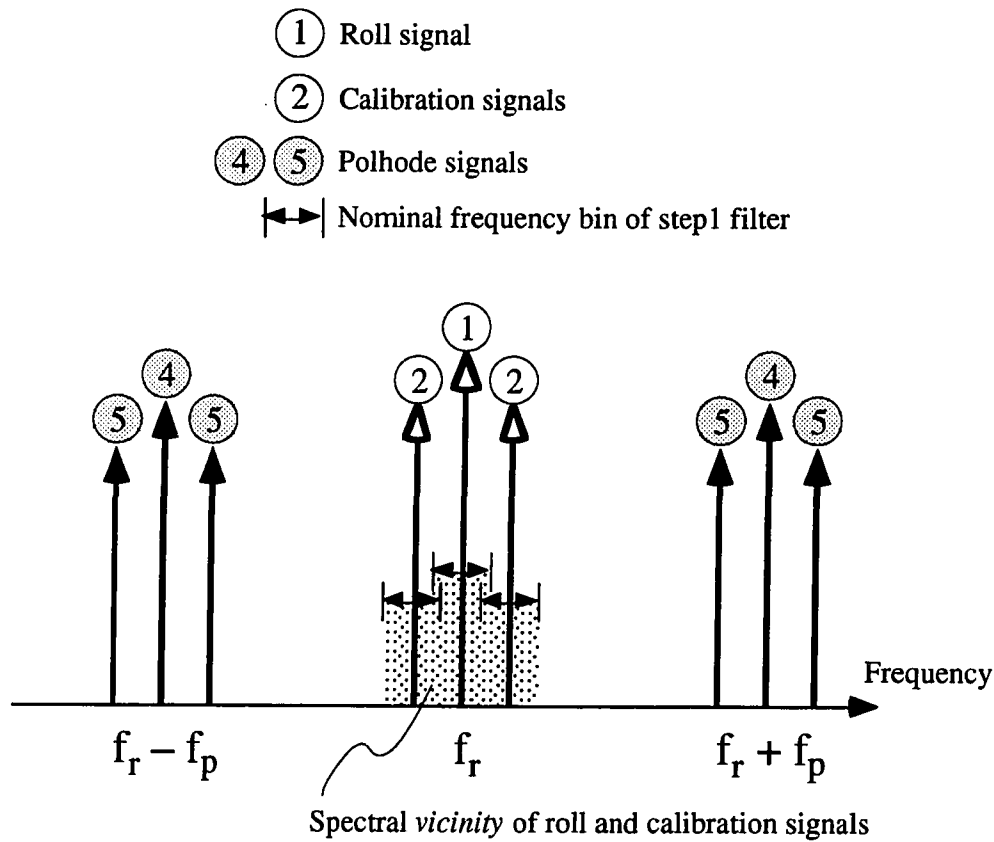


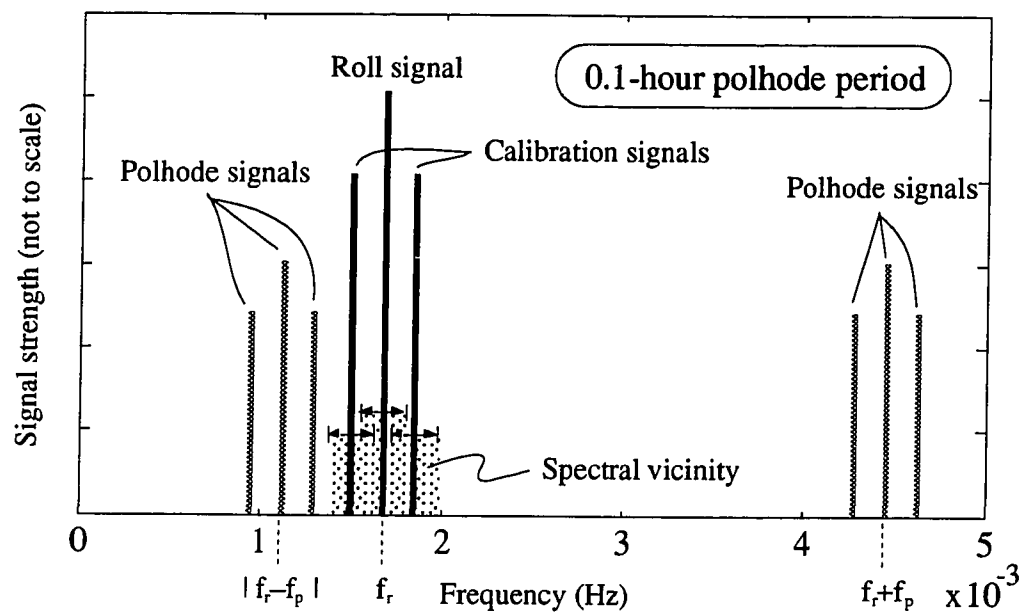
Figure 5.9 Frequency components of a science signal with polhode modulation of the scale factor (f_r =roll frequency, f_o =orbital frequency, f_p =polhode frequency).

vicinity by the shaded area around the roll signal for one-orbit step 1 window, which is the default window size. If the polhode signals are located outside of the vicinity, the step 1 filters should be able to resolve the roll and calibration signals because each step 1 filter provides finer frequency resolution with Δf_1 smaller than the polhode frequency. If the polhode signals move into the vicinity, the step 1 filters can no longer distinguish the roll signal from the polhode signals. Therefore, one can predict interference from the polhode signals by examining the location of polhode signals with respect to this vicinity.

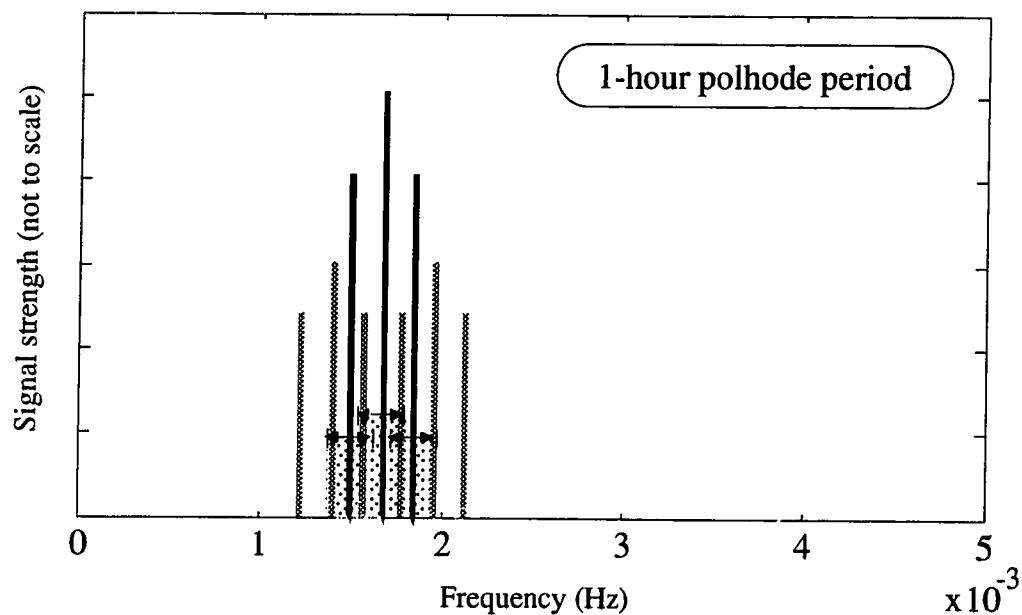
Figures 5.10 (a), (b), and (c) show the spectra of the science signal with 0.1-hour, 1-hour, and 10-hour polhode periods, respectively. At 0.1-hour period, the polhode frequency $f_p=2.8e-3$ Hz is about sixteen times higher than the orbital frequency $f_o=1.7e-4$ Hz. Thus, the polhode signals exist outside of the vicinity and have little effect on the step 1 filtering [see Figure 5.10 (a)]. The last scheme with a fifteen-orbit window and a polhode estimation resulted in the best accuracy while all the schemes were stable. Note that the lower peak of the polhode signal is a reflection of it at the negative frequency. At one-hour period, the polhode frequency $f_p=2.8e-4$ Hz is close to the orbital frequency, and the polhode signals are within the vicinity of the roll signal [see Figure 5.10 (b)]. The step 1 filters could not calibrate the scale factor and the phase bias and yielded the worst results because of the corruption of the calibration signals by the polhode signals. The first two schemes became unstable, and the last scheme was stable but gave unsatisfactory results. At ten-hour period, the polhode frequency $f_p=2.8e-5$ Hz is about 6.5 times slower than the orbital frequency. Thus, the polhode signals move further into the roll signal [see Figure 5.10 (c)]. Even though the calibration signals are corrupted by the polhode signals, the estimation accuracy was slightly improved over the case with one-hour polhode period. All the schemes were stable but the final estimation accuracy was worse than the expected accuracy.

According to the results summarized in Figure 5.8, the faster polhode period showed better results by spectrally separating the polhode signals from the roll and calibration signals, and the longer step 1 window improved the estimation accuracy by providing finer frequency resolution. The optimal polhode period can be determined by examining the location of the polhode signals with respect to the vicinity of roll signal. The polhode signals should be as far as possible from the vicinity without causing the reflection of the spectrum. The polhode frequency that satisfies this condition is given by

$$f_p \equiv f_r \quad (5.14)$$

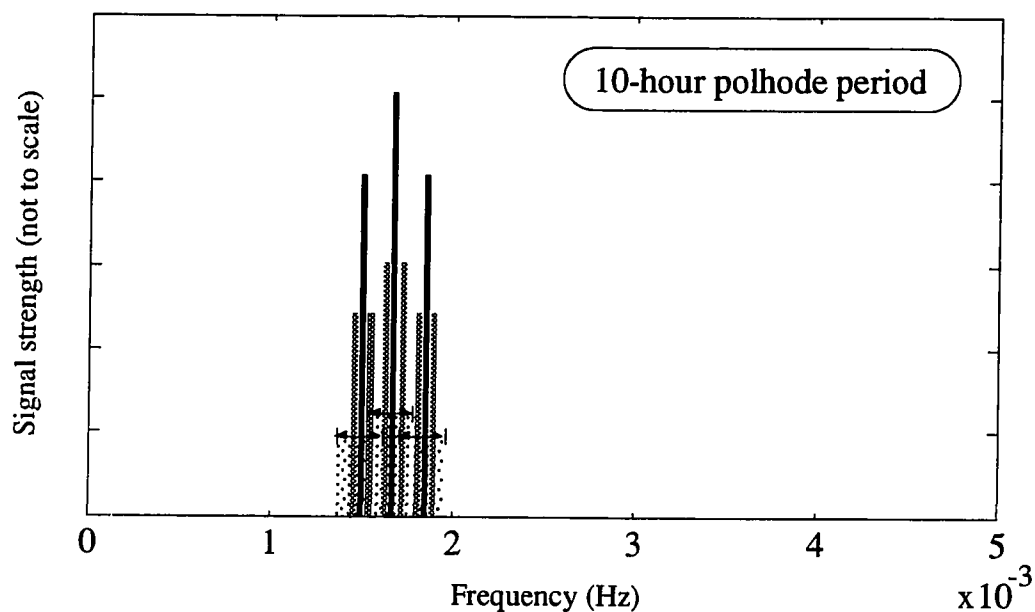


(a) Spectral decomposition of the science signal with a 0.1-hour polhode period.



(b) Spectral decomposition of the science signal with a 1-hour polhode period.

Figure 5.10 Spectral decomposition of the science signal with various polhode periods (continued on next page).



(c) Spectral decomposition of the science signal with a 10-hour polhode period.

Figure 5.10 Spectral decomposition of the science signal with various polhode periods (continued from previous page).

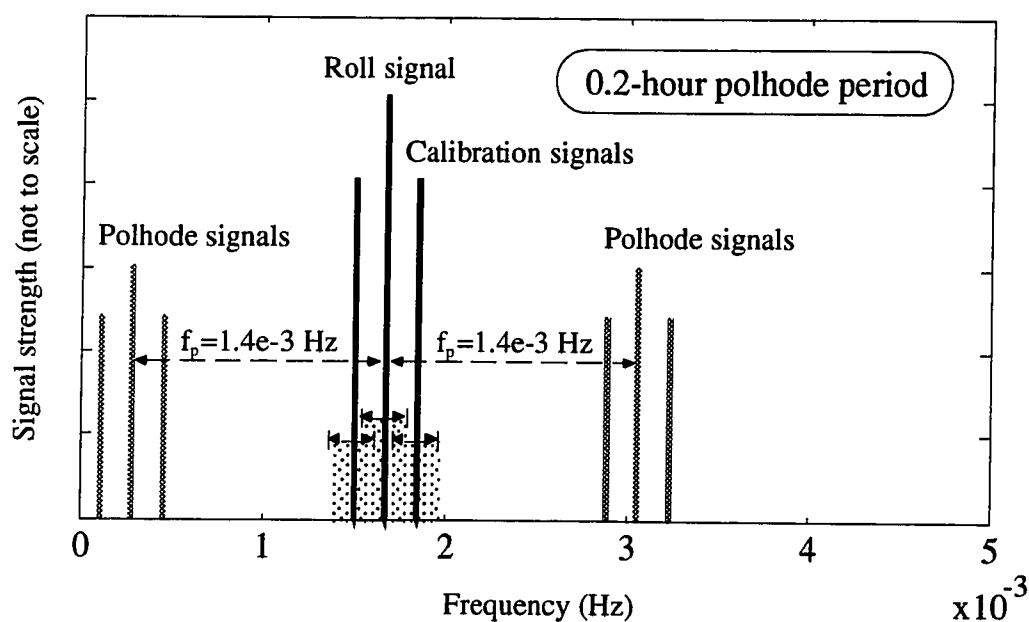


Figure 5.11 Spectral decomposition of the science signal with an optimal polhode period 0.2 hour. Spectral separation between the roll signal and the polhode signals is about 1.4 mHz.

For the ten-minute roll period, the optimal polhode period is about 0.2 hour. Figure 5.11 shows the spectrum of the science signal with $f_p=1.4\text{e-}3$ Hz. The lower peak of the polhode signal is now located near dc, and the polhode signals are spectrally separated from the roll/calibration signals. I should point out that this conclusion is based on the signal model (Equation 5.10), which assumed that the trapped flux on the gyroscope with a polhode motion affected the readout scale factor. As I mentioned at the beginning of this section, this model is over-simplified, and a more precise model for the trapped flux signal has to be used to verify the claim (Equation 5.14). L. L. Wai and Y. M. Xiao developed more precise models of the trapped flux signal, which should be implemented in the niobium bird truth model (Ref. 54, 55).

5.4.3 Effects on Gyroscope Dynamics and Requirements of Readout System

The analysis in the previous section showed that the optimal polhode period is about 0.2 hour for ten-minute roll, and I will discuss the effect of shorter polhode period on the gyroscope dynamics and the requirements of the readout system. I assume a symmetric rotor to simplify the analysis. The polhode frequency can be determined by the spin frequency, the inertia matrix of a gyroscope, and the separation angle between the spin axis and the inertia principal axis. The inertia matrix of a symmetric rotor in principal axes is given by

$$\mathbf{I} = \begin{bmatrix} I & 0 & 0 \\ 0 & (1 + \varepsilon_i)I & 0 \\ 0 & 0 & (1 + \varepsilon_i)I \end{bmatrix} \quad (5.15)$$

where ε_i : inertia unbalance coefficient of rotor

Then, the polhode frequency is given by the following equation (Ref. 50):

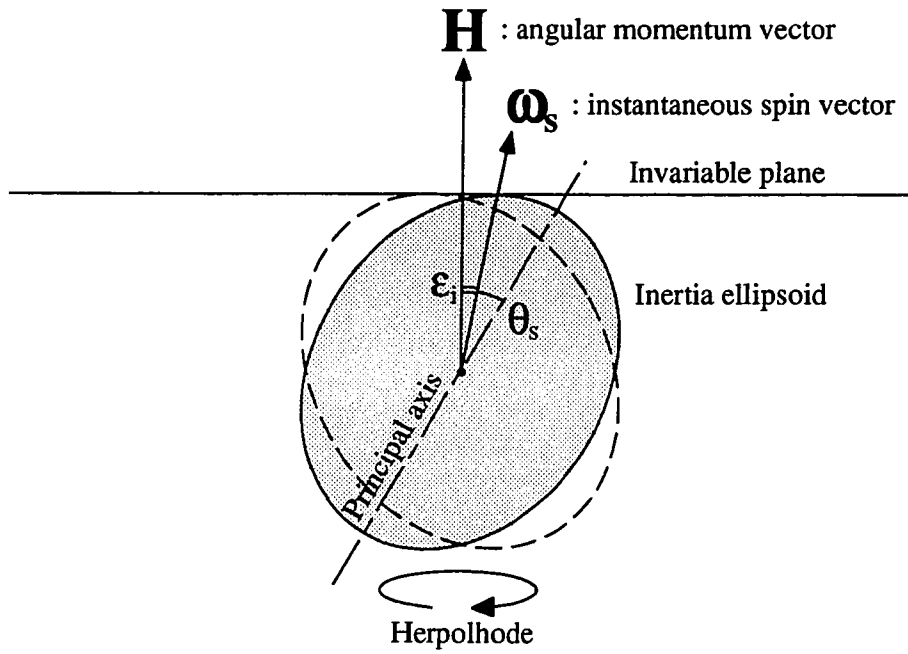


Figure 5.12 Poinsot's inertia ellipsoid and an invariable plane.

$$\omega_p = \frac{\varepsilon_i}{1 + \varepsilon_i} \omega_s \cos \theta_s \quad \text{for } 0 < \theta_s < \pi \quad (5.16)$$

$$\approx \varepsilon_i \omega_s \cos \theta_s$$

where ω_p : polhode frequency (radians per second)
 ω_s : spin frequency (radians per second)
 θ_s : separation angle between spin vector and inertia principal axis of symmetry (radians) [see Figure 5.12]

Assuming that the separation angle is small, which is likely when friction causes an energy dissipation, Equation 5.16 can be further approximated as

$$\omega_p \approx \varepsilon_i \omega_s \quad (5.17)$$

Thus, faster polhode means larger inertia unbalance ϵ_i , or vice versa, given constant spin frequency. If I assume 170-Hz spin frequency and 0.2-hour polhode period, the inertia unbalance coefficient is

$$\epsilon_i = 8.2 \times 10^{-6} \quad (5.18)$$

This coefficient corresponds to about 1.7 arcseconds of displacement between the gyroscope's spin axis and the angular momentum vector. This angle is better described by a Poinsot's inertia ellipsoid [see Figure 5.12]. The angle between the instantaneous spin vector ω_s and the angular momentum vector H is about 1.7 arcseconds, and the spin vector travels around the angular momentum vector at about the spin frequency in inertial space; this motion is called *herpolhode*. In Figure 5.12, note that the general relativity influences the direction of angular momentum. Even though we are trying to measure the relativity effects on the angular momentum, the SQUID readout system measures the direction of the instantaneous spin axis, to which the London moment is aligned. Thus, the output of the SQUID magnetometer, the science signal, includes not only the relativistic precession of the gyroscope but also the herpolhode of the spin axis. During the data reduction synthesis in Chapter 4, I neglected the herpolhode because it is modulated at the spin frequency and can be averaged by integrating over the ten-second sampling period. Even though this claim is valid during the filter synthesis, the SQUID still has to track the herpolhode signal. If the polhode frequency becomes higher, the angle of herpolhode ϵ_i becomes larger, and the slew rate of the signal increases as a result. Thus, higher polhode frequency imposes a tighter requirement on the slew rate of the SQUID, which reduces the stability of SQUID operation. I did not investigate this issue any further, but one should address the slew rate requirement on the SQUID in determining the requirement on the polhode frequency of the science gyroscope.

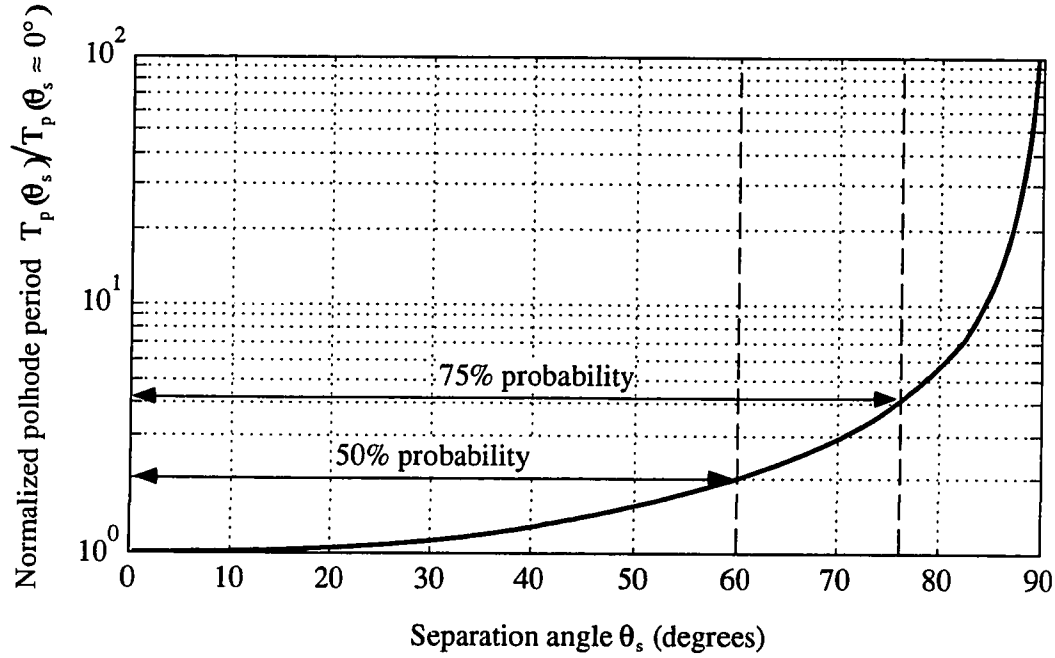


Figure 5.13 Normalized polhode period vs. separation angle between the spin vector and the inertia principal axis of symmetry with $\omega_s=170$ Hz, $\epsilon_i=8.2 \times 10^{-6}$.

Another important case regarding the gyroscope dynamics is the polhode with a large separation angle between the spin vector and the inertia principal axis. This scenario is possible for the GP-B program because the gyroscope is levitated in vacuum with almost no energy dissipation. Thus, depending on the spin-up condition, the spin vector can be close to the separatrix (or separatrices for an asymmetric gyroscope). In this case, the approximation made by Equation 5.17 is not valid anymore, and the polhode period T_p is given by

$$T_p = \frac{2\pi}{\epsilon_i \omega_s \cos \theta_s} \quad \text{for } 0 < \theta_s < \frac{\pi}{2} \quad (5.19)$$

where

ϵ_i : inertia unbalance coefficient of rotor

- ω_s : spin frequency (radians per second)
- θ_s : separation angle between spin vector and inertia principal axis of symmetry (radians)

As shown in Figure 5.13, the polhode period goes to infinity as the separation angle approaches 90 degrees with a constant ϵ_i . Assuming that there is no energy dissipation so that the probability distribution function of the spin vector is uniform over the surface of the gyroscope, the dashed lines in Figure 5.13 indicate 50% and 75% cumulative probability boundaries. The separation angle will be less than 60 degrees with 50% probability and less than 76 degrees with 75% probability. The actual polhode period is two times longer at 60 degrees and about four times longer at 76 degrees than that at $\theta_s \approx 0^\circ$. This implies that, although we can choose a gyroscope with 0.2-hour polhode period at $\theta_s \approx 0^\circ$ so that the Kalman filter can separate the trapped flux signal better, the actual polhode period can be much longer than what we expect depending on the separation angle θ_s . Note that I made a very crude assumption on the distribution of the spin axis when I calculated the cumulative probability. There will be an energy dissipation during the spin-up caused by the friction of helium gas, which may bring the spin vector close to the maximum inertia axis. Then, the probability distribution function of the spin vector is not uniform over the gyroscope surface. Since the spin-up condition is hard to simulate, this needs to be tested by the experiment. One should spin up the gyroscope many times and observe the separation angle between the spin vector and the maximum inertia axis. The actual probability distribution function can be estimated from these experimental results and used to calculate the mean polhode period with a constant ϵ_i .

5.5 Effects of Pointing Error

The realistic measurement equations of the science signal (Equations 4.73a and 4.73b) include the pointing error terms because the SQUID magnetometer measures the angle between the gyroscope's spin axis and the satellite's telescope axis. These pointing error terms can affect the final estimation accuracy of two-step Kalman filters depending on their magnitude. I investigated the effect of the telescope pointing error on the filters by varying its rms value, and this section presents the results of that analysis.

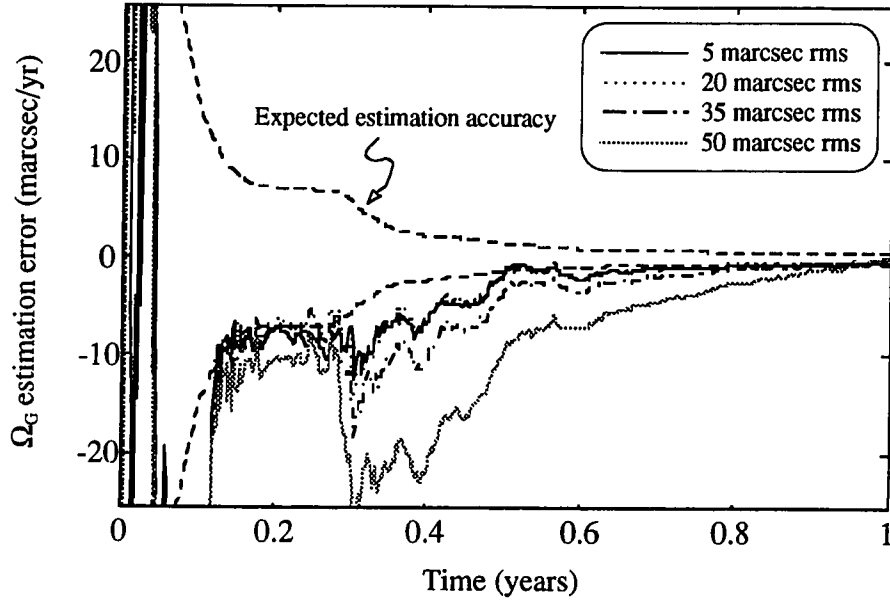
R. S. DiEsposti (Ref. 19) initially investigated the telescope pointing error and developed the gain-matching scheme to subtract the pointing error terms from the science signal. Even though he demonstrated that the scheme successfully matched the gyro and telescope scale factors within 1% after a few days of integration, he did not discuss how much improvement in the final estimation accuracy he could attain by implementing the matching scheme, which lead to the ongoing debate whether we need to subtract the telescope pointing error from the science signal. N. J. Kasdin (Ref. 26, 56) later designed the telescope pointing controller and showed that the telescope axis can be controlled within 20-milliarcsecond rms of the optical direction of Rigel. Kasdin selected 10 Hz as the sampling frequency for the controller. I tested the two-step filters with various pointing errors around the nominal rms value, which is 20 milliarcseconds, and found that the nominal pointing error had little effect on the final estimation accuracy and, therefore, that the gain-matching scheme may not be necessary during normal operation. The following sections present the results from the Monte Carlo simulations that I conducted.

The simulations were based on the truth model that I developed in Chapter 4. I tried four cases with different pointing error levels; 5, 20, 35, and 50-milliarcsecond rms values. Figures 5.14 (a) and (b) show the time history of geodetic and frame-dragging precession estimation, respectively. The pointing error with 20-milliarcsecond rms value

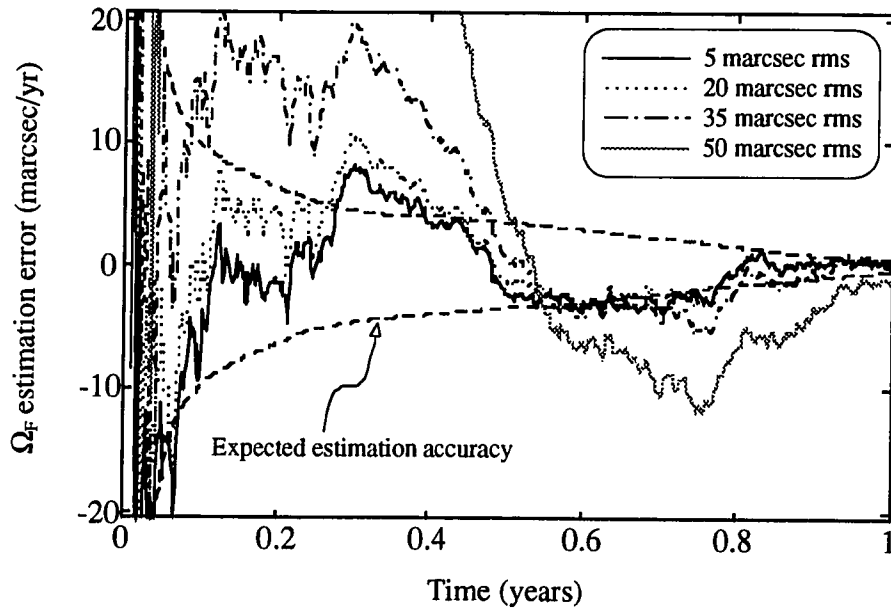
showed very little effect on the time history of estimation error compared with the 5-milliarcsecond rms value. With 35-milliarcsecond rms value, the pointing error became dominant compared with the 5-hour SQUID noise, and the estimation error started to show large deviation from the 5 and 20-milliarcsecond cases. Thus, these Monte Carlo simulations showed that the pointing error with 20-milliarcsecond rms value did not degrade the final estimation accuracy of relativistic precession rates. Even though these results suggest that we do not need to implement the gain-matching scheme under current design specifications, further investigation is still needed in determining whether we should abandon the gain-matching scheme because we may still need the scheme in four cases: (1) faster satellite roll, (2) better SQUID with higher signal-to-noise ratio, (3) unexpectedly large pointing error caused by abnormal operation of the control system, and (4) bias in the pointing error. In the case of faster satellite roll, the SQUID noise has less power at the roll frequency because of the $1/f$ noise characteristics explained in Chapter 4. Thus, the pointing error with a 20-milliarcsecond rms can become dominant compared with the SQUID noise because of improved signal-to-noise ratio in the SQUID. In this case, we need to subtract the telescope pointing error terms from the science signal or improve the pointing accuracy accordingly. For the same reason, the better SQUID with higher signal-to-noise ratio implies the need for subtracting the pointing error. The last case, the unexpectedly large pointing error can pose a threat to the whole program, but with the gain-matching scheme, we may be able to subtract the pointing error larger than the nominal value.

I mentioned the need for further investigation of the effect of the pointing error on the final estimation accuracy in this section. Along with the data reduction analysis, we need to clarify the meaning of the 20-milliarcsecond rms for the pointing error. Kasdin did not show the power spectral density of the pointing error of his simulation and did not state the integration time he used to calculate the rms value. The integration time of my

simulation were 10 seconds, and the scaling I used for the pointing error might not be correct if Kasdin's integration time was other than 10 seconds. In order to calculate the rms value for the pointing error correctly, we need to define the power spectral density of the pointing error in the continuous domain and convert it to its discrete equivalent according to the integration time.



(a) Time history of Ω_G estimation error with various pointing errors (rms).



(b) Time history of Ω_F estimation error with various pointing errors (rms).

Figure 5.14 Time history of the estimation error of the relativistic precession rates with various telescope pointing errors.

5.6 Effects of Roll Period

I investigated the effect of the satellite's roll period on the final estimation accuracy of relativistic precession rates. The science signal is modulated at the roll frequency, and the signal-to-noise ratio can be improved by speeding up the satellite's roll because the SQUID noise has $1/f$ power spectral density. I tested the data reduction scheme with a one-minute roll period and a ten-minute roll period. The following sections describe the results of these simulations.

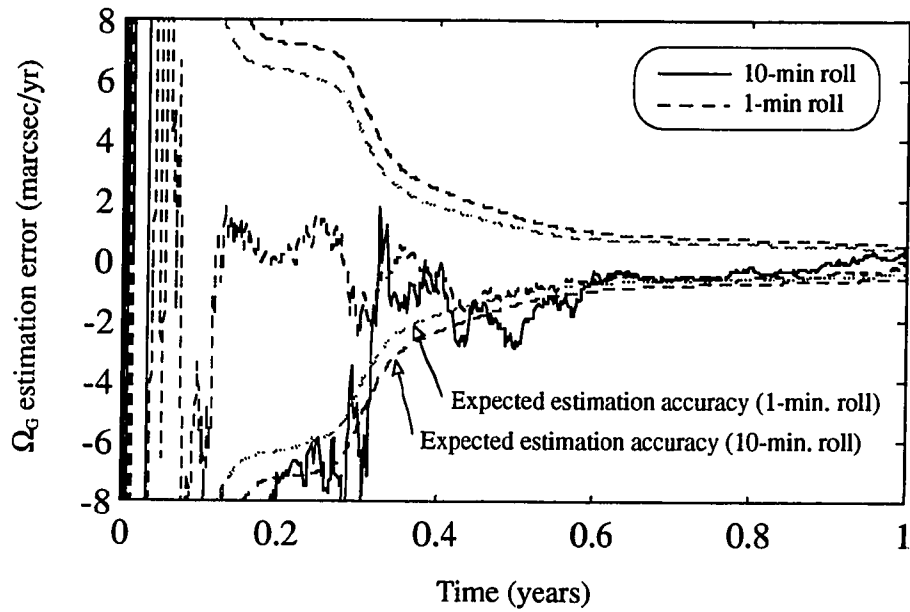
Figures 5.15 (a) and (b) show the estimation errors of the geodetic and frame-dragging precession rates, respectively, during a one-year simulation. The solid line in each figure indicates the estimation error with a ten-minute roll period, and the dashed line indicates that with a one-minute roll period. The estimation errors are bounded by the one-sigma envelopes of the expected estimation accuracy calculated by the Kalman filters. The outside envelopes are for the ten-minute case and the inner ones are for the one-minute case. Table 5.6 compares the final estimation accuracy for both roll periods. I could improve the final estimation accuracy of the geodetic precession rate by 24% and that of the frame-dragging precession rate by 22% when I speeded up the roll period from ten minutes to one minute. However, these improvements were not as impressive as I expected given the gain of signal-to-noise ratio in the SQUID magnetometer. If the satellite's roll is speeded up by a factor of 10, the noise power at the roll frequency is reduced by the same factor as shown in Figure 1.5. Thus, the final estimation accuracy should be improved by a factor of $\sqrt{10}$. The simulation showed less improvement because of following reasons⁶:

- Conservative tuning for the one-minute roll case;
- Linearization error became dominant compared with the SQUID noise;

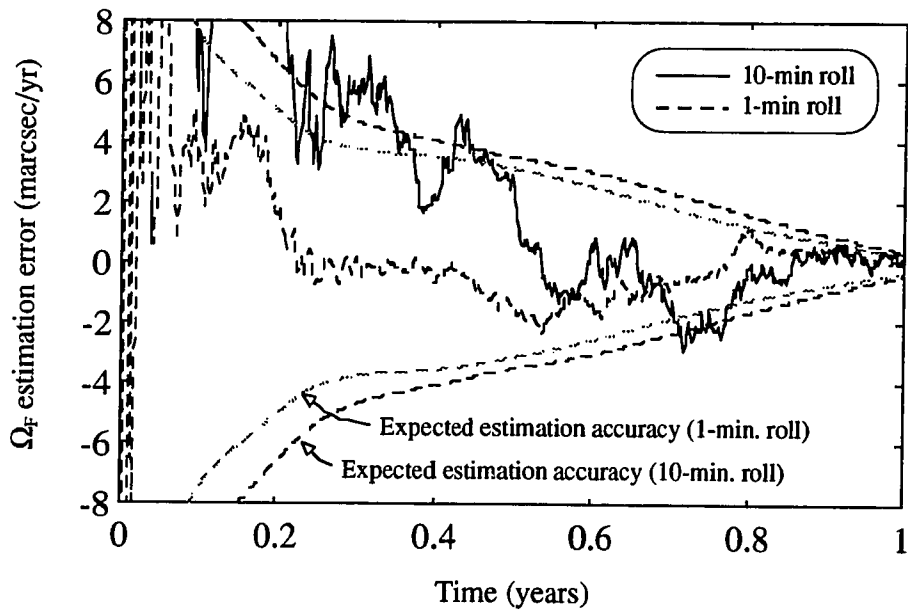
⁶ I did not have time to investigate each effect to determine the dominant error source because the investigation of the one-minute roll started too late for the publication of this thesis.

- Other error sources such as telescope pointing error, roll phase error, and quantization error became dominant compared with the SQUID noise.

The linearization error is especially large at the beginning of the filtering and is proportional to the quadratic function of the estimation error. Even though the estimation error associated with the initial error decays exponentially for the linear filters, it decays slower for the non-linear filters and has larger effects on the final estimation accuracy. Thus, the requirements on the initial estimation errors have to be re-investigated for the one-minute roll case. The same argument is possible for the other error sources such as the telescope pointing error, roll phase error, quantization error, etc. For example, I found that the telescope pointing error with a 20-milliarcsecond rms had little effect on the final estimation accuracy for the ten-minute roll case, but this claim may not be true for the one-minute roll case. The nominal value for the telescope pointing error should be improved according to the improvement of the SQUID's signal-to-noise ratio, i.e., the nominal value should be about 6-milliarcsecond rms for one-minute roll. Another example is the quantization error in the A-to-D converter. Qin (Ref. 20) found that the quantization error in an A-to-D converter with a 14-bin resolution has equivalent rms value of the 5-hour SQUID noise with ten-minute roll. In my simulation, I assumed an A-to-D converter with a 16-bit resolution, which leaves about two bits in resolution before the quantization error becomes dominant compared with the SQUID noise. Two extra bits of an A-to-D converter reduces the quantization error by a factor of four, but the SQUID noise is improved by a factor of $\sqrt{10}$ at the same time with one-minute roll. Thus, the 16-bit resolution becomes marginal with one-minute roll and may not provide sufficient accuracy. These issues have to be investigated more thoroughly when determining the roll period for the GP-B satellite.



(a) Time history of Ω_G estimation error with various roll periods.



(b) Time history of Ω_F estimation error with various roll periods.

Figure 5.15 Time history of the estimation error of the relativistic precession rates with various satellite roll periods.

Table 5.6 Final estimation accuracy of two-step filters with various roll periods

Filter states	Final estimation accuracy with ten-minute roll (milliarcseconds per year)	Final estimation accuracy with one-minute roll (milliarcseconds per year)
Geodetic precession rate Ω_G	0.53	0.40
Frame-dragging precession rate Ω_F	0.42	0.33

5.7 Summary of Data Reduction Synthesis

In Chapter 5, I reformulated Qin's two-step filters with slightly different filter states and implemented the recursive algorithm. I verified the two-step filters with the truth model that I developed in Chapter 4 and found that the final estimation accuracy was better than 0.5 milliarcsecond per year for the relativistic precession rates. The recursive algorithm consistently showed 15 to 18% better results. I investigated the effects of gyroscope's polhode motion on the filters. I modeled the polhode signal with a scale factor variation and modified the filters to estimate polhode parameters. The modified filters with extra polhode states showed more stability and better results than the original filters. The optimal polhode period that I found from my model was about 0.2 hour, but a more precise model of the trapped flux signal has to be used to verify this claim. I also investigated the effects of the telescope pointing error and the roll period. The telescope pointing error with a 20-milliarcsecond rms had little effect on the final estimation accuracy, and the gain-matching scheme may not be necessary to improve the accuracy. The final estimation accuracy was improved by 22 to 24% with a one-minute roll, but the improvement was not a factor of $\sqrt{10}$ as I expected. A complete error analysis must be conducted to determine which error sources become dominant under current specifications if the roll period is shortened to one minute.

CHAPTER 6. EXPERIMENTAL VERIFICATION

6.1 Introduction

In Chapter 6, I will describe the set-up, the calibration, and the results from the latest niobium bird experiment. I tested the two-step Kalman filters that I formulated in Chapter 5 with the experimental data measured by a commercially available dc SQUID magnetometer. The experimental verification of the data reduction scheme was the most important task among the three objectives of the niobium bird project [see Figure 1.6 (b)] because this was the first time that the full-size Kalman filters were tested with actual SQUID measurements. The niobium bird experiment enabled us to sort out unforeseen requirements on the readout hardware by testing the data reduction scheme with a real SQUID signal. The first phase of the niobium bird experiment was to test the filters with a commercially available SQUID magnetometer, and it revealed some interesting requirements on the temperature sensitivity of the SQUID system.

The following sections describe the experimental configuration of the niobium bird experiment, the calibration results of the readout instruments, and the results of the latest niobium bird experiment with the Kalman filters.

6.2 Experimental Configuration

As the conceptual diagram of the experiment shows in Figure 1.6 (a), the programmed current generated by the D-to-A converter was injected into a coil inductively coupled to the SQUID readout system, and the readout system measured the magnetic flux induced by the current. The Kalman filters then processed the SQUID measurement data, and I evaluated the estimation accuracy. In order to conduct a credible testing of the Kalman filters, I had to establish a realistic readout system similar to that of the science mission and, therefore set up a cryogenic dewar to keep the critical components, such as the SQUID probe, pickup loops, and niobium shielding, superconducting throughout the experiment.

Figure 6.1 shows the configuration of the niobium bird experiment, which consists of three parts: (1) data injection instruments, (2) SQUID instruments, and (3) data sampling instruments. The data injection instruments generated the simulated science signal and controlled the timing of data injection to the SQUID readout system. The next block of the experiment was the cryogenic instruments, which included the pickup loops and the SQUID probe. The last block was the data sampling instruments, which digitized the output of the SQUID magnetometer through an anti-aliasing lowpass filter and sent the data to the Kalman filters. The following sections explain each block in detail.

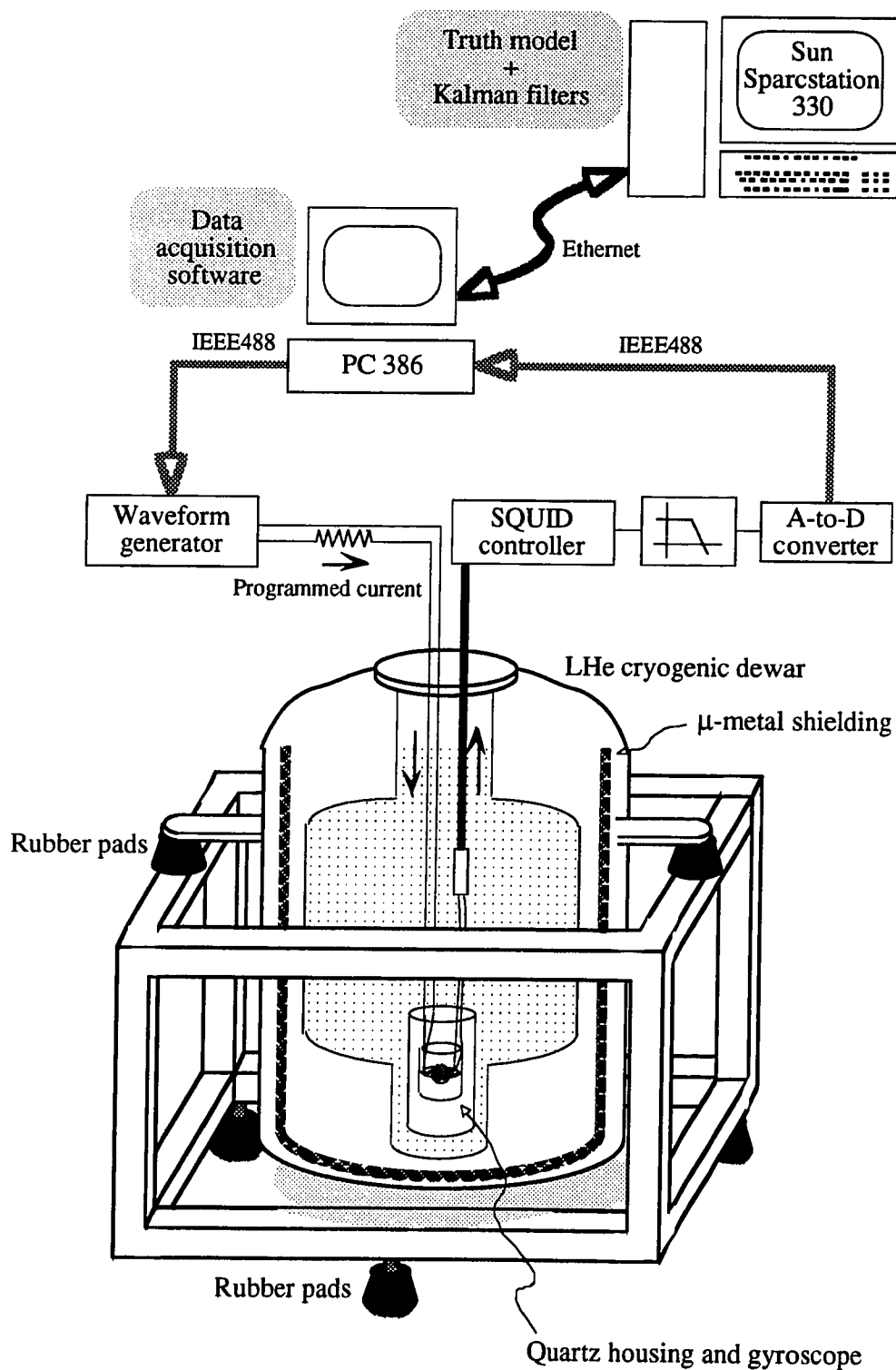


Figure 6.1 Experimental configuration of the niobium bird experiment.

6.2.1 Data Injection Instruments

The data injection instruments included a Sun Sparcstation 330, a PC-386, a waveform generator, and a voltage divider. The truth model developed in Chapter 4 and the Kalman filters developed in Chapter 5 resided in the Sparcstation. The PC-386, which was connected to the Sparcstation via Ethernet, controlled the timing of data injection and sampling through an IEEE488 interface. The truth model within the Sparcstation created a simulated science signal, and the PC read the ASCII file that contained the science signal over the Ethernet. I used Hewlett-Packard's *Universal Source*, Model HP3245A, as a waveform generator. It accepted the GPIB command to generate a programmed voltage according to the simulated science signal. The data injection update rate was 1 Hz, that is, the HP3245A accepted each GPIB command every second to output new voltage. The voltage divider then converted the voltage to a current, which, in turn, was injected into the calibration coil around the gyroscope. The programmed current injected into the calibration coil induced a magnetic flux within the loop, which was equivalent to the London moment signal of the science mission, and the SQUID magnetometer measured the magnetic flux. This last part was conducted in a cryogenic environment and will be explained in the next section.

6.2.2 Cryogenic Instruments

The cryogenic instruments were the most critical components of the niobium bird experiment because they included the SQUID probe, the pickup loop, and the calibration coil. They can be categorized into three blocks: the supporting structures, the SQUID sensor, and the temperature control system. I will explain each block in detail in the following sections.

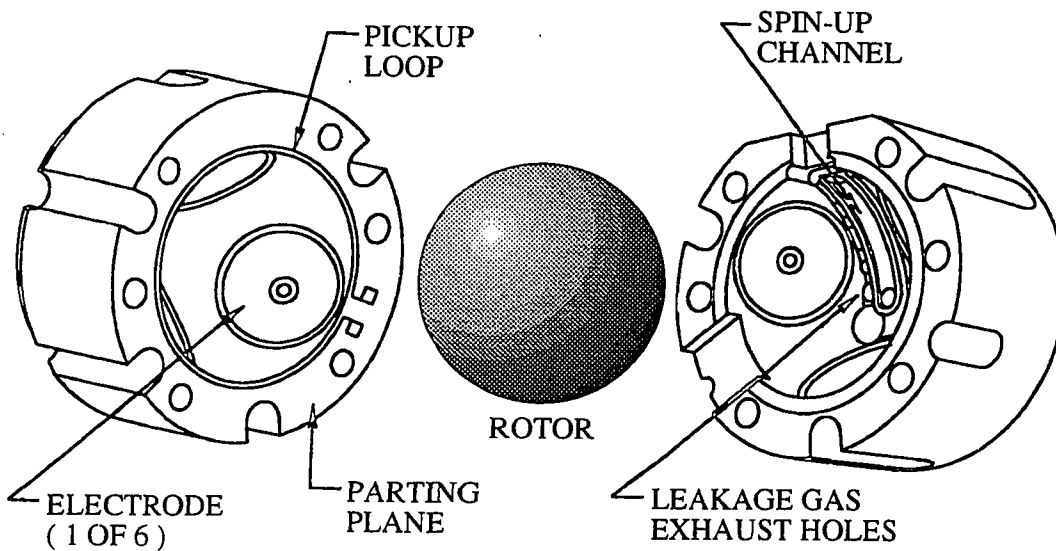


Figure 6.2 Quartz housing and gyroscope with niobium coating.

6.2.2.1 Supporting Structures

The supporting structures consisted of a cryogenic dewar, an outer frame, and μ -metal¹ shield. The dewar held about 80 liters of liquid helium and kept the niobium parts such as pickup loops and gyroscope superconducting for three to four weeks without refilling with liquid helium. The outer frame was standing on the lab floor through three contact points to eliminate any skew and supported the dewar through rubber pads in order to isolate the dewar from vibration in the floor. The dewar had a μ -metal shield, which had been installed by the manufacturer, to attenuate the external magnetic field.

6.2.2.2 SQUID Readout System

The readout instruments included SQUID probe, one-turn pickup loop, one-turn calibration coil, gyroscope, niobium shielding, rf filters, and SQUID controller. All but

¹ Mu-metal is an iron alloy with high permeability (μ value), which is often used for magnetic shielding purposes.

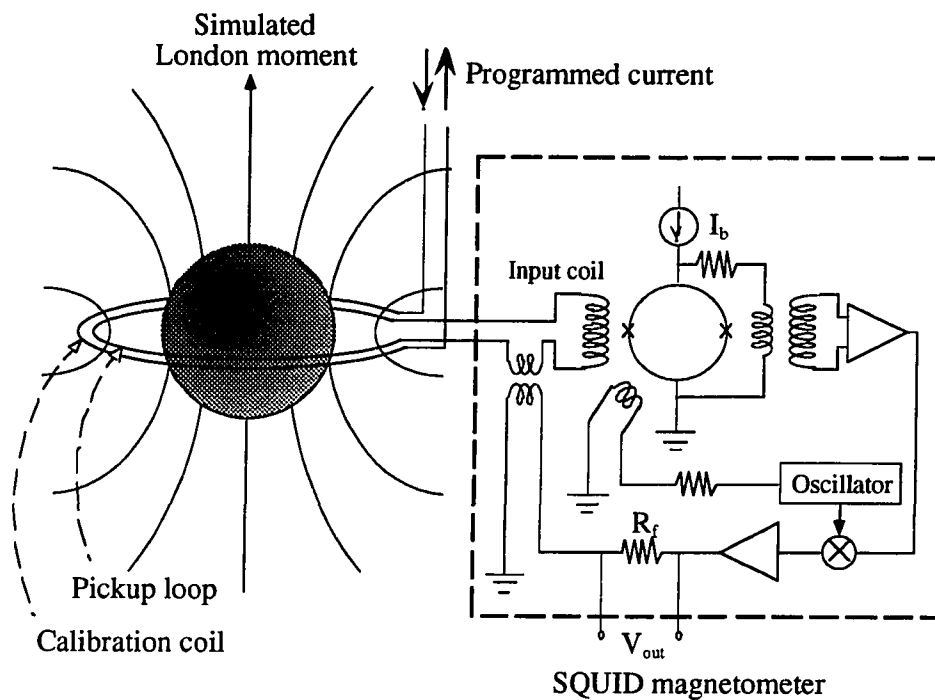
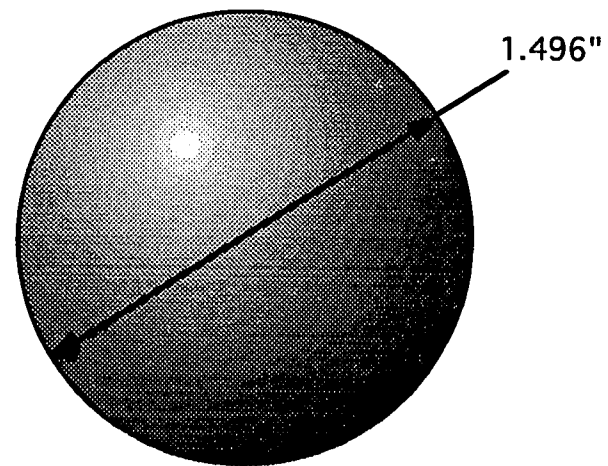
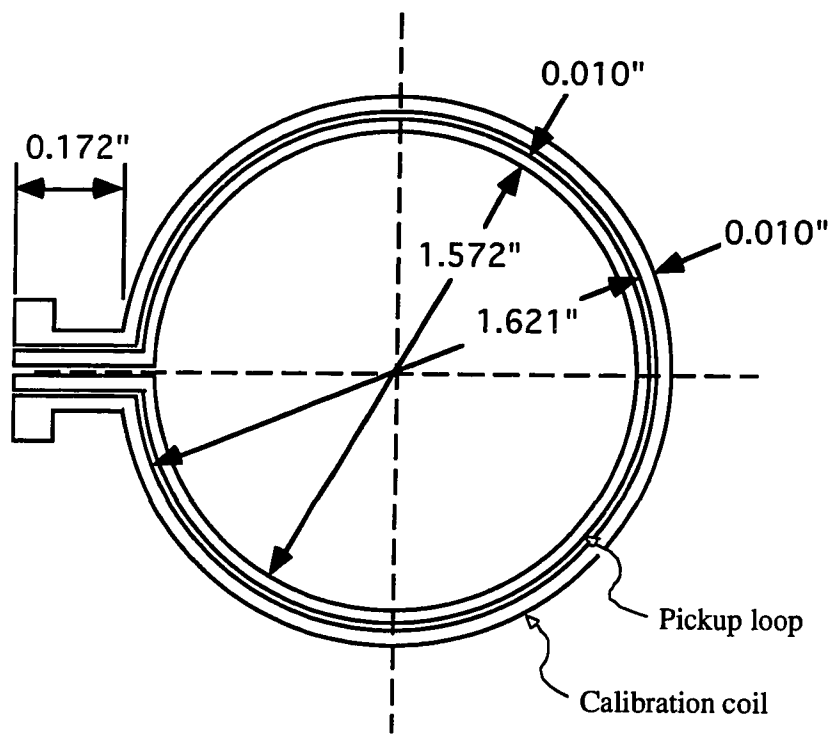


Figure 6.3 Simulated London moment and SQUID readout system for the niobium bird experiment.

the rf filters and the SQUID controller were immersed in liquid helium and were kept at a temperature of 4.2 K or less. As I explained in Section 1.2.6, the SQUID magnetometer is a flux-to-voltage converter, and the output is a voltage proportional to the magnetic flux within the SQUID loop. Figure 1.4 shows the SQUID readout system for the science mission. The London moment created by the spinning superconducting object induces a current in the pickup loop, which is, in turn, coupled to the input coil of the SQUID. Then, the output of the SQUID magnetometer is a voltage proportional to the component of the London moment that is perpendicular to the plane of the pickup loop. In the niobium bird experiment, I used a commercially available dc SQUID magnetometer manufactured by Quantum Design, Inc.

Figure 6.2 shows the quartz housing and the gyroscope installed in the dewar. Figure 6.3 shows the core of the niobium bird's readout system. Compared with the actual readout system for the science mission (Figure 1.4), the niobium bird's readout system had an essential difference, which was the non-spinning gyroscope. The quartz housing, which contained the gyroscope, was installed in the dewar for the niobium bird experiment [see Figure 6.2]. Even though the gyroscope was coated with niobium and superconducting, it was not spinning, and, therefore, it did not have a London moment. The levitation of the gyroscope under 1-g environment would have required a high voltage suspension system, which would have introduced an unacceptable level of interference to the SQUID. Instead of spinning the gyroscope and measuring the London field, I measured an artificially created magnetic field within the pickup loop. I had an extra loop around the gyroscope called the *calibration coil*, located just outside the pickup loop [see Figure 6.3]. The waveform generator at room temperature was connected to the calibration coil and injected the programmed current. The injected current generated a magnetic field near the coil, which was inductively coupled to the pickup loop. As a result, any change in the injected current induced a change in the current in the pickup loop. I programmed the waveform generator so that the induced magnetic field within the pickup loop was equivalent to the London moment of the science mission. Thus, I called the magnetic field of the niobium bird experiment the *simulated London moment*, which assures the main objective of the niobium bird experiment: to provide a realistic input to the SQUID readout system. The SQUID magnetometer measured the flux of the simulated London field. The scaling of the injected current, so that the resulting simulated London field would be equivalent to that of the science mission, depended on the configuration of the calibration coil, the pickup loop, and the gyroscope, which is shown in Figure 6.4. I will discuss this scaling issue in Section 6.3.



Quartz gyroscope with niobium coating

Figure 6.4 Dimensions of the gyroscope, pickup loop, and calibration coil.

In order to isolate the simulated London field from the ambient magnetic field, I had to shield the core elements magnetically, including the pickup loop, the calibration coil, and the SQUID probe. I used three layers of niobium and lead shielding (Ref. 57) in addition to the μ -metal shielding and self-shielding of the gyroscope. Two inner layers were niobium tubes, and I used a lead sheet to wrap the quartz housing and the SQUID probe.

6.2.2.3 Temperature Control System

I implemented a temperature control system to reduce the bias drift in the SQUID readout that depended on the temperature of the SQUID probe. The SQUID probe was immersed in liquid helium, and I stabilized the temperature of the probe by regulating the temperature of liquid helium. Figure 6.5 shows the diagram of the temperature control system. A vacuum pump and a butterfly valve were used to keep the gas pressure below atmospheric pressure, and a germanium resistance thermometer (GRT) and a temperature bridge were used to measure the temperature. The GRT was attached to the SQUID probe to measure the temperature of the probe. To measure and regulate the temperature, I used a temperature bridge and a PID controller manufactured by Linear Research Inc., Model LR-400-20K/130. The temperature of liquid helium at atmospheric pressure is about 4.2 K, and I selected the controller set point below that temperature. The vacuum pump kept the helium gas pressure below atmospheric pressure and the temperature under 4.2 K, while the PID controller sent a current to the heater in the liquid helium to regulate the temperature. I adjusted the opening of the butterfly valve for the appropriate temperature range. The results of temperature regulation are presented in Section 6.3.

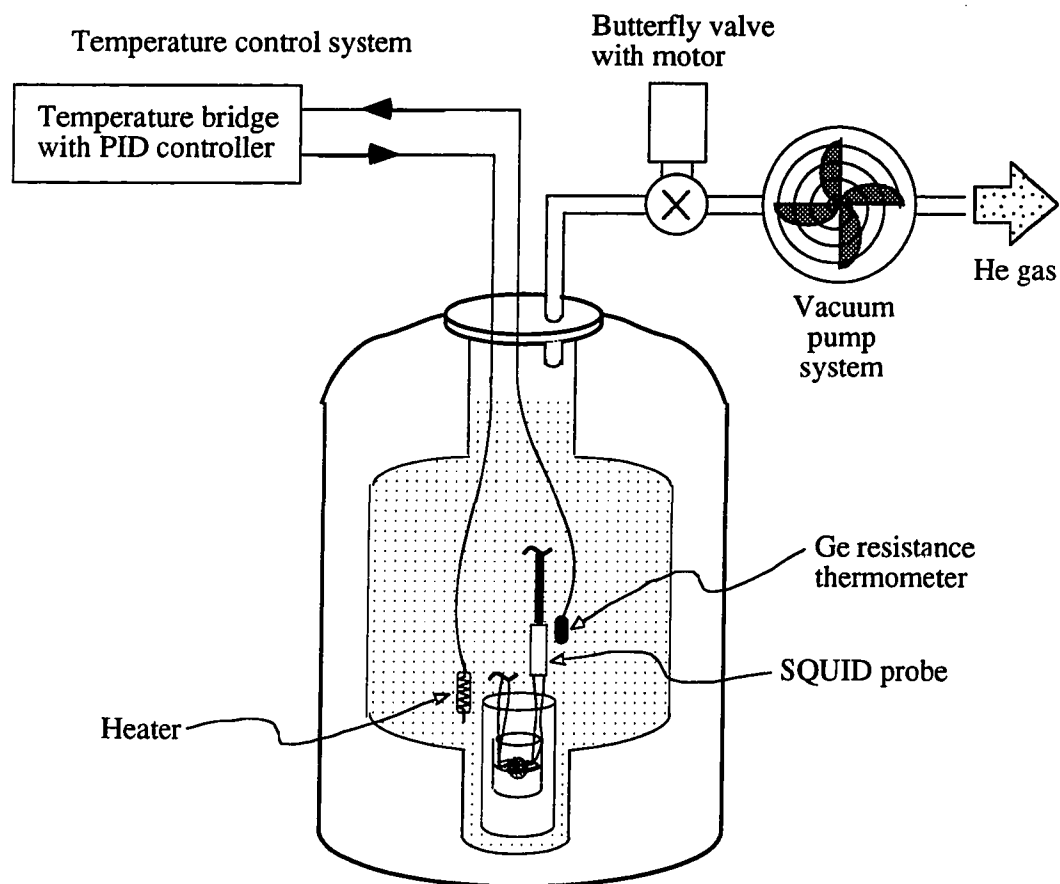


Figure 6.5 Temperature control system of liquid helium with vacuum pump, Ge resistance thermometer, heater, temperature bridge, and PID controller.

6.2.3 Data Sampling Instruments

The data sampling instruments included the lowpass filter, the A-to-D converter, and the PC-386. The lowpass filter prevented aliasing in the digitized data, and the PC controlled the timing of the sampling through IEEE488 so that the sampling was always synchronized with data injection. The sampling frequency was 0.1 Hz, which was ten times slower than the data injection rate. The cut-off frequency of the lowpass filter was 0.04 Hz, which was 80% of the Nyquist frequency. I used a Keithley' Model 196 Digital Multimeter as the A-to-D converter and a Krohn-Hite Model 3905B with Model 30A-3 as

the lowpass filter. The lowpass filter used a 7-th order elliptical function and provided 115 dB/octave attenuation above the cut-off frequency.

6.3 Calibration of Niobium Bird Experiment

I conducted the calibration of most of the instruments used in the niobium bird experiment. The calibration process isolated the source of errors within the experiment and the error budget was compared with the assumptions made in the Kalman filters. The calibration included

- Temperature regulation of liquid helium;
- Setting of SQUID magnetometer and analysis of SQUID noise;
- Stability analysis of scale factor and bias in SQUID magnetometer;
- Scaling of input current to the calibration coil, which induced the simulated London moment;
- Calibration and noise analysis of data injection instruments such as the HP3245A and the voltage divider;
- Calibration and noise analysis of data sampling instruments such as Keithley's Model 196, Krohn-Hite's lowpass filter.

The results of these calibrations are presented in the following sections.

6.3.1 Results of Temperature Regulation of Liquid Helium

The temperature of the liquid helium within the dewar was regulated about the set point by the control system explained in Section 6.2.2.3. I chose 1.93 K as the set point, and Figure 6.6 shows the temperature regulation error around the set point over five minutes. Even though the error showed larger spikes on one side, the PID controller regulated the temperature within $\pm 2 \mu\text{K}$ rms. The PID controller manufactured by Linear Research Inc. had adjustments for the feedback gain, and the gain was adjusted by trial-and-error. Below 2 K, the liquid helium becomes superfluid, which means that the

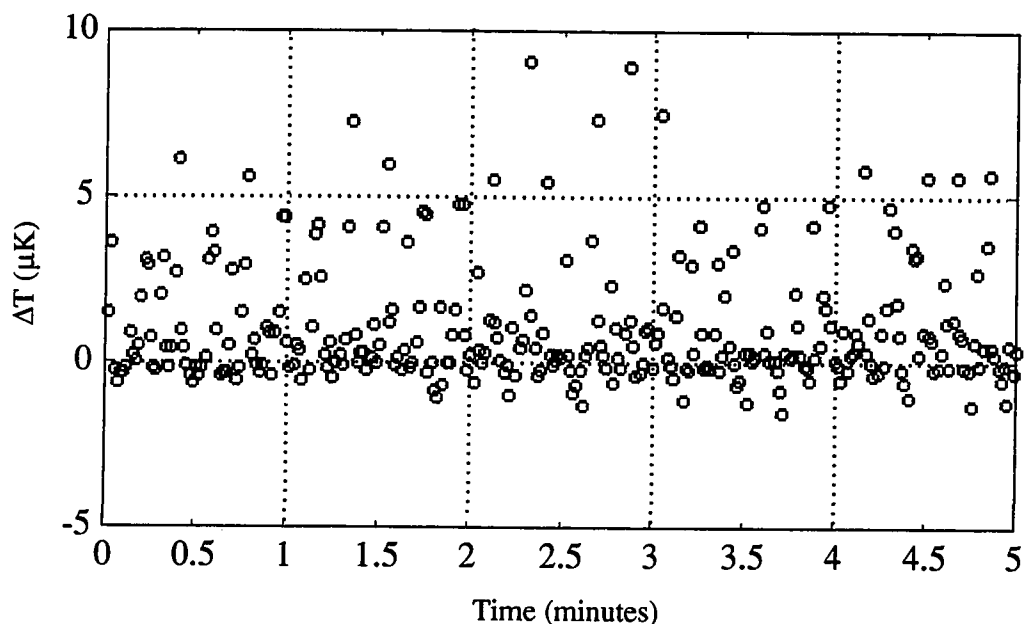


Figure 6.6 Temperature regulation error of liquid helium with a set point of 1.93 K.

effective heat conductivity of the liquid becomes very large. At 1.93 K, the liquid helium is a superfluid, and the temperature of the liquid is very uniform within the dewar. Thus, the delay which is usually associated with a temperature gradient, was minimized, and the control loop was stable throughout the experiment.

6.3.2 Settings and Noise Performance of SQUID Magnetometer

I conducted the first phase of the niobium bird experiment to test the Kalman filters with a commercially available SQUID magnetometer. I used a dc SQUID magnetometer Model 5000 manufactured by Quantum Design, Inc., which had an auto-tuning function for the bias current. The settings of the magnetometer were selected from the key pads on the front panel. Some of the settings that I used were:

- Reversing bias current option on (YAMS)

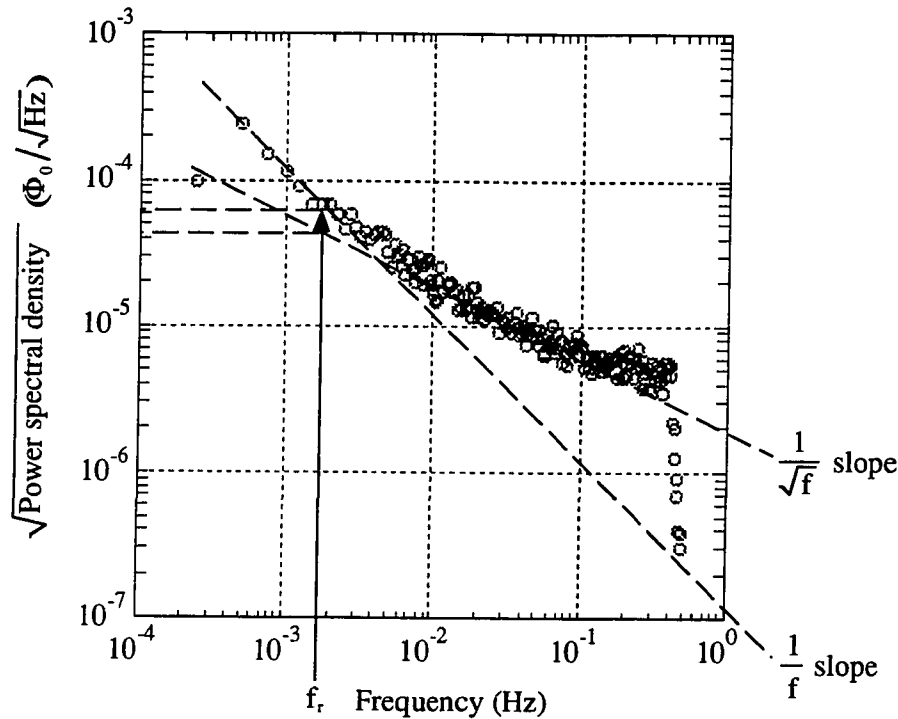


Figure 6.7 Square-root power spectral density of Quantum Design dc SQUID noise (indicated by o's).

- Internal filter: 1 kHz cutoff frequency
- Range: 5 flux quanta full scale with stability option (5S)
- Output gain: 7.50 volts per flux quantum²

With the settings above and the temperature regulation of the liquid helium presented in Section 6.3.1, I sampled the output of the SQUID magnetometer for 10 hours at 1 Hz³ with the data injection instruments disconnected from the calibration coil so that no input signals were present. Thus, the measured noise in the output of the SQUID magnetometer represented the noise floor of the SQUID readout system. I calculated the

² Even though the manual provided by Quantum Design Inc. implies that the gain is 10 volts per flux quantum, a calibration test by J. M. Lockhart and B. Muhlfelder (Ref. 58) showed that the actual gain is only 7.50 volts per flux quantum with about 2% uncertainty.

³ While the nominal sampling rate for the niobium bird experiment was 0.1 Hz, I used a faster sampling rate for the noise calibration to observe the noise floor of the dc SQUID.

power spectral density of the SQUID noise using the method presented in Section 3.2.2⁴. Figure 6.7 shows the square-root power spectral density of the measured SQUID noise in units of $\Phi_0/\sqrt{\text{Hz}}$. It also shows two linear slopes, $1/f$ and $1/\sqrt{f}$ slopes, in square-root power. Even though the square-root power spectral density of the measured SQUID noise showed a $1/\sqrt{f}$ trend at higher frequencies, it clearly showed a $1/f$ trend at lower frequencies, which may have been caused by the temperature drift in the readout system. As indicated by the dashed line in the figure, the noise level at the roll frequency was about $60 \mu\Phi_0/\sqrt{\text{Hz}}$, and the integration time required to resolve a one-milliarcsecond signal was thus about 11 to 14 hours for the Quantum Design dc SQUID. As far as the signal-to-noise ratio at the roll frequency is concerned, the experimental measurements should yield the estimation accuracy which is only a few times worse than the simulation. This claim will be tested in Section 6.3. If we can remove the $1/f$ trend at lower frequencies by reducing the temperature drift in the readout system, it may improve the noise level at the roll frequency to about $40 \mu\Phi_0/\sqrt{\text{Hz}}$, which corresponds to a 5 to 7-hour SQUID.

6.3.3 Stability of Scale Factor and Bias in SQUID Readout

The stability of the scale factor and the bias in the SQUID readout affects the estimation accuracy of the Kalman filters because the step 1 filters estimate the scale factor and the bias as slowly varying constants as described in Section 5.2.1. Within the process model of the step 1 filter, I modeled the SQUID scale factor and the bias as constant parameters with driving white noises, which I assumed to be independent Gaussian. The strength of the driving noise, i.e., the process noise, is determined by the stability of each parameter over the sampling period and is specified by the rms value. If the process noise of the filter model correctly represents the actual drift, the solutions of

⁴ The window size M was 4096 with an overlap among segments by a half window size (2048 data points). The sampling frequency was 1 Hz with an anti-alias filter at 0.4 Hz. I used the Hanning window to condition the data and corrected the PSD estimate for the noise equivalent band-width (Equation 3.19).

the Kalman filters are optimized between the measurement noise and the uncertainty in the filter model, and the filters are properly *tuned*. If the filters are not properly tuned, the resulting estimation accuracy can be too conservative or too optimistic. Thus, even though I verified the Kalman filters by the simulations in Chapter 5, I had to verify that the filters are correctly tuned by comparing the assumption that I made for the simulations and the actual drift in the SQUID readout in the niobium bird experiment. In this section, I will discuss the assumptions that I made for the stability of these parameters when I verified the filters and compare them with what I observed in the actual SQUID signal.

In order to calibrate the stability of the scale factor and the bias in the SQUID signal, I injected a square wave into the calibration coil and sampled the output of the SQUID magnetometer, which was a delayed square wave with the same frequency. I could calibrate the scale factor by comparing the amplitude of input and output square waves, and calibrate the bias drift by averaging the output square wave over each period. The frequency of the square wave was 0.05 Hz, and the sampling frequency was 1 Hz. Figure 6.8 shows the setup for the calibration. With the same setting for the SQUID controller as given in Section 6.3.2, the overall scale factor was

$$\frac{V_{out}}{V_{in}} = 0.995857 \pm 0.000013 \quad (6.1)$$

where

V_{out} : output voltage at the SQUID controller
 V_{in} : input voltage at the voltage divider

Figure 6.9 shows the calibration results of the scale factor. I changed the input voltage amplitude from -10 volts to +10 volts and calculated the scale factor at each point. I calculated the overall scale factor by averaging all the data points.

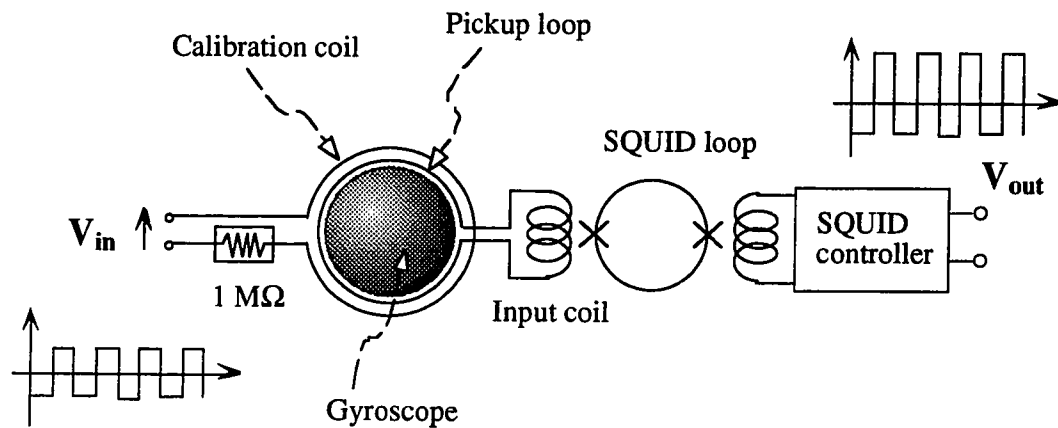
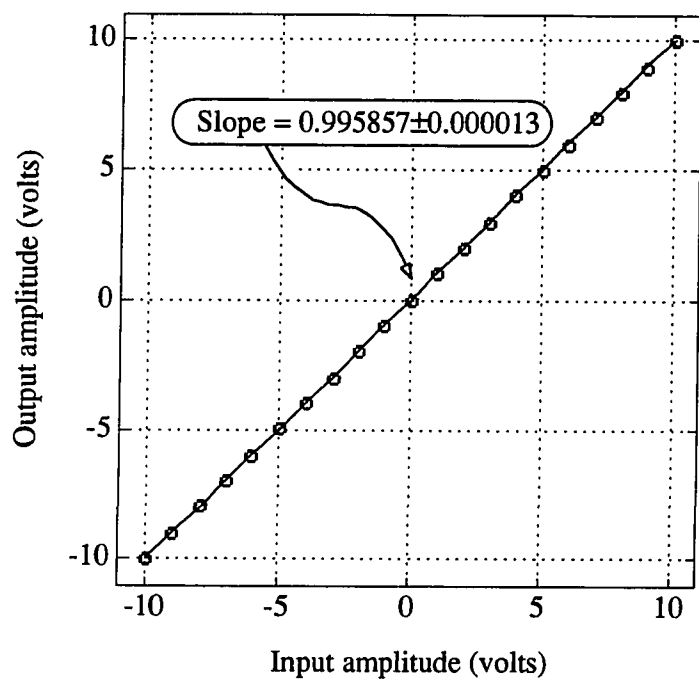


Figure 6.8 Calibration of scale factor and bias drift in the SQUID readout system.

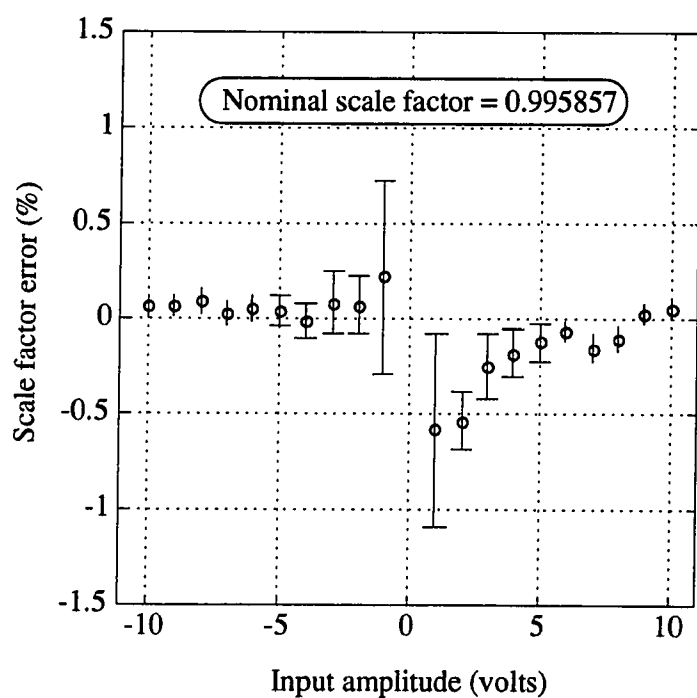
I conducted the calibration for a day and investigated the stability of the scale factor and the bias. Then, I compared the assumptions that I made for the simulations with the actual stability in Table 6.1. The stability of the scale factor was about the same, but that of the bias drift was about twenty times worse than I assumed in the simulation, which means that the process noise that I gave to the bias state of the Kalman filters was too small compared with the actual bias drift. If I increase the process noise on the bias state by a factor of twenty, the final estimation accuracy will be degraded. As a hypothetical case, if we use Quantum Design's SQUID controller for the science mission instead of flight instruments, I expect that the final estimation accuracy of the relativistic precession rates will be about 10 milliarcseconds per year.

Table 6.1 Stability of SQUID Scale Factor and Bias -- Comparison Between Simulation and Experiment

	Simulation	Experiment
Scale factor stability	5e-3 %/day	7e-3 %/day
Bias drift stability	0.05 arcsecond/day	1 arcsecond/day

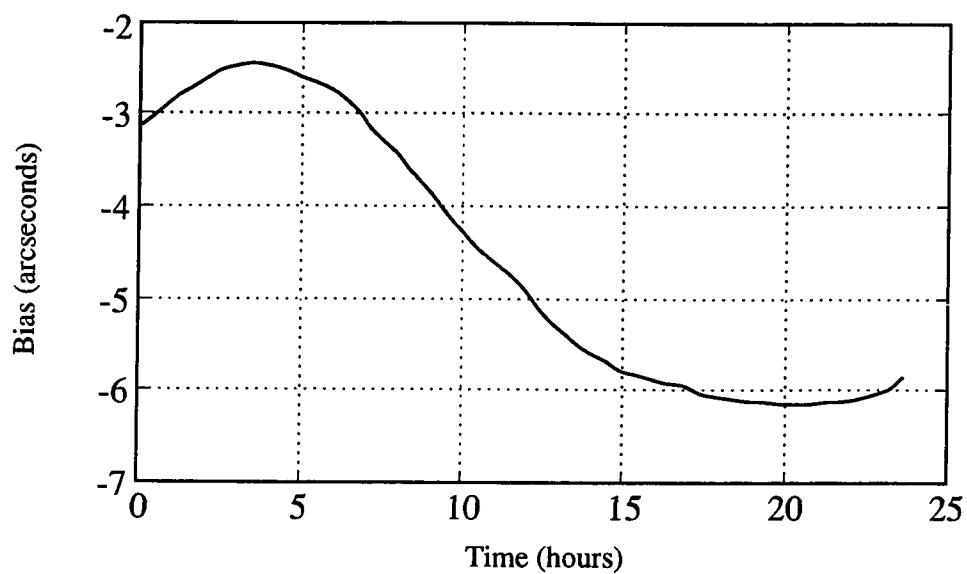


(a) Output amplitude vs. input amplitude to the SQUID readout system.

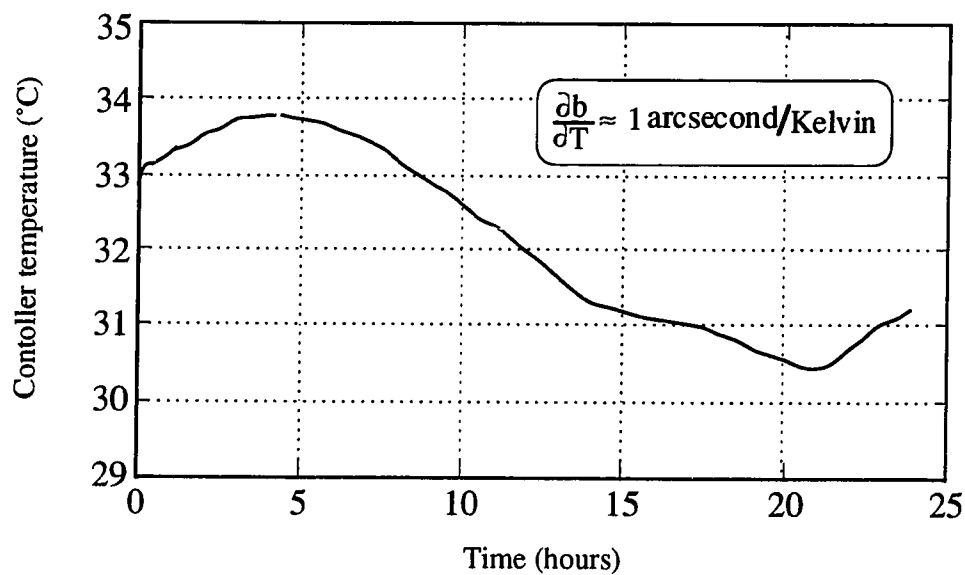


(b) Calibration error of the scale factor in percentage.

Figure 6.9 Calibration results of the SQUID scale factor.



(a) Bias drift in the SQUID readout.



(b) Temperature of the SQUID controller.

Figure 6.10 Correlation between the bias in the SQUID readout and the temperature of the SQUID controller.

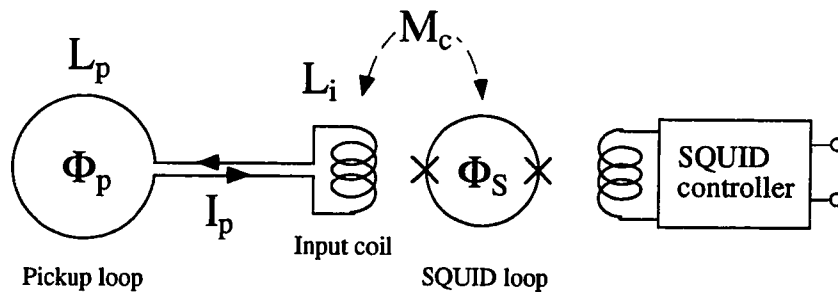
The large bias drift observed in the SQUID signal did not improve even with the temperature regulation of the liquid helium, which was supposed to attenuate the temperature-dependent bias drift in the SQUID probe. This fact lead to the investigation of additional temperature dependency within the readout system. I measured the temperature of the SQUID controller, which was kept at room temperature, during the calibration and investigated the correlation between the controller temperature and the bias drift in the SQUID readout. Figures 6.10 (a) and (b) show the bias drift in the SQUID readout and the temperature drift of the SQUID controller in 24 hours, respectively. The bias and the controller temperature showed strong correlation with a cross-correlation coefficient of 0.968, and the temperature coefficient of the SQUID bias was

$$\frac{\partial b_{sq}}{\partial T} \approx 1 \text{ arcsecond per Kelvin} \quad (6.2)$$

According to this coefficient, the temperature of the SQUID controller⁵ has to be regulated within ± 100 mK at dc⁶ in order to isolate the bias drift from the relativistic precession rates. The SQUID controller that I used, Quantum Design's Model 5000, did not have internal temperature regulation, and the room temperature mainly determined the controller's temperature. Even though the temperature-dependent bias drift in the Model 5000 was considerably larger than what the Kalman filters assumed (Table 6.1), it can be reduced for the science mission by using a SQUID controller with a smaller temperature coefficient and installing a temperature regulation system to the controller. The temperature coefficient of the readout bias can be reduced by selecting controller components that are less sensitive to the temperature variation. Thus, the design of the

⁵ A SQUID controller designed for the science mission will have a smaller temperature coefficient, which will relax the requirement on the temperature regulation.

⁶ I calculated the requirement on the temperature regulation from the assumptions that I made for the simulation [see Tables 5.1 and 5.2].



- L_p : self inductance of pickup loop
- L_i : self inductance of input coil
- M_c : mutual inductance between input coil and SQUID loop
- Φ_p : total flux within pickup loop
- Φ_s : flux in SQUID loop coupled from input coil
- I_p : induced current in pickup loop

Figure 6.11 Inductive coupling of the SQUID readout system for the science mission.

SQUID controller for the GP-B program should include (1) installation of a temperature regulation system and (2) a design with a smaller temperature coefficient.

6.3.4 Scaling of Injection Current to Calibration Coil

After I calibrated the scale factor of the SQUID readout system, I calculated the scaling of the voltage output from the waveform generator (HP3245A). I adjusted the gain of the waveform generator so that the resulting simulated London moment was equivalent to that of the science mission. The inductive coupling of the SQUID readout system designed for the science mission has a different configuration from that for the niobium bird experiment [see Figure 6.11]. For example, the inductance of the pickup loop and that of the input coil are balanced at $2\ \mu\text{H}$ for the science mission, but they have different values in the niobium bird experiment. I made the following assumptions for the SQUID readout system used in the science mission:

$$\begin{aligned}
r_0 &= 19.05 \text{ mm} \\
f_s &= 170 \text{ Hz} \\
N &= 5 \text{ turns} \\
N^* &= 4.4 \text{ turns} \\
L_p &= 2 \text{ } \mu\text{H} \\
L_i &= 2 \text{ } \mu\text{H}
\end{aligned} \tag{6.3}$$

where

- r_0 : mean radius of the pickup loop
- f_s : gyroscope's spin frequency
- N : number of turns in the pickup loop
- N^* : effective number of turns in the pickup loop (Ref. 57)
- L_p : self inductance of the pickup loop
- L_i : self inductance of the input coil in the SQUID probe

Under these assumptions, the magnitude of London field B_L is given by

$$B_L = 1.22 \times 10^{-8} \text{ Tesla} \tag{6.4}$$

According to the formulation by J. M. Lockhart (Ref. 57), the total magnetic flux within the pickup loop, the induced current, and the flux coupled to the SQUID loop can be calculated as follows:

$$\begin{aligned}
\Phi_p &= N^* B_L \pi r_0^2 \\
&= 6.12 \times 10^{-11} \text{ Weber}
\end{aligned} \tag{6.5}$$

$$I_p = \frac{\Phi_p}{L_{total}} \sin \theta_L = \frac{\Phi_p}{L_p + L_i} \sin \theta_L \tag{6.6}$$

where

- Φ_p : total magnetic flux within the pickup loop
- I_p : induced current in the pickup loop
- θ_L : angle between the London moment and the pickup loop

The angle between the London moment and the pickup loop is very small because the nominal spin-up axis is in the pickup plane. Thus,

$$I_p \approx \frac{\Phi_p}{L_p + L_i} \theta_L \quad (6.7)$$

For $\theta_L = 1$ arcsecond, the induced current in the pickup loop is

$$I_p = 7.42 \times 10^{-8} \text{ mA} \quad (6.8)$$

Thus, a one-arcsecond displacement of the London moment corresponds to about 7×10^{-8} mA of the induced current in amplitude for the science mission. If I inject this current into the input coil of the Quantum Design's Model 5000, the flux coupled to the SQUID loop can be calculated as follows. The coupling of the input coil to the SQUID loop for the Model 5000 was calibrated by the manufacturer⁷ and was given by

$$M_c = 5.0 \Phi_0 / \mu\text{A} \quad (6.9)$$

where M_c : mutual inductance of input coil to SQUID loop
 Φ_0 : flux quantum = 2.07×10^{-15} Wb

Hence, the change in flux in the SQUID loop resulted from a one-arcsecond displacement of the London moment is

$$\begin{aligned} \Phi_s &= M_c I_p \\ &= 0.37 \times 10^{-3} \Phi_0 \text{ (in amplitude)} \end{aligned} \quad (6.10a)$$

where Φ_s : change in flux in the SQUID loop coupled from the input coil for 1 arcsecond

⁷ Serial number: dc SQUID A4.17. Manufacturing date: 01/07/92.

or in rms value

$$\Phi_s = 0.25 \times 10^{-3} \Phi_0 \text{ (in rms)} \quad (6.10b)$$

Now, I can calculate the transfer function of the waveform generator from the gain of the niobium bird's readout system (Equation 6.1) and the transfer function of the science mission's readout system (Equation 6.10a) so that the magnitude of the simulated London moment becomes equivalent to that of the London moment.

According to the setting of the SQUID controller presented in Section 6.3.2, the transfer function of the SQUID controller (Ref. 58) is given by

$$\frac{V_{out}}{\Phi_s} = 7.50 \text{ volts}/\Phi_0 \quad (6.11)$$

I also know the overall gain of the SQUID readout for the niobium bird experiment from Equation 6.1. Thus, the gain from the input voltage to the input flux can be calculated as

$$\frac{\Phi_s}{V_{in}} = \frac{V_{out}}{V_{in}} \cdot \frac{\Phi_s}{V_{out}} \approx 0.13 \Phi_0/\text{volt} \quad (6.12)$$

From Equation 6.10a, we know that a one-arcsecond displacement corresponds to $0.37 \times 10^{-3} \Phi_0$ of SQUID flux. Therefore, the transfer function of the waveform generator is given by

$$\begin{aligned} \frac{V_{in}}{\theta_L} &= 2.8 \text{ mV/arcsecond} \\ &\approx 3 \text{ mV/arcsecond} \end{aligned} \quad (6.13)$$

I used 4 mV per arcsecond to scale the input to the calibration coil⁸. That is, if the amplitude of the simulated science signal at time t is one arcsecond, then the waveform generator (in this case an HP3245A) outputs 4 mV, and the current injected into the calibration coil induces an simulated London moment whose amplitude is equivalent to the normal component of the London moment with a one-arcsecond⁹ displacement.

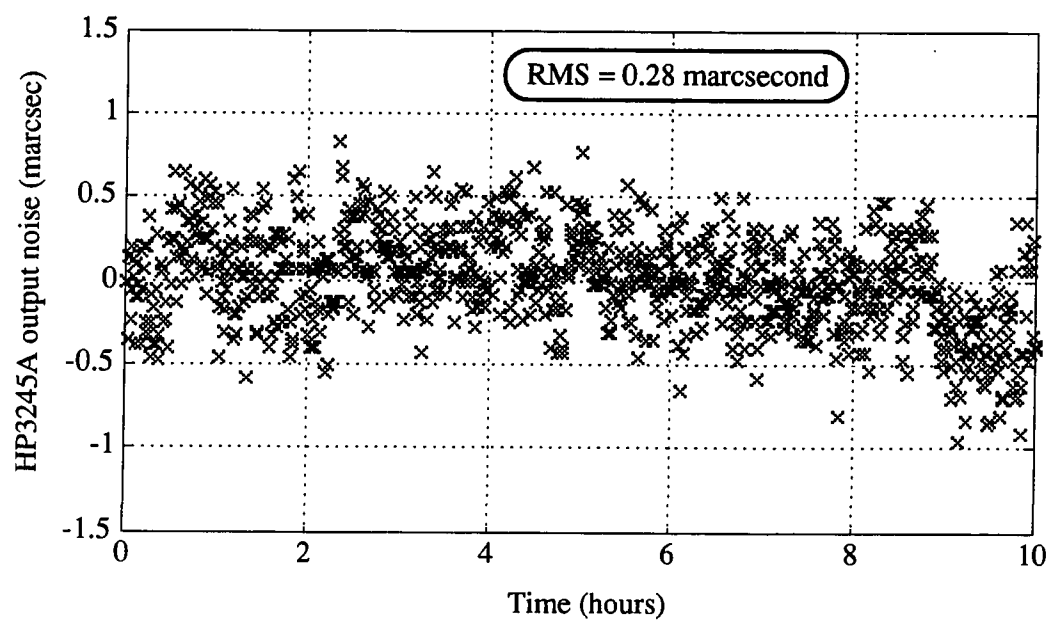
6.3.5 Calibration of Data Injection Instruments

I calibrated the data injection instruments including the waveform generator (Hewlett Packard Model HP3245A) and the voltage divider in terms of the noise performance. The HP3245A provides a programmed voltage output with one-microvolt resolution, which corresponds to 0.25 milliarcsecond of displacement of the London moment according to the input scaling (Equation 6.13). Thus, it provides adequate resolution to generate an simulated London moment equivalent to a displacement angle less than one milliarcsecond. I measured the output and the temperature of the Model HP3245A for 24 hours. Figures 6.12 (a) and (b) show the output noise and the temperature drift, respectively. The rms value of the output noise was about 0.28 milliarcsecond with a cutoff frequency of 0.5 Hz, which agreed with the resolution of the waveform generator, and the temperature drift of the waveform generator had no significant effects on the output drift. Figure 6.13 shows the power spectral density of Quantum Design's SQUID and that of the HP3245A output. The power spectral density of the waveform generator was about 40 dB better than that of the SQUID noise, and, therefore, the Model HP3245A provided adequate resolution and noise performance to generate the simulated London moment for the niobium bird experiment.

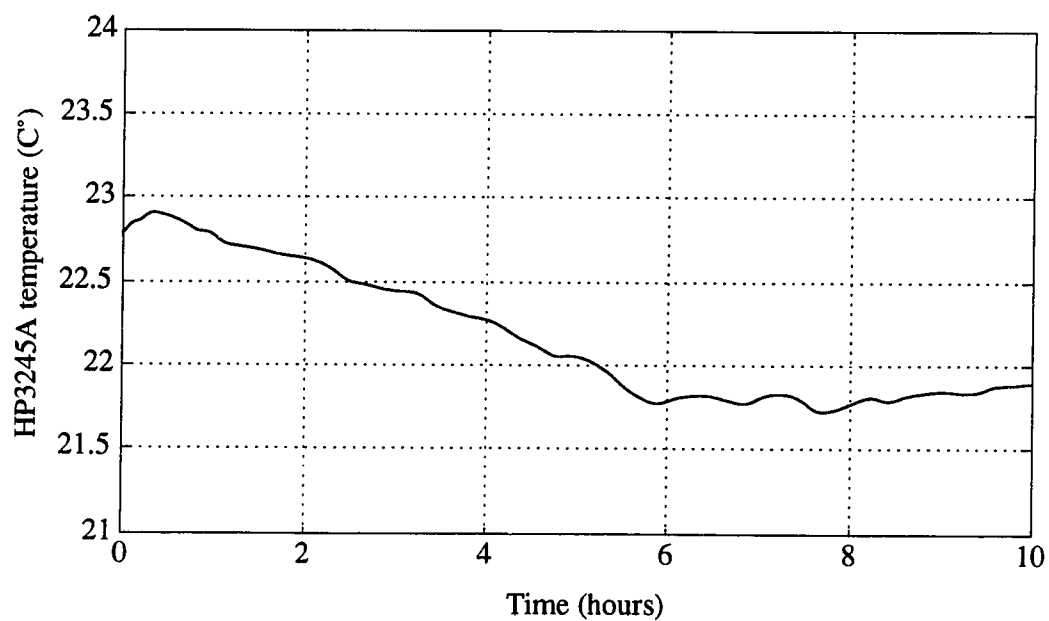
⁸ I determined the scale by a previous calculation, which assumed the transfer function of the SQUID controller to be 10 volts per Φ_0 in Equation 6.11. A calibration test conducted by J. M. Lockhart and B. Muhlfelder later revealed that the actual value was only 7.50 volts per Φ_0 .

⁹ If I use the actual transfer function (Equation 6.13), which was corrected for the gain in the controller, 4 mV output corresponds to a displacement of about 1.4 arcseconds.

In addition to the waveform generator, I also calibrated the resistor box, which was used as a voltage divider. The voltage divider converted the voltage from the waveform generator to a current, which was injected into the calibration coil of the niobium bird experiment. Similar to the calibration of waveform generator, I measured the output and the temperature of the voltage divider, which are shown in Figures 6.14 (a) and (b), respectively. Even though the temperature drift had no significant effects on the output drift, the output of the voltage divider was much noisier than that of the waveform generator. Figure 6.15 shows the power spectral density of the output noise. The power spectral density of the output noise of the voltage divider was marginal compared with the SQUID readout noise. I also found glitches in the output signal as I tapped the resistor box, which suggested that the higher noise could have resulted from improper grounding of the resistor box. I should mention that I measured the output of the resistor box with an open end, which also may have increased the noise level. Even though the noise introduced by the resistor box was not a dominant noise, the grounding still needs to be improved for later experiments.



(a) Output noise of Universal Source HP3245A.



(b) Temperature drift of Universal Source HP3245A.

Figure 6.12 Output noise and temperature of the waveform generator HP3245A.

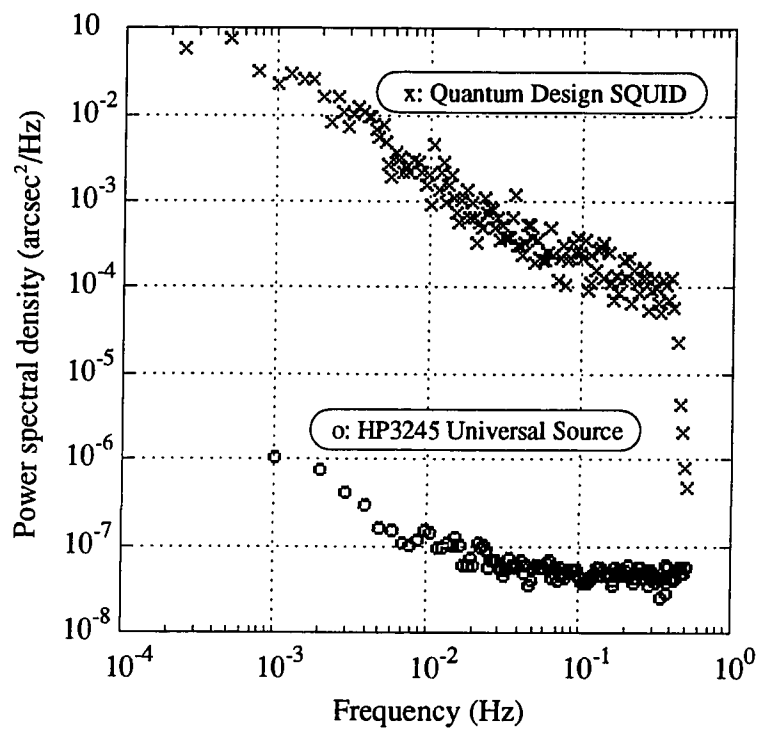
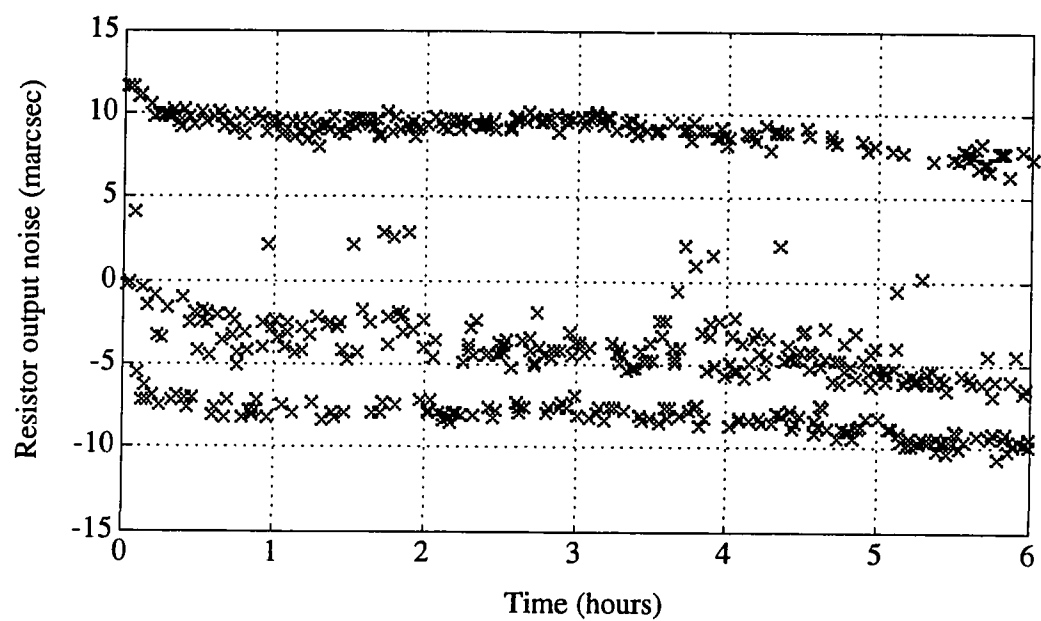
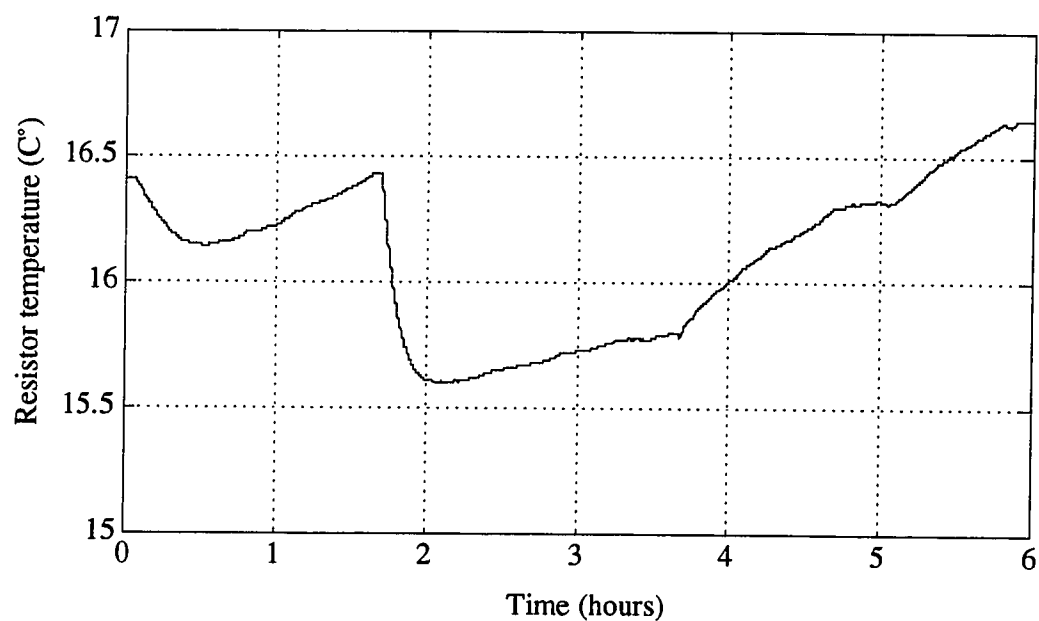


Figure 6.13 Power spectral density of the SQUID noise (Quantum Design Model 5000) and the output noise of the waveform generator (HP3245A).



(a) Output of the voltage divider with an open end.



(b) Temperature of the voltage divider.

Figure 6.14 Output noise and temperature of the voltage divider.

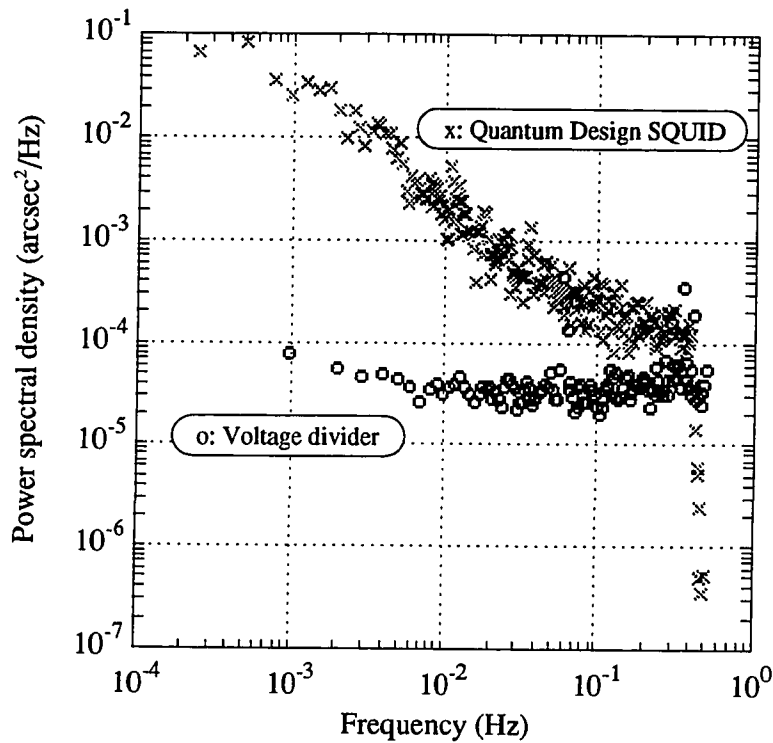


Figure 6.15 Power spectral density of the SQUID noise (Quantum Design Model 5000) and the output noise of the voltage divider.

6.3.6 Calibration of Data Sampling Instruments

I calibrated the data sampling instruments, including the anti-alias lowpass filter and the A-to-D converter (Keithley's Model 196). The Model 196 provided approximately 22-bit resolution, which was equivalent to 0.1 milliarcsecond assuming the gain of 7.50 volts per flux in the SQUID controller and unity gain in the lowpass filter. Similar to the calibration of the data injection instruments, I shorted the input to the Model 196 and measured the voltage and the temperature for 10 hours. The temperature drift did not have any significant effect on the measurement bias drift, and the power spectral density of the measurement noise was about 100 dB better than the Quantum Design SQUID and about 50 dB better than the waveform generator [see Figure 6.16].

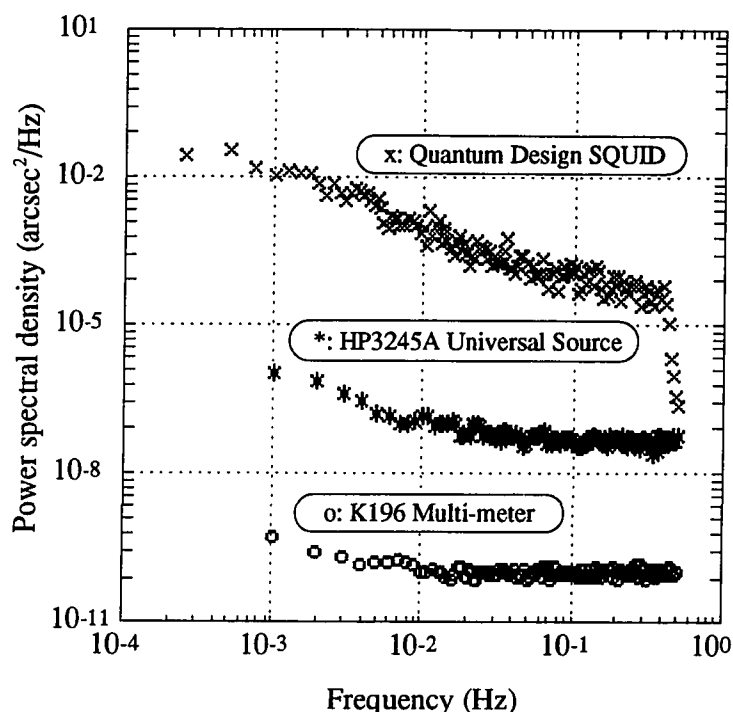


Figure 6.16 Comparison of noise performance among signal generator (HP3245A), sensor (Quantum Design SQUID), and signal sampler (K196).

Thus, the Keithley's Model 196 provided adequate stability and resolution for the niobium bird experiment.

The last instrument that I tried to calibrate was the lowpass filter, which I found the most difficult to calibrate. The lowpass filter was necessary for the readout system to avoid aliasing in the sampled data. I tried several commercially available lowpass filters, but the first two filters including one manufactured by Wavetek, Inc., did not provide adequate stability in phase and gain, and I observed glitches in the output. Then, I switched to the main-frame filter manufactured by Krohn-Hite Co., a combination of Model 3905B and Model 30A-3, which provided the best stability among the lowpass filters that I tested. For the science mission, the same stability requirements are imposed on the lowpass filter as the SQUID magnetometer because the science signal is sampled

at the output of the lowpass filter. Thus, the lowpass filter should be designed so that the following requirements, which are imposed by the Kalman filters, are satisfied:

- Scale factor drift $< 5\text{e-}3\%/ \text{day}$
- Bias drift $< 0.05 \text{ arcsecond/day}$
- Phase noise $< 10 \text{ arcseconds after 10-second integration}$

6.3 Experimental Results

After the calibrations described above, I injected the simulated science signal into the calibration coil and measured the output of the SQUID magnetometer. The SQUID magnetometer was the same unit that I calibrated, Model 5000 manufactured by Quantum Design, Inc. Even though this unit was a commercially available unit, and its design and specifications did not necessarily meet our requirements, the experiment revealed important design issues such as the temperature-dependent bias drift. The findings in the niobium bird experiment will be taken into account when we design the readout system for the science mission.

I processed the sampled data through the Kalman filters that I developed in Chapter 5 and evaluated the filter performance against the simulation results. I ran two sets of Kalman filters: one with nominal parameters as the simulations in Chapter 5 and the other with modified parameters according to the actual stability of the readout system. The results showed that the filters became unstable with nominal parameters because the process noise given to the Kalman filters was too small compared with the actual drift, especially the temperature-dependent bias drift. By increasing the process noise on the bias term of the filter states, I could stabilize the filters but the estimation accuracy degraded accordingly.

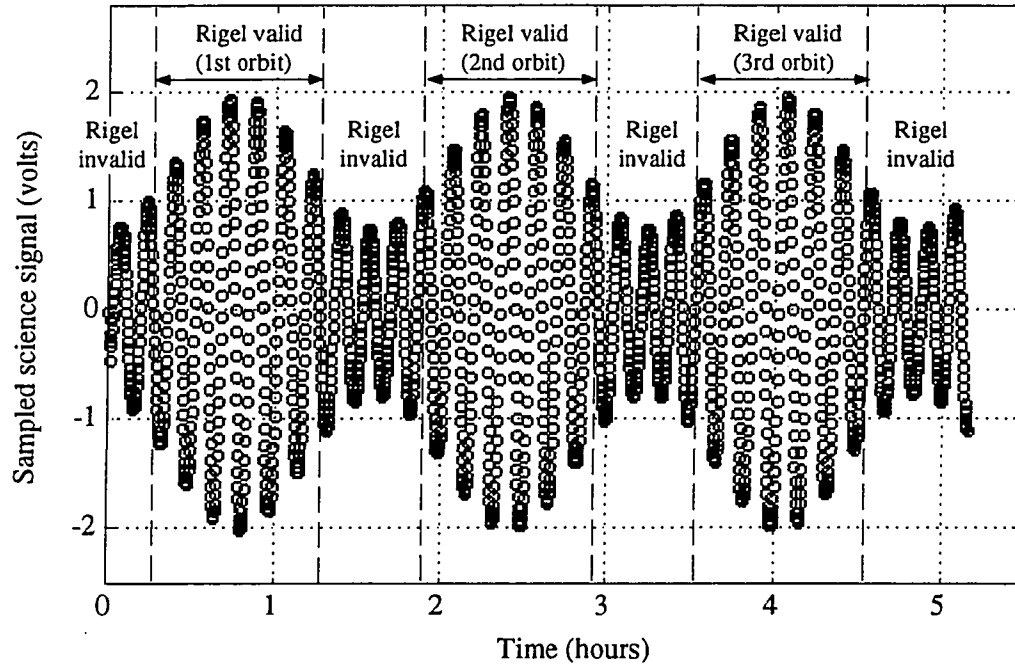


Figure 6.17 Sampled science signal in the niobium bird experiment.

I sampled the SQUID measurement for about five hours, which corresponded to three orbits of data [see Figure 6.17]. I divided the data into three segments each of which corresponded to a Rigel-valid period during each orbit and processed three segments through the step 1 filters. Each segment consisted of about 370 data points at a 0.1 Hz sampling rate. The gain setting of the SQUID magnetometer was 7.50 volts per flux quantum, and I increased the input gain of the lowpass filter to 30 dB in order to increase the signal-to-noise ratio in the filter.

Once I obtained the measurements, I tested the step 1 filters with the initial conditions given in Table 6.2 and two different sets of process noise, Case I and Case II, given in Table 6.3. Case I used the same process noise as used in the simulations in Chapter 5. Case II used the adjusted process noise according to the calibration of the readout system. Although the process noises for the scale factor and the phase bias were

unchanged for Case II, the process noise for the bias was increased to track the temperature-dependent bias drift found in the SQUID magnetometer [see Table 6.1].

Table 6.2 Initial Conditions for Step 1 Filters in the Niobium Bird Experiment

State Variables (Units)	Initial Estimates	Estimation Accuracy
C_G (volts/arcsec)	0.126	0.0005
$\delta\phi_r$ (radians)	-0.2094	0.005
b_{sq} (arcseconds)	-0.01	0.5
NS_s (arcseconds)	0.0	5.0
EW_s (arcseconds)	0.0	5.0

Table 6.3 Nominal (Case I) and Adjusted Process Noises (Case II) for Step 1 Filters in the Niobium Bird Experiment

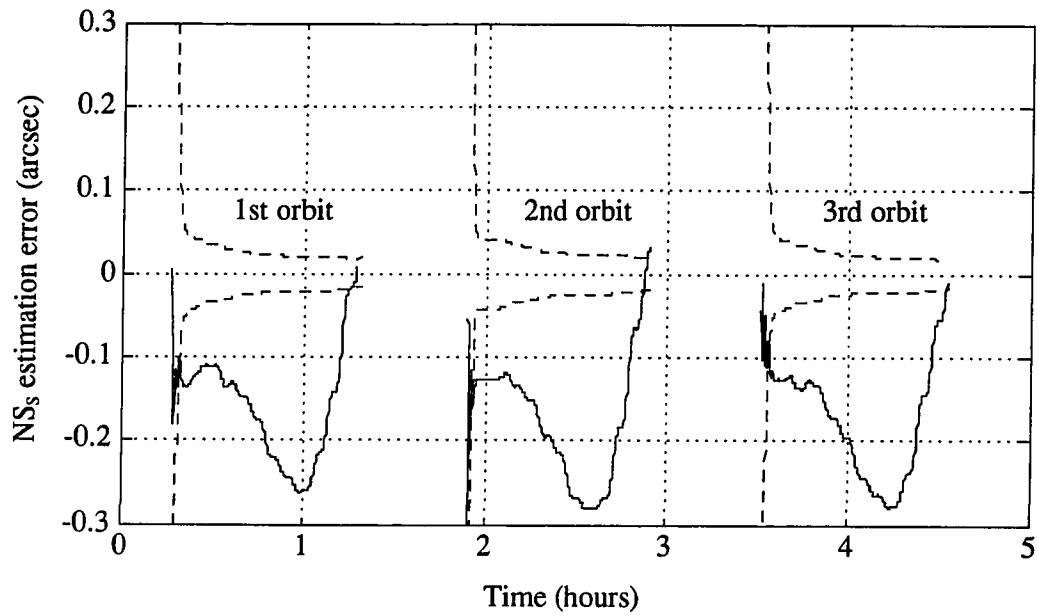
State Variables (Units)	Process Noise Case I (Nominal Values)	Process Noise Case II (Adjusted Values)
C_G (volts/arcsec)	1.0e-10	1.0e-10
$\delta\phi_r$ (radians)	1.0e-9	1.0e-9
b_{sq} (arcseconds)	1.0e-10	1.0e-2

6.3.1 Step 1 Filtering with Nominal Process Noise (Case I)

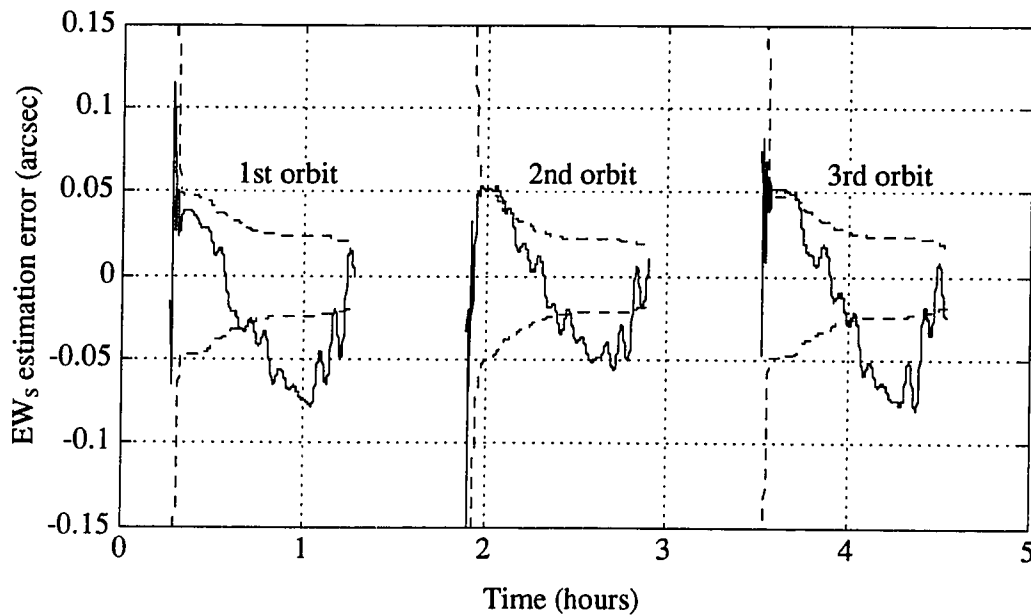
I processed the experimental data through three step 1 filters with nominal process noise given in Table 6.3. Figures 6.18 (a) and (b) show the estimation errors of NS_s and EW_s , respectively. The dashed lines are the envelopes of the expected estimation accuracy, and the solid lines are the actual estimation errors. Even though the estimation

errors at the end of each orbit were mostly within the expected accuracy, the intermediate estimation errors overshot widely outside the expected accuracy. In fact, as Figure 6.19 shows, these step 1 filters were unstable because the estimation residuals diverged. The filters diverged mainly because the process noise on the bias term was too small compared with the actual bias drift. As a result, the estimated bias always lagged the actual bias, and the estimation error grew with time. Another cause was the unmodeled lowpass filter within the Kalman filter. The phase delay in the lowpass filter, which I used as an anti-aliasing filter, depended on the frequency of the input signal, and the science signal contained three spectrally separated signals, the roll signal at f_r and the calibration signals at $f_r \pm f_0$, as shown in Figure 5.2. Thus, the phase delays in the roll and the calibration signals were different. On the other hand, the step 1 filters estimated the overall phase delay as a roll bias¹⁰ that effectively included the phase delays introduced by the roll controller, the SQUID readout, and the anti-alias lowpass filter, and the filters assumed the phase delay to be the same for the roll and the calibration signals. The lack of modeling of the phase delay explains the repeated pattern in the estimation errors over three orbits because the phase delay was the only factor that was repeatable over multiple orbits.

¹⁰ The step 1 filters included the roll bias as the second element of the state vector (Equation 5.1).



(a) NS_s (North-South static term) estimation error by three step 1 filters (Case I).



(b) EW_s (East-West static term) estimation error by three step 1 filters (Case I).

Figure 6.18 Estimation errors of NS_s and ES_s terms by three step 1 filters with nominal process noise (Case I) and SQUID measurements from the niobium bird experiment.

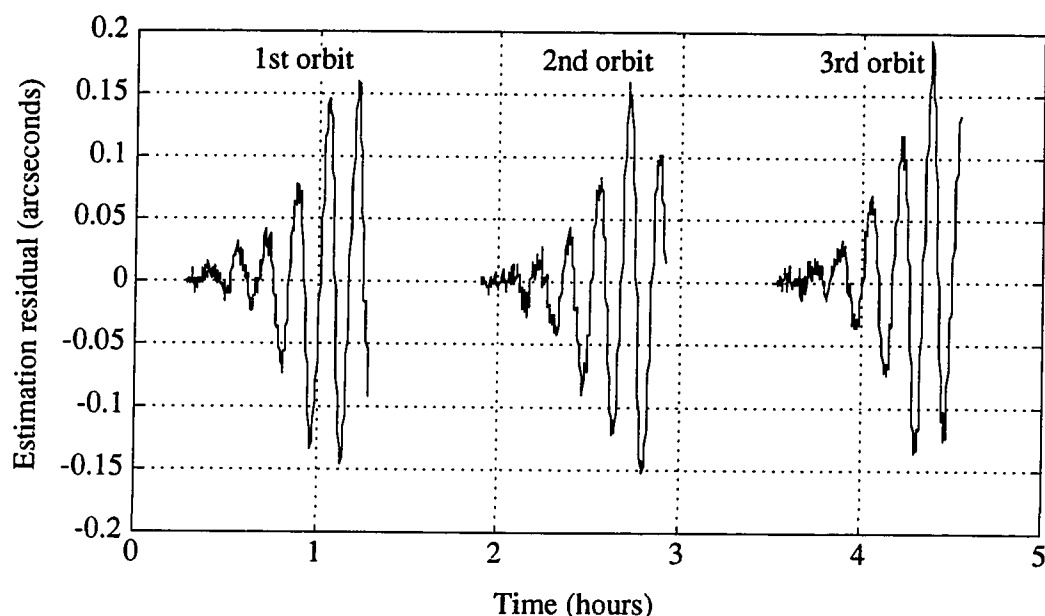
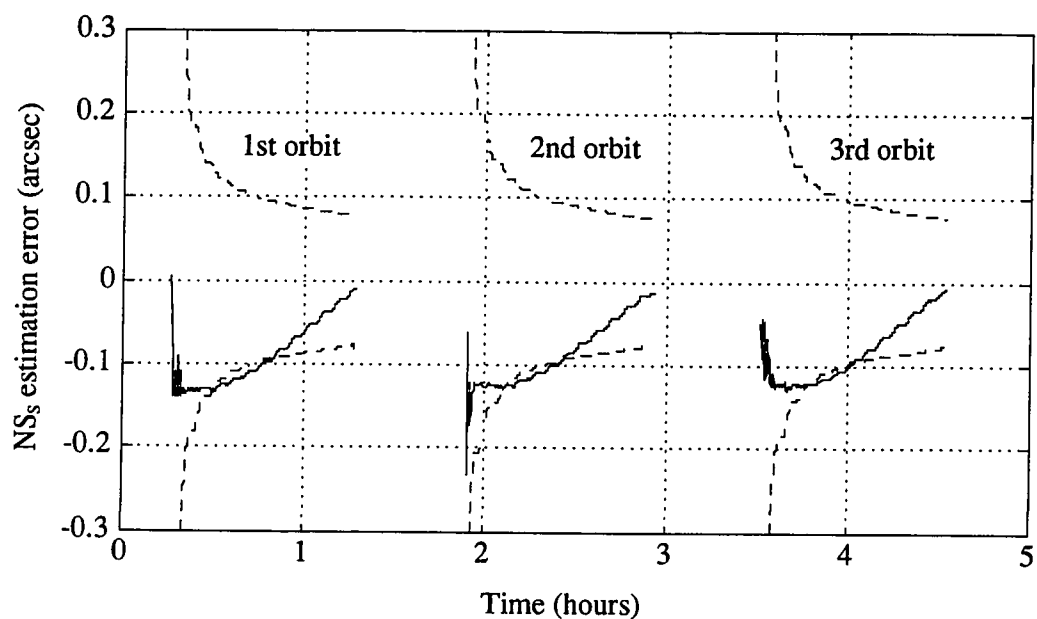


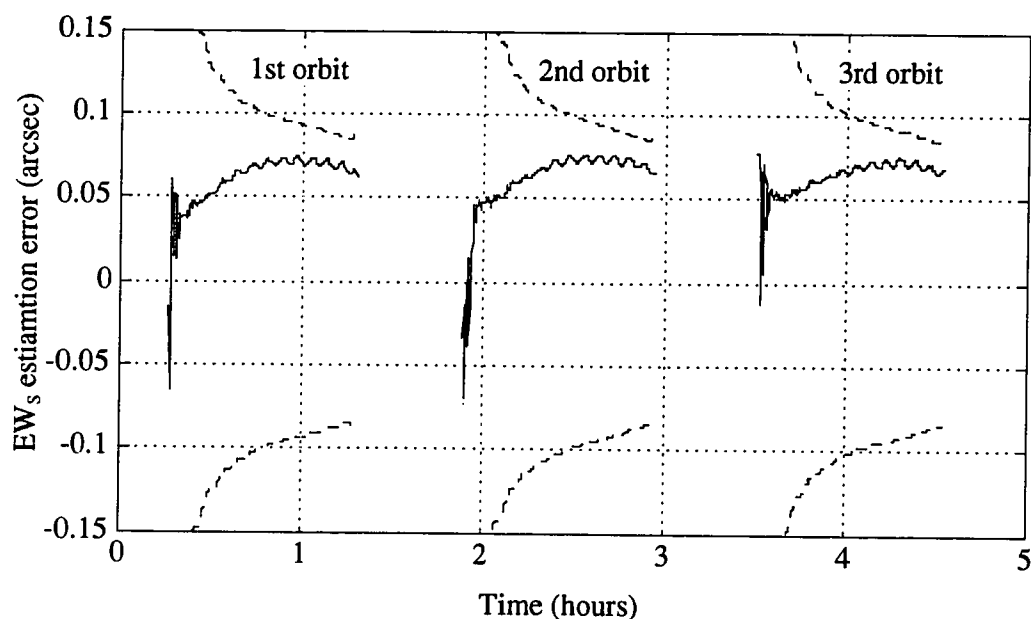
Figure 6.19 Estimation residual of three step 1 filters with nominal process noise (Case I) and SQUID measurements from the niobium bird experiment.

6.3.2 Step 1 Filtering with Adjusted Process Noise (Case II)

I adjusted the process noise in the step 1 filters as shown in Table 6.3 and processed the experimental data through three step 1 filters. Figures 6.20 (a) and (b) show the estimation errors of NS_s and EW_s , respectively, and Figure 6.21 shows the estimation residual of the three step 1 filters. The maximum value of estimation residual was reduced by a factor of more than 36, and the step 1 filters were successfully stabilized by increasing the process noise on the bias term. The estimation errors of NS_s and EW_s always stayed within the expected estimation accuracy. Table 6.4 compares the final estimation accuracy of each step 1 filter with the experimental science signal (Case II) and the simulated science signal. The expected estimation accuracy obtained from the experimental data was about four times worse for the North-South static term, NS_s , and about eleven times worse for the East-West static term, EW_s , compared with the simulation results.



(a) NS_s (North-South static term) estimation error by three step 1 filters (Case II).



(b) EW_s (East-West static term) estimation error by three step 1 filters (Case II).

Figure 6.20 Estimation errors of NS_s and ES_s terms by three step 1 filters with adjusted process noise (Case II) and SQUID measurements from the niobium bird experiment.

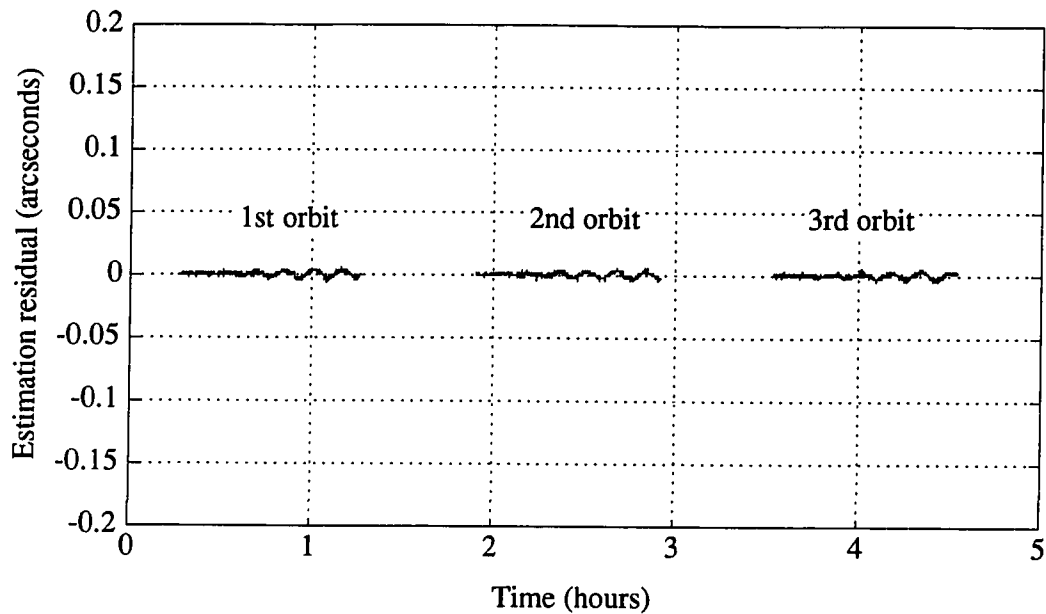


Figure 6.21 Estimation residual of three step 1 filters with adjusted process noise (Case II) and SQUID measurements from the niobium bird experiment.

Table 6.4 Final Estimation Accuracy of Step 1 Filter – Simulation vs. Experiment (Case II)

Filter States	Expected Estimation Accuracy (arcseconds) at the End of a Step 1 Filter: Simulation	Expected Estimation Accuracy (arcseconds) at the End of a Step 1 Filter: Experiment
NS _s	0.018	0.076
EW _s	0.008	0.084

6.3.3 Summary of Experimental Results

I tested the performance of the dc SQUID magnetometer manufactured by Quantum Design, Inc., by processing the experimental data through the step 1 filters. As the calibration of the magnetometer revealed, the bias drift in the SQUID signal was much bigger than what was assumed in the simulation, and the step 1 filters became

unstable as a consequence when the process noise on the readout bias term was too small. Although I could stabilize them by increasing the process noise, the resulting estimation accuracy degraded accordingly and was four times worse for the NS_s term and eleven times worse for the EW_s term. As a hypothetical case, if we use the Quantum Design's SQUID magnetometer for the science mission, the final estimation accuracy of the geodetic precession rate will be about 2 milliarcseconds per year, and that of the frame-dragging precession rate will be about 5 milliarcseconds per year. When we design the SQUID magnetometer for the science mission, we can reduce the temperature-dependent bias drift by implementing a temperature regulation system to the magnetometer and by reducing the temperature coefficient of each component. The final estimation accuracy can also be improved by modeling the phase delay in the lowpass filter in the Kalman filter's model.

CHAPTER 7. CONCLUSIONS

7.1 Conclusions

I designed and conducted the niobium bird experiment that comprised the truth model, the Kalman filters, and the prototypical readout system with a commercially available dc SQUID magnetometer and an anti-aliasing filter. The truth model simulated the science signal that was injected into the SQUID readout system through a waveform generator. The SQUID magnetometer measured the magnetic flux created by the injected current, and the measurement was sampled and stored. The step 1 filters processed the sampled data, and I evaluated the filter performance by analyzing the estimation time history.

I constructed the truth model by defining the standardized coordinate frames and the rotational matrices among them and by defining and generating the random sequences to simulate error signals. The standardized coordinate frames clarified the simulation of

the science signal with no ambiguity in signs, and the careful analysis and generation of the random sequences gave credibility to the noise simulation. This truth model should provide a solid platform for the future testing, and the source codes are available on request.

I extended X. Qin's work and reformulated the two-step Kalman filters. My two-step filters used the same algorithm, the square-root information filter, but had simplified states and a better initialization scheme. I first verified the filters by simulation using the truth model that I developed. With a 5-hour SQUID and a ten-minute roll period, the two-step filters yielded the estimation accuracy of 0.5 milliarcsecond per year for the geodetic precession rate, Ω_G , and 0.4 milliarcsecond per year for the frame-dragging precession rate, Ω_F , after a simulation of a one-year mission. In addition to Qin's filters, I installed the recursive algorithm that improved the final estimation accuracy by 18% for Ω_G and 15% for Ω_F . I also investigated the effects of other factors such as the polhode signal induced by trapped flux, the pointing error, and a faster roll period. I modeled the polhode signal by modulation of the scale factor and reached the following conclusions:

- A 0.1-hour polhode period, which was closest to the roll period among 0.1-hour, 1-hour, and 10-hour polhode periods, gave the best estimation accuracy because the spectral separation of the polhode signal from the science signal was maximized;
- Estimation of the amplitude and the phase of the polhode signal with extra filter states improved the estimation accuracy;
- A longer step 1 window improved the estimation accuracy because the longer window gave a better frequency resolution.

I tested the two-step Kalman filter with various pointing errors whose rms value ranged from 5 to 50 milliarcseconds. Even though DiEposti demonstrated the effectiveness of his gain matching scheme using the satellite's dither motion, I concluded that the gain matching scheme was not necessary because the readout noise with a 5-hour SQUID was

larger than the error introduced by the telescope's pointing error with 20 milliarcseconds rms. The simulations showed that the final estimation accuracy did not degrade even when the pointing error terms were not subtracted from the science signal. I should note that I assumed a zero mean of the pointing error during the simulation, which may limit the validity of the conclusion and may require further investigation of the effect of a non-zero mean pointing error. The last issue that I investigated by simulation was the effect of the faster roll period. I speeded up the roll period from ten minutes to one minute, which effectively increased the signal-to-noise ratio by a factor of $\sqrt{10}$. The simulations showed that the final estimation accuracy was improved by 24% for Ω_G and by 22% for Ω_F . These improvements were not as dramatic as I expected compared with the gain in the signal-to-noise ratio. Although the ten-time better signal-to-noise ratio suggested that the estimation accuracy should be improved by $\sqrt{10}$, the actual estimation accuracy did not improve as much because the other error sources such as the telescope pointing error, the quantization error in the A-to-D converter, and the roll phase error could become dominant over the SQUID readout noise. Thus, one should conduct a complete error analysis for the one-minute roll period to assess the realistic improvement in the estimation accuracy.

Finally, I conducted the first phase of the niobium bird experiment that employed a commercially available dc SQUID magnetometer. I first calibrated the data injection instruments, the SQUID magnetometer, and the data sampling instruments to isolate the error sources. I found a large temperature-dependent bias drift in the SQUID magnetometer, Model 5000, manufactured by Quantum Design, Inc. The bias drift was about twenty times worse than what was assumed in the simulations. I then injected the simulated science signal into the readout system and sampled the output of the SQUID magnetometer. I tested the step 1 filters with the experimentally sampled science signal. The step 1 filters became unstable when the process noise on the bias term was too small.

Even though I could stabilize the filters by increasing the process noise, the estimation accuracy of step 1 filters degraded by a factor of four in the North-South direction and by a factor of eleven in the East-West direction. As a hypothetical case, if I project the performance of the Quantum Design dc SQUID magnetometer for the one-year mission, the final estimation accuracy will be 2 milliarcseconds per year for the geodetic precession rate and 5 milliarcseconds per year for the frame-dragging precession rate. The final estimation accuracy can be easily improved to 0.5 milliarcseconds per year by installing less temperature-sensitive components and a temperature regulation system to the SQUID magnetometer for the science mission.

Although the first phase of the niobium bird experiment showed that the bias drift in a commercially available dc SQUID magnetometer was too large to accomplish the mission requirements, the experiment was a significant success in the sense that it revealed an important design issue that was previously overlooked and established a baseline for an integrated test environment. With less sensitive circuits and a tighter temperature control, the bias drift should meet the GP-B specification, but this must be verified.

7.2 Limitations of This Study and Recommendations for Future Work

Even though I completed the first phase of the niobium bird experiment, it only marked the beginning of a series of tests conducted within the niobium bird experiment. In this section, I will discuss the limitations of my work and recommendations for future research. The truth model that I developed in Chapter 4 provides a solid baseline for a long-term analysis, however, it does not model the short-term effects such as the trapped flux signal at the spin frequency and the interference from the suspension system. In Section 5.3, I stated that the Kalman filters yielded best results when the polhode frequency was closest to the roll frequency. This analysis was based on a simplified

model of the trapped flux signal, the modulation of the scale factor at the polhode frequency. Although this model was adequate for the preliminary investigation, a more precise model that the spin frequency signals and the flux jumps should be used to test the validity of my claim. G. M. Gutt and G. Haupt are currently working on a more precise model of the trapped flux signal, which includes random distribution of flux quanta on the gyroscope's surface and a universal curve of the coupling between the trapped flux and the pickup loop (Ref. 54). Their model should provide better tool for investigating the effects of the trapped flux on the data reduction. In Section 5.5, I found that the final estimation accuracy was improved only by 22 to 24% when the satellite's roll speeded up from ten minutes to one minute. Although I listed the possible error sources other than the SQUID noise that contributed to the unexpectedly small improvement, I could not isolate the error source that contributed the most because the investigation started too late to be included in this thesis. The faster roll period is advantageous in the sense that one can increase the signal-to-noise ratio by moving the science signal to a higher frequency because the SQUID noise has $1/f$ spectral power density. However, the other factors such as the pointing error and the quantization error start to affect the final estimation accuracy. It may be possible to improve the final estimation accuracy as much as the improvement in the SQUID noise if all the factors are taken into consideration and tuned accordingly.

The niobium bird experiment completed its first phase successfully. The second and later phases should include the science mission instruments such as the SQUID controller, the lowpass filter, the A-to-D converter and the clock generator that we design for the Gravity Probe B program. As I pointed out in Section 6.3, the design of the SQUID controller should minimize the temperature-dependent variation in the SQUID readout and should implement a temperature regulation system. One should test the two-step Kalman filters with the niobium bird experiment as more and more flight

instruments replace the commercially available units. The experiment should also test the interference between the suspension system and the SQUID readout system. The niobium bird experiment has enough injection terminals to the low temperature core so that the simulated suspension signals can be injected into the electrodes.

The data reduction for the GP-B program was developed and analyzed by many GP-B staff members including former graduate students, R. Vassar, T. G. Duhamel, R. S. DiEsposti, and X. Qin. Late J. V. Breakwell inspired many of us in this effort, and Qin, who developed the two-step filters, was the last Ph.D. student he advised. Research by each individual was closely related and formed a firm foundation for the success of this mission. The niobium bird experiment was established on the basis of these efforts and provides a low cost, realistic, integrated test environment for the data reduction and the readout system. I sincerely hope this experiment will become an irreplaceable asset for the Gravity Probe B program.

REFERENCES

1. R. R. Shannon, "The Hubble Space Telescope: Technical and Managerial Aberrations," *Optics & Photonics News* , pp. 24-27 (1991).
2. M. C. Weisskopf, "The Advanced X-Ray Astrophysics Facility (AXAF)," *Acta Astronautica* **17**, pp. 575-578 (1988).
3. V. Neal, G. Fishman, D. Kniffen, "Gamma-Ray Observatory: The Next Great Observatory in Space," *Mercury* , pp. 98-111 (1990).
4. L. I. Schiff, "On Experimental Tests of the General Theory of Relativity," *American Journal of Physics* **28**, pp. 340-343 (1959).
5. L. I. Schiff, "Possible New Experimental Test of General Relativity Theory," *Physical Review Letters* **4**, pp. 215-217 (1960).
6. R. Vassar, J. V. Breakwell, C. W. F. Everitt, R. A. Van Patten, "Orbit Selection for the Stanford Relativity Gyroscope Experiment," *Journal of Spacecraft and Rockets* **19**, pp. 66-71 (1982).

7. R. Vassar, "Error Analysis for the Stanford Relativity Gyroscope Experiment," Ph.D. Dissertation, Stanford University (1982), SUDAAR 531.
8. C. W. F. Everitt, "The Stanford Relativity Gyroscope Experiment (A): History and Overview," in *Near Zero: New Frontiers of Physics*, J. D. Fairbank, J. B. S. Deaver, C. W. F. Everitt, P. F. Michelson, Eds. (W. H. Freeman and Company, New York, 1988), pp. 587-639.
9. P. Axelrad, "A Closed Loop GPS Based Orbit Trim System for Gravity Probe B," Ph.D. Dissertation, Stanford University (1990), SUDAAR 598.
10. B. W. Parkinson, private communication on feasibility and effects of speeding up the satellite roll (Oct. 1992).
11. B. W. Parkinson, J. R. Crier, "Phase-Lock Roll Control for Inertially-Pointing Spacecraft by Correlations of Star Intensity Profiles with a Stored Reference," *Journal of Guidance and Control* **72**, pp. 3-23 (1990).
12. Report on a Program to Develop a Gyro Test of General Relativity in a Satellite and Associated Control Technology, edited by C. W. F. Everitt, W. W. Hansen Experimental Physics Laboratory, Stanford University (1980). Contributors: J. T. Anderson, et al.
13. F. London, *SUPERFLUIDS Macroscopic Theory of Superconductivity* (Dover Publications, Inc., New York, 1961), vol. 1.
14. J. T. Anderson, "The Stanford Relativity Gyroscope Experiment (C): London Moment Readout of the Gyroscope," in *Near Zero: New Frontiers of Physics*, J. D. Fairbank, J. B. S. Deaver, C. W. F. Everitt, P. F. Michelson, Eds. (W. H. Freeman and Company, New York, 1988), pp. 659-670.
15. G. M. Gutt, private communication on operational principle of dc SQUID magnetometer (Dec. 1992).

16. T. V. Duzer, C. W. Turner, *Principles of Superconductive Devices and Circuits* (Elsevier, New York, 1981).
17. S. T. Ruggiero, D. A. Rudman, *Superconducting Devices* (Academic Press, Inc., 1990).
18. T. G. Duhamel, "Contributions to the Error Analysis in the Relativity Gyroscope Experiment," Ph.D. Dissertation, Stanford University (1984), SUDAAR 540.
19. R. S. DiEsposti, "Data Reduction Simulation for the Stanford Relativity Gyroscope Experiment," Engineer Dissertation, Stanford University (1986).
20. X. Qin, "Data Reduction Analysis for the Stanford Relativity Gyroscope Experiment," Ph.D. Dissertation, Stanford University (1991), SUDAAR 611.
21. C. W. F. Everitt, "The Gyroscope Experiment I: General Description and Analysis of Gyroscope Performance," in *Experimental Gravitation*, B. Bertotti, Eds. (Academic Press, Inc., New York, 1973), pp. 361-380.
22. C. W. F. Everitt, A Superconducting Gyroscope to Test Einstein's General Theory of Relativity, Proceedings of the Society of Photo-Optical Instrumentation Engineers (1978).
23. I. I. Shapiro, M. E. Ash, R. P. Ingalls, W. B. Smith, D. B. Campbell, R. B. Dyce, R. F. Jurgens, G. H. Pettengill, "Fourth Test of General Relativity: New Radar Result," *Physical Review Letters* **26**, pp. 1132-1135 (1971).
24. I. I. Shapiro, "New Method for the Detection of Light Deflection by Solar Gravity," *Science* **157**, pp. 806-808 (1967).
25. E. B. Fomalont, R. A. Sramek, "The Deflection of Radio Waves by the Sun," *Comments on Astrophysics* **7**, pp. 19-33 (1977).
26. N. J. Kasdin, "Precision Pointing Control of the Spinning Gravity Probe B Spacecraft," Ph.D. Dissertation, Stanford University (1991), SUDAAR 606.

27. H. W. Sorenson, "On the Development of Practical Nonlinear Filters," *Information Sciences* **7**, pp. 253-270 (1974).
28. K. W. Iliff, R. E. Maine, "Observations on Maximum Likelihood Estimation of Aerodynamic Characteristics from Flight Data," *Journal of Guidance and Control* **2**, pp. 228-234 (1979).
29. H. Uematsu, W. W. Hansen Experimental Physics Laboratory, Proposal for a Standardized Set of GP-B Coordinate Systems, internal report (Apr. 1990).
30. Department of Defense World Geodetic System 1984 - Its Definition and Relationships with Local Geodetic Systems, edited by R. W. Smith, Defense Mapping Agency (30 Sep. 1987). Contributors:
31. J. S. Bendat, A. G. Piersol, *Random Data: Analysis and Measurement Procedures* (Wiley, New York, 1986).
32. A. V. Oppenheim, R. W. Schaffer, *Discrete-Time Signal Processing*. A. V. Oppenheim, Eds., Prentice Hall Signal Processing Series (Prentice Hall, Englewood Cliffs, New Jersey, 1989).
33. K. S. Shanmugan, A. M. Breipohl, *Random Signals: Detection, Estimation and Data Analysis* (John Wiley & Sons, New York, 1988).
34. S. Ross, *A First Course in Probability* (Macmillan Publishing Company, New York, 1976).
35. Nautical Almanac Office, United States Naval Observatory, *Astronomical Almanac* (1987).
36. A. E. Roy, D. Clarke, *Astronomy: Principles and Practice* (Adam Hilger Ltd., Bristol, 1982).
37. V. A. Brumberg, "Astronomical Measurements and Coordinate Conditions in Relativistic Celestial Mechanics," *Celestial Mechanics* **20**, pp. 329-342 (1979).

38. J. T. Anderson, C. W. F. Everitt, Department of Physics, Stanford University, Limits on the Measurement of Proper Motion and the Implications for the Relativity Gyroscope Experiment, unpublished report (1979).
39. H. Uematsu, Stanford University, Department of Aeronautics and Astronautics, True Gyroscope Signal Generator for the Niobium Bird Test - BMODEL.PAS Ver 1.0, AA290 Report (16 Jun. 1988).
40. N. J. Kasdin, W. W. Hansen Experimental Physics Laboratory, Gravity Probe-B Twelve Science Requirements, internal report (7 Jan. 1992).
41. C. F. Van Loan, "Computing Integrals Involving the Matrix Exponential," *IEEE Transactions of Automatic Control* **AC-23**, 3 (1978).
42. A. E. Bryson, Stanford University, AA278B Lecture Notes (Spring Quarter, 1988).
43. J. M. Lockhart, N. J. Kasdin, W. W. Hansen Experimental Physics Laboratory, SQUID Sensor Noise Definition and GP-B Data Reduction, internal report (11 Mar. 1992).
44. J. M. Lockhart, private communication on operational range of the SQUID magnetometer for the science mission (Aug. 1993).
45. B. M. Gordon, "Linear Electronic Analog/Digital Conversion Architectures, Their Origins, Parameters, Limitations, and Applications," *IEEE Transactions of Circuits and System* **CAS-25**, pp. 391-418 (Jul. 1978).
46. P. Horowitz, W. Hill, *The Art of Electronics* (Cambridge University Press, Cambridge, 1980).
47. G. F. Franklin, J. D. Powell, *Digital Control of Dynamic Systems* (Addison-Wesley Publishing Company, Reading, Massachusetts, 1980).
48. R. A. Van Patten, private communication on feasibility of installing a space qualified A-to-D converter with 16-bit resolution for the GP-B science mission (1990).

49. H. Goldstein, *Classical Mechanics* (Addison-Wesley Publishing Company, Reading, Massachusetts, 1980).
50. D. T. Greenwood, *Principles of Dynamics* (Prentice-Hall, Inc., Englewood Cliffs, New Jersey, 1965).
51. Final Report on NASA Grant 05-020-019 to Perform a Gyro Test of General Relativity in a Satellite and Develop Associated Control Technology, edited by C. W. F. Everitt, W. W. Hansen Experimental Physics Laboratory, Stanford University (1977). Contributors: J. T. Anderson, B. Cabrera, R. R. Clappier, D. B. Debra, J. A. Lipa, G. J. Siddall, F. J. v. Kann, R. A. Van Patten.
52. G. J. Bierman, *Factorization Methods for Discrete Sequential Estimation*. R. Bellman, Eds., Mathematics in Science and Engineering (Academic Press, Inc., San Diego, CA, 1977), vol. 128.
53. B. W. Parkinson, "Closed-Form Solution for Motion of a Spinning Rigid Body," *Journal of Spacecraft and Rockets* (1968).
54. L. L. Wai, "The Effect of Trapped Magnetic Flux Quanta on the London Readout in GP-B," Bachelor of Science Thesis in Physics Department, Stanford University (1989).
55. Y. M. Xiao, W. W. Hansen Experimental Physics Laboratory, Stanford University, Effects of Trapped Magnetic Flux on the Readout of the GP-B Experiment, internal memo (Jul. 1991).
56. B. W. Parkinson, N. J. Kasdin, "Twenty Milliarcsec Pointing System For the Rolling GP-B Spacecraft," *Guidance and Control, Advances in the Astronautical Sciences* **66**, pp. 65-89 (1988).
57. J. M. Lockhart, SQUID Readout and Ultra-low Magnetic Fields for Gravity Probe-B (GP-B), SPIE Cryogenic Optical Systems and Instruments II (Society of Photo-Optical Instrumentation Engineers, Los Angeles, California, 1986), vol. 619, pp. 148-156.

58. J. M. Lockhart, B. Muhlfelder, private communication on calibration results of Model 5000 output gain (Jul. 1993).
59. J. M. Lockhart, W. W. Hansen Experimental Physics Laboratory, Stanford University, Notes on Estimation of Power Spectral Densities via Fast Fourier Transform, internal memo (Aug. 1993).
60. J. M. Lockhart, W. W. Hansen Experimental Physics Laboratory, Stanford University, Estimation of Power Spectral Densities via Fast Fourier Transform—Notes on the Normalization of Standard Software Packages, internal memo (Sep. 1993).

APPENDICES

Appendix A. Program Lists of Truth Model

The truth model comprises two C programs, *gpb.c* and *crandom.c*. *Gpb.c* contains the various models that were discussed in Chapter 4 such as the earth motion model, the satellite motion model, the pointing error model and so on. *Crandom.c* contains the random number generators that were discussed in Chapter 3.

Gpb.c produces the simulated science signal at a user-specified sampling rate and stores the data in an output file, *meas.bin*. A user can specify the sampling rate and the duration of simulation by specifying input arguments. The error models such as the pointing error, the roll phase error, the SQUID noise can be toggled by flags stored in an input file, *cond.dat*. The header file, *globals.h*, contains constants such as astronomical unit, Rigel's right ascension and declination, starting date of science mission and the

declaration of various structures. The followings are an example of *cond.dat*, the program list of *globals.h*. The program list of *gpb.c* is available on request.

A.1 Example of Conditional File COND.DAT

The last column of *cond.dat* contains the conditional flags for the error models. If the flag is asserted, the corresponding error model is active in the simulation. Otherwise, the error model is turned off during the simulation, and that specific error becomes zero. For the example below, the simulation includes the SQUID readout noise only.

(1) Squid Noise Flag	%	1
(2) A/D Error Flag	%	0
(3) Proper Motion of Rigel	%	0
(4) Roll Phase Control Error Flag	%	0
(5) Control Error Flag	%	0
(6) Fixed Random Number Flag	%	0
(7) Trapped Flux Flag	%	0
(8) Scale Factor Variation Flag	%	0
(9) Roll Phase Measurement Noise Flag	%	0
(10) Rigel Initial Misalignment	%	0

A.2 Program List of GLOBALS.H

Globals.h contains the definition of constant values that are necessary for the simulation such as the celestial coordinates of Rigel, the satellite's altitude, the gravitational constant, the speed of light, and parameters used for the error models.

```

/*-----
  CONSTANTS
-----*/
/**** Constants *****/
  AUNIT      : astronomical unit (meter/au)
  RAD2SEC    : radian to arcsecond conversion factor
  SEC2RAD    : arcsecond to radian conversion factor
  DEG2RAD    : degree to radian conversion factor
  *****/
#define pi          3.14159265358979
#define AUNIT      1.49597870e11      /* meter/au */
#define RAD2SEC    (180.0*3600.0/pi)  /* arcsec/rad */
#define SEC2RAD    (pi/180.0/3600.0)  /* rad/arcsec */
#define DEG2RAD    (pi/180.0)         /* rad/deg */

```

```

/**** Mission Constants ****
SDATE          : day of year when the science mission is started (day)
LAMDA_RIGEL    : right ascension of Rigel (radian)
DELTA_RIGEL    : declination of Rigel (radian)
DISTN_RIGEL    : distance from earth to Rigel (meter)
DAYS_OF_YEAR   : number of days per year (day)
YEAR2SEC       : year to second conversion factor
****/

#define SDATE          245.0
#define LAMDA_RIGEL    1.36980711901732 /* rad */
#define DELTA_RIGEL    -1.43388494324956e-1 /* rad */
#define DISTN_RIGEL    8.215712857408999e+07 /* au (=1300ly) */
#define DAYS_OF_YEAR   365.25 /* day */
#define YEAR2SEC       (DAYS_OF_YEAR*24.0*3600.0) /* sec/year */

/**** Physical Constants ****
YCLIGHT        : speed of light (meter/sec)
GRUD_SUN       : gravitational radius of sun (meter)
GCON_ETH       : gravitational constant of earth (meter^3/sec^2)
RDIUS_ETH      : mean radius of earth (meter)
SPIN_ETH       : spin angular velocity of earth (rad/sec)
****/

#define VCLIGHT        299792458.0 /* meter/sec */
#define GRUD_SUN       1476.625016 /* meter */
#define GCON_ETH       3.986005e14 /* meter^3/sec^2 */
#define RDIUS_ETH      6370998.9 /* meter */
#define SPIN_ETH       0.7292115147e-4 /* rad/sec */

/**** Satellite Parameters ****
ANVEL_SAT      : satellite's angular velocity (rad/sec)
RDIUS_SAT      : radius of GPB orbit (meter)
IPHAS_SAT      : initial phase angle of GPB orbit (rad)
INCTN_SAT      : inclination of GPB orbit (rad)
OMEGA_SAT      : right ascension of GPB orbit (rad)
OCL_RDIUS      : occultation radius of GPB orbit (meter)
ROLL_PRD       : satellite's roll period (sec) (default value)
****/

#define ANVEL_SAT      1.073175037e-3 /* rad/sec */
#define RDIUS_SAT      7020998.9 /* meter */
#define IPHAS_SAT      pi /* rad */
#define INCTN_SAT      1.57079632679490 /* rad */
#define OMEGA_SAT      1.36980711901732 /* rad */

#define OCL_RDIUS      (RDIUS_ETH+100.0e3) /* meter */

#define ROLL_PRD       600.0 /* sec */

/**** A/D converter parameters ****
A2D_RANGE = 200arcsec : A/D conversion range
A2D_BITS = 16bits     : A/D resolution bits
A2D_BIAS = 0.0arcsec  : A/D bias
A2D_SF = 1            : A/D scale factor
****/

```



```

#define          A2D_RANGE      (200.0*SEC2RAD)          /* rad */
#define          A2D_BITS      16.0                    /* bits */
#define          A2D_BIAS      0.0                      /* rad */
#define          A2D_SF        1.0                      /* rad/rad */

/**** RIGEL initial misalignment parameter *****/
RGLMSL_RMS = 5 arcsec      : Rigel initial misalignment rms
*****/
#define          RGLMSL_RMS    5.0                      /* arcsec */

/**** SQUID bias variation parameters *****/
SQUID_ALPHA = (1arcsec)^2/year : 1arcsec variation over one year
SQUID_TCNST = 10 hrs          : variation time constant
*****/
#define          SQUID_ALPHA    (1.0/YEAR2SEC)          /* arcsec^2/sec */
#define          SQUID_TCNST    (10.0*3600.0)           /* sec */

/**** Cg scale factor variation parameters *****/
SFC_ALPHA = (0.1%)^2/yr : 0.1% variation over one year
SFC_TCNST = 1 day        : variation time constant
*****/
#define          SFC_ALPHA      (0.01/YEAR2SEC)         /* %^2/sec */
#define          SFC_TCNST      (24.0*3600.0)           /* sec */

/**** Attitude control error parameters *****/
ATTCNT_TCNST = 2.0 sec      : attitude control time constant
ATTCNT_RMS = 20 marcsec     : attitude control error rms
*****/
#define          ATTCNT_TCNST    2.0                    /* sec */
#define          ATTCNT_RMS      20e-3                  /* arcsec */

/**** Roll phase control error parameters *****/
RLLCNT_TCNST = 10.0 sec     : roll phase control time constant
RLLCNT_RMS = 10.0 arcsec    : roll phase control error rms
*****/
#define          RLLCNT_TCNST    10.0                   /* sec */
#define          RLLCNT_RMS      10.0                   /* arcsec */

/**** Roll phase measurement error parameter *****/
RLLMEAS_RMS = 10.0 arcsec   : roll phase measurement error rms
*****/
#define          RLLMEAS_RMS     10.0                   /* arcsec */

/-----
TYPE Definitions
-----*/
typedef      unsigned char      BYTE;

typedef struct {
    double tsec;    /* sec */      /* elapsed time since mission initialization */
    double sg;      /* arcsec */   /* science signal */
    double croll;   /* rad */      /* command roll angle */
    double ab1;     /* arcsec */   /* North-South aberration */

```

```

    double ab2;      /* arcsec */      /* East-West aberration */
} meas_type;

typedef struct {
    double tsec;      /* sec */      /* elapsed time since mission initialization */
    double Res_c[3]; /* au */      /* position of earth in C-0 frame */
} celestial_type;

typedef struct {
    char squid_noise;      /* flag for squid noise */
    char a2d_error;      /* flag for A/D converter error */
    char prop_rigel;      /* flag for proper motion of Rigel */
    char roll_control_error; /* flag for roll control error */
    char control_error; /* flag for pointing control error */
    char fixed_random; /* flag for fixed random sequence */
    char trapped_flux; /* flag for trapped flux model */
    char scale_factor_var; /* flag for scale factor variation */
    char roll_meas_noise; /* flag for roll measurement noise */
    char init_misalignment; /* flag for initial misalignment of gyro spin axis */
} cond_type;

```

Appendix B. Formulation of SQUID Noise Shaping Filter

I designed the SQUID shaping filter described in Section 4.2.5.1 by MATLAB. I listed the m-files that I used for the design in the following sections. A continuous shaping filter was formulated first in a classical form, which was then converted into a state-space form. I used the Van Loan's algorithm to discretize the filter (Ref. 41). A. E. Bryson (Ref. 42) provided the m-file *cvrtq.m* that converts a continuous filter into a discrete filter using the algorithm. Section B.1 lists the m-file *gsquid.m*, which I used to check the design, and Section B.2 lists *cvrtq.m*, which was provided by A. E. Bryson.

B.1 Program List of GSQUID.M

The continuous filter expressed in a classical form was determined by trial-and-error to simulate the 1/f power spectral density. It was then converted into a discrete filter with 10-second sampling period. I also checked the validity of the discrete filter by calculating the power spectral density of the simulated noise in MATLAB. Note

that the MATLAB function, *spectrum.m*, was corrected by a factor of a sampling period because this function assumes 1-second sampling period.

```
% SQUID noise shaping filter
% 8/7/89 Hiro Uematsu

% Continuous shaping filter
z1=6*pi*10^(-4); z2=6*pi*10^(-3); z3=6*pi*10^(-2);
p1=2*pi*10^(-4); p2=2*pi*10^(-3); p3=2*pi*10^(-2); p4=2*pi*10^(-1);
ks=1/0.19263154277073;
num=ks*conv(conv([1/z1 1],[1/z2 1]),[1/z3 1]);
den=conv(conv([1/p1 1],[1/p2 1]),conv([1/p3 1],[1/p4 1]));

omega=logspace(-5,2,100); freq=omega/2/pi;
[mc,pc]=boded(num,den,omega);
loglog(freq,mc.*conj(mc),freq,1/600.0./freq),grid
xlabel('frequency (Hz)'), ylabel('power spectral density (arcsec^2*sec)')
pause
semilogx(freq,pc),grid
xlabel('frequency (Hz)'), ylabel('phase response (deg)')

% Conversion to a discrete equivalent filter
a=den(2:length(den))*p1*p2*p3*p4;
b=num*p1*p2*p3*p4;
% Observer canonical form
F=[-a',[1 0 0 0]';[0 1 0 0]';[0 0 1 0]'];
G=b'; H=[1 0 0 0];
% Conversion using Van Loan's algorithm
Q=0.018; TS=10.0;
[PHI,W]=cvrtq(F,G,Q,TS);
GAMMA=sqrt(diag(W));

% Gain on the additional background white noise
fcut=0.1;
if TS==10,
    D=dboded(PHI,GAMMA,H,[0],1,2*pi*0.053*TS);
else
    D=dboded(PHI,GAMMA,H,[0],1,2*pi*fcut*TS);
end

% Simulate the SQUID noise
nsim=input('If you want to run the simulation, let Y=1. Y=? ');
if nsim==1,
    rand('normal')
    u=rand(2^14,1);
    N=2048;M=N/2;
    y=dlssim(PHI,GAMMA,H,D,u);
    P=spectrum(y,N)*TS; % spectrum.m must be corrected for the case with TS!=1.0
    f=0:1/TS/2/M:1/TS/2*(1-1/M);
    axis([-5 0 -5 0])
    loglog(freq,Q*mc.*conj(mc),f,P(:,1)).',1/600.0,Q,'')
    xlabel('frequency (Hz)'),ylabel('PSD (arcsec^2/Hz)')
```

```

        grid,title('Predicted vs. Simulated PSD of SQUID Noise')
        axis
    end

```

B.2 Program List of CVRTQ.M

A. E. Bryson provided the following m-file, *cvrtq.m*, during the lecture of AA278B (Winter 1987/88) at Stanford University. This program converts a continuous filter in a state-space form into a discrete equivalent filter using the Van Loan's algorithm.

```

function [PHI,W]=cvrtq(F,GA,Q,TS)
% [PHI,W]=cvrtq(F,G,Q,TS)
% Determines covariance W of full-rank random sequence wd(k)
% that is equivalent to white noise w(t) having spectral
% density Q and distribution matrix GA, with sampling
% time TS, i.e.  $\dot{x} = Fx + GA^T w$  is equivalent to  $x(k+1) =$ 
%  $PHI^T x(k) + wd(k)$  at  $t = k^T TS$ .
%  $W = \text{Integral}[PHI(t)^T GA^T Q GA^T PHI'(t) dt]$  over 0 to TS; 5/30/89.
    [NS,ND]=size(GA);
    S=[-F,GA^T*Q*GA^T;zeros(NS),F'];
    C=expm(S*TS);
    G2=C([1:NS],[NS+1:2*NS]);
    F3=C([NS+1:2*NS],[NS+1:2*NS]);
    PHI=F3';
    W1=F3'*G2;W=(W1+W1')/2;

```